IPPT Reports on Fundamental Technological Research
2/2025

Mariusz Ostrowski

Semi-Active Control of Energy Transfer Between Vibration Modes in Mechanical Structures

Institute of Fundamental Technological Research
Polish Academy of Sciences

Semi-Active Control of Energy Transfer Between Vibration Modes in Mechanical Structures

IPPT Reports on Fundamental Technological Research

Institute of Fundamental Technological Research
Polish Academy of Sciences
Warsaw

IPPT Reports on Fundamental Technological Research
2/2025

Semi-Active Control of Energy Transfer Between Vibration Modes in Mechanical Structures

Mariusz Ostrowski

Institute of Fundamental Technological Research
Polish Academy of Sciences

Warsaw 2025

The monograph is based on a doctoral dissertation entitled 'Semi-active control of energy transfer between vibration modes in mechanical structures', written under the supervision of Bartłomiej Błachowski, PhD, Eng., Prof. IPPT PAN and assistant supervision of Grzegorz Mikułowski, PhD, Eng., defended in June 2025 at the Department of Intelligent Technologies at the Institute of Fundamental Technological Research of the Polish Academy of Sciences.

Reviewers:
dr hab. inż. Paweł Kudela, Prof. IMP PAN
dr hab. inż. Andrzej Myśliński, Prof. IBS PAN
prof. dr hab. inż. Jerzy Warmiński

Proofreading:
Ewa Kiczko

Graphic design cover:
Eliza Jezierska

ISSN 2299-3657
ISBN 978-83-65550-65-1 (print)
ISBN 978-83-65550-64-4 (online)
DOI: https://doi.org/10.24423/9788365550644

Received on 2 October 2025

Institute of Fundamental Technological Research Polish Academy of Sciences
(Instytut Podstawowych Problemów Techniki Polskiej Akademii Nauk (IPPT PAN))
Pawińskiego 5B, 02-106 Warsaw
Phone 48 22 826 60 22, e-mail: reports@ippt.pan.pl
https://reports.ippt.pan.pl

Typesetting in LaTeX: Katarzyna Jezierska
Printed in Poland by: EXDRUK, Rysia 6, 87-800 Włocławek, Poland

Acknowledgements

I would like to express special gratitude to Jehovah, the God of armies, especially for His creations, which we humans can marvel at, learn and study. Because of His inconceivable wisdom and the great love that went into the creation, we will never fully fathom them, as Solomon said:

"*He has made everything beautiful in its time. He has even put eternity in their heart; yet mankind will never find out the work that the true God has made from start to finish.*"

(Ecclesiastes 3:11; NWT).

I would like to thank my supervisor, Professor Bartłomiej Błachowski, in particular for his enormous contribution to my scientific development. Professor Błachowski not only guided me in learning about the issues of dynamics and control of structures, sharing his extensive experience and knowledge with me, but also taught me appropriate values referring to scientific ethics. On many occasions, he reminded me that science is not about points, statistics and citations, but about hard work resulting in deepening knowledge and understanding of the phenomena studied.

I would like to thank my assistant supervisor, Doctor Grzegorz Mikułowski, for his dominant contribution to the experiments described in Chapter 5 of this dissertation and the hardware implementation of the proposed control strategy. This work required great persistence, which resulted in obtaining unique experimental results and deepening knowledge on the proposed strategy. I also thank for instructive thoughts and conversations on scientific research methodology.

I would also like to thank Doctor Dominik Pisarski and Professor Łukasz Jankowski for helping me, together with the Professor Błachowski, to choose novel and interesting direction of research at the very beginning of my doctoral studies. Seminars given by Doctor Pisarski were an inspiration for implementation of the instantaneously optimal approach in the control strategy proposed in this thesis.

I would like to thank Professor Łukasz Jankowski also for creating a favourable atmosphere in Department of Intelligent Technologies, for his management and invaluable advice on scientific issues.

Thanks are also due to my wife, Małgorzata, for encouraging me to finish my dissertation, supporting me in my professional and private life, taking care of the warmth of our home and for being patient with me.

Streszczenie rozszerzone

W niniejszej rozprawie skupiono się na nowej strategii półaktywnego sterowania modalnego, pozwalającego na precyzyjne przenoszenie energii pomiędzy poszczególnymi postaciami drgań konstrukcji mechanicznej. Sterowanie jest realizowane za pomocą blokowanych połączeń rotacyjnych – blokowanych węzłów – zainstalowanych w wybranych miejscach konstrukcji ramowej. Połączenie takie może być dynamicznie zablokowane i przenosić moment gnący między belkami konstrukcji lub być odblokowane i pracować jak zawias. Przenoszony moment gnący odpowiada za sprzężenie modalne, co skutkuje wymianą energii mechanicznej między postaciami drgań. Sterowanie ma zastosowanie zarówno w tłumieniu drgań, jak i usprawnianiu procesu odzyskiwania energii z drgań (*energy harvesting*). Praca obejmuje również inne aspekty strategii sterowania, takie jak optymalne rozmieszczenie sensorów do filtracji modalnej oraz optymalne rozmieszczenie blokowanych połączeń. Nowa strategia sterowania została zweryfikowana zarówno numerycznie, jak i eksperymentalnie.

Wstęp, przegląd literatury i motywacja

Przegląd literaturowy będący częścią tej rozprawy pokazał, że choć zagadnienie sterowania drganiami konstrukcji jest badane od dekad, to nadal jest aktualne z uwagi na fakt, że drgania są często szkodliwe, a nawet mogą być źródłem niebezpieczeństw [1]. Jednak coraz większym zainteresowaniem cieszy się również odzyskiwanie energii z drgań i konwertowanie jej na energię elektryczną [2].

Z ważniejszych prac w kontekście niniejszej rozprawy należy wymienić te opisujące nieliniowe urządzenia (*nonlinear energy sink*, NES), które nie tylko pochłaniają energię drgań, lecz również powodują zmianę rozkładu spektralnego energii drgań konstrukcji w dziedzinie częstotliwości [3–7]. W zdecydowanej większości są to urządzenia pasywne. Zmiana udziału energetycznego w poszczególnych częstościach drgań konstrukcji jest powodowana przez sprzężenie modalne wywołane nieliniowymi charakterystykami pracy tych urządzeń. Powoduje to przeniesienie energii do postaci drgań konstrukcji wyższych rzędów, które zazwyczaj charakteryzują się dużym tłumieniem w porównaniu do podstawowych postaci drgań. Efekt ten można również uzyskać przez półaktywne sterowanie lokalnymi zmianami sztywności konstrukcji. Onoda i inni zaproponowali sterowanie konstrukcjami kratownicowymi wyposażonymi w człony o zmiennej sztywności [8]. Podczas ruchu konstrukcja ulega deformacji, co powoduje akumulację energii potencjalnej w odkształceniach. Nagłe zmniejszenie sztywności powoduje wtedy uwolnienie części tej energii w wysokoczęstotliwościowych drganiach swobodnych odpowiadających postaciom drgań wyższych rzędów. Następnie energia ta jest efektywnie tłumiona w materiale konstrukcji. Ten rodzaj strategii sterowania jest rozwijany również dzisiaj z zastosowaniem w konstrukcjach ramowych wyposażonych w blokowane rotacyjne węzły lub w konstrukcjach warstwowych, gdzie zmiana sztywności odbywa się przez delaminację [9–14]. Z uwagi na charakterystyczne dla tej grupy metod akumulowanie i uwalnianie nagromadzonej energii odkształceń są one nazywane „Prestress Accumulation–Release" (PAR). Mimo że lokalna zmiana sztywności wywołuje efekt sprzężenia modal-

nego, a w efekcie – wymianę energii między postaciami drgań, sterownik nie ma informacji o stanie konstrukcji wyrażonym za pomocą amplitud czy prędkości modalnych. W związku z tym PAR jest heurystycznym podejściem.

Głównym problemem w odzyskiwaniu energii z drgań mechanicznych jest nie tylko zwiększanie efektywności, lecz również poszerzenie roboczego pasma częstotliwości przetwornika elektromechanicznego [15]. Aby uzyskać jak najlepszy kompromis między szerokością pasma roboczego a szczytową wydajnością przetworników elektromechanicznych, celowo wprowadza się nieliniowości do charakterystyki tych urządzeń, np.: sprężyste zderzenia ciał w celu zwiększenia prędkości magnesu oddziałującego na cewkę elektromagnetyczną [16, 17] lub wprowadzenie zderzaków sprężynowych ograniczających skok magnesu [18]. Testowane są również przetworniki o więcej niż jednym stopniu swobody zaprojektowane tak, aby uzyskać kilka pików rezonansowych [19]. W ostatnim czasie intensywnie badany jest również wpływ rezonansu wewnętrznego w nieliniowych przetwornikach elektromechanicznych na poszerzenie roboczego pasma częstotliwościowego oraz na możliwość pracy urządzenia w wielu postaciach drgań [20]. Rezonans wewnętrzny i jego wpływ na wymianę energii między postaciami drgań jest często badany analitycznie.

W przeciwieństwie do zagadnienia odzyskiwania energii oraz wielu pasywnych nieliniowych układów (np. NES) sprzężenie modalne i jego wpływ na tłumienie drgań nie zostały dokładnie przebadane w strategiach półaktywnego sterowania, jak np. PAR. W szczególności mało znany jest mechanizm przenoszenia energii między postaciami drgań. Było to motywacją do podjęcia badań nad nową strategią półaktywnego sterowania modalnego. Proponowana strategia wykorzystuje rotacyjne blokowane węzły do precyzyjnego przenoszenia energii mechanicznej między wybranymi postaciami drgań. Sterowanie jest chwilowo optymalne i opiera się na analitycznych wyprowadzeniach opisujących wpływ zablokowania węzła na sprzężenie modalne skutkujące wymianą energii między poszczególnymi postaciami drgań. Proponowana strategia umożliwia nie tylko tłumienie drgań z narzuceniem priorytetu na poszczególne postacie, ale też usprawnienie procesu odzyskiwania energii z drgań. W drugim przypadku odbywa się to przez przeniesienie energii drgań do wybranej (docelowej) postaci, która współpracuje optymalnie z zamontowanym na konstrukcji przetwornikiem elektromechanicznym.

Dynamika konstrukcji z blokowanymi połączeniami

Zablokowanie lub odblokowanie węzła jest odwzorowane przez narzucenie lub odrzucenie więzów kinematycznych na odpowiednie rotacyjne stopnie swobody konstrukcji. W związku z tym zmieniają się: efektywna liczba stopni swobody sterowanej konstrukcji, jej właściwości dynamiczne oraz baza wektorów własnych reprezentujących postacie drgań, jak i jej wymiar (rys. 2.1 na s. 59).

Zauważono, że aby sterować konstrukcją, wystarczy opisać jej ruch w bazie wektorów własnych uzyskanej dla wszystkich węzłów w stanie odblokowanym. Jest to możliwe ze względu na największy i wystarczający wymiar tej bazy. Konieczne jest natomiast uwzględnienie efektu sprzężenia modalnego w modalnych równaniach ruchu opisanych w tej bazie. Pozwala to prawidłowo odwzorować efekt zablokowania i jego wpływ

na zachowanie konstrukcji. Zaletą takiego sformułowania jest to, że sprzężenie modalne pozwala opisać wymianę energii między postaciami drgań. Aby wprowadzić czytelnika w te zagadnienia, najpierw omówiono je na przykładzie prostego układu o dwóch stopniach swobody, a później zagadnienie rozszerzono na konstrukcje ramowe o dowolnej liczbie stopni swobody.

W celu ułatwienia obliczeń zaproponowano również używanie osłabionych więzów kinematycznych, gdy węzeł jest zablokowany. Takie więzy są realizowane za pomocą sterowanego współczynnika tłumienia wiskotycznego między rotacyjnymi stopniami swobody opisującymi blokowane węzły (rys. 2.11 na s. 78). Gdy węzeł jest zablokowany, współczynnik tłumienia osiąga bardzo dużą wartość, efektywnie usztywniając blokowane połączenie. W rezultacie otrzymujemy dwuliniowe równania ruchu, a uwzględniając ograniczenia nałożone na stan węzłów (całkowicie odblokowany lub całkowicie zablokowany), układ jest liniowy przedziałami (co po uwzględnieniu pętli sprzężenia zwrotnego stanowi klasę układów nieliniowych).

Mierzone wielkości fizyczne, optymalne rozmieszczenie sensorów i blokowanych węzłów

Algorytm sterowania jest oparty na oszacowaniu chwilowej wartości przepływu energii między postaciami drgań, czego nie można zmierzyć bezpośrednio. Wielkość tą można oszacować, znając prędkości modalne oraz momenty gnące przenoszone przez zablokowane węzły. Prędkości modalne monitorowanych postaci drgań są estymowane za pomocą filtracji modalnej. Momenty gnące natomiast są estymowane na podstawie pomiarów odkształceń w pobliżu każdego blokowanego węzła.

Aby ograniczyć wpływ szumu pomiarowego oraz wpływ postaci drgań wyższego rzędu na filtrację modalną, sensory rozmieszczono tak, aby uzyskać maksymalną wartość wyznacznika macierzy informacji Fishera. Jest to zadanie o charakterze kombinatorycznym, stąd aby zredukować nakład obliczeniowy, posłużono się nową metodą przybliżoną opartą na wypukłej relaksacji (zastąpieniu problemu dyskretnego jego ciągłym odpowiednikiem) [21].

W celu zapewnienia efektywnego działania sterowania zaproponowano również miarę sterowalności poszczególnych postaci drgań stosowaną w niniejszej pracy do optymalnego rozmieszczenia blokowanych węzłów. Standardowe miary sterowalności poszczególnych postaci drgań, jak np. gramian sterowalności, nie odzwierciedlają dokładnie zdolności węzłów do przenoszenia energii między postaciami drgań.

Prawo i algorytm sterowania, możliwe aplikacje

Zaproponowano chwilowo optymalne prawo sterowania, które w każdej chwili czasu zapewnia najbardziej stromy spadek funkcji celu. Funkcja celu jest ważoną sumą energii stowarzyszonych z poszczególnymi monitorowanymi postaciami drgań. Dobór wag ma kluczowe znaczenie i zależy od aplikacji proponowanej strategii sterowania.

W przypadku zastosowania do tłumienia drgań wszystkie wagi są dodatnie. Wtedy minimalizacja funkcji celu wymusza przepływ energii z monitorowanych postaci drgań do

pozostałych (niemonitorowanych) postaci – zazwyczaj wyższych rzędów. Odpowiedni dobór wag pozwala również na wymuszenie przepływu z każdej postaci drgań z pożądanym priorytetem.

W przypadku zastosowania do usprawnienia procesu odzyskiwania energii z drgań waga odpowiadająca docelowej postaci drgań ma wartość ujemną. Minimalizowanie funkcji celu będzie zatem wymuszało przepływ energii do tej postaci. Zakładając, że przetwornik elektromechaniczny jest dostrojony do docelowej postaci drgań, będzie on pracował zawsze w rezonansie, nawet jeżeli wymuszenie zewnętrzne pobudza konstrukcję w postaciach drgań dalekich od częstotliwości drgań własnych przetwornika. Węzły blokując się, nie wykonują pracy nad układem, sterowanie takie zatem nie destabilizuje układu podczas drgań swobodnych.

Zaproponowany algorytm sterowania pozwala zaimplementować prawo sterowania z uwzględnieniem ograniczeń sprzętowych. Wykazano, że naturalną własnością tego algorytmu jest blokowanie węzłów, gdy odpowiednie rotacyjne stopnie swobody mają równe prędkości (lub równe w przybliżeniu), co pozwala unikać udarów.

Weryfikacja numeryczna

Weryfikacja numeryczna obejmuje badania symulacyjne zarówno dla zastosowania strategii sterowania do tłumienia drgań, jak i usprawniania odzyskiwania energii. Do testów wykorzystano autorskie oprogramowanie oraz komputerowe modele MES płaskich konstrukcji ramowych. Prędkości w różnych punktach konstrukcji służą do filtracji modalnej w celu oszacowania prędkości modalnych. Pomiar odkształceń jest odwzorowany z funkcji kształtu belowych elementów skończonych i znanych wymiarów przekroju. Mierzone odkształcenia służą oszacowaniu momentu gnącego przenoszonego przez każdy blokowany węzeł. Lokalizacje pomiarów prędkości znaleziono za pomocą algorytmu opartego na wypukłej relaksacji.

W weryfikacji numerycznej skuteczności w tłumieniu drgań były rozważane dwie konfiguracje konstrukcji: (1) z węzłami umieszczonymi optymalnie według miary sterowalności zaproponowanej w niniejszej pracy oraz (2) z węzłami umieszczonymi nieoptymalnie, w celu sprawdzenia odporności algorytmu na nieoptymalne rozmieszczenie węzłów (np. z uwagi na ograniczenia konstrukcyjne). W obu konfiguracjach proponowana strategia sterowania była porównana ze strategią PAR dla drgań swobodnych, wymuszenia harmonicznego oraz losowego. Choć obie metody dawały zadowalające wyniki, proponowane sterowanie umożliwiało narzucenie priorytetu tłumienia poszczególnych monitorowanych postaci drgań przez odpowiedni dobór wag. Dzięki temu sterowanie modalne lepiej tłumiło drgania pierwszej postaci. Proponowane sterowanie modalne wymagało również mniejszej liczby przełączeń stanu blokowanych węzłów. Różnice w efektywności tłumienia drgań z użyciem porównywanych metod były bardziej widoczne dla konfiguracji drugiej (nieoptymalnie rozmieszczone węzły).

W przypadku testowania możliwości usprawniania odzyskiwania energii z drgań węzły zostały tak umiejscowione, aby wszystkie monitorowane postacie drgań były dobrze sterowalne. Uwzględniony również został model przetwornika elektromechanicznego konwertującego energię drgań na energię elektryczną. Rozważano dwie konfiguracje ukła-

du, gdzie przetwornik elektromechaniczny jest dostrojony do: (1) pierwszej postaci drgań oraz (2) drugiej postaci drgań sterowanej konstrukcji. W tym przypadku energia mechaniczna miała być przenoszona odpowiednio do pierwszej lub drugiej postaci. W obydwu konfiguracjach konstrukcja była poddawana różnym rodzajom wymuszeń kinematycznych. Wykazano, że przenoszenie energii zarówno w kierunku niższych częstotliwości (konfiguracja 1), jak i tych wyższych (konfiguracja 2) niż częstotliwość wzbudzenia znacząco poprawia wydajność pracy przetwornika elektromechanicznego. W przypadku szerokopasmowych wymuszeń jest jednak rekomendowane zaprojektowanie całego układu tak, aby najbardziej podstawowa postać drgań była jednocześnie docelową.

Walidacja eksperymentalna

Walidację eksperymentalną proponowanej strategii przeprowadzono na laboratoryjnym demonstratorze drgań, którym jest rama wysięgnikowa wyposażona w sześć blokowanych węzłów. Rama i jej wymiary są przedstawione na rysunku 5.1 (s. 163). Efekt zablokowania/odblokowania był realizowany przez piezo stos zmieniający siłę docisku między powierzchniami ciernymi węzła. Aby wyznaczyć niezbędne dla algorytmu parametry modalne oraz mieć możliwość porównania wyników eksperymentalnych z symulacją komputerową, przygotowano model konstrukcji metodą elementów skończonych (MES). Model MES został skalibrowany z użyciem zidentyfikowanych eksperymentalnie postaci drgań konstrukcji. Algorytm sterowania zaimplementowano na sterowniku FPGA. Z uwagi na jego ograniczoną pamięć możliwe było sterowanie jedną parą węzłów na raz – pozostałe były w tym czasie pasywnie zablokowane. Monitorowane były pierwsze trzy postacie drgań demonstratora.

Przetestowano skuteczność tłumienia drgań swobodnych oraz wymuszonych (przemiatanie częstotliwości wzbudnikiem modalnym). Drgania swobodne analizowano w dziedzinie czasu, natomiast wymuszone – głównie w dziedzinie częstotliwości za pomocą funkcji odpowiedzi częstotliwościowej oraz funkcji widmowej gęstości mocy. Charakteryzowane były zarówno przemieszczenia, jak i przyśpieszenia swobodnego końca konstrukcji. W zależności od dobieranych wag algorytmu możliwe było selektywne tłumienie poszczególnych postaci drgań. Eksperymentalnie wykazano przeniesienie energii do drgań w postaciach wyższych rzędów spoza zakresu wzbudzenia konstrukcji przez wzbudnik. Widoczne jednak były rozbieżności między wynikami symulacyjnymi a eksperymentem, głównie ze względu na fakt, że węzły są prototypami i mają istotne wady: w stanie odblokowanym pozostaje resztkowa siła docisku między okładzinami ciernymi, natomiast w stanie zablokowanym następuje poślizg między okładzinami ciernymi z uwagi na przekroczenie maksymalnego momentu przenoszonego przez węzły.

Walidacja przenoszenia energii do wybranej postaci została zweryfikowana tylko w drganiach wymuszonych. Testowane było przenoszenie energii do pierwszej oraz do drugiej postaci drgań. W obu przypadkach wzbudnik modalny nie pobudzał docelowych postaci drgań, co pozwalało na wyraźne zademonstrowanie możliwości przenoszenia energii między postaciami drgań w obu kierunkach. Wyniki przedstawiono w postaci funkcji widmowej gęstości mocy – z uwagi na zawężony zakres wzbudzenia. W obu przypadkach wykazano wyraźne zwiększenie poziomu przemieszczeń i przyśpieszeń docelowych

postaci drgań kosztem tych wzbudzanych przez wzbudnik. Towarzyszyło temu również niezamierzone przeniesienie części energii do postaci drgań wyższego rzędu.

Konkluzje

Zaproponowano sterowanie umożliwiające precyzyjne przenoszenie energii między wybranymi postaciami drgań przez blokowanie półaktywnie sterowanych węzłów. Bazuje ono na autorskich wyprowadzeniach opisujących wpływ zablokowania węzła na efekt sprzężenia modalnego skutkującego przepływem energii między postaciami drgań. Zaproponowano również dedykowane metody optymalnego rozmieszczania węzłów i sensorów. Sterowanie pozwala nie tylko efektywnie tłumić niskoczęstotliwościowe drgania przez przeniesienie ich energii do lepiej tłumionych postaci drgań wyższych rzędów, ale umożliwia również przenoszenie energii do wybranej postaci drgań, co ma zastosowanie w odzyskiwaniu energii z drgań. W tłumieniu drgań sterowanie pozwala narzucać priorytet na wybrane postacie drgań oraz wymaga mniejszej liczby przełączeń stanu węzła niż metoda PAR. Eksperymentalnie pokazano, że mimo znacznych niedoskonałości blokowanych węzłów nieujętych w modelu konstrukcji, sterowanie nadal działa, co udowadnia jego odporność na błędy modelowania.

Abstract

This thesis is devoted to a new semi-active modal control methodology of frame structures. The control allows for precise transfer of the mechanical energy between structural vibration modes. It is realised by the lockable joints connecting structural beams. These joints can be dynamically locked and work as rigid connections, transmitting the bending moments between the adjacent beams, or can be unlocked and work as hinges. The locking effect introduces modal coupling that results in energy exchange between the vibration modes. The proposed control methodology has two potential applications: attenuation of low-frequency vibration and enhancement of the energy harvesting process. In the former application, the vibration energy is transferred into the high-frequency vibration modes and then effectively dissipated due to the higher damping coefficients of these modes. In the latter possible application, the energy harvester is attached to the controlled structure. Then, the energy is transferred from the currently excited structural vibration modes into the preselected one that cooperates well with the energy harvester in terms of installation location and natural frequency.

This research is motivated by the fact that existing semi-active control strategies aimed at inducing energy transfer are heuristic in nature and typically capable of transferring energy only towards higher vibration frequencies. They do not employ any feedback from the state expressed in terms of modal parameters. Furthermore, any knowledge about the influence of the locking effect on modal coupling and modal energy transfer is very limited. An additional motivation for the research is the recent effort devoted to improve the balance between peak efficiency and operational frequency bandwidth of energy harvesters by introducing intentional nonlinearities, studying internal resonance phenomena and designing adaptive devices.

Investigation of the locking effect focuses on the fact that locking and unlocking joints changes the dynamic properties of the structure, effective number of structural degrees of freedom, modal basis and its dimension. It is shown that the highest-dimension modal basis that is obtained for all joints in the unlocked state can be adopted for investigation of the structural behaviour even if joints become locked. Then, the modal coupling effect is included for proper description of the structural behaviour. It allows for investigation of the energy exchange between the vibration modes. These analytical derivations are later used to develop the instantaneously optimal control law and control algorithm as well as to select the measured quantities. Moreover, the control methodology includes dedicated metric of controllability of the energy transfer to/from particular vibration modes, which is used for selection of locations of lockable joints providing their efficient operation. Also a new convex-relaxation-based method for efficient sensor layout optimisation for the purpose of modal filtering is adopted.

The control strategy has been validated both numerically and experimentally. It is demonstrated that due to the insight into modal coupling effects the proposed methodology mitigates low-frequency vibration requiring significantly smaller number of the joint

state switches than the prestress accumulation–release (PAR) method that is adopted as a benchmark. Moreover, the proposed modal approach allowed for damping of particular vibration modes with assigned various priority levels, which is not possible in the PAR method. The proposed control algorithm also allows for significant enhancement of the energy harvesting process. It has been shown both numerically and experimentally that the control allows for precise energy transfer both towards lower frequencies and vice-versa.

Publications related to the thesis

Journal articles

1. **M. Ostrowski**, B. Błachowski, B. Popławski, D. Pisarski, G. Mikułowski, Ł. Jankowski, Semi-active modal control of structures with lockable joints: General methodology and applications, *Structural Control and Health Monitoring*, 28(5): e2710, 2021, https://doi.org/10.1002/stc.2710.

2. B. Błachowski, A. Świercz, **M. Ostrowski**, P. Tauzowski, P. Olaszek, Ł. Jankowski, Convex relaxation for efficient sensor layout optimization in large-scale structures subjected to moving loads, *Computer-Aided Civil and Infrastructure Engineering*, 35(10): 1085–1100, 2020, https://doi.org/10.1111/mice.12553.

3. **M. Ostrowski**, B. Błachowski, M. Bocheński, D. Piernikarski, P. Filipek, W. Janicki, Design of nonlinear electromagnetic energy harvester equipped with mechanical amplifier and spring bumpers, *Bulletin of the Polish Academy of Sciences: Technical Sciences*, 68(6): 1373–1383, 2020, https://doi.org/10.24425/bpasts.2020.135384.

4. **M. Ostrowski**, G. Mikułkowski, B. Błachowski, Ł. Jankowski, Experimental assessment of Bayesian and mode matching approaches for parametric identification of bolted connections, *Mechanical Systems and Signal Processing*, 201: 110652, 2023, https://doi.org/10.1016/j.ymssp.2023.110652.

5. **M. Ostrowski**, B. Błachowski, G. Mikułowski, Ł. Jankowski, Influence of noise in computer-vision-based measurements on parameter identification in structural dynamics, *Sensors*, 23(1): 291, 2023, https://doi.org/10.3390/s23010291. This is an invited paper belonging to a special issue entitled: *Intelligent Sensing Technologies in Structural Health Monitoring*.

Conference articles

1. **M. Ostrowski**, B. Błachowski, G. Mikułowski, Ł. Jankowski, Semi-active control of modal energy transfer by means of lockable joints: Theory and applications, In: *International Conference on Noise and Vibration Engineering / International Conference on Uncertainty in Structural Dynamics*, ISMA – USD, 2024.

2. G. Mikułowski, **M. Ostrowski**, B. Błachowski, Ł. Jankowski, Semi-active control of modal energy transfer by means of lockable joints: experimental verification, In: *International Conference on Noise and Vibration Engineering / International Conference on Uncertainty in Structural Dynamics*, ISMA – USD, 2024.

3. **M. Ostrowski**, B. Błachowski, G. Mikułowski, Ł. Jankowski, Semi-active modal control based on the energy transfer between structural vibration modes, In:

10th ECCOMAS Thematic Conference on Smart Structures and Materials, SMART, pp. 526–537, 2023, https://doi.org/10.7712/150123.9807.444377.

4. G. Mikułowski, **M. Ostrowski**, B. Błachowski, Ł. Jankowski, Experimental verification of a semi-active modal control algorithm for structures with lockable joints, In: *10th ECCOMAS Thematic Conference on Smart Structures and Materials*, SMART, pp. 572–581, 2023, https://doi.org/10.7712/150123.9811.446236.

5. B. Błachowski, **M. Ostrowski**, G. Mikułowski, Ł. Jankowski, Mode matching vs Bayesian approach for model updating of frame structure with uncertain bolted connection, In: *International Conference on Noise and Vibration Engineering / International Conference on Uncertainty in Structural Dynamics*, ISMA – USD, pp. 1325–1334, 2022, http://past.isma-isaac.be/downloads/isma2022/proceedings/Contribution_539_proceeding_3.pdf.

6. B. Błachowski, A. Świercz, **M. Ostrowski**, P. Tauzowski, Ł. Jankowski, Multitype sensor placement for structural health monitoring of tied-arch bridges, In: *10th European Workshop on Structural Health Monitoring*, EWSHM, pp. 286–297, 2021, https://doi.org/10.1007/978-3-030-64594-6_29.

7. B. Błachowski, **M. Ostrowski**, P. Tauzowski, A. Świercz, Ł. Jankowski, Sensor placement for structural damage identification by means of topology optimization, In: *4th Polish Congress of Mechanics and 23rd International Conference on Computer Methods in Mechanics*, PCM-CMM, pp. 020002–1–11, 2020, https://doi.org/10.1063/5.0007817.

8. **M. Ostrowski**, B. Błachowski, Ł. Jankowski, D. Pisarski, Inverse Lyapunov based method for semi-active control of energy transfer between vibration modes, In: *9th ECCOMAS Thematic Conference on Smart Structures and Materials*, SMART, pp. 345–356, 2019, https://congress.cimne.com/smart2019/frontal/doc/EbookSMART2019.pdf.

Book chapters

1. **M. Ostrowski**, B. Błachowski, Ł. Jankowski, D. Pisarski, Structural vibration control using semi-actively switched lockable joints, In: Mańka M., Mendrok K. (Eds.), *Projektowanie i dynamika urządzeń mechatronicznych*, pp. 221–228, Katedra Robotyki i Mechatroniki, AGH, Cracow, 2019.

Contents

Nomenclature

Symbols often used in the present thesis are listed below, whereas symbols used only locally are defined within the text of thesis. In justified cases some indices can be omitted, e.g. index k in $\widetilde{\mathbf{C}}_k$ matrix is removed in situations when k can be equal to 1 only. Scalar quantities are characterized by cursive letters (both lowercase and uppercase), vectors are denoted by lowercase bold letters, whereas matrices are denoted by uppercase bold letters. Abbreviations are listed at the end.

$\dot{(\cdot)}$, $\ddot{(\cdot)}$	–	first-order and second-order derivative with respect to time: $\mathrm{d}(\cdot)/\mathrm{d}t$ and $\mathrm{d}^2(\cdot)/\mathrm{d}t^2$, respectively,
$\overline{(\cdot)}$	–	mean value,
$(\cdot)^+$	–	Moore–Penrose matrix inverse (pseudoinverse),
$(\cdot)^{\mathrm{T}}$	–	matrix transpose,
A	–	area of the cross-section,
$\mathbf{B}$	–	transformation matrix between full configuration space and one of reduced dimension after locking all joints,
$\mathbf{B}_0$	–	transformation matrix between full configuration space and one of reduced dimension after locking particular joints,
$\mathbf{B}_1$	–	transformation matrix between full configuration space and one related to DOFs redundant after locking of particular joints,
$c_{\max}$	–	large damping factor representing joint lock,
$\mathbf{C}$	–	material-damping matrix,
$\widetilde{\mathbf{C}}_k$	–	sparse damping matrix representing the locking effect of k-th joint,
$\mathbf{d}(t)$	–	vector of external forces,
E	–	Young modulus,
$E(t)$	–	total mechanical energy,
$E_m(t)$	–	m-th modal energy (mechanical energy associated with m-th unlocked mode),
$f_k(t)$, $\widehat{f_k}(t)$	–	actual value and estimate of bending moment transmitted by k-th lockable joint, respectively,
$f_k^{\mathrm{l}\max}$, $f_k^{\mathrm{u}\max}$	–	maximal bending moment that can be transmitted without slipping when the real joint is locked or unlocked (residual moment), respectively,

$\mathbf{f}(t)$	–	vector of bending moments transmitted by the lockable joints,
$\mathbf{F}$	–	modal filter,
g_p	–	controllability metric of p-th unlocked vibration mode,
h	–	height of beam cross-section,
i, j	–	index of degree of freedom,
I	–	geometrical or mass moment of inertia,
$\mathbf{I}$	–	identity matrix,
k	–	index of the lockable joint or stiffness,
$\mathbf{K}$	–	stiffness matrix for all joints unlocked,
$\widetilde{\mathbf{K}}$	–	stiffness matrix of reduced dimension for all joints locked,
l, L	–	length,
$\mathbf{l}_k$	–	signed sparse Boolean vector ($\mathbf{l}_k \in \{-1, 0, 1\}^{N_\mathrm{d}}$) selecting rotational degrees of freedom involved in k-th lockable joint,
$\mathbf{l}_\mathrm{x}$	–	signed Boolean vector selecting translational horizontal degrees of freedom,
$\mathbf{L}_\mathrm{q}$	–	transformation (in particular sparse Boolean) matrix between structural displacements and measured displacements,
m, n	–	index of vibration mode,
m_J	–	mass of the lockable joint,
M	–	mass of the rigid rod,
$\mathbf{M}$	–	mass matrix for all joints unlocked,
$q(t)$	–	rotational displacement of the two-DOF system after joint lock,
$q_i(t)$	–	rotational or translational displacement of i-th degree of freedom,
$\mathbf{q}(t)$	–	displacement vector containing both rotational and translational displacements,
$\mathbf{q}_0$, $\dot{\mathbf{q}}_0$	–	initial conditions for displacement and velocity vector, respectively,
$q_{\mathrm{M}i}(t)$	–	i-th measured displacement
$\mathbf{q}_\mathrm{M}(t)$	–	vector of measured displacements,
N_c	–	number of candidate sensor locations,
N_d	–	number of degrees of freedom equal to the total number of unlocked vibration modes,
N_k	–	number of independently controlled lockable joints,
N_p	–	number of monitored unlocked vibration modes,
t	–	time,
t_l, t_u	–	time instances of locking and unlocking any joint in the structure, respectively,
t_lock, t_unlock	–	selected time periods of waiting of the control algorithm after any joint lock or unlock, respectively,

$u_k(t)$ – k-th control signal,
$\mathbf{u}(t)$ – vector of control signals,
$\dot{V}_W(t)$ – weighted sum of modal energy transfer rates to the monitored unlocked vibration modes,
$\dot{\hat{V}}_{Wk}(t)$ – estimate of weighted sum of modal energy transfer rates to the monitored unlocked vibration modes through k-th lockable joint,
$\dot{W}_{\mathrm{H}}(t)$ – total modal energy transfer rate to all higher-order unlocked vibration modes,
$\dot{W}_{\mathrm{H}k}(t)$ – total modal energy transfer rate to all higher-order unlocked vibration modes resulting from locking of k-th joint,
$\dot{W}_m(t)$ – modal energy transfer rate to m-th unlocked vibration mode,
$\dot{W}_{\mathrm{M}}(t)$ – total modal energy transfer rate to all monitored unlocked vibration modes,
$\dot{W}_{\mathrm{M}k}(t)$ – total modal energy transfer rate to all monitored unlocked vibration modes resulting from locking of k-th joint,
$\mathbf{W}_\alpha$ – diagonal matrix collecting algorithm weights α_p,
α, β, γ – parameters of assumed proportional damping model,
α_p – selected algorithm weight associated with p-th monitored unlocked vibration mode,
β_p – weight assigned to p-th controllability metric g_p,
γ_{kmn} – element in m-th row and n-th column of matrix $\mathbf{\Gamma}_k$,
$\mathbf{\Gamma}_k$ – modal coupling matrix related to k-th lockable joint,
$\mathbf{\Gamma}_{\mathrm{MM}k}$ – sub-matrix of $\mathbf{\Gamma}_k$ coupling only monitored unlocked vibration modes,
$\mathbf{\Gamma}_{\mathrm{MH}k} = \mathbf{\Gamma}_{\mathrm{HM}k}^{\mathrm{T}}$ – sub-matrix of $\mathbf{\Gamma}_k$ coupling monitored unlocked vibration modes with higher-order ones,
$\mathbf{\Gamma}_{\mathrm{HH}k}$ – sub-matrix of $\mathbf{\Gamma}_k$ coupling only higher-order unlocked vibration modes,
Δq_k – difference of rotational displacements in k-th lockable joint,
Δt – integration step or sampling period,
$\Delta\phi_k^{(m)}$ – difference of rotational displacements in k-th lockable joint for m-th unlocked mode shape,
$\mathbf{\Delta\phi}_{\mathrm{M}k}$ – vector collecting differences of rotational displacements $\Delta\phi_k^{(m)}$ for all monitored unlocked vibration modes in k-th joint,
$\varepsilon_{\mathrm{M}k}(t)$ – measured bending strains in vicinity of k-th lockable joint,
$\zeta^{(m)}$ – m-th modal damping factor,
$\mathbf{Z}$ – diagonal matrix collecting all modal damping factors,
$\boldsymbol{\eta}(t)$ – vector collecting all modal coordinates for unlocked vibration modes,

$\boldsymbol{\eta}_{\mathrm{H}}(t)$ – vector collecting actual values of modal coordinates related to the higher-order unlocked vibration modes,
$\boldsymbol{\eta}_{\mathrm{M}}(t)$ – vector collecting actual values of modal coordinates related to the monitored unlocked vibration modes,
$\dot{\widehat{\boldsymbol{\eta}}}_{\mathrm{M}}(t)$ – estimated vector of monitored modal velocities,
κ_1, κ_2 – selected thresholds of estimated weighted modal energy transfer rate in control algorithm for unlocked and locked joint, respectively,
κ_{ε} – selected threshold related to changes in estimated strain energy (PAR algorithm),
$\phi_i^{(m)}$ – i-th element of eigenvector describing m-th unlocked mode shape,
$\boldsymbol{\phi}^{(m)}$ – eigenvector describing m-th unlocked mode shape,
$\widetilde{\boldsymbol{\phi}}^{(m)}$ – eigenvector describing m-th locked mode shape,
$\boldsymbol{\Phi}$ – modal matrix collecting all unlocked eigenvectors in columns,
$\boldsymbol{\Phi}_{\mathrm{M}}$ – modal matrix collecting eigenvectors related to the monitored unlocked vibration modes,
$\boldsymbol{\Phi}_{\mathrm{H}}$ – modal matrix collecting eigenvectors related to the higher-order unlocked vibration modes,
$\omega^{(m)}$ – m-th unlocked natural frequency, [rad/s],
$\widetilde{\omega}^{(m)}$ – m-th locked natural frequency, [rad/s],
$\boldsymbol{\Omega}$ – diagonal matrix collecting all unlocked natural frequencies, [rad/s],

AIC – adaptive intelligent control,
AMD – active mass damper,
CR – convex relaxation,
DOF – degree of freedom,
EFI – effective independence method,
EH – energy harvester,
EMEH – electromagnetic energy harvester,
ER – electrorheological fluid,
FE – finite element,
FEM – finite element method,
FIM – Fisher information matrix,
FNA – fast nonlinear analysis,
FRF – frequency response function,
LQR – linear-quadratic regulator,
MDOF – multi-degree-of-freedom,
MR – magnetorheological fluid,

NES	–	nonlinear energy sink,
PAR	–	prestress accumulation–release (vibration damping method),
PBH test	–	Popov–Belevitch–Hautus eigenvector test,
PEH	–	piezoelectric energy harvester,
PID	–	proportional-integral-derivative,
PSD	–	power spectral density function,
RMS	–	root mean square,
SDOF	–	single-degree-of-freedom,
SISO	–	single-input-single-output,
SNA	–	strongly nonlinear absorber,
TLCD	–	tuned liquid column damper,
TMD	–	tuned mass damper,
VI-NES	–	vibro-impact nonlinear energy sink.

1. Introduction

In this chapter the reader is introduced to the thesis. Firstly, state of the art is provided by the literature review in the first section. This literature review discusses various techniques and aspects of broad field of vibration control followed by a discussion on advances in vibration-based energy harvesting. Then, aims, scope and the stated thesis are specified in Section 1.2. Section 1.3 summarises novelty of the control methodology proposed in this thesis and contributions into the current state of the science.

1.1. Literature review

Vibration is usually undesired phenomenon in mechanical engineering and civil structures. It can cause decrease of efficiency of industrial processes such as machining or robot arm manipulation. Vibration can cause also fatigue damages of mechanical parts or even emergency situations that are dangerous for people as, e.g. famous collapse of the Tacoma Narrows Bridge in 1940. Consequently, vibration reduction has been the subject of intensive research for decades, and many different approaches to structural vibration control have been developed. The most important control strategies and their applications until 1997 have been discussed in an extensive review done by Housner *et al.* [22]. The authors concluded that despite the significant progress in structural control and various engineering applications considerable effort are still required and will be put into development of methods of vibration attenuation, especially in fields: algorithms and controlling devices, modelling of nonlinear dispersed structures, smart materials, structural health monitoring and damage detection, sensor technology, near-field-earthquake problems and improved collaboration for comparison of large-scale tests. Indeed, the intensive effort in these topics has not decreased until today and still there are aspects that need further study, e.g. modelling of nonlinear structural behaviour, experimental validation of some control strategies aiming at their implementation, development of control strategies tolerant of malfunctions and semi-active as well as hybrid control strategies that are not only fault-tolerant to some degree but also relatively cheap [23]. Additional reason for the amount of work done in the field of vibration control is its multidisciplinary nature. Vibration control includes: control algorithm, optimal placement of sensors and actuators as well as their design and integration with the remaining

parts of the control system and the controlled structure. It causes that the structure equipped with such a control system is often called "smart structure" [24]. Various devices designed to actuate the state of controlled structure, e.g. active mass dampers, dampers with negative stiffness, shape memory and piezoelectric materials or semi-active devices was reviewerd by Ghaedi *et al.* [1]. Vibration attenuation methods can be divided into three groups according to the way of working and required energy consumption: passive damping working without any external power supply, active control supplied with the energy from the external source and semi-active control requiring usually a little amount of energy. They are discussed in Subsections 1.1.1–1.1.3.

During vibration mitigation the mechanical energy is usually dissipated. However, it is also possible to recover some part of the energy and convert it into other usable form, e.g. electrical energy. This process is called energy harvesting. Sometimes, vibration is even desired phenomenon as the source of energy in the energy harvesting process. Due to development of the modern energy-saving electronics the energy harvesting is the topic of the growing importance [2]. Methods of enhancement of the energy harvesting process are discussed in Subsection 1.1.5.

1.1.1. Passive versus active vibration control

The most common vibration reduction methods are passive ones such as stiffening, damping or isolation with use of, e.g., viscous fluids, passive piezoelectrics [25] or tuned mass dampers (TMDs) [26]. Simplicity of this approach often is the main advantage of the passive systems. It determines that they are more reliable than active control systems. Hence, they can work together with active control systems as a hybrid control, not only decreasing the costs of the installation but also providing a certain level of vibration energy dissipation in the case of the failure of the active control system [27]. Due to this valuable properties, the passive systems are utilised in large scale structures such as, e.g. the Millennium Bridge, equipped with tuned mass dampers and viscous fluid dampers [28, 29], and the CN Tower in Toronto, equipped with tuned mass dampers in the form of rings [30]. This method of vibration attenuation is employed since XIX century. The first noticed passive device similar to the TMD was described and published in 1883 [31]. The first TMD device was patented in 1911 [32]. However, it can be observed that the ease of designing linear TMDs comes at the cost of a compromise between peak efficiency occurring at the resonance frequency and operational frequency bandwidth. Thus, many researchers have attempted to expand the frequency bandwidth and improve the overall efficiency of the TMDs using nonlinear components. E.g. Gatti showed that nonlinear stiffness of the TMD affects one of the peaks of the frequency response function (FRF) introduced usually by the TMD that improve the bandwidth [33]. Pisal [34] researched influence of the dry friction in the TMD on vibration reduc-

tion of seismically excited system. An analogous rule of working can be found in the tuned liquid column dampers (TLCD), where instead of mass on spring the liquid moving in a U-shaped pipe attenuates the structural vibration. The range of applications of the TLCDs is similar to that of TMDs, e.g. Alkimim *et al.* [35] showed how to optimise parameters of the TLCD for reducing vibration of a wind turbine based on an arbitrary stochastic wind model with known power spectral density. Adaptable TLDCs discussed in Subsection 1.1.2 as a sub-class of the semi-active control systems.

It is also possible to expand the operational frequency bandwidth of the damping device by nonlinear absorbers called in the literature nonlinear energy sinks (NESes). In addition to the ability to dissipate energy locally, the NES can provide nonlinear coupling between the vibration modes of usually linear structure and redistribute the energy among different vibration modes, enhancing effectiveness of the vibration mitigation [36]. A simple example of the vibro-impact NES (VI-NES) attached to a single-degree-of-freedom (SDOF) system is discussed in [3]. Due to the single-DOF modal coupling is not possible, however, a similar idea employing the multi-degree-of-freedom (MDOF) system has been described in [4]. Here, the energy is dissipated not only in the impact but also transferred to the higher-order vibration modes of the structure, which are excited during the impact. These modes usually are characterised by greater material damping coefficients, hence after their excitation the mechanical energy is effectively dissipated in structural volume. In the later studies, performance of the single VI-NES and two-VI-NESes system have been compared and discussed in [5]. It has been found that the use of two dissimilar VI-NESes provides better robustness of vibration suppression with respect to the excitation amplitude and extends the operational frequency range of the vibration mitigation system. The National Aeronautics and Space Administration (NASA) provided the experiment aiming at testing the influence of gaps in pin joints installed in the precise space truss structures on vibration damping under low-gravity conditions [37]. These joints operate similarly to NESes, as apart energy dissipated locally in friction also the higher-order vibration modes are induced by impacts caused by the interface clearance. Both friction and impacts are recognised as significant sources of damping of low-frequency vibrations. The investigated structure is of high precision and any preload, e.g. by the gravity, limits the damping effect due to the lack of relative motion of the parts within the joint interfaces. However, among the advantages of such a damping system are: low weight, simplicity and expected high durability, as well as the absence of any fluids which often is in demand in space applications. Motato *et al.* [38] demonstrated the effectiveness of the mechanical energy transfer to the higher-order vibration modes also for NES used in a MDOF drive-train system. Due to energy transfer from the lower-order vibration modes, the first four vibration modes of the investigated drive-train system equipped with two NESes have significantly increased the normalised

effective damping factor. Study of the effectiveness of a strongly nonlinear absorber (SNA), which is also a kind of NES device, in attenuation of vibration of nine-story building was investigated by Li *et al.* [6]. In this case, the SNA is a mass damper with strongly nonlinear stiffness. The nonlinearity is purely geometrical. They studied both SDOF and two-DOF SNAs and observed that both SNAs cause the the quick redistribution of the energy from the excited low-order modes into the higher-order ones, however, the two-DOF SNA is more effective. The energy transferred into higher frequencies is later effectively dissipated in the material damping. The intended modal energy transfer provided by NESes discussed above is recognised as very effective and promising in a vibration attenuation method of low-frequency vibrations that are usually the most difficult to be damped. Thus, employment of this phenomenon in semi-active control is discussed also in Subsection 1.1.3.

Another example of a lightweight passive damping system is a piezoelectric patch connected to a shunted electrical circuit, which converts mechanical energy into electrical and dissipates it through resistive losses. First works describing this approach were published by Forward as well as Edwards and Miyakawa [39, 40]. The first validated mathematical model describing effective mechanical impedance of the shunted piezoelectric was written by Hagood and von Flotow [41]. This topic of passive vibration damping still is researched. A fully passive nonlinear piezoelectric tuned vibration absorber that is able to adapt to nonlinearities of the structure was developed by Lossouarn *et al.* [42] in 2018. In this work, the electrical circuit of the absorber includes an electromagnetic coil that not only provides the electrical resonance, increasing effectiveness of the damping system, but also due to the ferrite-material core of the coil it provides desired nonlinear characteristics of the electrical circuit. Due to a proper design of the coil, it is possible to compensate the nonlinearities of the structure, hence vibration are effectively mitigated in a wider range of excitation amplitudes. Another concept of the electromagnetic coil with variable inductance was also used for compensating the temperature dependant variations of electrical circuit parameters [43]. Utility of the shunted piezoelectric transducers with two configurations of shunt circuits: resistive and resistive–inductive has been evaluated by Sales *et al.* [44]. It has been shown that due to possibility of miniaturization of the shunted circuit it is applicable in the spacecrafts but in the case of mitigation of low-frequency oscillations a high value of inductance is in demand.

An interesting example of the passive vibration mitigation is shown in [45]. The authors proposed the passive damping system aiming at preventing an impact when displacement capacity is limited, it is activated only in the cases when displacement is beyond the preselected threshold. The proposed approach is to calculate the optimal control forces and trajectories (as in active control) and to design a passive system that will have similar characteristics. The problem of the near-fault kinematic excitation is considered also during the design

of a seismic isolation systems. Near-fault displacements in the seismic isolation system were taken into consideration by Tsai *et al.* [46]. They proposed the friction pendulum system with curvature lengthened with the displacement. Also the finite element formulation was proposed for this isolation system. Shahbazi and Taghikhany [47] evaluated 120 cases of polynomial functions describing the variable curvature of friction pendulum aiming at minimisation of the floor accelerations and displacements.

Contrary to the passive vibration reduction, the active control provides high performance at the expense of much higher application costs caused by the need to use the efficient power supply, a controller with uploaded algorithm and a set of sensors and actuators. In one of the first studies of structural active control Swigert and Forward [48] showed that for two orthogonal modes of a cylindrical mast two electronic circuits are required, which additionally increases the cost of installation. This suggests that the application of active control techniques may be difficult and require in-depth knowledge. Well-systematised guidelines about active control have been collected by Fuller *et al.* [49]. This book among other important topics discusses the feedback and feedforward control architectures, which are considered as two main approaches to active vibration control design, as indicated also in the review paper by Alkhatib and Golnaraghi [50]. Another excellent book, written by Preumont [51], describes the active control of structures modelled using the finite element method (FEM), controllability and observability problems, collocated and optimal control, and other important topics related to the control theory.

Feedback control architecture is used commonly in many engineering applications because of the relative ease of designing process. It does not require a reference signal depending on the disturbance, nor the accurate mathematical model of the controlled object, even for certain optimal approaches. Zhang *et al.* [52] proposed sliding mode control of a 76 storey building using a the rotating active mass damper (AMD), where for the controller design purposes the building model was simplified to the single-storey structure. Zhang *et al.* compared the proposed control strategy with benchmark results obtained by Yang *et al.* [53] based on a linear-quadratic regulator (LQR) employing a reduced 12-DOF model for controller design purposes. Despite the significantly simpler model used to design the controller, sliding mode control achieved performance close to the LQR control which is optimal in the sense of Pontryagin's maximum principle.

A feedforward control approach requires a mathematical model of the controlled plant or at least knowledge about its basic properties. This is because, in a purely feedforward control system, the control signal is generated solely based on the reference (set-point) input or known disturbances, without any information about the current state of the plant. Its effectiveness increases when combined with other strategies, particularly in set-point tracking tasks where rapid control of rigid-body modes induces residual vibrations in flexible modes.

Bruijnen and Dijk [54] showed feedforward control with assistance of input shaping filter and a feedback loop for damping of residual vibration aiming at improving tracking accuracy. Dhanda *et al.* [55] proposed a solution of a similar problem with near-time-optimal control of flexible modes by means of the input shaping filters. Very interesting example of modern control utilising measurement of excitation in the form of an earthquake and feedback with respect to Kalman's filter-based observation has been proposed by Wasilewski *et al.* [56]. In this case, the authors proposed optimal control approach in the sense of Pontryagin's maximum principle, where measurement of the ground acceleration is used to calculate an autoregression-based prediction which is included in the optimal control problem.

A serious disadvantage of the active control is the possibility of destabilisation of the controlled plant, especially when the control is sensitive to the measurement noises, modelling errors or communication time delays [22, 57]. Hence, the attention is paid to the resistance of the control to the modelling errors, measurement noises or delays. This property of the control system is called robustness. Among many approaches in robust control, a branch based on pole-placement should be noticed, e.g. using the singular value or QR decomposition [58]. In this case, robustness refers to the insensitivity of the closed-loop eigenvalues with respect to system parameters or modelling errors. An interesting example of robust pole placement for structural control using receptance data has been proposed proposed by Tehrani *et al.* [59]. The pole placement is robust with respect to noise in the measured receptances. They proposed a method of pole placement for subsequent modes in such a way that each successive column in the input matrix changing poles for the current vibration mode does not affect pole placement related to all modes in previous steps of the procedure. Other example of commonly used control approaches characterised by the robustness is sliding mode control. It allows the state of the structure to "slide" along a designed sliding surface in the state space due to the discontinuous control signal. However, there appears a phenomenon of chattering, which often causes the wear of the system components or even possibility of the fatigue damage. There are numerous algorithms reducing the chattering phenomenon and one of the simplest is time-dependent reduction the sliding gain function simultaneously with a decreasing amplitude of vibration [60].

The robustness can be also improved by a suitable arrangement of sensors and actuators. Apart maximisation of various measures of the controllability and observability of vibration modes dominant in the structural response (which are discussed in Subsection 1.1.4), the robustness with respect to the stability can be provided also by collocated architecture of the control system [51]. The pair sensor-actuator is collocated if they are attached to the same degree of freedom (DOF) of the structure. Then, the single-input-single-output (SISO) control loop is characterised by the root locus plot insensitive to changes in

the structural parameters and does not go beyond the complex left half plane indicating the stability. However, due to present practical limitations the pairs sensor-actuator sometimes cannot be collocated or despite the same location they are not collocated according to the DOF type, e.g. a sensor measures translational DOF and an actuator acts on rotational DOF at the same location. In such a situation the system is only conditionally stable and there are required more advanced control algorithms or intentional structural modifications as proposed by Gatti *et al.* [61], where the concentrated mass added at the sensor location improved the system stability.

The term "collocated" relates to the placement of sensors and actuators and should not be confused with decentralised control as it was emphasized in [62]. The term "centralised" refers to the control architecture, where all actuators and sensors are operated by one controller. In other cases, the control is called non-centralised that is not always the same as decentralised. Pisarski *et al.* [63] compared the newly proposed scalable distributed optimal control, where the control system is divided into sub-modules that can communicate with neighbouring sub-modules with two other control approaches: (1) a decentralised control system, where the modules do not communicate with other ones and (2) a centralised control. All three compared strategies were based on the LQR approach. The conclusion was that the proposed scalable control combines the advantages of the decentralised control that are reliability of the whole system in the case of any module failure with high performance close to centralised control due to the possibility of communication.

In the case of presence of significant parameter uncertainties of the used plant model or unmodeled dynamics, an adaptive intelligent control (AIC) can be used. Control algorithms classified as AIC due to their adaptability and learning ability are suitable for these design problems. The AIC control methods can be categorised into machine learning, evolutionary game theory, reasoning systems and adaptive filters [64]. A good example of the use of machine learning in structural control is an artificial-neural-network-based controller, called the neuro-controller, proposed by Błachowski and Pnevmatikos [65]. They compared the neuro-controller with the classical LQR approach on two numerical examples of structures: a SDOF structure and realistic example of 12-storey tall building. They found that the neuro-controller effectively attenuates vibration caused by an earthquake. An example of 12-storey building was adopted from another excellent work done by Jiang and Adeli [66], where they showed that the proposed structural control based on fuzzy wavelet neural network was able to manage both geometric and material nonlinearities of irregular building structures. An interesting example of reasoning system based on fuzzy logic used to control a composite plate has been proposed by Zorić *et al.* [67]. The authors also used a heuristic method called particle-swarm optimisation to find sizes and places of the actuators as well as controller membership function parameters

and output matrices. An example of intelligent model identification designed for nonlinear problems can be found in [68], where the authors proposed the filter structure including the neural finite impulse response modules and the tapped-delay-line linear combiner, which can be learned more effectively than two other benchmark examples.

Concluding this section, the active vibration control provides better performance than passive vibration mitigation, however, it is more difficult and expensive in practical implementations. It needs an efficient power source. Awareness of possible destabilisation of the controlled plant is required during the control system design. Thus, often sophisticated mathematical apparatus is required to provide stability – especially when model uncertainties are present.

1.1.2. Semi-active control

The semi-active control yields the compromise between passive damping and active control. In this approach, the controlled plant is equipped with semi-active devices able to dynamically modify local parameters of the system, e.g. stiffness or damping coefficient. Contrary to fully active control, it does not require efficient power supply but simultaneously is sufficient to mitigate vibration with efficiency close to the active vibration control [69]. Hence, the semi-active control systems can be significantly cheaper, which sometimes is more important than the control performance [62]. A detailed overview and comparison of classic semi-active control systems with passive and active control systems is presented in the article [70]. Similarly to the active control, the semi-active control also requires the control law and dedicated semi-active devices able to modify structural properties [71]. This class of devices usually cannot add energy to the controlled plant, but only dissipate it. Thus, naturally, the semi-active strategies cannot destabilise the object in free vibration, unlike the active control. The effort put into designing various semi-active devices was motivation for undertaking work on measuring the potential achievable performance of the semi-active device. This problem was discussed in [72], where the authors proposed the procedure based on constrained optimal control.

Semi-active dampers based on controlled damping properties mostly can be divided into viscous-based and friction-based devices. The first group of the devices is widely accepted to use for car-suspension control as well as in other vibrating structures. One of the most popular types of the viscous-based dampers are magnetorheological fluid dampers (MR dampers). In this type of damper, the fluid contains magnetisable particles that when subjected to the external magnetic field can change parameters of the fluid, resulting in different damping coefficient of the MR damper. Due to the highly nonlinear characteristics of the MR dampers and inherent dynamics, a variety of mathematical models have been developed. Among many works on modelling the behaviour of MR-damper,

we should distinguish a paper describing a phenomenological model proposed by Spencer *et al.* [73] based on the Bouc–Wen hysteresis model and comparing the proposed model with several others. MR dampers can be used in many mechanical systems due to their relatively small dimensions and possibility of quick change of the controlled properties. A control scheme based on H_∞ methods realised by the MR damper was proposed by Du *at al.* [74]. It was shown that the semi-actively controlled MR damper presented similar effectiveness as the active damper. Yang *et al.* [75] have proposed recently a new semi-active suspension control strategy utilising the negative stiffness included to the suspension in parallel to the MR damper and spring. Negative stiffness is realised by magnets. Strong nonlinearities of such a system pursued the use of an advanced control algorithm based on the Takagi–Sugeno fuzzy logic approach. The negative stiffness force and controlled always-resistant MR damper force allowed to achieve characteristics such as for the active suspension system but still keeping advantages of the semi-active systems. It has been verified both numerically and experimentally. An interesting industrial example of the use of MR damper has been proposed by Michajłow *et al.* [76]. They proposed optimal semi-active control strategy in the sense of Pontryagin's maximum principle for attenuation of torsional vibration of a drivetrain system driven by an electrical motor. The proposed semi-analytical procedure allowed for finding the optimal control function for mitigation of steady-state vibration. Capability of semi-active MR damping devices to transfer loads occurring during vibrations of civil structures has been demonstrated in design considerations by Li *et al.* [77]. In the further research, Li and Jianchun [78] studied characteristics of the device and proposed the computationally effective model. Usefulness of the MR dampers due to their low power consumption and desirable characteristics for seismic events was demonstrated with the clipped-optimal control algorithm by Dyke *et al.* [79]. Ha *et al.* [80] showed that despite the nonlinear character of the MR dampers the design of the controller employing the Lyapunov function and direct control of the current supplying MR damper coils is possible. To this end, they used the hysteresis model of the MR damper behaviour that does not involve the internal dynamics of the device [81]. The possibility of generation of relatively large forces by semi-active dampers with simultaneous low power consumption was employed to mitigate vibration of a beam structure subjected to a travelling load, as demonstrated first time by Bogacz and Bajer [82]. As this approach was recognised to be effective, later it was investigated also by other authors, e.g. Wasilewski and Pisarski [83] proposed a methodology for development of the near-optimal control based on the algebraic Lyapunov equation. The effectiveness of the control was demonstrated numerically on a simply supported beam subjected to the load moving with changing speeds.

Regarding the decentralised control approach, an interesting semi-active device, the switching oil damper, intended for such a control architectures was

proposed by Kurino *et al.* [84]. This device is represented by the Maxwell model that consists of spring and switching (controlled) damper which are connected in series. The way of working can be described by three following steps: (1) during the structural motion the damping factor of the device is switched into its maximal value, (2) the deformation across the device increases along with structural motion, hence the strain energy is accumulated in the spring element, (3) at the time instance when the strain energy achieves its local maximum the damping factor is switched into its minimal value, resulting in the release of the energy accumulated in the spring and its quick local dissipation in the viscous damping. The effectiveness of this method of vibration attenuation was confirmed by real applications, as reported in [85]. This control strategy is similar to the prestress accumulation–release (PAR) [12] method which is treated as a benchmark for the control strategy proposed in this thesis. The difference is that the PAR method results in release of the structural strain energy in high-frequency oscillation, in higher-order modes of the controlled structure contrary to the decentralised device proposed by Kurino *et al.* that dissipates the energy locally. The PAR method is discussed in detail in Subsection 1.1.3.

The friction-based damping modification also found its wide-range applications. One of such devices was the controllable friction-based sliding isolation system proposed by Feng *et al.* [86]. The variable friction force was realised by chamber connected to the pressure control system. Feng *et al.* indicated that because of the nonlinear character of the friction force the linear control theory cannot be applied to design the control algorithm for such a device. Thus, they proposed two control algorithms for their device based on: instantaneous optimality and bang-bang approach. Later, Inaudi [87] proposed the straightforward and effective approach called modulated homogeneous friction. The contact force between frictional surfaces is assumed to be piece-wise constant and proportional to the last peak value of the deformation of the friction-based damping device. As the amplitude of vibration decreases the contact force values also gradually decrease. The friction-based device controlled in such a way exhibits rectangular hysteresis loop whose area is proportional to the square of the device deformation. Laflamme *et al.* [88] developed a friction-based semi-active device intended for large-scale structures capable to transmit force of 200 kN with power-source voltage of 12 V. The device transmits forces through stiffness element, viscous damper and the friction-based breaking mechanism, which are composed in parallel. The friction-based breaking mechanism is responsible for providing the control force while viscous damper and stiffness elements serve as the fail-safe mechanism in the case of failure of the breaking mechanism. Aiming at simulation of the friction phenomenon exhibiting its strongly nonlinear nature, the LuGre model was used. Laflamme *et al.* suggested that their device can be controlled by two decoupled controllers. The first, LQR in this case, calculates a required friction force. The second, termed “internal”, con-

troller calculates a required clamping force allowing the device to achieve the required friction force which is treated as the set-point signal. Zhang *et al.* [89] proposed the optimal robust control strategy of building isolation system. This control system also is based on combination of two controllers: LQR and robust compensator. The former one pursues optimality, however, it is restricted to the linear control plants. Hence, the later controller compensates nonlinearity resulting from the frictional base isolation system. More examples of friction-based control strategies dedicated to flexible truss-like structures are discussed in Subsection 1.1.3.

Regarding passive TMDs from the previous section, Hrovat *et al.* [90] showed that due to variability of the damping in semi-actively controlled TMD it is possible to achieve both smaller structural displacements and accelerations as well as TMD stroke. Semi-actively controlled TMD with a ground-hook control approach was compared with passive TMD by Setareh [91]. One of the limitations of TMDs designed for buildings is related to the required space for their motion for efficient operation. The problem of the influence of the limited stroke on efficiency of various algorithms controlling semi-active TMDs was studied by Demetriou *et al.* [92]. Chu *et al.* [93] proposed a leverage-type variable stiffness mechanism for semi-active TMD reducing both the stroke demand of the semi-active TMD as well as energy consumption comparing to the hybrid TMD. Liu *et al.* [94] described the concept design of a tall building with division of the structure on substructure separated from a superstructure by a semi-active mid-story isolation system. In this case, the superstructure acts as semi-actively controlled TMD, although it can also be used by humans, and the mass ratio between super and superior structure is different than from that of "traditional" TMDs, thus overcoming the problem of the space limitations.

Satisfactory results can be obtained by an arbitrary change of the natural frequency of the TMD device, keeping it always well-tuned to the frequency of oscillations. Brzeski *et al.* [95] introduced the concept of an adaptable TMD, where change of its mechanical properties is realised by an inerter connected through the continuously variable transmission system. In further research the authors showed experimentally that due to variable inertance the TMD is able to mitigate vibration of the host structure at almost each frequency with peak-efficiency of the traditional TMD [96]. Another device similar to TMD intended for high-rise structures with adaptable natural frequency as well as the damping factor is U-shaped semi-active liquid column damper proposed by Altay and Klinkel [97]. Here, the natural frequency is adapted by change of the cross-sectional area of the columns, whereas the damping factor is modified by movable panels in the horizontal segment of the U-shaped tank.

Another possibility for controlled modification of the structure properties is the use of magnetorheological elastomers (MR elastomers). The change of the magnetic flux density across the MR elastomer modifies the shear modulus rather

than the damping properties as it is in the case of MR dampers. Moreover, the dependence of the shear modulus on the magnetic flux density is near-linear until saturation of the magnetic field does not occur [98]. This valuable property makes the design of the controller easier. Dyniewicz *et al.* [99] researched the semi-active damping control strategy for a layered beam (sometimes called also a "sandwich beam" in the literature) equipped with MR elastomers between the beam layers. They considered both damping and stiffness factor modifications, however, they suggested that the sudden change of the share stiffness of the MR elastomers in appropriate time instances is a suitable approach for effective vibration attenuation. Pisarski *et al.* [100] proposed control strategy based on the Lyapunov method for vibration mitigation of the double layered beam equipped with MR elastomers. They discretized the system using FEM receiving bilinear equations of motion. According to the near-linear dependence of the MR elastomer properties on the magnetic flux density, the bilinear form in the equation of motion allowed for both properly describing MR elastomer behaviour and keeping the ease of the design process of an instantaneously optimal controller. Later, Pisarski [101] studied the influence of the decentralised architecture of the control system on its effectiveness in reducing vibration. It has been concluded that the ability of the local controllers to collect the structure state information in their neighbourhood – not only at their locations – increases performance of the decentralised system to the level comparable with the centralised control system. MR elastomers can be used also for applications other than layered beam structures, e.g. vibration isolation, absorbers, base or sensors. These applications along with a critical review of the advances in the field of MR elastomers were presented by Li *et al.* [102].

An interesting approach to semi-active control has also recently been proposed by Lu *et al.* [7]. They developed semi-actively controlled VI-NES (called in this paper "semi-active impact damper") which is devoted to civil structures subjected to the earthquakes. Similarly to the passive VI-NESes, the semi-active one also allows for transfer of the vibration energy from low-order vibration modes into the higher-order ones and further its quick dissipation in material damping. Here, semi-active VI-NES consists of controlled slider and linear slide. The control strategy imposes an impact at particular position of the slide due to controlled pawl. The impact time instance is selected in such a way that the momentum exchange between the slider and the primary structure is maximised.

1.1.3. Semi-active control for light-weight structures

In this subsection, the attention is paid to the semi-active vibration control of light-weight structures, e.g. telecommunications masts or flexible space structures equipped with measurement apparatus. Light-weight structures are usu-

ally weakly damped because of their flexibility, thus the increase of the energy-dissipation ability can be required for their proper operation [103]. Hence, vibration mitigation in these systems often requires the dedicated approach. Various semi-active control strategies intended for truss-like structures are discussed below.

One of the most accepted approaches is dissipation of the energy in friction joints, because it does not significantly increase either the weight or the complexity of the controlled structure. One of the first examinations of this energy dissipation approach was conducted by Ferri and Heck [104] on a simple structure consisting of two beams interconnected by the friction joint. Gaul and Nitsche [105] demonstrated, using a similar structure, that semi-active control of the clamping force in a friction joint enables a significant increase in damping efficiency compared to its purely passive counterpart. The semi-active joint was controlled by means of the instantaneous minimization of the Lyapunov function equal to the mechanical energy of the system. The contact force between the frictional surfaces was realised with piezo stack actuator. Later, Gaul *et al.* [106, 107] conduced research on the semi-active vibration control methodology for the space truss-like structures. This methodology includes the control algorithm as well as placement of sensors and semi-active joints, which is based on the employed FE model of the structure. Two control algorithms were tested. The first one was based on the decentralised approach employing the local-loop control of each joint independently of each other and instantaneous minimisation of the Lyapunov function. The second control approach was the clipped-optimal control, which was composed of two sub-controllers similarly to strategies intended for friction-based devices discussed in Subsection 1.1.2 [88, 89]. The LQR controller generates a signal representing the optimal control forces, similar to fully active control. Then, the local controllers responsible for appropriate values of the contact force in the friction interface in each joint treat the LQR signals as the set-point values. Controllability and observability gramians were used to formulate the optimality criterion for distribution of sensors and actuators. The combination of the LQR approach with an algorithm calculating the required control signal for nonlinear semi-active device was also proposed by Onoda *et al.* [108]. However, such a control strategy was dedicated for a semi-active control device equipped with an electrorheological fluid damper (ER damper). The working principle of the ER dampers is similar as for MR dampers but the electric field is applied to vary damping properties of the damper instead of the magnetic field. The disadvantage of this ER dampers is that they often require high voltages, hence they are less popular. The semi-active device proposed by Onoda *et al.* controlled by their algorithm essentially works similarly to the device proposed by Kurino *et al.* [84] that is described in Subsection 1.1.2. The potential energy is accumulated in the spring and released in an appropriate moment to be dissipated in the damper, which are inherent parts of the device. However, Onoda *et al.* intended their con-

trol strategy to the light-weight space structures, which usually are more flexible and have lower material damping than civil structures, thus excitation of the higher-frequency vibrations is visible. It is due to the fact that the potential energy is accumulated during the increase in structural deformation both in the ER damper and structural members. Hence, when the ER damper switches its state suddenly reducing its effective stiffness, then the accumulated energy is partially released also in the free vibration of the higher-order modes. The control strategy has great potential in vibration attenuation of light-weight structures, however, an experimental verification exhibited that at the current stage of this research it is not possible to suppress the residual vibration of very small amplitude. The reason is that the prototype ER damper effectively always remains some residual stiffness and for a sufficiently low vibration level works as the passive truss member.

The use of the advanced control algorithms represented by the term generating the setpoint value and term following-up this value by regulation of the contact force in the semi-active joints results from the complex and nonlinear nature of the friction phenomenon. Thus, modelling of the friction-based structural joints is an important topic and a significant effort has been devoted also to this problem. Segalman [109] in a review paper indicated that linear approximations of the joint behaviour are restricted to the load range to which the linear model was tuned. Moreover, data for calibration of the device are required. Hence, nonlinear phenomenological models are widely used. Various approaches to describe the nonlinear behaviour of the friction joints as well as applications are discussed in the review paper by Gaul and Nitsche [110]. They concluded that phenomenological models, e.g. the LuGre model, are a good choice for the control design and simulation purposes. These models have a reduced number of DOFs but still provide ability to estimate energy dissipation rates in the friction interfaces.

The control strategies described above are designed to enhance the dissipation of the mechanical energy in semi-active devices, i.e. locally. However, the semi-active control also covers strategies, where energy dissipation in the whole volume of the structure is controlled by means of the dynamic modifications of local properties of the structure. One of the first of such semi-active control strategies was proposed by Onoda *et al.* [8]. A semi-actively controlled friction device was proposed to allow local modification of the structural stiffness. It is possible due to the clamping force that is sufficiently large for locking relative motion between the friction parts. Truss members equipped with this device were called "variable-stiffness members". If the device is locked, the variable-stiffness member behaves like regular beam of the structure but if the device is unlocked, relative motion between ends of the variable-stiffness member is possible and the local stiffness of the structure is switched to the lower value. Onoda *et al.* tested three control strategies intended for the use of variable-stiffness

members. All of them are based on the principle that the potential energy accumulated in strains during the structural motion can be suddenly released into free vibration of the higher-order structural modes after dynamic unlocking the variable-stiffness members. The high-frequency oscillations in these modes decreases quickly because the higher-order modes are characterised by greater inherent material damping. Moreover, the higher-order modes usually have small amplitudes of motion, hence their vibration does not disturb significantly the overall motion of the structure. The strategies tested by Onoda *et al.* differ only in the type of the feedback signal and criterion of the unlocking the variable-stiffness members. In the first strategy, the variable-stiffness member is unlocked for short time when the structural tip displacement reaches a maximal value (zero velocity). It is assumed to correspond approximately to the maximum potential energy of the structure, a portion of which is expected to be released in free vibration of the higher-order modes. The second control strategy uses signal feedback from the strain gauges placed on variable-stiffness members. The assumption is that the square of these strains (representing load transmitted by the lockable member) is proportional to the energy accumulated by these members and their neighbourhood, which is to be released in the higher-order modes. The variable-stiffness member is suddenly unlocked when the measured strain has its maximal value. This control strategy can be easily implemented in the decentralised control system. Finally, the third control strategy unlocks the semi-active device at time instance when the estimated energy to be released has the maximal value. However, the third control strategy was evaluated only numerically as opposed to the two remaining ones, which were validated both experimentally and numerically.

Minesugi and Kondo [111] conducted research on developing this approach with the use of the modal control theory. However, the fact that variable-stiffness member has ability to be locked at arbitrary relative displacement of the friction surfaces was ignored by them in the equations of motion of the system. It is manifested by a lack of the static-force term representing the lock of the variable-stiffness member at non-zero relative displacement, hence these equations of motion do not describe the system dynamics properly – especially the crucial energy prestress-release mechanism. This mechanism has been well described using an illustrative example of the spring-mass system in the continuation of the research initiated by Onoda *et al.* [9, 10]. The spring-mass system was equipped with two springs set in parallel: one uncontrolled and one detachable (controlled). The control strategy is as follows. Both springs accumulate the strain energy during motion of the system. When mass reaches a maximal displacement a detachable spring is disconnected for a short moment. It causes the release of the strain energy into the spring vibration and its quick dissipation. After a short time, the spring is reattached and the whole process is repeated, however, the equilibrium point of the spring mass system is changed.

This occurs because the detachable spring is reattached in a different position than before due to strain relaxation during disconnection. The change of an equilibrium point, manifested in the piece-wise constant term in the equation of motion, enhances efficiency of the damping strategy. The simple explanation is that reattaching the spring immediately after detaching it allows the strain accumulation process to begin earlier. Authors of such a strategy called it "prestress accumulation–release" (PAR) and demonstrated the effectiveness of the PAR approach using both the numerical model and experimental setup of the layered beam structure [10]. A change in stiffness analogous to the SDOF introductory example is achieved by delaminating the layers of the structure. Sudden delamination at the suitable moment causes the release of the strain energy in free vibration of the higher-order modes. This mechanism corresponds to the energy dissipation in the detachable spring. In this paper, it was indicated that the PAR method has applications in pedestrian bridges, pipeline systems, truss-like structures – including space industry and small-scale mechanisms. Indeed, Mróz *et al.* later proposed the PAR approach for control of the space structures. However, they used dedicated semi-active joints instead of changing stiffness through a delamination mechanism. Such joints have ability to be locked and transmit the bending moment between structural members or to be unlocked and work as hinges [11]. In this case, the principle of working also is analogous to the SDOF introductory example. The motion of the truss-like structure with currently locked joints causes accumulation of the strains. When strain responsible for the bending moment near the semi-active joint achieves its maximal value, the joint is dynamically unlocked, resulting in the release of the strain energy in free vibration of higher-order modes and its quick dissipation in the associated material damping. The vibration can be suppressed with the PAR method in its several lowest-mode cycles. Performance of the PAR was also demonstrated by Popławski *et al.* [12, 13] both in the numerical model of a multi-bay frame structure as well as experimental tests on the frame structure demonstrator equipped with two lockable joints. The amplitude reduction of 66–94 % in the forced vibration response at the first natural frequency during the experiments was reported in [13]. Orłowska *et al.* [14] investigated the possibility of employing the PAR approach also in structures where instead lumped or local change in the structural properties (such as locking/unlocking of the joint) it is provided by a smart material. They studied the layered beam structure equipped with a controllable core between two outside beam layers. Particular sections of the core material change its damping properties depending on the control signal that provides dynamical effect similar to the delamination. Applicability of various smart materials such as MR elastomers or pneumatically controlled granular structure in vibration mitigation of layered beam structures was investigated with other semi-active control laws also in [99, 112]. The variety of the structures and possible ways to change the structural properties demonstrates the potential range

of applications of semi-active control strategies transferring the energy into the higher-order vibration modes.

It should be noted that for the control techniques described in [8–14, 111] realised by the lockable joints or variable-stiffness members, it was sufficient to replace the complex and nonlinear model of the friction interfaces with constraints which are dynamically imposed on (or removed from) the DOFs describing the current state of the device. It is due to the fact that, contrary to the vibration attenuation based on the local energy dissipation approaches, the semi-active devices have only two steady states: fully locked or fully unlocked. Any transient states are assumed to be very short. Thus, any significant energy dissipation does not appear in the interface of semi-active device.

The second important note to works [8–14] is that they describe effective strategies of vibration mitigation by transferring the mechanical energy to the higher-order vibration modes. However, these control methodologies do not take the full advantage of the shifting of the energy into the higher modes because the control algorithms do not receive information about the current state of the structure in terms of the modal coordinates. Control strategies processing such information are discussed in general in the next subsection.

1.1.4. Modal control

The modal control approach allows for taking the advantage from representation of the controlled system in the eigenvalue-eigenvector formulation. Inman indicated that modal control was developed in two scientific disciplines: structural dynamics and control theory [113]. Regarding the later one, the state space equations are transformed into decoupled first-order ordinary differential equations, enabling lower computational effort. Control strategies refer to the pole placement problem [114]. The desired change of the poles (system eigenvalues) associated with particular vibration modes of the closed system, i.e. including control loop, can be achieved during design of the feedback controller. The possibility of decoupling the state equations simplifies the controller design, particularly for large-scale MDOF structures. An extensive review of the robust design of the modal control strategies using the control theory-based formulation has been given in a tutorial book by Magni [115]. The book contains review and description of the tools for the robust design as well as examples of their use with MATLAB® functions belonging to the accompanying toolbox for use with MATLAB® software. With regard to modal control developed within the former scientific discipline, Gould and Murray-Lasso [116] proposed modal control for structures in 1966. In this class of modal control strategies, the equations of motion describing structural behaviour in physical coordinates are decoupled with the aid of modal analysis. Hence, each vibration mode can be considered as the SDOF oscillator described by the second-order equation of motion and is decou-

pled from the remaining vibration modes. Of course, eigenvectors representing mode shapes obtained from modal analysis provide the same information on vibration modes as ones used in the control theory but formulation is different.

Modelling of the continuous or MDOF systems exactly requires including infinite or large number of vibration modes, respectively, whereas it is possible also to model only several ones because of practical reasons. The reasonable strategy is to model only lowest-order vibration modes usually taking significant participation in the structural motion and use only these modes during the design of the controller. The reason is that they are naturally weakly damped and easy to excite by external loads. Nevertheless, such a modal truncation of the investigated system can lead the controller designed only for these, controlled, vibration modes to excite vibration in higher-order, residual, vibration modes causing instability of the system. This phenomenon was investigated by Balas [117]. Balas demonstrated that a necessary condition for such instability is the presence both control spillover and measurement spillover. The first type of spillover is undesired excitation of the residual modes by the actuators controlling intentionally the set of the controlled modes. Measurement spillover is the disturbance of measurement of the controlled modes by the presence of residual modes at the sensor locations. The control spillover does not cause instability issues itself yet. It rather only decreases the control performance. However, if the additionally measurement spillover effect is present, then the closed-loop system provides bidirectional coupling between controlled and residual modes, introducing the negative damping into the closed-loop system. Such a phenomenon does not appear always but, as Balas indicated, each modal controller should be designed with particular emphasis on this effect.

Later, the active control methodology termed "independent modal-space control" was introduced and developed by Meirovitch and Coauthors [118–120]. The idea of this methodology was to control a set vibration modes of the structure in such a way that each particular mode is controlled independently of each other. In other words, the control does not couple modal equations or this effect is not significant. It requires at least as many actuators as many modes are to be controlled. This control methodology reduces control spillover effects, i.e. remaining modes are affected by the actuators very weakly. It allows concentrate the control effort on the preselected set of the controlled modes that usually are characterised by low material damping and high participation in the structural response. Meirovitch and Baruch also proposed the concept of a modal filter operator. The modal filtering is a process of extraction of the modal coordinates or velocities from the available measurement data. The modal filter is represented by matrix reciprocal to the matrix collecting controlled mode shapes at sensor locations. In this case, it is kind of spatial filtration that is equivalent to fitting particular mode shapes into measured displacement or velocities with the least squares method. If sensors are properly arranged on the controlled struc-

ture, then modal filtering allows for avoiding contamination of modal quantities by the noise and reduces the measurement spillover effect. Various approaches in optimal sensor placement for modal filtering purposes are discussed later in this section. The control spillover is reduced by suitable distribution of the forces corresponding to particular controlled mode among the actuators. Meirovitch and Baruh [121] also showed that the use of the independent modal-space control with the aid of modal filtering is robust with respect to the system uncertainties.

Lu [122] proposed an active modal control with direct output feedback dedicated to the mitigation of seismically excited structural vibration. Lu demonstrated that the modal control allows for vibration mitigation when limited information about state of the structure is available with performance close to the control with full-state knowledge. It is a valuable property of the modal control. Later, Lu [123] adopted the active modal control concept in semi-active control capable to generate dissipative control forces characterised by hysteresis loops similar to its active counterpart, pursuing greater values of the modal damping factors for the controlled vibration modes. It is due to the fact that active control forces often are also mainly dissipative, i.e. they have an opposite direction to the increments of actuator deformation. Hence, the semi-active modal control proposed by Lu has almost the same performance as for the active control. Moreover, both modal approaches proposed by Lu [122, 123] are resistant to measurement noise.

Basu and Nielsen [124] proposed a modal control algorithm combining the pole placement technique and integral resonant controller. Such a control methodology allows for broadening the set of the controlled vibration modes. A pole placement is used to achieve the desired modal damping factors of the higher controlled modes, while the integral-resonant term effectively attenuates low-order vibration modes. Performance of this control strategy was demonstrated both numerically and experimentally using a cantilever beam equipped with the single strain-gauge and piezoelectric actuator.

Belyaev *et al.* [125] compared the modal control approach with a local one in an experiment employing the cantilever beam equipped with two collocated pairs of piezoelectric sensors and actuators. In this case, the sensor–actuator pairs were located at the points at which the two controlled mode shapes have extreme modal deformations. These two first modes were mitigated with aid of modal control characterised by the designed transfer function – similarly for the benchmark local controller. The superiority of the modal approach over the local one was shown. The presented modal control was able to effectively reduce vibration for both resonances: of the first mode and of the second one, while the local approach was able to suppress effectively only first or only second resonance.

An interesting example of the control based on the concept of independent modal-space control with example of application to mitigate the response of a tall

building excited by an earthquake was proposed by Etedali [126]. The control of the preselected set of modes was proposed to be realised with the modal proportional–integral–derivative (PID) controller. It was demonstrated that the modal PID outperforms the well known LQR that was also implemented within the methodology of independent modal-space control. Parameters of the modal PID controller were optimised with the cuckoo search algorithm searching for the trade-off in the multi-objective optimisation problem for each controlled mode. Moreover, Etedali showed that the modal PID controller is more robust against structural stiffness uncertainties than the benchmark LQR control example.

Modal coordinates describe deformation of the whole structure, of course with some loss of accuracy related to the modal truncation error. However, the modal approach can be also adopted to minimise vibration amplitude at the particular location of the structure – e.g. at the location of measurement equipment. To this end, a new approach of semi-active sliding mode control employing the lockable joints was investigated by Ostrowski *et al.* [127]. In this control approach, a hyperplane is formulated in the modal space in such a way that any modal displacement within this plane results in zero structural displacement at the preselected location within the structure. Then, lockable joints are controlled aiming at minimisation of the distance of the actual modal displacements from the hyperplane. The advantage of formulation of the problem in modal coordinates is the possibility of reduction of the problem to only few modal coordinates since only several first vibration modes participate predominantly in the structural displacements. This approach provides satisfactory preliminary results, where the full state of the system is known.

Regarding the mentioned earlier influence of the sensor and actuator placement on the measurement and control spillover reduction, respectively, it is one of the key aspects of the modal control. The sensor placement can be related to various measures of observability, e.g. the observability gramian which was adopted by Gaul *et al.* in earlier discussed work [107]. However, as attention is paid to modal control approaches not only in this subsection but also in the research undertaken in the present thesis, sensor placement techniques referring directly to modal filtering, identification of modal parameters and modal control are further discussed. One of the simplest approaches for the sensor placement is their location at highest amplitudes, inclinations or deformations (depending on the sensor type) of particular mode shapes belonging to the set of controlled modes. An example of such an approach is shown in the work of Belyaev *et al.* [125] that is mentioned earlier. This method is suitable only for simple structures and for small sets of only several controlled modes. Here, only two first modes of cantilever thin beam were controlled. In practice, FE models with a large number of DOFs often are used, where usually a much smaller subset of DOFs is selected as sensor locations. In this case, an optimal sensor placement becomes a combinatorial task requiring a tremendous computational effort. Thus, variety of criteria

and methods of approximation of the optimal sensor locations were invented and developed. Chepuri and Leus [128] discussed optimisation criteria based on the covariance matrix of the error of estimated parameters. It was noticed that calculation of the covariance matrix and using it in numerical procedures during optimisation can be difficult or even practically impossible. Hence, a weaker criterion based on Cramér–Rao bound was considered. Here, instead of the covariance matrix the Fisher information matrix (FIM) can be used. Therefore, optimality criteria for selection of sensor locations relate to the maximisation of FIM norms, e.g. its trace or determinant. Papadimitriou and Beck [129] showed that the use of the norm of the FIM other than determinant is not recommended in some cases. In the case of estimation of the modal coordinates, the determinant of FIM represents a trade-off between values of mode shapes (related motion amplitudes) at sensor locations and their linear independence. After selection of appropriate optimality criteria the algorithm allowing for obtaining the near-optimal solution is required. One of the simplest approaches to sensor placement referring to the linear independence of the mode shapes was proposed by Schedlinski and Link [130]. They did not formulate the Fisher information matrix explicitly but proposed to use a vector basis composed of rows of the modal matrix, where the rows correspond to the particular DOFs of the structure, which also finds near-maximal determinant of FIM. First, the row vector with the highest norm is selected. Later, the vector whose projection on the plane perpendicular to all already selected vectors has the largest norm is selected in iterative manner until the desired number of rows (sensors) is not achieved. This method is also used in solving under-determined linear equation sets by using QR decomposition with pivoting to select the most representative solution basis, e.g. in MATLAB® software. Kammer proposed the famous effective independence method (EFI) whose formulation is explicitly based on FIM [131]. This method removes particular sensor locations from the set of the candidate sensor locations in iterative manner providing the lowest decrease of the determinant of FIM. The algorithm is stopped when the number of desired sensor locations decrease to the number of available sensors. Recently, highly efficient convex-relaxation-based algorithm to maximise the determinant of FIM has been proposed by Błachowski *et al.* [21]. In this method, the discrete problem is replaced with its continuous counterpart. During the optimisation process instead removing candidate sensor locations a sensor density vector is obtained. Elements of this vector that converge to the ones denote that the corresponding candidate locations are selected to be sensor locations, whereas elements converging to zeros denote rejected candidate sensor locations. This method has been selected to be used for a sensor placement in the present research – more details can be found in Section 3.2.

The proper actuator placement is related to the controllability of the structure. The controllability condition proposed by Kalman used classically in the control theory allows to investigate if the system is controllable or not. It is not

the measure quantifying the degree of controllability. Hence, in the case of the optimal actuator placement, other mathematical tools are employed. Additionally, for large MDOF systems often used in the engineering practice, Kalman's criterion may lead to numerical difficulties. The Popov–Belevitch–Hautus eigenvector test (PBH test) allows for indicating both the observability of the mode from the particular sensor location and its controllability from the particular actuator, avoiding the numerical problems [51]. In both cases the mode shapes must have nonzero values at the sensor/actuator location and corresponding eigenvalues must have unique values, i.e. there must not be any multiple eigenvalue. The PBH test provides also some metric about controllability and observability. The bigger displacement of the mode shape at the sensor/actuator location is, the greater is the associated observability/controllability. However, dynamic properties associated with modes such as modal damping coefficients or natural frequencies are not included into controllability measure, despite their real influence on the control performance. Hence, an alternative approach to quantify the controllability of the vibration modes can be obtained with the controllability gramians [132]. This controllability metric was used by Gaul *et al.* [107] in the multicriteria problem of an optimal placement of the semi-active joints. Gaul *et al.* [106] also used controllability and observability gramians to calculate the Hankel singular values providing information about simultaneously most controllable and observable modes. Indication of these modes allowed to reduce the structural model for the purpose of controller design. An interesting example of the robust optimal actuator placement was proposed by Li *et al.* [133]. Uncertainties of the structural parameters that affect eigenvalues of the controllability gramian were taken into account during optimisation of the actuator positions. The optimisation problem is formulated in such a way that it is possible to choose the trade-off between pure optimality and robustness with respect to the uncertainties of the structural parameters.

Summarising this subsection, literature on modal control shows that this approach has several important advantages in relation to control approaches based on the feedback from the state expressed in the form of physical coordinates. Superiority in terms of both performance and the frequency bandwidth of the modal control over local approaches can be achieved due to the physical insight resulting from modal analysis (e.g. Belyaev *et al.* [125]). Additionally, modal control can achieve performance close to the full-state feedback (e.g. Lu [122]), whereas it keeps the ease of the design process, lower computational effort and robustness with respect to the structural parameter uncertainties.

1.1.5. Energy harvesting

As it was mentioned, energy harvesting technology has growing importance in both science and industry, e.g. it can be used for battery-less supplying wire-

less sensors and other devices connected to the Internet of Things. It is crucial for, e.g. predictive maintenance, real-time data processing, monitoring of supply chains and other approaches belonging to the Industry 4.0 [134]. Energy harvesting technologies allow for not only energy salvage but also can reduce costs of applications requiring network of devices, e.g. such as sensors, due to avoiding the wired power source. There is a variety of devices scavenging energy from its various environmental sources, among others: the well known photo voltaic cells and wind turbines, thermoelectric, friction-based mechanisms and, finally, vibration-based technologies. In this subsection, the attention is focused on the vibration-based energy harvesting. There exist many different types of vibration-based EHs, whose principle of working is based on different physical phenomena, e.g. electrostatics or magnetostriction phenomenon, however, mainly the two most popular are: electromagnetic energy harvesters (EMEHs), based on Farady's law, and piezoelectric energy harvesters (PEHs), based on piezoelectricity phenomenon [135]. EMEHs often operate at lower operational frequencies than PEHs. Vibration-based energy harvesting is associated usually with small-scale applications allowing for lower-rates of generated power used in supplying, e.g. sensors or micro electromechanical systems (MEMS), however, also bigger or even large-scale applications are possible, e.g. in human motion, automotive industry and buildings [136, 137].

In recent times, significant effort has been devoted to improve operation of EHs not only in terms of efficiency and size, but also expanding operational frequency bandwidth. An interesting example of shape modifications aiming at enhancement of the device operation was proposed by Kundu and Nemade [138]. In this PEH, the beam structure has been designed with a variable cross-section to ensure uniform stresses along the beam length. It increased the produced power by 20 % comparing with conventional PEH having an uniform cross-section. Another example of PEH with application in medicine was proposed by Anand and Kundu [139]. The proposed PEH is dedicated to pacemaker. Due to a spiral shape of the cantilever-beam structure, the natural frequency of PEH is reduced to the frequency of the heart beat allowing work under resonance while simultaneously keeping a small size. Regarding expanding of the operational frequency bandwidth, it can be achieved with collection of several oscillators in the MDOF structure, resulting in several frequency peaks. Such an EMEH device containing three electromagnetic coils and moving magnets connected through V-shape plate was discussed by El-Hebeary *et al.* [19]. The device allows for operation in three frequency-different vibration modes. Chen and Fan discussed recent advances in the utilisation of the internal resonance phenomena in enhancing nonlinear EH operational characteristics [20]. Internal resonance allows for operation of nonlinear EH in a wider operational bandwidth due to the coupling of the vibration modes and their energy exchange as well as possibility of multi-mode and multi-directional operation.

If EH is to be installed between two bodies that relatively move then a mechanism called a mechanical amplifier can be employed [140]. The principle of working of such mechanisms is that relative motion between bodies is transmitted to the attached EH simultaneously magnifying the amplitude. Hence, velocities and accelerations acting on the EH also are increased.

Zhang *et al.* [15] showed that for the EHs exhibiting linear behaviour the expanded operational frequency bandwidth can be achieved only at the expense of the peak-efficiency at the resonance. Hence, the designer of the EH must consider the trade-off between these two criteria of the device performance. On the other hand, analysis of dynamics of nonlinear EHs, whose behaviour differs from linear systems, is difficult, e.g. the highest vibration amplitude does not have to cause the biggest produced output power. Due to the nonlinearities, the EH can return some amount of the energy to the excitation above a certain vibration amplitude level. To tackle this problem Zhang *et al.* proposed using the condition of the global resonance for maximisation of EH effectiveness. This condition is satisfied when excitation does not perform negative work over EH at any time instant. It is related to the shaping of the EH potential well and can be used both for single-frequency vibration source and multi-frequency one. Ostrowski *et al.* [18] considered both varying electromechanical coupling coefficient and varying inductance of the electromagnetic coil. Both of them depend on the magnet position inside the electromagnetic coil. For the vibration amplitude above a certain level, the nonlinearities and the influence of internal dynamics of electrical circuit are strongly exhibited in EMEH behaviour. Then, increasing the excitation amplitude can even decrease the produced power. For each value of the excitation frequency, one optimal value of excitation amplitude can be found resulting in the maximal generated power. A size of the device was limited by spring bumpers, between which the magnet was moving. This additional mechanical nonlinearity expands the operational frequency bandwidth.

Cottone *et al.* [16] proposed the use of elastic collisions of the magnet with the moving mass to amplify the velocity of the magnet that was moving inside the coil. Such an intentional mechanical nonlinearity introduced to the system increased the generated power level by 33 times comparing to the device based on a single mass. The broadened operational frequency bandwidth was the additional benefit. The collision phenomenon can be used in frequency-up conversion in energy harvesting. Halim *et al.* [17] proposed EMEH device employing the collision-driven frequency-up mechanism dedicated for human-limb excitation. The frequency-up mechanism is similar to velocity amplification proposed by Cottone *et al.* due to the principle of conservation of momentum. In this case, a mass freely moves between two magnets mounted on springs. These magnets interact with electromagnetic coils. They vibrate with high frequency after collision with the moving free mass. It allows to convert the low-frequency human motion into the high-frequency oscillations of the moving magnets resulting in

enhanced power generation and simultaneously keeping a relatively small size of the device. Another example of the impact-driven frequency-up conversion was discussed by Wang *et al.* [141]. In this device, the frequency-up mechanism was realised by collision of a mass mounted on beam tip with piezoelectric beams. The operational frequency bandwidth was additionally expanded with the aid of magnets in vicinity of the moving mass. These two types of intentional nonlinearities affecting the potential well of the EH increased significantly the level of generated power. The problem of the tread-off between peak efficiency and an operational frequency range can be avoided with an adaptable EH. Alevras and Theodossiades [142] proposed a self-tunable EMEH intended for rotating structures, e.g. shafts, operating with varying rotational velocities resulting in varying excitation frequencies for the EMEH. The natural frequency of the proposed EMEH is tuned to the expected vibration frequency due to the centrifugal force acting on a tuning mass. Such a structure allows the proposed EMEH to operate under resonance in the wide frequency range.

Literature on vibration-based energy harvesting shows that significant effort is devoted to expanding the operational frequency range and increasing the effectiveness of the EHs. To tackle the trade-off between the frequency range of efficient operation and resonance peak efficiency various nonlinear devices are developed and studied, including modal coupling phenomena driven by the internal resonance.

1.2. Motivation, aims, assumptions and scope of the thesis

From the literature review it is concluded that the known attempts to dampen vibrations have been made for a century and a half. However, due to the often harmful impact of vibrations, this topic is intensively researched to this day. Despite the effectiveness of active vibration control, mainly the passive approaches are employed. It is due to the higher costs of the active control systems related to the required power source and actuators, and the fact that the active control system does not work in the case of the power source failure. Semi-active control provides a reasonable trade-off between passive and active vibration control, requiring relatively small amount of energy to change the state of the semi-active devices. It can result in effectiveness close to the purely active approach simultaneously keeping the advantages of the passive systems. Thus, attention of the present author is focused on semi-active vibration control. However, instead of local dissipation of the vibration energy in the controlled semi-active devices the control strategies stimulating global damping mechanism are considered. Here, vibration energy associated with the lower-order vibration modes that are usually the most participating in structural motion can be transferred into the higher-order vibration modes and quickly dissipated in the structural volume due to material damping. This mechanism is recognised as a very efficient in suppress-

ing the structural vibration due to the fact that the higher-order vibration modes have significantly higher damping coefficients than the lower-order ones, which in turn, are usually the most difficult to be attenuated.

As the mechanism of the modal coupling in the case of passive systems and resulting in nonlinear interaction between vibration modes is well researched in the literature, the semi-actively controlled modal energy transfer is less investigated. There are only a few works explaining the theoretical basis of the modal coupling effect caused by switching of the local stiffness properties realised by locking or unlocking the relative motion between structural DOFs. For example the PAR method, despite its high effectiveness, is a heuristic approach based on local strain measurements. It does not take the advantage from information about the structural behaviour expressed in terms of modal coordinates. The literature review shows also that modal control approaches can have performance close to control strategies employing the full-state knowledge but still keep the advantages carried by modal truncation: low computational effort and the ease of the design process. Thus, an investigation of modal interactions during semi-actively controlled energy exchange between vibration modes and its potential application in the controller design process seems to be a very interesting and important problem.

Regarding the vibration-based energy harvesting, as the literature review shows, the significant effort is devoted to enhance the operation of the EHs in terms of among others: expanding of the operational frequency bandwidth, dealing with the trade-off between the operational frequency bandwidth and EH peak efficiency, providing multi-modal and multi-directional operation of EHs or amplify the EH motion. Intentionally introduced nonlinearities, including internal resonance phenomenon resulting in the energy transfer between the coupled vibration modes, aim at achieving these enhancements. These directions in the research on energy harvesting lead to the question: Is it feasible to develop semi-active control strategy allowing for effective and precise transfer of the energy from currently excited vibration modes into the vibration mode whose vibration provides EH peak-efficiency?

The considerations described above motivated the author of the thesis to conduce research on the novel semi-active modal control strategy that is able to precisely transfer the mechanical energy to or out from the selected structural vibration modes. Transfer of the energy is induced by the modal coupling effect resulting from locking/unlocking of the lockable joints installed in the controlled frame structure. Such a methodology can be potentially applied both for vibration mitigation and energy harvesting.

In the former case the vibration damping of light-weight structures is considered. Similarly to the PAR method, the proposed control strategy also allows for the transfer of the energy into the high-frequency vibration modes and its efficient dissipation in material damping. Due to the semi-active character of the control it does not require the efficient energy source that is a great advantage

for light-weight structures. The proposed control methodology is especially attractive to be used in space structures. Apart from the possible lower weight, this control strategy has also other advantages valued in this field. First, the locking effect of the joints can be realised by friction-based interface with varying clamping force that is more favoured in the space industry than other solutions, e.g. containing fluids. It allows for operation of the vibration mitigation systems in high-cleanliness or vacuum environment to which fluid-based solutions are sensitive. Second, the control is of semi-active type, thus it cannot destabilise the structure in free vibration. Third, the joints can be designed in a way increasing the reliability of the overall system. In the case of any failure of the control system, e.g. controller or actuator within a semi-actively controlled lockable joint, the clamping force can be kept at the level providing friction-based local damping within the joint. Then, despite the lower effectiveness of the system, it can still reduce vibration. And the last advantage is related to the results reported in [37]. Passive pinned joints intended for the space structure, which have similar advantages and attenuate low-frequency vibration by both friction and transferring the vibration energy towards higher-order vibration modes, unfortunately are very sensitive to any preload of the structure. Their use requires high-precision of the truss assembly and invariant operational conditions. It is due to the fact that these joints provide these two damping effects due to the clearance between the interface parts which can be eliminated when the structural geometry is even slightly changed. The proposed semi-active control allows us to avoid this problem as the joints can be locked/unlocked at any rotational positions between adjacent structural members and still operate properly.

Regarding the energy harvesting applications, the mechanical energy is to be transferred from the currently excited vibration modes into the preselected (targeted) vibration mode. Here, it is assumed that EH is attached to the controlled structure and is tuned with the preselected structural mode. In this situation, EH works under resonance conditions even if frequency of external excitation is far from that, being within the resonance range of any other monitored vibration mode of the structure.

The control methodology described above requires the deep insight into the behaviour of vibration modes interacting with each other during modal energy exchange. These problems undertaken have been led to formulation of the following thesis:

Dynamic reconfiguration of frame structures by locking and unlocking rotational joints can be used for precise transfer of mechanical energy between selected vibration modes in a chosen direction. Such a reconfiguration is a generalization of the "Prestress Accumulation–Release" (PAR) strategy and, in addition to being used to mitigate vibrations, can increase the efficiency of energy harvesting when necessary.

Aiming at proving the stated thesis the main goal of the present work is to propose and validate a new methodology of the semi-active modal control that allows for precise and efficient energy transfer between vibration modes (as opposed to PAR approach which allows for the transfer only from lower-order to higher-order vibration modes, in practice only in the heuristic manner). The proposed control strategy, at the current preliminary stage of the research, is limited to flat frame structures and is to be realised by controlled lockable joints. Depending on the control signals such joints can be locked and transmit the bending moments between adjacent structural members or can be unlocked and work as a hinges. The methodology described in this thesis consists of:

- Theoretical analysis of the influence of the locking effect on modal coupling effect and modal energy transfer, aiming at: designing of the controller, better understanding the control strategy, allowing for its eventual further improvements and its application for structures different from ones proposed in the thesis. Here, a special attention is paid to the fact that when any joint becomes locked a reconfiguration of the system occurs that results in the change of no. of structural DOFs and modal basis.
- Selection of the physical quantities required to estimate the instant value of the modal energy transfer rate required for operation of the control algorithm.
- Methods for optimal placement of both sensors required for modal filtering and lockable joints controlling the structural behaviour.
- Control law which is directly based on the theoretical analysis and control algorithm that additionally includes equipment limitations and other practical issues. The control algorithm instantaneously maximises the weighted transfer rate between particular monitored structural vibration modes in the desired direction.

The following assumptions are made in the present thesis for analysing reconfigurable structures to be controlled:

1. Beams of flexible frame structures are made from linear-elastic and isotropic material, whereas lumped members of relatively large stiffness (e.g. lockable joints, their components) are modelled as ideally rigid components, e.g. by using lumped mass parameters and offsets. The exception is an illustrative example of two-degrees-of-freedom system, introduced for clarification of the dynamics of reconfigurable systems, where rods (that are not lumped members) also are ideally rigid.
2. Small vibration is assumed, thus apart from the usefulness of the above assumption also the geometrical nonlinearities are neglected.
3. Flexible frame structures are discretized with the aid of FEM, which results in relatively big but a finite number of structural DOFs.

4. The proportional model of material damping is assumed or omitted.
5. The transient state during locking of the joint is assumed to be very short and later the coupled rotational DOFs involved in the joint have common rotational velocity, thus it is modelled with the aid of the law of conservation of angular momentum and kinematic constraints imposed on appropriate rotational DOFs or with the aid of a relaxed constraint represented by viscous joint model.
6. Additional assumptions for modelling of the EMEH in the numerical study are made: stiffness of the spring providing the restoring force for the moving magnet is constant, damping of the magnet motion inside the electromagnetic coil is viscous, inductance of the electromagnetic coil and electromechanical coupling coefficient are constant.

Apart from the current chapter allowing for determination how this work relates to the current state of the art, the scope of the further part of the thesis is as follows:

Chapter 2. This chapter describes the influence of the locking of the joint on the structural dynamics. Locking/unlocking of the joint is treated as a kind of reconfiguration resulting in imposing/removing kinematic constraints, which changes the number of structural DOFs, the modal basis along with its dimension, and other structural properties. Useful relaxation of these kinematic constraints by employing the viscous-based joint model with a large damping coefficient is described. These issues are first introduced using a simple two-degree-of-freedom system, followed by a derivation applicable to MDOF structures. The modal coupling effect and modal energy transfer which result from the locking of the joints are described. Additionally, a suitable method of integration of equations of motion is recommended.

Chapter 3. In this part of the thesis, various aspects of the control strategy devoted for the structures from the previous chapter are introduced and discussed. First, measured physical quantities, which are required for proper operation of the control, are indicated and some specific issues related to the measurement in reconfigurable structure are discussed. Later, optimal placement of sensors and lockable joints is studied. Novel method of finding optimal sensor layout providing maximal determinant of the Fisher information matrix is described. This method is based on convex relaxation that allows for replacement of the discrete optimisation problem with its continuous counterpart. Novel controllability measures are introduced aiming at indication of optimal locations of the lockable joint. Finally, the novel control law based on instantaneous maximisation of the weighted modal energy transfer rates in desired direction is proposed for both vibration attenuation and energy harvesting application. The control

law serves as a basis to a control algorithm that is adapted to equipment limitations and other practical issues.

Chapter 4. Effectiveness of the proposed methodology is verified numerically for both kinds of applications: vibration attenuation and energy harvesting. The controlled structures are subjected to various excitations. The performance of the proposed control strategy in vibration attenuation is compared with the PAR approach for each test excitation. Moreover, optimal and non-optimal (e.g. in the case of construction limitations) placement of the lockable joints is considered. In the numerical testing concerning the energy harvesting application, a small-scale frame structure with the attached EMEH is investigated.

Chapter 5. Applicability and the performance of the method in control of real frame structures is validated experimentally on laboratory frame demonstrator. Both the ability to dampen vibration and transfer the energy to the preselected vibration mode (here without any EH) is studied. Free (hook release) and forced (frequency sweeps) vibrations are controlled during the experiments. The FE model of the controlled structure is updated to experimentally identified modal data and then used for calculation of the parameters used in the control algorithm as well as performing numerical simulations to compare the numerical results with the experimental ones. During this comparison, attention is given to the imperfections of the lockable joint prototypes, which constitute the primary source of discrepancies between simulation and experimental control performance. Despite these discrepancies, the experimental results are satisfactory and prove the applicability, effectiveness and robustness of the developed control strategy.

Chapter 6. In the last chapter of the thesis, the conclusions on each aspect of the proposed methodology and its validation, both numerical and experimental, are drawn. It is followed by comments on unresolved issues and future research.

1.3. Contributions

The contributions of this thesis are summarised as follows:

1. Author's analysis of the reconfiguration effect provided by the locking and unlocking of the joints of plane frame structures, and its influence on kinematics of the structure and its dynamic properties.
2. Author's derivation inspired by fast nonlinear analysis (FNA) [143] for describing the influence of operation of semi-actively controlled lockable joints of plane frame structures on modal coupling effect and resulting energy exchange between vibration modes.

3. Selection of the physical quantities to be measured for operation of the control algorithm under realistic conditions.
4. Co-authorship in development of the novel method based on convex relaxation for optimal sensor placement in the sense of maximisation of determinant of the Fisher information matrix for modal filtering.
5. The proposition and development of the method for optimal placement of the lockable joints, dedicated to the proposed control methodology and enabling maximisation of energy exchanged between vibration modes during joint lock.
6. Development of the control strategy providing instantaneous optimality of the modal energy transfer rates to/from particular structural vibration modes consisting of: control law based on derivations indicated in the second point and the control algorithm developed with taking into account measured quantities and equipment limitations.
7. Extensive numerical evaluation of the performance of the proposed control methodology and its comparison with the PAR method in vibration attenuation for various excitations as well as optimal and non-optimal placement of the lockable joints.
8. Extensive numerical evaluation of the performance of the proposed control methodology in enhancement of the energy harvesting process for various excitations and two different cases of the targeted mode. Simulations include the model of EMEH.
9. Extensive experimental verification of the proposed control methodology based on experimental data provided by Doctor Grzegorz Mikułowski, using laboratory frame demonstrator equipped with lockable joints. Comparison of experimental results with simulations employing the FE model updated to the modal data of the real structure was conduced both for vibration attenuation and energy harvesting applications (EH was not included into the experiment). Free and forced (frequency sweeps) vibration cases were investigated.

The contributions enumerated above are described in publications: five articles in widely respected journals, eight conference papers in prestigious international conferences and one book chapter. All these publications are listed in pages 15 and 16.

2. Dynamics of the reconfigurable structure equipped with lockable joints

In this chapter dynamics of structures equipped with lockable joints is considered. Locking of the joints causes that local stiffness is increased and one rotational DOF per each locked joint is effectively removed. Such a possibility of dynamic reconfiguration causes that a special attention should be paid to description of the structural motion in terms of the modal coordinates. Modal basis obtained for the system with currently locked joints differs from one obtained for the unlocked ones. It is illustrated in Fig. 2.1, where three mode shapes of a certain three-DOF system equipped with a lockable joint form, namely, the unlocked modal basis $\{\boldsymbol{\phi}^{(1)}, \boldsymbol{\phi}^{(2)}, \boldsymbol{\phi}^{(3)}\}$. When the joint is locked the system has only two DOFs. Then, namely, the locked modal basis is reduced to two eigenvectors $\{\widetilde{\boldsymbol{\phi}}^{(1)}, \widetilde{\boldsymbol{\phi}}^{(2)}\}$ that are different from the unlocked ones. Moreover, the equilibrium point can shift from point $\mathbf{0}$ into $\widetilde{\mathbf{q}}_{\mathrm{l}}$ if the joint is locked when a structure is deformed (non-zero rotational displacement at DOFs involved in the joint). An important observation is that vectors of locked modal basis can be described in terms of vectors of the unlocked modal basis that, generally, has as many more dimensions as many joints are currently locked. Thus, it is possible to describe structural behaviour using only the unlocked modal basis, even if joints are locked, by employing modal coupling effect.

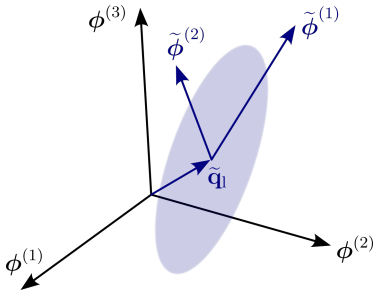

Fig. 2.1. Example of possible relation between modal spaces of a reconfigurable three-DOF system which are obtained for the joint in the unlocked and locked states.

To understand dynamics of structures equipped with lockable joints these issues are discussed step-by-step in the present chapter. The derivations presented in this chapter enable us in the further part of the thesis for:

- formulation of an efficient numerical model of semi-actively controlled lockable joint,
- derivation of the energy transfer rates between vibration modes of the structure serving as a basis for development of the control law, and
- optimal placement of sensors and lockable joints within structure of various kinds of topology.

2.1. Dynamics of a reconfigurable system with two degrees of freedom

Before discussion on the general case of MDOF structures equipped with lockable joints a simple illustrative example of a reconfigurable system with two degrees of freedom (two-DOF system) is considered. This example allows for understanding crucial issues of dynamics of the structures with the lockable joints. These issues are:

- the influence of the reconfiguration effect on the system dynamics and modal basis, mentioned on page 59 (discussed in Subsections 2.1.2–2.1.4),
- dynamical effects caused by the sudden lock of the joints (Subsection 2.1.3),
- modal coupling effect and choice of the modal basis (for locked or unlocked joints) to describe the structural motion (Subsection 2.1.5).

These problems are described in detail using a kinematic constraint first. However, this approach causes additional difficulties in calculations that can be omitted with a relaxed constraint representing the locking effect, as shown in Subsection 2.1.6.

2.1.1. Reconfigurable system with 2 DOFs

The considered two-DOF system is shown in Fig. 2.2a. It consists of two rigid rods of mass $M = 1$ kg and length $l = 1$ m. The rods are connected together via lockable joint and rotational spring of stiffness $k = 5000$ Nm/rad. The first rod is connected to the support via rotational node characterised by the same rotational stiffness k. It is assumed that the system is undamped and vibration is within small amplitudes.

Motion of the two-DOF system is described by the equation of motion

$$\begin{cases} \underbrace{\begin{bmatrix} I_{11} & I_{12} \\ I_{21} & I_{22} \end{bmatrix}}_{\mathbf{M}} \begin{bmatrix} \ddot{q}_1(t) \\ \ddot{q}_2(t) \end{bmatrix} + \underbrace{\begin{bmatrix} k_{11} & k_{12} \\ k_{21} & k_{22} \end{bmatrix}}_{\mathbf{K}} \underbrace{\begin{bmatrix} q_1(t) \\ q_2(t) \end{bmatrix}}_{\mathbf{q}(t)} = \begin{bmatrix} 1 \\ -1 \end{bmatrix} f(t), \quad t > 0, \\ \mathbf{q}(0) = \mathbf{q}_0, \\ \dot{\mathbf{q}}(0) = \dot{\mathbf{q}}_0, \end{cases} \tag{2.1}$$

where:

$$\mathbf{M} = Ml^2 \begin{bmatrix} 4/3 & 1/2 \\ 1/2 & 1/3 \end{bmatrix}, \qquad \mathbf{K} = k \begin{bmatrix} 2 & -1 \\ -1 & 1 \end{bmatrix},$$

are mass[1] and stiffness matrices, respectively, $q_1(t)$ and $q_2(t)$ are rotations of rigid rods as shown in Fig. 2.2b and $f(t)$ is the current value of the bending moment transmitted by the lockable joint. It is equal to zero, when the joint is in the unlocked state. Then, only rotational spring transmits the bending moment. In the locked state a pair of self-equilibrated moments acts on the connected structural members as shown in Fig. 2.2c, keeping the connection rigid. The lockable joint can be locked at any time instant and any relative rotational displacement between the connected structural members.

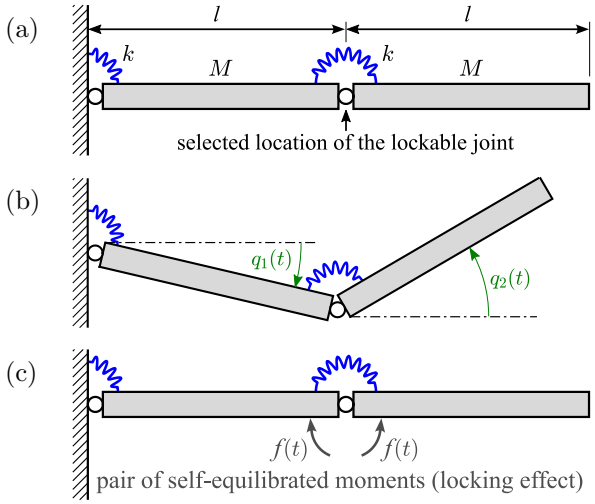

Fig. 2.2. Two-DOF system equipped with lockable joint: (a) schematic view, (b) coordinates describing system displacements and (c) pair of self-equilibrated moments representing the locking effect of the joint.

Below system dynamics is described for: motion when the joint is unlocked, joint being locked, and when the lockable joint is being unlocked again.

2.1.2. Phase 1: unlocked joint

When the joint is in the unlocked state, i.e. $f(t) = 0$, $t \in [0, t_1]$, where t_1 is time instant when the joint is being locked, the system described in Eq. (2.1) has two vibration modes satisfying the eigenvalue problem:

[1] In further part of the thesis "mass matrix" refers to generalised mass matrix $\mathbf{M}$ corresponding to both translational and rotational DOFs of MDOF structure. Thus, seeking for the simplicity matrix in Eq. (2.1) also is termed as "mass matrix".

$$\left(-\begin{bmatrix} I_{11} & I_{12} \\ I_{21} & I_{22} \end{bmatrix}\omega^{(m)2} + \begin{bmatrix} k_{11} & k_{12} \\ k_{21} & k_{22} \end{bmatrix}\right) \underbrace{\begin{bmatrix} \phi_1^{(m)} \\ \phi_2^{(m)} \end{bmatrix}}_{\boldsymbol{\phi}^{(m)}} = \mathbf{0}, \qquad m = 1, 2, \tag{2.2}$$

where $\omega^{(m)}$ and $\boldsymbol{\phi}^{(m)}$ are m-th natural frequency and mode shape, respectively. Mode shapes are normalised with respect to the mass matrix. Vibration modes of the structure shown in Fig. 2.2 are shown in Fig. 2.3. Vibration modes $(\omega^{(m)}, \boldsymbol{\phi}^{(m)})$ and basis $\{\boldsymbol{\phi}^{(m)}\}$, $m = 1, 2$, are further called "unlocked vibration modes" and "unlocked modal basis", respectively.

(a) $\omega^{(1)} = 41.3$ rad/s, $\phi_1^{(1)} = -0.556$ rad, $\phi_2^{(1)} = -0.734$ rad

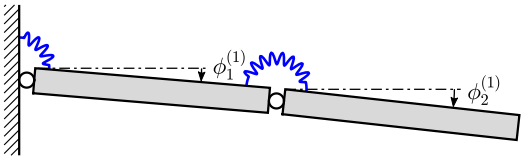

(b) $\omega^{(2)} = 274.7$ rad/s, $\phi_1^{(2)} = -1.185$ rad, $\phi_2^{(2)} = 2.514$ rad

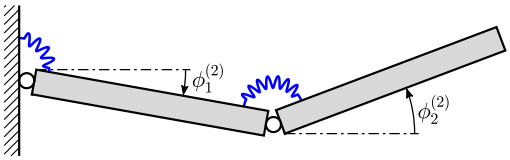

Fig. 2.3. Vibration modes of the two-DOF system for the joint in the unlocked state.

2.1.3. Phase 2: locking effect

Motion of the structure with currently locked joint is subjected to the constraint:

$$q_2(t) - q_1(t) = \Delta q, \qquad t \in (t_\mathrm{l}, t_\mathrm{u}], \tag{2.3}$$

where:

$$\Delta q = q_2(t_\mathrm{l}) - q_1(t_\mathrm{l}) = \mathrm{const}$$

is the difference of rotational displacements at the time instant t_l, when the joint is being locked, and t_u is time instant of the joint unlocking. In the consequence one DOF is lost after the joint lock. Then, we have:

$$\begin{bmatrix} q_1(t) \\ q_2(t) \end{bmatrix} = \underbrace{\begin{bmatrix} 1 \\ 1 \end{bmatrix}}_{\mathbf{B}_0} q(t) + \underbrace{\begin{bmatrix} 0 \\ 1 \end{bmatrix}}_{\mathbf{B}_1} \Delta q, \qquad t \in (t_\mathrm{l}, t_\mathrm{u}]. \tag{2.4}$$

For matrices $\mathbf{B}_0$ and $\mathbf{B}_1$ selected as shown in equation above

$$q(t) = q_1(t), \qquad t \in (t_\mathrm{l}, t_\mathrm{u}]. \tag{2.5}$$

If the constraint in Eq. (2.4) is satisfied it follows that its derivative also is satisfied, then the corresponding constraint imposed on rotational velocities should be noticed:

$$\dot{q}_2(t) - \dot{q}_1(t) = 0, \qquad t \in (t_\mathrm{l}, t_\mathrm{u}]. \tag{2.6}$$

The joint can be locked at any time instant t_l, thus we assume that rotational velocities when the joint is being locked do not have to be equal:

$$\dot{q}_2(t_\mathrm{l}) \neq \dot{q}_1(t_\mathrm{l}). \tag{2.7}$$

Thus, there is a discontinuity of rotational velocities at time instant t_l. When the joint is locked rotational velocities can be described by one common rotational velocity as follows:

$$\begin{bmatrix} \dot{q}_1(t) \\ \dot{q}_2(t) \end{bmatrix} = \begin{bmatrix} 1 \\ 1 \end{bmatrix} \dot{q}(t), \qquad t \in (t_\mathrm{l}, t_\mathrm{u}]. \tag{2.8}$$

Due to the discontinuity the common rotational velocity $\dot{q}(t)$ is to be found after the joint lock, i.e. at the time instant $t_\mathrm{l} + \varepsilon_t$, where ε_t is the infinitesimal time interval.

Independently of the realisation of the locking effect the law of conservation of angular momentum can be used to find the rotational velocity common for both rotational DOFs (Eq. (2.8)). Due to the fact that both rotational DOFs have the same rotational velocity after the locking it can be treated as ideally inelastic collision. Knowing that angular momentum of the system before and after locking of the joint is the same and taking into account Eq. (2.8) we have the following equation:

$$\underbrace{\begin{bmatrix} 1 & 1 \end{bmatrix} \mathbf{M} \begin{bmatrix} 1 \\ 1 \end{bmatrix}}_{I_\mathrm{l}} \dot{q}^+ = \begin{bmatrix} 1 & 1 \end{bmatrix} \mathbf{M} \begin{bmatrix} \dot{q}_1^- \\ \dot{q}_2^- \end{bmatrix}, \tag{2.9}$$

where $\dot{q}^+ = \dot{q}(t_\mathrm{l} + \varepsilon_t)$ is the common rotational velocity after joint locking, whereas $\dot{q}_1^- = \dot{q}_1(t_\mathrm{l})$ and $\dot{q}_2^- = \dot{q}_2(t_\mathrm{l})$ are rotational velocities before joint locking. Thus

$$\dot{q}^+ = \frac{1}{I_\mathrm{l}} \begin{bmatrix} I_{11} + I_{21} & I_{12} + I_{22} \end{bmatrix} \begin{bmatrix} \dot{q}_1^- \\ \dot{q}_2^- \end{bmatrix} = \mathbf{A}_\mathrm{l} \dot{\mathbf{q}}^-. \tag{2.10}$$

Due to the fact that rotational velocity $\dot{q}^+$ is common for both DOFs after the lock of the joint some amount of kinetic energy is lost (converted to its other forms, e.g. the heat, as analogy to inelastic collision) when the rotational velocities are different before locking.

By substitution of Eq. (2.4) into Eq. (2.1) and left-multiplying by $\mathbf{B}_0^{\mathrm{T}}$ we receive:

$$\underbrace{\mathbf{B}_0^{\mathrm{T}} \begin{bmatrix} I_{11} & I_{12} \\ I_{21} & I_{22} \end{bmatrix} \mathbf{B}_0}_{I_{\mathrm{l}}} \ddot{q}(t) + \underbrace{\mathbf{B}_0^{\mathrm{T}} \begin{bmatrix} k_{11} & k_{12} \\ k_{21} & k_{22} \end{bmatrix} \mathbf{B}_0}_{k_{\mathrm{l}}=k} q(t)$$

$$+ \underbrace{\mathbf{B}_0^{\mathrm{T}} \begin{bmatrix} k_{11} & k_{12} \\ k_{21} & k_{22} \end{bmatrix} \mathbf{B}_1}_{0} \Delta q(t) = \underbrace{\mathbf{B}_0^{\mathrm{T}} \begin{bmatrix} 1 \\ -1 \end{bmatrix}}_{0} f(t), \quad t \in (t_{\mathrm{l}}, t_{\mathrm{u}}]. \quad (2.11)$$

Finally, the motion of the two-DOF system when the joint is locked is described, including initial conditions for the considered range of time, as follows:

$$\begin{cases} I_{\mathrm{l}}\ddot{q}(t) + k_{\mathrm{l}} q(t) = 0, \quad t \in (t_{\mathrm{l}}, t_{\mathrm{u}}], \\ q(t_{\mathrm{l}} + \varepsilon_t) = q(t_{\mathrm{l}}), \\ \dot{q}(t_{\mathrm{l}} + \varepsilon_t) = \mathbf{A}_{\mathrm{l}} \dot{\mathbf{q}}^{-}. \end{cases} \quad (2.12)$$

After the transformation between configuration spaces shown in Eq. (2.11) the information about angle Δq and potential energy stored in the second spring is lost in the resulting equation. Δq should be then stored separately. Furthermore, reduction of the configuration space by one DOF due to the locking effect reduces modal basis into one, single-DOF mode shape, denoted as $\widetilde{\phi}$, and one natural frequency:

$$\widetilde{\omega} = \sqrt{\frac{k_{\mathrm{l}}}{I_{\mathrm{l}}}} \quad (2.13)$$

that is usually different from both $\omega^{(1)}$ and $\omega^{(2)}$ is obtained. This modal basis is insufficient to describe a full state of the two-DOF system due to the lost information about Δq. This issue is illustrated in Fig. 2.4. The vibration mode $(\widetilde{\omega}, \widetilde{\phi})$ and single-dimensional modal basis $\{\widetilde{\phi}\}$ are further called "locked vibration mode" and "locked modal basis", respectively.

If information about Δq is available then current displacements of the structure with the joint in the locked state can be expressed in terms of the unlocked modal basis (even if this basis does not describe dynamical properties of the system for the locked joint). It is due to the fact that locked vibration mode illustrated in Fig. 2.4 can be expressed as superposition of two unlocked vibration modes. The similar relationship between locked and unlocked modal basis

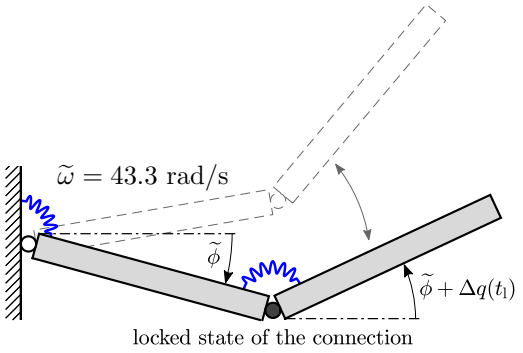

Fig. 2.4. Vibration mode of the two-DOF system with currently locked joint; $\widetilde{\phi}$ is insufficient to describe full state of the system.

for the certain three-DOF system is shown in Fig. 2.1. For the two-DOF system this relation is as follows:

$$\mathbf{B}_0 \underbrace{\widetilde{\phi}\widetilde{\eta}(t)}_{q(t)} + \mathbf{B}_1 \Delta q = \underbrace{\begin{bmatrix} \phi_1^{(1)} & \phi_1^{(2)} \\ \phi_2^{(1)} & \phi_2^{(2)} \end{bmatrix}}_{\mathbf{\Phi}} \underbrace{\begin{bmatrix} \eta_1(t) \\ \eta_2(t) \end{bmatrix}}_{\boldsymbol{\eta}(t)}, \tag{2.14}$$

where $\mathbf{\Phi}$ is called modal matrix that collects unlocked mode shapes and $\boldsymbol{\eta}(t)$ is the vector of corresponding modal coordinates. Then:

$$\boldsymbol{\eta}(t) = \mathbf{\Phi}^{-1} \left(\mathbf{B}_0 q(t) + \mathbf{B}_1 \Delta q \right). \tag{2.15}$$

Analogous derivations for modal velocities lead to the following equation:

$$\dot{\boldsymbol{\eta}}(t) = \mathbf{\Phi}^{-1} \mathbf{B}_0 \dot{q}(t). \tag{2.16}$$

In the equations above the modal coordinates $\boldsymbol{\eta}(t)$ and velocities $\dot{\boldsymbol{\eta}}(t)$ do not change in time as for the system with the unlocked joint. Their time histories are affected by the modal coupling effect that is discussed in detail in Subsection 2.1.5. It is also discussed in Subsection 2.1.6 for the relaxed kinematic constraint representing the locking effect.

2.1.4. Phase 3: unlocking of the joint

When the lockable joint is unlocked at time instant t_u then there is no any discontinuities. Motion of two-DOF system is described again in two dimensional configuration space. Initial conditions for the time interval $(t_\mathrm{u}, t_\mathrm{l}]$, where t_l is time

instant of eventual next joint locking, are computed from Eqs. (2.4) and (2.8). Finally, we have:

$$\begin{cases} \begin{bmatrix} I_{11} & I_{12} \\ I_{21} & I_{22} \end{bmatrix} \begin{bmatrix} \ddot{q}_1(t) \\ \ddot{q}_2(t) \end{bmatrix} + \begin{bmatrix} k_{11} & k_{12} \\ k_{21} & k_{22} \end{bmatrix} \begin{bmatrix} q_1(t) \\ q_2(t) \end{bmatrix} = \mathbf{0}, \quad t \in (t_{\mathrm{u}}, t_{\mathrm{l}}], \\ \mathbf{q}(t_{\mathrm{u}} + \varepsilon_t) = \mathbf{B}_0 q(t_{\mathrm{u}}) + \mathbf{B}_1 \Delta q, \\ \dot{\mathbf{q}}(t_{\mathrm{u}} + \varepsilon_t) = \mathbf{B}_0 \dot{q}(t_{\mathrm{u}}). \end{cases} \tag{2.17}$$

The two-DOF system again is characterised by two unlocked vibration modes as discussed in Subsection 2.1.2.

2.1.5. Selection of the modal basis

From the considerations above it follows that modal basis of the structure depends on its actual configuration. However, as demonstrated in Subsection 2.1.3, it is possible to describe structural motion using only unlocked modal basis $\{\boldsymbol{\phi}^{(1)}, \boldsymbol{\phi}^{(2)}\}$ both for locked and unlocked state of the joint, since the dimension of this basis is equal to the maximal dimension of the configuration space of the system. To this end, the modal coupling effect is to be taken into account.

Motion of the two-DOF system is expressed in terms of unlocked modal basis $\{\boldsymbol{\phi}^{(1)}, \boldsymbol{\phi}^{(2)}\}$ according to the transformation:

$$\mathbf{q}(t) = \boldsymbol{\Phi} \boldsymbol{\eta}(t). \tag{2.18}$$

By substitution of Eq. (2.18) into Eq. (2.1) and left-multiplication by $\boldsymbol{\Phi}^{\mathrm{T}}$ we receive:

$$\underbrace{\boldsymbol{\Phi}^{\mathrm{T}} \begin{bmatrix} I_{11} & I_{12} \\ I_{21} & I_{22} \end{bmatrix} \boldsymbol{\Phi}}_{\mathbf{I}} \ddot{\boldsymbol{\eta}}(t) + \underbrace{\boldsymbol{\Phi}^{\mathrm{T}} \begin{bmatrix} k_{11} & k_{12} \\ k_{21} & k_{22} \end{bmatrix} \boldsymbol{\Phi}}_{\boldsymbol{\Omega}^2} \boldsymbol{\eta}(t) = \boldsymbol{\Phi}^{\mathrm{T}} \begin{bmatrix} 1 \\ -1 \end{bmatrix} f(t), \quad t \in \mathbb{R}_+, \tag{2.19}$$

where $\mathbf{I}$ is the identity matrix and $\boldsymbol{\Omega}^2$ is the diagonal matrix collecting squares of unlocked natural frequencies. Finally we have:

$$\begin{bmatrix} \ddot{\eta}_1(t) \\ \ddot{\eta}_2(t) \end{bmatrix} + \begin{bmatrix} \omega^{(1)} & 0 \\ 0 & \omega^{(2)} \end{bmatrix} \begin{bmatrix} \eta_1(t) \\ \eta_2(t) \end{bmatrix} = \begin{bmatrix} \Delta\phi^{(1)} \\ \Delta\phi^{(2)} \end{bmatrix} f(t), \quad t \in \mathbb{R}_+, \tag{2.20}$$

where $\Delta\phi^{(m)} = \phi_1^{(m)} - \phi_2^{(m)}$ is the relative angle between structural members at the joint for m-th unlocked mode shape (normalised with respect to the mass matrix).

In the equation above unlocked vibration modes are decoupled when $f(t) = 0$ (joint unlocked). In the opposed case these vibration modes are coupled through the right-hand-side of this equation. Then, the two-DOF system vibrates with frequency $\widetilde{\omega}$ and modal coordinates $\eta_1(t)$ and $\eta_2(t)$ have such values at each $t \in (t_\mathrm{l}, t_\mathrm{u}]$ that constraints (2.4) and (2.8) are satisfied.

The value of $f(t)$, when different from zero, depends on configuration coordinates, thus it can be expressed in terms of modal coordinates. To this end, Eq. (2.4) is substituted into Eq. (2.1) that is later left-multiplied by $\mathbf{B}_1^\mathrm{T}$. Then we have:

$$\underbrace{\mathbf{B}_1^\mathrm{T} \begin{bmatrix} I_{11} & I_{12} \\ I_{21} & I_{22} \end{bmatrix} \mathbf{B}_0}_{I_{21}+I_{22}} \ddot{q}(t) + \underbrace{\mathbf{B}_1^\mathrm{T} \begin{bmatrix} k_{11} & k_{12} \\ k_{21} & k_{22} \end{bmatrix} \mathbf{B}_0}_{k_{21}+k_{22}=0} q(t)$$

$$+ \underbrace{\mathbf{B}_1^\mathrm{T} \begin{bmatrix} k_{11} & k_{12} \\ k_{21} & k_{22} \end{bmatrix} \mathbf{B}_1}_{k_{22}} \Delta q = \underbrace{\mathbf{B}_1^\mathrm{T} \begin{bmatrix} 1 \\ -1 \end{bmatrix}}_{-1} f(t), \quad t \in (t_\mathrm{l}, t_\mathrm{u}]. \quad (2.21)$$

Hence, finally:

$$f(t) = -(I_{21} + I_{22})\ddot{q}(t) - k_{22}\Delta q, \qquad t \in (t_\mathrm{l}, t_\mathrm{u}]. \quad (2.22)$$

Aiming at expression of $f(t)$ in terms of the unlocked modal basis the following substitutions are to be made in the equation above using Eq. (2.18):

$$\Delta q = -\Delta\phi^{(1)}\eta_1(t_\mathrm{l}) - \Delta\phi^{(2)}\eta_2(t_\mathrm{l}) \quad (2.23)$$

and, taking into account Eqs. (2.4) and (2.5),

$$\ddot{q}(t) = -\frac{k_\mathrm{l}}{I_\mathrm{l}} q(t) = -\frac{k_\mathrm{l}}{I_\mathrm{l}} \left(\phi_1^{(1)}\eta_1(t) + \phi_1^{(2)}\eta_2(t) \right), \quad t \in (t_\mathrm{l}, t_\mathrm{u}]. \quad (2.24)$$

By substitution of Eqs. (2.22)–(2.24) into Eq. (2.20), finally, we receive:

$$\ddot{\boldsymbol{\eta}}(t) + \left(\boldsymbol{\Omega}^2 + \boldsymbol{\Theta}_1 \right) \boldsymbol{\eta}(t) + \boldsymbol{\Theta}_2 \boldsymbol{\eta}(t_\mathrm{l}) = \mathbf{0}, \qquad t \in (t_\mathrm{l}, t_\mathrm{u}], \quad (2.25)$$

where:

$$\boldsymbol{\Theta}_1 = -\frac{(I_{11} + I_{22})k_\mathrm{l}}{I_\mathrm{l}} \begin{bmatrix} \Delta\phi^{(1)}\phi_1^{(1)} & \Delta\phi^{(1)}\phi_1^{(2)} \\ \Delta\phi^{(2)}\phi_1^{(1)} & \Delta\phi^{(2)}\phi_1^{(2)} \end{bmatrix}$$

and

$$\boldsymbol{\Theta}_2 = -k_{22} \begin{bmatrix} \Delta\phi^{(1)2} & \Delta\phi^{(1)}\Delta\phi^{(2)} \\ \Delta\phi^{(2)}\Delta\phi^{(1)} & \Delta\phi^{(2)2} \end{bmatrix}$$

are matrices representing the locking effect of the joint. They are not diagonal that provides the modal coupling effect.

As it can be seen, Eq. (2.25) has the same dimension as for the unlocked joint. This allows us to describe system dynamics using one equation of motion for both configurations of the system. To this end, the control signal $u(t) \in \{0, 1\}$ is introduced. When the joint is unlocked $u(t) = 0$ and when locked then $u(t) = 1$. Finally, we have:

$$\begin{cases} \ddot{\boldsymbol{\eta}}(t) + \left(\boldsymbol{\Omega}^2 + u(t)\boldsymbol{\Theta}_1\right)\boldsymbol{\eta}(t) + u(t)\boldsymbol{\Theta}_2\boldsymbol{\eta}(t_\mathrm{l}) = \mathbf{0}, & t \in \mathbb{R}_+, \\ \dot{\boldsymbol{\eta}}^+ = \mathbf{A}_\mathrm{l}^\Phi \dot{\boldsymbol{\eta}}^-, \\ \boldsymbol{\eta}(0) = \boldsymbol{\Phi}^{-1}\mathbf{q}_0, \\ \dot{\boldsymbol{\eta}}(0) = \boldsymbol{\Phi}^{-1}\dot{\mathbf{q}}_0, \end{cases} \tag{2.26}$$

where:

$$\dot{\boldsymbol{\eta}}^+ = \dot{\boldsymbol{\eta}}(t_\mathrm{l} + \varepsilon_t) = \boldsymbol{\Phi}^{-1}\mathbf{q}^+, \quad \dot{\boldsymbol{\eta}}^- = \dot{\boldsymbol{\eta}}(t_\mathrm{l}) = \boldsymbol{\Phi}^{-1}\mathbf{q}^-, \quad \mathbf{A}_\mathrm{l}^\Phi = \boldsymbol{\Phi}^{-1}\left(\begin{bmatrix}1\\1\end{bmatrix}\mathbf{A}_\mathrm{l}\right)\boldsymbol{\Phi}$$

for each time instant t_l when the joint is being locked.

Using the unlocked modal basis along with modal coupling terms to describe structural motion is not only more convenient. It also provides a physical insight to the concept of energy transfer between vibration modes, since off-diagonal elements of coupling matrices allow for the exchange of the mechanical energy between unlocked vibration modes. This phenomenon is discussed in detail in Subsection 2.2.4 using unlocked modal basis.

The drawback of Eq. (2.26) is that for each locking of the joint there is the required calculation of: (1) term depending on t_l that needs to be computed for each locking of the joint and (2) modal velocities representing common rotational velocity for DOFs coupled by the locked joint. The next subsection discusses relaxed kinematic constraint allowing for avoiding these problems.

2.1.6. Relaxed kinematic constraints with (equivalent) viscous model of the joint

In this subsection four key aspects of the replacement of the exact kinematic constraints with their relaxed counterpart are discussed. They are: viscous joint model, its influence on dynamics of the two-DOF system, modal coupling effect and comparison between exact and relaxed constraint on the example of free vibration of the two-DOF system.

Viscous joint model

The relaxed counterpart of kinematic constraints (see: Eqs. (2.3) and (2.6)) is pursued:

$$q_2(t) - q_1(t) \approx \Delta q, \qquad t \in (t_\mathrm{l}, t_\mathrm{u}], \tag{2.27}$$

and

$$\dot{q}_2(t) - \dot{q}_1(t) \approx 0, \qquad t \in (t_\mathrm{l}, t_\mathrm{u}]. \tag{2.28}$$

It is done with the viscous model of the lockable joint explicitly describing the dependence between locking moment $f(t)$ on actual state of the system. This model is schematically shown in Fig. 2.5, where rotational DOFs are coupled/decoupled by the controlled large viscous damping factor $c(t)$. The moment $f(t)$ is then described as:

$$f(t) = -\underbrace{u(t)c_\mathrm{max}}_{c(t)} \begin{bmatrix} 1 & -1 \end{bmatrix} \begin{bmatrix} \dot{q}_1(t) \\ \dot{q}_2(t) \end{bmatrix}, \tag{2.29}$$

where c_max is the constant large damping factor and $u(t) \in \{0, 1\}$, as previously. When the joint is in the unlocked state, i.e. $u(t) = 0$, then also $f(t) = 0$ and rotational DOFs are decoupled. When $u(t) = 1$ the joint behaves closely to the rigid connection due to large c_max and the relaxed constraint in Eq. (2.28), and in consequence (2.27), is satisfied, despite the fact that Eq. (2.29) does not provide explicitly any constraint.

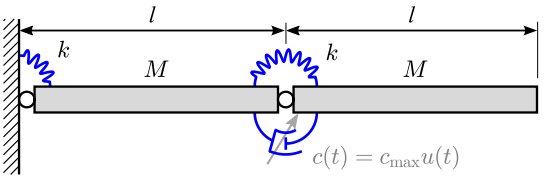

Fig. 2.5. Two-DOF system equipped with lockable joint represented by controllable viscous damper with large damping factor.

After substitution of Eq. (2.29) into Eq. (2.1) the bilinear equation of motion is obtained:

$$\begin{cases} \begin{bmatrix} I_{11} & I_{12} \\ I_{21} & I_{22} \end{bmatrix} \begin{bmatrix} \ddot{q}_1(t) \\ \ddot{q}_2(t) \end{bmatrix} + u(t) \underbrace{c_\mathrm{max} \begin{bmatrix} 1 & -1 \\ -1 & 1 \end{bmatrix}}_{\widetilde{\mathbf{C}}} \begin{bmatrix} \dot{q}_1(t) \\ \dot{q}_2(t) \end{bmatrix} \\ \qquad + \begin{bmatrix} k_{11} & k_{12} \\ k_{21} & k_{22} \end{bmatrix} \begin{bmatrix} q_1(t) \\ q_2(t) \end{bmatrix} = \begin{bmatrix} 0 \\ 0 \end{bmatrix}, \quad t \in \mathbb{R}_+, \\ \mathbf{q}(0) = \mathbf{q}_0, \\ \dot{\mathbf{q}}(0) = \dot{\mathbf{q}}_0. \end{cases} \tag{2.30}$$

The equation of motion above is sufficient to describe behaviour of the two-DOF system for both states of the lockable joint. Due to given explicitly $f(t)$ (Eq. (2.29)) the law of conservation of angular momentum then is not needed (but still is satisfied) to calculate the common velocity of rotational DOFs when the joint is being locked. Moreover, there are no piecewise-constant terms depending on t_1.

The influence of the viscous joint model on dynamics of the two-DOF system

Modal parameters provide the insight into structural dynamics for both locked and unlocked joint of the two-DOF system. For the unlocked joint ($u(t) = 0$) the two-DOF system described by Eq. (2.30) is characterised by two unlocked vibration modes as described in Subsection 2.1.2. For the locked joint ($u(t) = 1$) non-proportional damping is provided by the matrix $\widetilde{\mathbf{C}}$. Then, we have an eigenvalue problem in the following form:

$$(\mathbf{A} - \lambda \mathbf{I}_{4\times 4})\,\boldsymbol{\xi} = \mathbf{0}, \tag{2.31}$$

where λ is eigenvalue sought, $\mathbf{I}_{4\times 4}$ is identity matrix of appropriate dimension,

$$\mathbf{A} = \begin{bmatrix} \mathbf{0}_{2\times 2} & \mathbf{I}_{2\times 2} \\ -\mathbf{M}^{-1}\mathbf{K} & -\mathbf{M}^{-1}\widetilde{\mathbf{C}} \end{bmatrix} \tag{2.32}$$

is the system matrix in the state space representation obtained for the two-DOF system with the locked joint ($u(t) = 1$), and $\boldsymbol{\xi}$ is the eigenvector sought. For the system matrix of the structure as shown in Eq. (2.32) $\boldsymbol{\xi}$ has the form:

$$\boldsymbol{\xi} = \begin{bmatrix} \boldsymbol{\phi}_{\mathrm{c}} \\ \lambda \boldsymbol{\phi}_{\mathrm{c}} \end{bmatrix}, \tag{2.33}$$

thus for simplicity $\boldsymbol{\phi}_{\mathrm{c}}$ also are called eigenvectors in the further part of the present subsection.

The eigenvalue problem in Eq. (2.31) has four solutions. The eigenvalues (transfer function poles) depend on $c_{\max}$ (see: Eq. (2.30)). This dependence is shown in Fig. 2.6. For $c_{\max} = 0$ the eigensolutions, as obviously, correspond to vibration modes of the unlocked system (Fig. 2.3):

$$\begin{aligned} \text{for } c_{\max} = 0: \qquad & \lambda^{(1)} = \lambda^{(2)*} = -\mathrm{j}\omega^{(1)}, \quad \boldsymbol{\phi}_{\mathrm{c}}^{(1)} = \boldsymbol{\phi}_{\mathrm{c}}^{(2)*} = \boldsymbol{\phi}^{(1)}, \\ & \lambda^{(3)} = \lambda^{(4)*} = -\mathrm{j}\omega^{(2)}, \quad \boldsymbol{\phi}_{\mathrm{c}}^{(3)} = \boldsymbol{\phi}_{\mathrm{c}}^{(4)*} = \boldsymbol{\phi}^{(2)}, \end{aligned} \tag{2.34}$$

where $\mathrm{j} = \sqrt{-1}$ is an imaginary unit and $(\cdot)^*$ denotes the complex conjugate.

The increase of $c_{\max}$ results in shifting of the eigenvalues towards negative real numbers. Moreover, due to not-proportional damping provided by the matrix $\widetilde{\mathbf{C}}$ eigenvectors contain elements relatively shifted in phase. In other words:

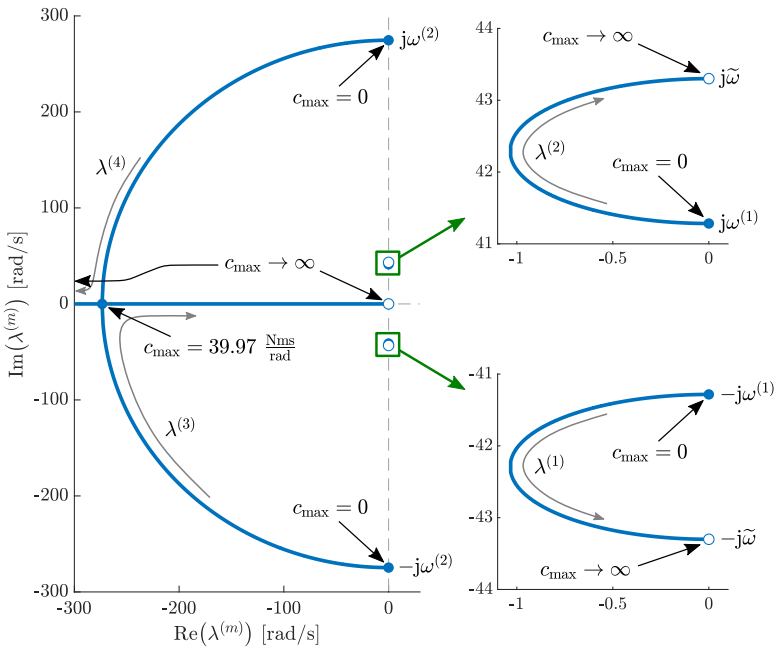

Fig. 2.6. Eigenvalues of two-DOF system with the viscous joint model in the locked state in dependence on damping factor $c_{\max}$.

$\arg \phi_{ci}^{(m)} \neq \arg \phi_{cj}^{(m)}$, $\boldsymbol{\phi}_{\mathrm{c}}^{(m)} \in \mathbb{C}^2$, $i \neq j$. For $c_{\max} > 39.97$ Nms/rad eigenvalues $\lambda^{(3)}$ and $\lambda^{(4)}$ related to the second vibration mode for the unlocked joint become real numbers. It is due to overdamping provided by the increasing $c_{\max}$ coefficient. Then the two-DOF system is represented by one vibration mode related to eigensolutions: $\left(\lambda^{(1)}, \boldsymbol{\phi}_{\mathrm{c}}^{(1)}\right)$, $\left(\lambda^{(2)}, \boldsymbol{\phi}_{\mathrm{c}}^{(2)}\right)$ and the second order system represented by the chain of two first-order systems. These first-order systems are characterised by the poles $\lambda^{(3)}$, $\lambda^{(4)}$ and eigenvectors $\boldsymbol{\phi}_{\mathrm{c}}^{(3)}$, $\boldsymbol{\phi}_{\mathrm{c}}^{(4)}$, respectively.

When $c_{\max}$ becomes large and tends to the infinity eigenvalues $\lambda^{(1)}$ and $\lambda^{(2)}$ tend to the complex counterpart of natural frequency of the two-DOF system with the locked joint $\widetilde{\omega}$. These values are denoted by empty dots in the zoomed areas in Fig. 2.6. $\lambda^{(3)}$ tends to zero representing constant solution reproducing rigidity of the locked joint and $\lambda^{(4)}$ tends to $-\infty$ representing short transient behaviour after locking of the joint. Then, also phase shifts between elements of vectors $\boldsymbol{\phi}_{\mathrm{c}}^{(m)}$ tend to zero (or $-\pi$ that occurs also for real eigenvectors) and, in result, they can be closely reproduced using only real numbers.

For the selected $c_{\max} = 5 \cdot 10^5$ Nms/rad eigenvalues and eigenvectors as shown in Fig. 2.7 are obtained. An imaginary part of elements of the first and second eigenvector is below 0.01 % of the corresponding real part, thus imaginary part

(a) $\lambda^{(1)} = -43.3\text{j rad/s}, \quad \phi_{c1}^{(1)} \approx \phi_{c2}^{(1)} = -0.612 \text{ rad}$

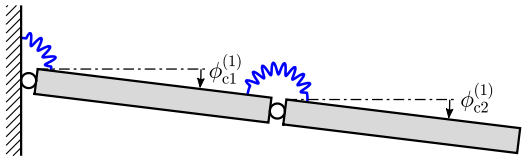

(b) $\lambda^{(2)} = 43.3\text{j rad/s}, \quad \phi_{c1}^{(2)} \approx \phi_{c2}^{(2)} = -0.612 \text{ rad}$

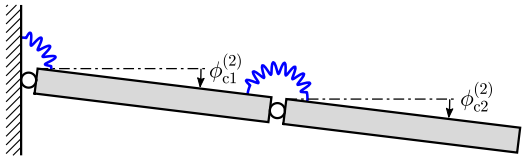

(c) $\lambda^{(3)} = -0.01 \text{ rad/s}, \quad \phi_{c1}^{(3)} = -2.9 \cdot 10^{-8} \approx 0 \text{ rad}, \quad \phi_{c2}^{(3)} = 1.732 \text{ rad}$

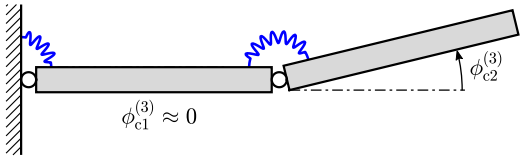

(d) $\lambda^{(4)} = -6.9 \cdot 10^{6} \text{ rad/s}, \quad \phi_{c1}^{(4)} = -1.157 \text{ rad}, \quad \phi_{c2}^{(4)} = 2.546 \text{ rad}$

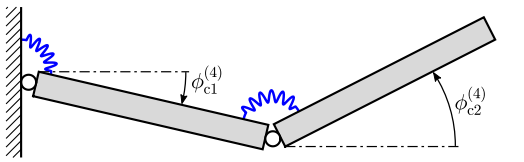

Fig. 2.7. Eigenvalues and eigenvectors of the two-DOF system for currently locked joint with viscous model for $c_{\max} = 5 \cdot 10^5$ Nms/rad.

is neglected. The third and fourth eigenvector are real due to the amount of damping introduced to the system (see: Fig. 2.6). Eigenvectors are normalised with respect to the mass matrix $\mathbf{M}$ but not orthogonal with respect to it.

The first two eigensolutions (Fig. 2.7a and b) correspond to a periodic component of motion of the two-DOF system with the locked joint. The third eigenvector (Fig. 2.7c) corresponds to eigenvalue that can be considered as negligible in relation to remaining ones ($\lambda^{(3)}$ tends to zero when $c_{\max}$ tends to ∞). Thus, if $c_{\max}$ is sufficiently large, this pair of eigenvector and eigenvalue represents the constant component of motion related to the relative angle Δq. Due to this eigensolution and the first two ones the structural motion can be represented similarly as shown in Fig. 2.4. The small absolute value of $\lambda^{(3)}$ causes that Eqs. (2.27) and (2.28) are satisfied. The last eigenvector (Fig. 2.7d) is related to a large negative eigenvalue. The corresponding time constant is then negligibly small

and relates to quick braking of relative motion between structural DOFs when the joint is being locked. After this transient state the rotational coordinates satisfy the relaxed kinematic constraints. It is worth to notice that elements of eigenvector $\boldsymbol{\phi}_{\mathrm{c}}^{(4)}$ are near-proportional to reciprocal elements of the matrix $\mathbf{A}_{\mathrm{l}}$ (see: Eq. (2.10)). Negligible disproportions result from the fact that the selected $c_{\max}$, despite its large value, still is finite and dynamics of the system also is affected by stiffness k.

Modal coupling effect

The modal coupling effect resulting from the interaction between the rotational DOFs through rotational controllable viscous damper is discussed below. Here, the modal equation of motion is obtained by substitution of Eq. (2.18) into Eq. (2.30) and left-multiplying by $\boldsymbol{\Phi}^{\mathrm{T}}$ analogously to Eq. (2.19). It also can be received by substitution of Eq. (2.29) expressed in terms of modal coordinates (Eq. (2.18)) into Eq. (2.20). Finally, we receive:

$$\begin{cases} \ddot{\boldsymbol{\eta}}(t) + u(t)\boldsymbol{\Gamma}\dot{\boldsymbol{\eta}}(t) + \boldsymbol{\Omega}^2\boldsymbol{\eta}(t) = \mathbf{0}, & t \in \mathbb{R}_+, \\ \boldsymbol{\eta}(0) = \boldsymbol{\Phi}^{-1}\mathbf{q}_0, \\ \dot{\boldsymbol{\eta}}(0) = \boldsymbol{\Phi}^{-1}\dot{\mathbf{q}}_0, \end{cases} \tag{2.35}$$

where:

$$\boldsymbol{\Gamma} = \begin{bmatrix} \gamma_{11} & \gamma_{12} \\ \gamma_{21} & \gamma_{22} \end{bmatrix} = \boldsymbol{\Phi}^{\mathrm{T}}\widetilde{\mathbf{C}}\Phi = c_{\max}\begin{bmatrix} \Delta\phi^{(1)2} & \Delta\phi^{(1)}\Delta\phi^{(2)} \\ \Delta\phi^{(2)}\Delta\phi^{(1)} & \Delta\phi^{(2)2} \end{bmatrix} \tag{2.36}$$

is the matrix representing the modal coupling effect resulting from the joint lock. Similarly to matrices $\boldsymbol{\Theta}_1$ and $\boldsymbol{\Theta}_2$ in Eq. (2.26) $\boldsymbol{\Gamma}$ also is not diagonal matrix.

It is worth to notice that Eq. (2.35) has advantages similar to Eq. (2.30) that are the avoidance of additional constant terms depending on the time instant of the joint locking and the additional equation employing the law of conservation of angular momentum.

Comparison with the exact constraints

The ability of the viscous lockable joint model to reproduce dynamics of the considered reconfigurable system is demonstrated in Fig. 2.8. This figure shows free vibration of the two-DOF system for the initial conditions $\mathbf{q}_0 = \left[-2.89^\circ \;\; -2.65^\circ\right]^{\mathrm{T}}$ and $\dot{\mathbf{q}}_0 = \mathbf{0}$. The lockable joint is locked at $t_{\mathrm{l}} = 0.1525$ s. Both initial conditions and time instant of the joint locking is selected aiming at demonstration of interesting dynamical effects. E_{p} and E_{k} in Fig. 2.8d relate to the potential energy of the system that is accumulated in both springs and to total kinetic energy of the two-DOF system, respectively.

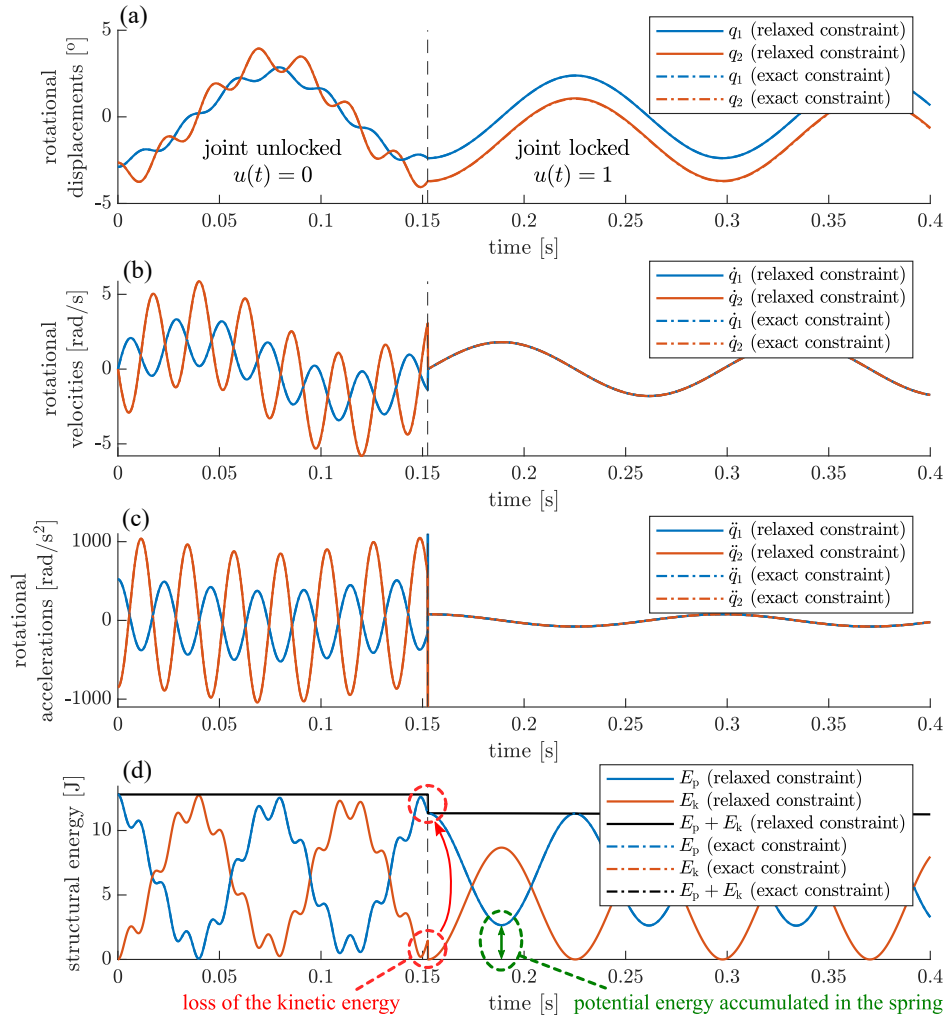

Fig. 2.8. Time histories representing structural behaviour before and after reconfiguration via joint lock using relaxed constraint (viscous damper) and exact constraint: (a) rotational displacements, (b) rotational velocities, (c) rotational accelerations and (d) structural energy: potential energy E_p, kinetic energy E_k and total energy $E_\mathrm{p} + E_\mathrm{k}$.

In all time histories shown in Fig. 2.8 continuous lines denote behaviour of the two-DOF system for the locking effect reproduced with the viscous damper, whereas dashed lines relate to the exact kinematic constraint. It is evident that the corresponding lines overlap within entire time history for each type of the structural response.

Unconstrained motion of two DOFs of the considered system is clearly visible in Fig. 2.8 until the joint is unlocked. When the joint is locked the two-DOF

system behaves like a single DOF oscillator with the natural frequency $\widetilde{\omega}$ for the exact constraint and $\widetilde{\omega}_{\mathrm{c}} = -\mathrm{Im}\lambda^{(1)} = \mathrm{Im}\lambda^{(2)} \approx \widetilde{\omega}$ for the relaxed constraint. The varying component of motion of the two-DOF system is represented by the first and second eigenvectors (Fig. 2.7a and b). The difference between rotational displacements of two DOFs is constant for the exact kinematic constraint case, as shown in Fig. 2.8a, whereas for the relaxed constraint quasi-constant. Due to the selected large $c_{\max}$ the drift of the rotational DOFs is negligibly small and slow. It relates to the near-zero eigenvalue $\lambda^{(3)}$ and corresponding eigenvector $\boldsymbol{\phi}_{\mathrm{c}}^{(3)}$ (see: Fig 2.7c) describing behaviour of the two-DOF system with the locked joint.

Rotational velocities become common after the joint lock (Fig. 2.8b). For the exact constraint they are exactly equal for $t > t_{\mathrm{l}}$ and have discontinuity at $t = t_{\mathrm{l}}$. Their value after the lock of the joint results from the law of conservation of angular momentum. For the relaxed constraint a quasi-common velocity is achieved in continuous manner but very quickly as related to eigenvalue $\lambda^{(4)}$ and eigenvector $\boldsymbol{\phi}_{\mathrm{c}}^{(4)}$ reproducing the inelastic collision (Fig. 2.7d).

Locking of the joint causes a large acceleration peak (Fig. 2.8c). In the case of exact constraint it is infinite and can be represented by the Dirac delta due to discontinuity of the rotational velocities at $t = t_{\mathrm{l}}$. In the case of relaxed constraint the acceleration peaks are finite but achieve large values which depend on selected $c_{\max}$. As it is shown in Section 3.4 the proposed control locks the joints when relative rotational velocity between the DOFs involved in the joint is zero or has very small values, reducing the structure jerking effect.

The two-DOF system is assumed undamped. Thus, before locking the total mechanical energy is constant, as shown in Fig. 2.8d. After locking the joint energy is also constant for the exact constraint and quasi-constant for the relaxed constraint. It demonstrates that for sufficiently large $c_{\max}$ the viscous damper does not add any significant damping to the system. Moreover, it also reproduces the amount of kinetic energy lost in the inelastic collision as shown in red dashed ovals in Fig. 2.8d. This loss of energy takes place when rotational velocities of DOFs involved in the joint are not equal during locking of the joint. When the joint is locked at nonzero Δq then the potential energy of value $\frac{1}{2}k\Delta q^2(t_{\mathrm{l}})$ is stored in the second spring. This energy is not dissipated in any way for the exact constraint, whereas for the relaxed constraint the dissipation is negligibly slow in relation to the vibration period and considered duration of the structural motion. After the joint unlock the potential energy accumulated in the second spring will be released into vibration energy.

Behaviour of the structure described in terms of the unlocked modal basis $\{\boldsymbol{\phi}^{(1)}, \boldsymbol{\phi}^{(2)}\}$ both for exact and relaxed constraints is shown in Fig. 2.9. It is evident that for both types of constraints the results are very close. Thus, only the influence of the locking effect on behaviour of the structure in the modal space is discussed.

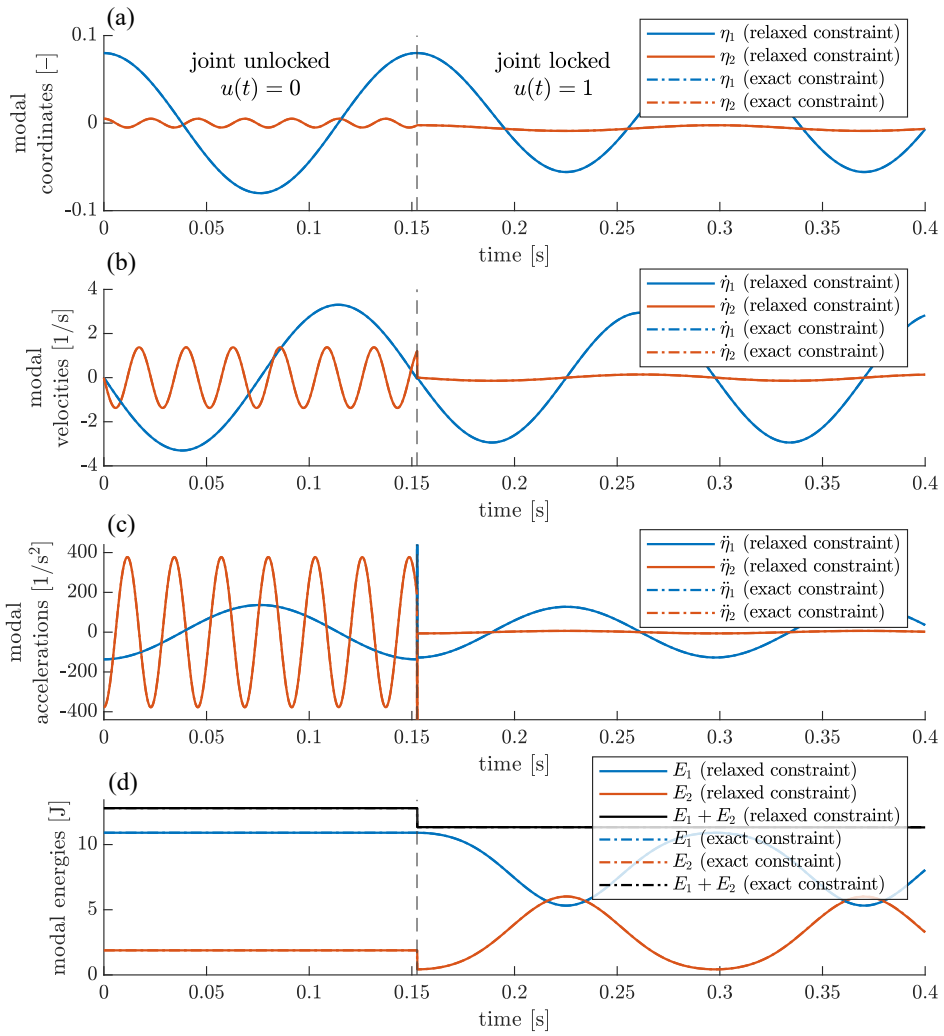

Fig. 2.9. Time histories representing structural behaviour before and after reconfiguration via joint lock using relaxed constraint (viscous damper) and exact kinematic constraint in terms of unlocked modal basis: (a) modal coordinates, (b) modal velocities, (c) modal accelerations and (d) modal energies.

It is evident that before locking of the joint vibration modes are not coupled. They vibrate with their individual natural frequencies (see: Fig 2.9a–c) and mechanical energies associated with these modes, namely: modal energies, are constant (Fig. 2.9d). Modal energies in the MDOF structure are defined in Eq. (2.66) which also relates to the two-DOF system. When the joint is in the locked state modal coordinates, velocities and accelerations oscillate with the frequency equal to $\widetilde{\omega}$ (or $\widetilde{\omega}_{\mathrm{c}}$ for relaxed constraint). It is due to the fact that su-

perposition of the unlocked vibration modes gives corresponding state variables of the two-DOF system (shown in Figs. 2.8a–c) also for the locked joint due to the modal coupling effect. After the joint lock both the equilibrium point and amplitudes of oscillation of modal coordinates are changed (Fig. 2.9a).

The joint lock causes sudden change of the modal velocities – mainly the second one (Fig. 2.9b). Second vibration mode $\boldsymbol{\phi}^{(2)}$ is highly correlated with the fourth eigenvector $\boldsymbol{\phi}_{\mathrm{c}}^{(4)}$ representing transient component structural velocities that is lost during lock as the consequence of the law of conservation of angular momentum (compare Figs. 2.3b and 2.7d). A sudden change of the first modal velocity is negligible in this case. For the exact constraint discontinuities are present at $t = t_1$.

After the joint lock the second modal acceleration reduces its value. The peak modal accelerations during the joint lock are noticeable analogously to the rotational accelerations in the configuration space (Fig. 2.8c).

Finally, the most important observation is that after the joint lock the vibration energy is exchanged between unlocked vibration modes due to the modal coupling effect. When the joint is continuously locked the modal energy transfer is periodic and alternating. However, locking and unlocking the joint in suitable time instances allows for directed energy flow between vibration modes. This essential observation is a foundation for the proposed control strategy that is developed in Chapter 3. Before that, the dynamics of MDOF structures is described.

2.2. Dynamics of reconfigurable MDOF structures

In this section, a concept of implementation of the lockable joint allowing for reconfiguration of the flexible MDOF structure is introduced and resulting dynamical effects are discussed. The effect of change of the modal basis, the modal coupling effect known from the two-DOF system are extended for MDOF structures. Additionally, the derivation of modal energy transfer rates between vibration modes are served. These considerations and derivations are a basis for development of the control strategy introduced in the next chapter. As opposed to the two-DOF system, here the energy is exchanged between a relatively big number of unlocked vibration modes including not-monitored ones which are usually of higher-order. The efficient method for numerical integration also is suggested.

2.2.1. Lockable joints in MDOF structure

One of possible realisations of the concept of the lockable joint is a friction clutch with varying clamping force generated by a piezo stack as shown in Fig. 2.10. When the joint is in the unlocked state, the friction surfaces are

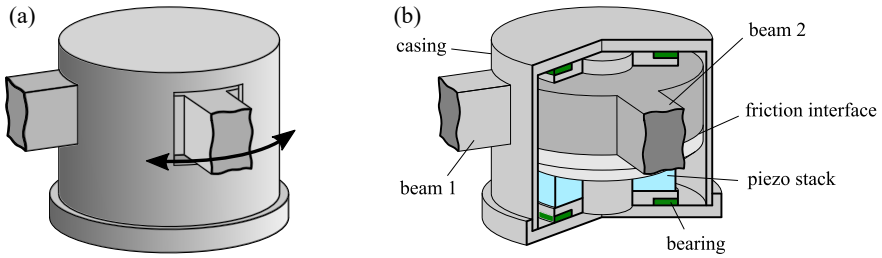

Fig. 2.10. Example of realisation of the lockable-joint concept [144]: (a) outside view and (b) internal components arranged as proposed by Nitche and Gaul [105].

detached and free relative rotation between the connected structural members is possible. However, in the opposite state the clamping force is sufficiently large to lock relative rotation between friction surfaces. Then, analogously to the previous section, the kinematic constraint on rotational DOFs involved in the joint is imposed:

$$\dot{q}_i(t) - \dot{q}_{i+1}(t) = 0, \qquad t \in (t_{\mathrm{l}k}, t_{\mathrm{u}k}], \tag{2.37}$$

where above $q_i(t)$ and $q_{i+1}(t)$ are rotational displacements at the time instant t involved in the k-th lockable joint, as shown in Fig. 2.11a, and $(t_{\mathrm{l}k}, t_{\mathrm{u}k}]$ is the time interval within which the k-th joint is locked. The constraint is kept by

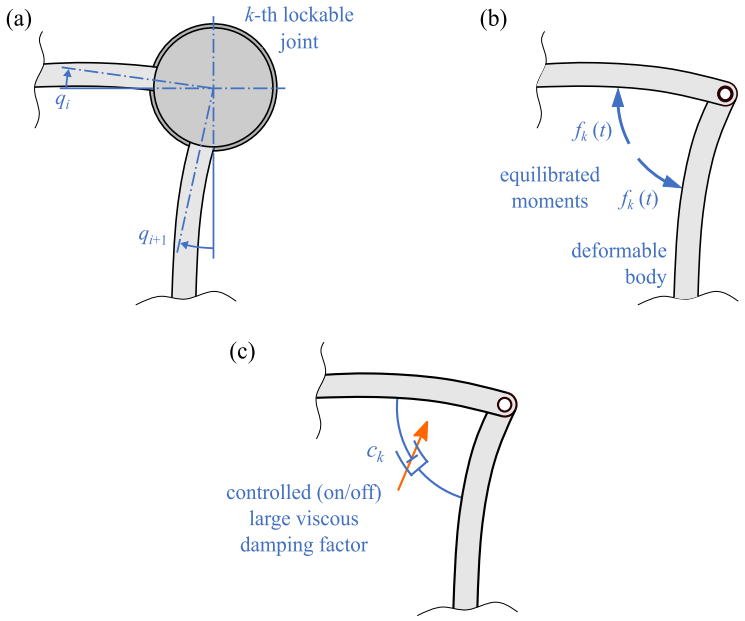

Fig. 2.11. Mathematical description of the lockable joint [144]: (a) independent rotation of the connected flexible structural members, (b) pair of self-equilibrated moments involved in k-th lockable joint and (c) simplified model employing controlled viscous damper.

the action of pair of self-equilibrated moments on friction surfaces in the lockable joint that are equal to the transmitted bending moment $f_k(t)$ as it is schematically shown in Fig. 2.11b.

For friction-based joints the transmitted bending moment generally can be represented by a nonlinear function of the k-th control signal $u_k(t)$ and the local state of the structure:

$$f_k(t) = f(u_k(t), q_i, q_{i+1}(t), \dot{q}_i(t), \dot{q}_{i+1}(t), t). \tag{2.38}$$

Selection of the function $f(u_k(t), q_i, q_{i+1}, \dot{q}_i, \dot{q}_{i+1}, t)$ plays an important role in simulation of the vibration damping process if vibration energy is to be dissipated in the semi-active joints, as e.g. in [107]. However, contrary to such approaches the friction surfaces do not move relatively in the proposed implementation, when the lockable joint is fully locked. Thus, the mechanical energy is dissipated not in the lockable joints but rather in the volume of the structure after shifting the energy into the higher-order vibration modes. It is assumed that the friction surfaces slide over each other only for a negligible short transient state and operate mainly in the two stable states: fully unlocked or fully locked. Moreover, the proposed control algorithm (Section 3.4) has natural property to locking the joints when the relative rotational velocity between DOFs involved in the joints is very small, limiting the sliding effect. Thus, behaviour of the lockable joint in the MDOF structure can be simplified analogously to the joint in the two-DOF system. Taking into account the reliability of the viscous model of the lockable joint and the ease of its use demonstrated in Subsection 2.1.6 one can adopt this model for reproduction of the locking effect in the reconfigurable MDOF structure and use for further derivations. Then, lockable joint is represented by the controlled viscous damper as shown in Fig. 2.11c. Equation (2.38) can be replaced with

$$f_k(t) = -u_k(t) c_{\max} \left(\dot{q}_i(t) - \dot{q}_{i+1}(t)\right), \qquad t \in \mathbb{R}_+, \tag{2.39}$$

where analogously to the two-DOF system $u_k(t) = 0$ when the k-th joint is unlocked and $u_k(t) = 1$ when the k-th joint is locked. Such a model ensures that when the joint is locked the constraint in Eq. (2.37) is closely satisfied:

$$\dot{q}_i(t) \approx \dot{q}_{i+1}(t), \qquad t \in (t_{\mathrm{l}k}, t_{\mathrm{u}k}]. \tag{2.40}$$

Also it is worth to notice that this approach has been experimentally validated using a different control strategy in which lockable joints also work in only two stable states: fully locked and fully unlocked [12, 13], despite the fact that in these works the viscous joint model was not investigated theoretically aiming at comparison with exact kinematic constraints.

2.2.2. Structure dynamics

Equation of motion of the MDOF structure

In this subsection the mathematical description of behaviour of a flexible MDOF structure equipped with lockable joints is presented. Small amplitudes of motion are assumed. Vibration of the MDOF structure is described by the equation of motion (2.41).

$$\begin{cases} \mathbf{M}\ddot{\mathbf{q}}(t) + \mathbf{C}\dot{\mathbf{q}}(t) + \mathbf{K}\mathbf{q}(t) = \mathbf{L}\mathbf{f}(t) + \mathbf{d}(t), \\ \mathbf{q}(0) = \mathbf{q}_0, \\ \dot{\mathbf{q}}(0) = \dot{\mathbf{q}}_0. \end{cases} \tag{2.41}$$

In the equation above $\mathbf{M}$, $\mathbf{C}$, $\mathbf{K} \in \mathbb{R}^{N_\mathrm{d} \times N_\mathrm{d}}$ are: mass, proportional material damping and stiffness matrices, respectively, $\mathbf{q}(t) \in \mathbb{R}^{N_\mathrm{d}}$ is the displacement vector collecting both translational and rotational DOFs, N_d is the number of structural DOFs for all joints unlocked, the vector

$$\mathbf{f}(t) = \begin{bmatrix} f_1(t) & f_2(t) & \cdots & f_{N_k}(t) \end{bmatrix}^\mathrm{T} \tag{2.42}$$

contains bending moments transmitted by N_k lockable joints, $\mathbf{L} = \begin{bmatrix} \mathbf{l}_1 & \mathbf{l}_2 & \cdots & \mathbf{l}_{N_k} \end{bmatrix} \in \mathbb{R}^{N_\mathrm{d} \times N_k}$ is the transformation matrix collecting vectors $\mathbf{l}_k$ selecting DOFs involved in lockable joints in the way ensuring self-equilibrium of the moments acting on the adjacent structural members (Fig. 2.11b):

$$\mathbf{l}_k = \begin{bmatrix} 0 & \cdots & 0 & 1 & 0 & \cdots & 0 & -1 & 0 & \cdots & 0 \end{bmatrix}^\mathrm{T},$$

and $\mathbf{d}(t) \in \mathbb{R}^{N_\mathrm{d}}$ is the vector of external disturbances.

Viscous joint model in MDOF structure

Substitution of the transmitted bending moments $f_k(t)$ in Eq. (2.41) with the right-hand-side of Eq. (2.39) results in the bilinear form of equation of motion:

$$\mathbf{M}\ddot{\mathbf{q}}(t) + \left(\mathbf{C} + \sum_{k=1}^{N_k} u_k(t) \widetilde{\mathbf{C}}_k \right) \dot{\mathbf{q}}(t) + \mathbf{K}\mathbf{q}(t) = \mathbf{d}(t), \tag{2.43}$$

where matrix

$$\widetilde{\mathbf{C}}_k = c_\mathrm{max} \mathbf{l}_k \mathbf{l}_k^\mathrm{T}$$

couples rotational DOFs involved in the k-th lockable joint in the sense of Eq. (2.40) when corresponding control signal $u_k(t) = 1$.

Important advantages of the use of matrices $\widetilde{\mathbf{C}}_k$ are emphasised in Subsection 2.1.6, below Eq. (2.30). Moreover, Eq. (2.43) remains piece-wise linear, as the control signals are piece-wise fixed.

State-space representation of MDOF structural behaviour and its simulation

The last advantage indicated above is helpful in the simulation process. Since the local truncation error is a common problem in the integration of differential equations, it can significantly slow down simulation due to the fact that higher-order vibration modes are also included into the computations. In other words, the model reduction with modal truncation is not used in the proposed control methodology because higher-order modes are responsible for the energy dissipation mechanism. Therefore, they require sufficiently small integration step if an appropriate solver is not used. The piece-wise linear character of Eq. (2.43) allows the use of the zero-order hold method to avoid this problem.

First, the equation of motion is transformed into the state-space representation, as follows:

$$\begin{cases} \dot{\mathbf{x}}(t) = \mathbf{A}(\mathbf{u}(t))\mathbf{x}(t) + \mathbf{B}\mathbf{d}(t), \\ \mathbf{y}(t) = \mathbf{C}_{\mathrm{y}}\mathbf{x}(t) + \mathbf{D}\mathbf{u}(t) + \mathbf{v}(t), \end{cases} \tag{2.44}$$

where:

$$\mathbf{x}(t) = \begin{bmatrix} \mathbf{q}(t) \\ \dot{\mathbf{q}}(t) \end{bmatrix}, \quad \mathbf{A}(\mathbf{u}(t)) = \begin{bmatrix} \mathbf{0} & \mathbf{I} \\ -\mathbf{M}^{-1}\mathbf{K} & -\mathbf{M}^{-1}\left(\mathbf{C} + \sum_{k=1}^{N_k} u_k(t)\widetilde{\mathbf{C}}_k\right) \end{bmatrix},$$

$$\mathbf{u}(t) = \begin{bmatrix} u_1(t) & u_2(t) & \cdots & u_{N_k}(t) \end{bmatrix}^{\mathrm{T}} \in \{0,1\}^{N_k}, \quad \mathbf{B} = \begin{bmatrix} \mathbf{0} \\ \mathbf{M}^{-1} \end{bmatrix},$$

$\mathbf{I}$ is the identity matrix of an appropriate dimension, $\mathbf{y}(t)$ is the output vector and $\mathbf{v}(t)$ is the measurement noise vector. The structure of matrices $\mathbf{C}_{\mathrm{y}}$, $\mathbf{D}$ and the vector $\mathbf{v}(t)$ is discussed in Chapter 3. If control signals $\mathbf{u}$ remain constant within a time interval of length Δt, the state-space equation can be replaced with its discrete counterpart:

$$\mathbf{x}_{\mathrm{d}}[l+1] = \mathbf{A}_{\mathrm{d}}^{\mathbf{u}}\mathbf{x}_{\mathrm{d}}[l] + \mathbf{B}_{\mathrm{d}}^{\mathbf{u}}\mathbf{d}_{\mathrm{d}}[l], \tag{2.45}$$

where:

$$\mathbf{A}_{\mathrm{d}}^{\mathbf{u}} = \mathrm{e}^{\mathbf{A}(\mathbf{u})\Delta t}, \quad \mathbf{B}_{\mathrm{d}}^{\mathbf{u}} = \mathbf{A}^{-1}(\mathbf{u})\left(\mathbf{A}_{\mathrm{d}}^{\mathbf{u}} - \mathbf{I}\right)\mathbf{B}, \quad \mathbf{u} = \text{const in } \left[l\Delta t, (l+1)\Delta t\right),$$

and e is Euler's number. In the case of free vibration ($\mathbf{d} \equiv \mathbf{0}$) $\mathbf{x}_{\mathrm{d}}[l+1]$ is the exact solution of the differential equation (2.44) for the initial condition taken as $\mathbf{x}_{\mathrm{d}}[l]$. Hence, the local truncation error is avoided even for time-steps Δt longer than a period of any higher-order vibration mode. In the case of the forced vibration ($\mathbf{d} \neq \mathbf{0}$) the time step must be appropriately smaller than a period of the highest harmonic component of the excitation. To avoid calculation of matrices $\mathbf{A}_{\mathrm{d}}^{\mathbf{u}}$ and $\mathbf{B}_{\mathrm{d}}^{\mathbf{u}}$ at each time step they can be computed for each possible control signal

vector **u** before the simulation process. Later, they are appropriately selected for substitution in Eq. (2.45) depending on the current control signals u_k indicated by the controller. If excitation **d** does not contain high-frequency components then the use of the Eq. (2.45) provides time-effective and accurate simulation.

2.2.3. Unlocked and locked modal basis, modal coupling effect

In this subsection, structural dynamics and modal bases obtained for various states of the lockable joints of the MDOF structure are described. The modal coupling effect in the MDOF structure caused by the action of lockable joints is introduced.

All joints in the unlocked state

Vibration modes obtained for all joints in the unlocked state are referred as "unlocked vibration modes". The eigenvalue problem formulated for all joints unlocked is formulated as follows:

$$\left(\mathbf{K} - \omega^2 \mathbf{M}\right) \boldsymbol{\phi} = \mathbf{0}. \tag{2.46}$$

The solution of the eigenvalue problem are unlocked natural frequencies $\omega^{(m)}$ and unlocked mode shapes $\boldsymbol{\phi}^{(m)} \in \mathbb{R}^{N_\mathrm{d}}$, $m = 1, 2, \ldots, N_\mathrm{d}$ denotes an index of the unlocked vibration mode. N_d is equal to the maximal number of DOFs (when all joints are unlocked). Motion of the structure can be expressed in modal coordinates $\boldsymbol{\eta}(t) \in \mathbb{R}^{N_\mathrm{d}}$ by the use of the transformation below

$$\mathbf{q}(t) = \boldsymbol{\Phi}\boldsymbol{\eta}(t). \tag{2.47}$$

In the equation above the matrix $\boldsymbol{\Phi} = \left[\boldsymbol{\phi}^{(1)} \;\; \boldsymbol{\phi}^{(2)} \;\; \cdots \;\; \boldsymbol{\phi}^{(N_\mathrm{d})}\right]$ collects unlocked mode shapes normalised with respect to the mass matrix, i.e.

$$\boldsymbol{\Phi}^\mathrm{T}\mathbf{M}\boldsymbol{\Phi} = \mathbf{I}. \tag{2.48}$$

Locking effect and locked vibration modes

Here, mainly the influence of the locking effect on structural modal parameters is discussed. First, to understand the changes in structural dynamics the exact kinematic constraint in Eq. (2.37) is recalled for any combination of currently locked joints:

$$\begin{aligned} \mathbf{q}(t) &= \mathbf{B}_0\widetilde{\mathbf{q}}(t) + \mathbf{B}_1\boldsymbol{\Delta}\mathbf{q}, \\ \dot{\mathbf{q}}(t) &= \mathbf{B}_0\dot{\widetilde{\mathbf{q}}}(t), \\ \ddot{\mathbf{q}}(t) &= \mathbf{B}_0\ddot{\widetilde{\mathbf{q}}}(t), \qquad\qquad t \in (t_\mathrm{l}, t_\mathrm{u}]. \end{aligned} \tag{2.49}$$

In equation above t_l and t_u are time instants of locking and unlocking of any joint, respectively, i.e. they limit the time interval within which the vector $\mathbf{u}(t)$ is constant. $\mathbf{B}_0 \in \{0,1\}^{N_\mathrm{d}\times(N_\mathrm{d}-N_\mathrm{l})}$, where N_l is the number of currently locked joints, is generalization of the corresponding transformation matrix in Eq. (2.4). For the MDOF structure $\mathbf{B}_0$ is obtained from the identity matrix, where for each currently locked joint the column related to one of DOFs involved in this joint is removed and added to the column related to the remaining DOF. For the single locked joint coupling DOFs i and j this matrix has the following form:

$$\mathbf{B}_0 = [\mathbf{s}_1 \;\; \mathbf{s}_2 \;\; \cdots \;\; \mathbf{s}_{i-1} \;\; \mathbf{s}_i + \mathbf{s}_j \;\; \mathbf{s}_{i+1} \;\; \cdots \;\; \mathbf{s}_{j-1} \;\; \mathbf{s}_{j+1} \;\; \cdots \;\; \mathbf{s}_{N_\mathrm{d}}], \tag{2.50}$$

where $\mathbf{s}_i \in \{0,1\}^{N_\mathrm{d}}$ is the Boolean vector indicating i-th DOF. This matrix depends on the control signal vector $\mathbf{u}$, including the change of number of its columns. The matrix $\mathbf{B}_1 \in \{0,1\}^{N_\mathrm{d}\times N_\mathrm{l}}$ contains columns removed from the matrix $\mathbf{B}_0$ (for the example above $\mathbf{B}_1 = \mathbf{s}_j$) and also is a generalization of the appropriate matrix defined in Eq. (2.4). The vector $\boldsymbol{\Delta}\mathbf{q}$ collects terms describing differences of rotational displacements of DOFs involved in each k-th of currently locked joint:

$$\Delta q_k = \mathbf{l}_k^\mathrm{T}\mathbf{q}(t_\mathrm{l}) = \text{const in } (t_\mathrm{l}, t_\mathrm{u}]. \tag{2.51}$$

By substitution of Eq. (2.49) into Eq. (2.41) and left-multiplying by $\mathbf{B}_0^\mathrm{T}$ we receive Eq. (2.52). For better clarity the matrix describing material damping and the initial conditions are omitted.

$$\underbrace{\mathbf{B}_0^\mathrm{T}\mathbf{M}\mathbf{B}_0}_{\widetilde{\mathbf{M}}_{00}}\ddot{\widetilde{\mathbf{q}}}(t) + \underbrace{\mathbf{B}_0^\mathrm{T}\mathbf{K}\mathbf{B}_0}_{\widetilde{\mathbf{K}}_{00}}\widetilde{\mathbf{q}}(t) + \underbrace{\mathbf{B}_0^\mathrm{T}\mathbf{K}\mathbf{B}_1}_{\widetilde{\mathbf{K}}_{01}}\boldsymbol{\Delta}\mathbf{q} = \underbrace{\mathbf{B}_0^\mathrm{T}\mathbf{L}\mathbf{f}(t)}_{\mathbf{0}} + \underbrace{\mathbf{B}_0^\mathrm{T}\mathbf{d}(t)}_{\widetilde{\mathbf{d}}(t)}. \tag{2.52}$$

In the equation $\widetilde{\mathbf{M}}_{00}$, $\widetilde{\mathbf{K}}_{00} \in \mathbb{R}^{(N_\mathrm{d}-N_\mathrm{l})\times(N_\mathrm{d}-N_\mathrm{l})}$ are mass and stiffness matrices, respectively, representing dynamical properties of the structure with locked particular joints at $\Delta q_k = 0$, whereas the matrix $\widetilde{\mathbf{K}}_{01} \in \mathbb{R}^{(N_\mathrm{d}-N_\mathrm{l})\times N_\mathrm{l}}$ is responsible for piece-wise static forces provided by locking the joints at nonzero Δq_k. As opposed to the two-DOF system investigated in Section 2.1, here this matrix usually is nonzero. It means that locking of any k-th joint at nonzero Δq_k causes deformation in the entire structure and changes equilibrium point of the system also in the configuration space reduced to the minimal number of DOFs. This equilibrium point can be calculated by substituting $\ddot{\widetilde{\mathbf{q}}}(t) = \mathbf{0}$ and $\widetilde{\mathbf{d}}(t) = \mathbf{0}$ in Eq. (2.52) as:

$$\widetilde{\mathbf{q}}_\mathrm{l} = -\widetilde{\mathbf{K}}_{00}^{-1}\widetilde{\mathbf{K}}_{01}\boldsymbol{\Delta}\mathbf{q}. \tag{2.53}$$

After substitution of

$$\widetilde{\mathbf{q}}(t) = \widetilde{\mathbf{q}}_\mathrm{eq}(t) + \widetilde{\mathbf{q}}_\mathrm{l}, \tag{2.54}$$

where $\widetilde{\mathbf{q}}_{\mathrm{eq}}(t)$ is the structural displacement with respect to the equilibrium point, into Eq. (2.52) the constant term disappears. Then, free vibration with respect to the equilibrium point $\widetilde{\mathbf{q}}_{\mathrm{l}}$ can be investigated using the eigenvalue problem:

$$\left(\widetilde{\mathbf{K}}_{00} - \widetilde{\omega}_0^2 \widetilde{\mathbf{M}}_{00}\right) \widetilde{\boldsymbol{\phi}}_0 = \mathbf{0}. \tag{2.55}$$

The above eigenvalue problem is the same as one obtained for the structure with particular joints locked at $\Delta q_k = 0$. Thus, modes describing vibration for $\Delta q_k = 0$ also are the same.

Finally, for the subset of currently locked joints the structural displacement depends on modal parameters as follows:

$$\mathbf{q}(t) = \mathbf{B}_0 \left(\widetilde{\boldsymbol{\Phi}}_0 \widetilde{\boldsymbol{\eta}}_0(t) + \widetilde{\mathbf{q}}_{\mathrm{l}}\right) + \mathbf{B}_1 \boldsymbol{\Delta}\mathbf{q}, \qquad t \in (t_{\mathrm{l}}, t_{\mathrm{u}}], \tag{2.56}$$

where: $\widetilde{\boldsymbol{\Phi}}_0 \in \mathbb{R}^{(N_{\mathrm{d}}-N_{\mathrm{l}})\times(N_{\mathrm{d}}-N_{\mathrm{l}})}$ is the modal matrix collecting all mode shapes obtained by solving the eigenvalue problem in Eq. (2.55) for a particular subset of joints that are currently locked and $\widetilde{\boldsymbol{\eta}}_0$ is the corresponding vector of the modal coordinates. The equation above allows for understanding that analogously to the two-DOF system the modal basis formed by $\widetilde{\boldsymbol{\Phi}}_0$ is insufficient to describe the full state of the structure. Information about the opening angles between beam ends coupled by the currently locked joints contained by $\boldsymbol{\Delta}\mathbf{q}$ is required – also in the reduced configuration space.

Corresponding vibration modes obtained from the eigenvalue problem in Eq. (2.55) differ for different joints selected to be locked:

$$\mathbf{B}_0 \widetilde{\boldsymbol{\phi}}_0^{(m)}\Big|_{\mathbf{u}=\mathbf{u}_1} \neq \mathbf{B}_0 \widetilde{\boldsymbol{\phi}}_0^{(m)}\Big|_{\mathbf{u}=\mathbf{u}_2} \quad \text{if} \quad \mathbf{u}_1 \neq \mathbf{u}_2, \tag{2.57}$$

where mode shapes obtained for both combinations of the locked joints (indicated by the control signals) are referred as "corresponding" in the sense that they are most correlated, e.g. accordingly to the highest modal assurance criterion (MAC).

Vibration modes obtained only for a subset of joints that are locked ($N_{\mathrm{l}} < N_k$) are not further used in this thesis because they are insufficient to describe the full state of the structure. However, vibration modes obtained for all joints in the locked state ($N_{\mathrm{l}} = N_k$) are further referred as "locked vibration modes" and are used to indicate optimal locations of the lockable joints (Section 3.3). The locked vibration modes and other corresponding quantities related to all joints in the locked state are denoted by symbols with omitted subscript "0". Then, the eigenvalue problem is:

$$\left(\widetilde{\mathbf{K}} - \widetilde{\omega}^2 \widetilde{\mathbf{M}}\right) \widetilde{\boldsymbol{\phi}} = \mathbf{0}, \tag{2.58}$$

where:

$$\widetilde{\mathbf{K}} = \mathbf{B}^{\mathrm{T}} \mathbf{K} \mathbf{B}, \qquad \widetilde{\mathbf{M}} = \mathbf{B}^{\mathrm{T}} \mathbf{M} \mathbf{B},$$

$\widetilde{\omega}$ and $\widetilde{\boldsymbol{\phi}} \in \mathbb{R}^{N_\mathrm{d}-N_k}$ are m-th locked natural frequency and m-th locked mode shape, respectively, and $\mathbf{B} \in \{0,1\}^{N_\mathrm{d}\times(N_\mathrm{d}-N_k)}$ is defined as $\mathbf{B}_0$ for all joints locked.

Similarly to the two-DOF system the vibration of the MDOF structure always can be described in the unlocked modal basis due its dimension equal to the highest dimension of the configuration space:

$$\boldsymbol{\eta}(t) = \boldsymbol{\Phi}^{-1}\left(\mathbf{B}_0\left(\widetilde{\boldsymbol{\Phi}}_0\widetilde{\boldsymbol{\eta}}_0(t) + \widetilde{\mathbf{q}}_\mathrm{l}\right) + \mathbf{B}_1\boldsymbol{\Delta}\mathbf{q}\right), \qquad t \in (t_\mathrm{l}, t_\mathrm{u}]. \tag{2.59}$$

Then time histories of modal coordinates in the unlocked modal basis $\boldsymbol{\eta}(t)$ are affected by the modal coupling effect which changes not only equilibrium point, as illustrated in Fig. 2.1, but also frequencies which in this case are related to the vibration modes obtained for current combination of the locked joints. The modal coupling effect and description of structural behaviour in the unlocked modal basis are discussed below.

Modal coupling effect in the unlocked modal basis

Based on the considerations above and ones in Section 2.1 vibration modes calculated for all joints unlocked are used for further analysis. Such a method of description of MDOF-system behaviour is similar to the fast nonlinear analysis (FNA) method proposed by Wilson [143]. FNA was designed to reduce the model order and enable fast simulation of nonlinear structures, in which nonlinearity is introduced locally and only through a finite number of nonlinear structural elements, while the rest of the structure remains linear. The structures considered in the thesis fulfil this requirement. In FNA the forces provided by nonlinear members can be treated as external loads acting on a linear structure (similarly to Eq. (2.41) in this thesis). However, contrary to approach adopted in this thesis FNA usually employs basis formed from load-dependent Ritz vectors instead of the structural mode shapes. In this situation a smaller number of load-dependent Ritz vectors is needed for suitable reconstruction of structural behaviour, as opposed to the wider spectrum of linear vibration modes. However, the load-dependent Ritz vectors do not provide sufficient information about structural dynamics, e.g. resonance frequencies, modal damping factors. Hence, the unlocked modal basis is utilized in this thesis to investigate the modal coupling effect, the phenomenon of modal energy transfer, and to support the design of the controller. Although the load-dependent Ritz vectors are not used in this thesis, they can be adopted for simulation of large-scale structure equipped with lockable joints if the model order reduction is required.

By substituting the transformation shown in Eq. (2.47) into Eq. (2.43) and its left-multiplying by $\boldsymbol{\Phi}^\mathrm{T}$ the equation of motion in the modal form is received as shown in Eq. (2.60):

$$\ddot{\boldsymbol{\eta}}(t) + \left(2\boldsymbol{\Omega}\mathbf{Z} + \sum_{k=1}^{N_k} u_k(t)\boldsymbol{\Gamma}_k \right) \dot{\boldsymbol{\eta}}(t) + \boldsymbol{\Omega}^2 \boldsymbol{\eta}(t) = \boldsymbol{\Phi}^{\mathrm{T}} \mathbf{d}(t). \tag{2.60}$$

In Eq. (2.60) $\mathbf{Z} = \operatorname{diag}\left(\left[\zeta^{(1)} \;\; \zeta^{(m)} \;\; \cdots \;\; \zeta^{(N_\mathrm{d})} \right]^{\mathrm{T}} \right)$ is diagonal damping matrix, $\boldsymbol{\Omega} = \operatorname{diag}\left(\left[\omega^{(1)} \;\; \omega^{(m)} \;\; \cdots \;\; \omega^{(N_\mathrm{d})} \right]^{\mathrm{T}} \right)$ is diagonal matrix containing the unlocked natural frequencies and

$$\boldsymbol{\Gamma}_k = \boldsymbol{\Phi}^{\mathrm{T}} \widetilde{\mathbf{C}}_k \boldsymbol{\Phi} \tag{2.61}$$

is the modal coupling matrix that is usually a full matrix as opposed to $\mathbf{Z}$ and $\boldsymbol{\Omega}$, thus the lock of any joint causes coupling between the unlocked vibration modes. Equation (2.60) can be written in the index notation:

$$\ddot{\eta}_m(t) + 2\zeta^{(m)}\omega^{(m)}\dot{\eta}_m(t) + \sum_{k=1}^{N_k}\sum_{n=1}^{N_\mathrm{d}} u_k(t)\gamma_{kmn}\dot{\eta}_n(t) + \omega^{(m)2}\eta(t) = \sum_{i=1}^{N_\mathrm{d}} \phi_i^{(m)} d_i(t). \tag{2.62}$$

The element γ_{kmn} of the coupling matrix $\boldsymbol{\Gamma}_k$ provides coupling between individual modes m and n through the k-th lockable joint.

For the modal coupling effect resulting from the relaxed kinematic constraint, modal coordinates closely satisfy Eq. (2.59) (exactly if $c_{\max}$ tends to infinity) when the joints are locked. It is despite the presence of term $\boldsymbol{\Omega}^2$ in Eq. (2.60).

By rewriting γ_{kmn} we receive

$$\gamma_{kmn} = \boldsymbol{\phi}^{(m)\mathrm{T}} \widetilde{\mathbf{C}}_k \boldsymbol{\phi}^{(n)} = c_{\max} \boldsymbol{\phi}^{(m)\mathrm{T}} \mathbf{l}_k \mathbf{l}_k^{\mathrm{T}} \boldsymbol{\phi}^{(n)} = c_{\max} \Delta\phi_k^{(m)} \Delta\phi_k^{(n)}, \tag{2.63}$$

where $\Delta\phi_k^{(m)}$ is the difference of rotations of the m-th unlocked mode shape at the DOFs involved in k-th lockable joint when unlocked. It is evident that values of opening angles of unlocked mode shapes at the location of lockable joint provide information about degree of coupling of these modes.

After moving the modal coupling term in Eq. (2.62) into its right-hand side, we obtain modal coupling term expressed in terms of bending moments transmitted by the lockable joints (analogously to Eq. (2.20) for the two-DOF system):

$$\begin{aligned} -\sum_{k=1}^{N_k}\sum_{n=1}^{N_\mathrm{d}} u_k(t)\gamma_{kmn}\dot{\eta}_n(t) \;&=\; -\sum_{k=1}^{N_k} u_k(t)\boldsymbol{\gamma}_k^{(m)}\dot{\boldsymbol{\eta}}(t) = -\sum_{k=1}^{N_k} u_k(t)\boldsymbol{\phi}^{(m)\mathrm{T}}\widetilde{\mathbf{C}}_k \underbrace{\boldsymbol{\Phi}\dot{\boldsymbol{\eta}}(t)}_{\dot{\mathbf{q}}(t)} \\ &=\; -\sum_{k=1}^{N_k} \underbrace{\boldsymbol{\phi}^{(m)\mathrm{T}}\mathbf{l}_k}_{\Delta\phi_k^{(m)}} \underbrace{u_k(t) c_{\max} \mathbf{l}_k^{\mathrm{T}} \dot{\mathbf{q}}(t)}_{-f_k(t)} \\ &=\; \sum_{k=1}^{N_k} \Delta\phi_k^{(m)} f_k(t), \end{aligned} \tag{2.64}$$

where $\boldsymbol{\gamma}_k^{(m)}$ is m-th row of the matrix $\boldsymbol{\Gamma}_k$. It is evident that the resultant modal force acting on the m-th mode can be expressed as the sum of the forces derived from all unlocked vibration modes (including the m-th one) in all lockable joints or the sum of the modal forces derived directly from pairs of self-equilibrated moments in all joints.

Equation (2.60) can be rewritten as shown in Eq. (2.65).

$$\begin{bmatrix}\ddot{\boldsymbol{\eta}}_{\mathrm{M}}(t)\\ \ddot{\boldsymbol{\eta}}_{\mathrm{H}}(t)\end{bmatrix}+\left(2\begin{bmatrix}\boldsymbol{\Omega}_{\mathrm{M}}\mathbf{Z}_{\mathrm{M}} & \mathbf{0}\\ \mathbf{0} & \boldsymbol{\Omega}_{\mathrm{H}}\mathbf{Z}_{\mathrm{H}}\end{bmatrix}+\sum_{k=1}^{N_k}u_k(t)\begin{bmatrix}\boldsymbol{\Gamma}_{\mathrm{MM}k} & \boldsymbol{\Gamma}_{\mathrm{MH}k}\\ \boldsymbol{\Gamma}_{\mathrm{HM}k} & \boldsymbol{\Gamma}_{\mathrm{HH}k}\end{bmatrix}\right)\begin{bmatrix}\dot{\boldsymbol{\eta}}_{\mathrm{M}}(t)\\ \dot{\boldsymbol{\eta}}_{\mathrm{H}}(t)\end{bmatrix}$$
$$+\begin{bmatrix}\boldsymbol{\Omega}_{\mathrm{M}}^2 & \mathbf{0}\\ \mathbf{0} & \boldsymbol{\Omega}_{\mathrm{H}}^2\end{bmatrix}\begin{bmatrix}\boldsymbol{\eta}_{\mathrm{M}}(t)\\ \boldsymbol{\eta}_{\mathrm{H}}(t)\end{bmatrix}=\begin{bmatrix}\boldsymbol{\Phi}_{\mathrm{M}} & \boldsymbol{\Phi}_{\mathrm{H}}\end{bmatrix}^{\mathrm{T}}\mathbf{d}(t). \quad (2.65)$$

The first row, denoted by the subscript M, is related to monitored unlocked vibration modes, whereas the second row is related to higher-order unlocked vibration modes and is denoted by the subscript H. This notation is further used to describe the energy flow between monitored and higher-order unlocked vibration modes which are coupled by sub-matrices $\boldsymbol{\Gamma}_{\mathrm{HM}k}$ and $\boldsymbol{\Gamma}_{\mathrm{MH}k}$.

2.2.4. Energy transfer between vibration modes

Equations describing transfer of the mechanical energy between unlocked vibration modes caused by the modal coupling, namely: modal energy transfer, are derived in this subsection. The control algorithm proposed in the next chapter is explicitly based on these equations.

Modal energies and modal energy transfer

First, the total mechanical energy of the structure $E(t)$ is decomposed into the energies $E_m(t)$ associated with particular unlocked vibration modes, namely: modal energies, as shown below:

$$\begin{aligned}E(t) &= \frac{1}{2}\dot{\mathbf{q}}^{\mathrm{T}}(t)\mathbf{M}\dot{\mathbf{q}}(t)+\frac{1}{2}\mathbf{q}^{\mathrm{T}}(t)\mathbf{K}\mathbf{q}(t)\\ &= \frac{1}{2}\dot{\boldsymbol{\eta}}^{\mathrm{T}}(t)\underbrace{\boldsymbol{\Phi}^{\mathrm{T}}\mathbf{M}\boldsymbol{\Phi}}_{\mathbf{I}}\dot{\boldsymbol{\eta}}(t)+\frac{1}{2}\boldsymbol{\eta}^{\mathrm{T}}(t)\underbrace{\boldsymbol{\Phi}^{\mathrm{T}}\mathbf{K}\boldsymbol{\Phi}}_{\boldsymbol{\Omega}^2}\boldsymbol{\eta}(t)\\ &= \sum_{m=1}^{N_{\mathrm{d}}}\frac{1}{2}\left(\dot{\eta}_m^2(t)+\omega^{(m)2}\eta_m^2(t)\right)=\sum_{m=1}^{N_{\mathrm{d}}}E_m(t). \quad (2.66)\end{aligned}$$

It is shown in this subsection that in free vibration any particular energy $E_m(t)$ can increase only at the expense of other modal energies when modal coupling is provided.

The derivative of m-th modal energy is calculated:

$$\dot{E}_m(t) = \dot{\eta}_m(t)\left(\ddot{\eta}_m(t) + \omega^{(m)2}\eta_m(t)\right). \tag{2.67}$$

After substitution of Eq. (2.62) into Eq. (2.67) we have:

$$\begin{aligned}\dot{E}_m(t) &= \dot{\eta}_m(t)\left(-\sum_{k=1}^{N_k}\sum_{n=1}^{N_\mathrm{d}} u_k(t)\gamma_{kmn}\dot{\eta}_n(t) - 2\zeta^{(m)}\omega^{(m)}\dot{\eta}_m(t) + \sum_{r=1}^{N_\mathrm{d}}\phi_i^{(m)}d_i(t)\right)\\ &= \underbrace{-\dot{\eta}_m(t)\sum_{k=1}^{N_k}\sum_{n=1}^{N_\mathrm{d}} u_k(t)\gamma_{kmn}\dot{\eta}_n(t)}_{\dot{W}_m(t)}\underbrace{-2\zeta^{(m)}\omega^{(m)}\dot{\eta}_m^2(t)}_{\dot{E}_m^{\mathrm{loss}}(t)} + \underbrace{\dot{\eta}_m(t)\sum_{r=1}^{N_\mathrm{d}}\phi_i^{(m)}d_i(t)}_{\dot{W}_m^{\mathrm{ext}}(t)}.\end{aligned} \tag{2.68}$$

In Eq. (2.68), $W_m(t)$ is the energy transferred to the m-th unlocked vibration mode from the remaining ones (the sign of this quantity indicates direction of the energy flow), $E_m^{\mathrm{loss}}(t)$ is the energy dissipated in material damping corresponding to the m-th unlocked mode and $W_m^{\mathrm{ext}}(t)$ is the work done by external excitations on the m-th modal coordinate. Derivatives of these terms in Eq. (2.68) are expressed in Watts. $\dot{W}_m(t)$ is further called the modal energy transfer rate.

By taking into account the derivation in Eq. (2.64), the following calculations can be done for the modal energy transfer rate from Eq. (2.68):

$$\begin{aligned}\dot{W}_m(t) &= -\dot{\eta}_m(t)\sum_{k=1}^{N_k}\sum_{n=1}^{N_\mathrm{d}} u_k(t)\gamma_{kmn}\dot{\eta}_n(t) = \dot{\eta}_m(t)\sum_{k=1}^{N_k}\Delta\phi_k^{(m)}f_k(t)\\ &= \sum_{k=1}^{N_k}\underbrace{\dot{\eta}_m(t)\Delta\phi_k^{(m)}}_{\Delta\dot{q}_k^{(m)}(t)}f_k(t) = \sum_{k=1}^{N_k}\Delta\dot{q}_k^{(m)}(t)f_k(t),\end{aligned} \tag{2.69}$$

where $\Delta q_k^{(m)}(t)$ is relative rotational displacement of the beams connected at k-th lockable joint corresponding to the m-th mode. It can be seen that energy transferred to the m-th unlocked vibration mode is equal to the work done by self-equilibrated moments on relative rotational displacement resulting from this mode at all lockable joints. Similarly, the total modal energy transfer rate is the sum of modal energy transfer rates over all lockable joints. Due to the constraint shown in Eq. (2.40) the condition that

$$u_k(t)\sum_{m=1}^{N_\mathrm{d}}\Delta\dot{q}_k^{(m)}(t) \approx 0 \tag{2.70}$$

is satisfied but $\Delta\dot{q}_k^{(m)}(t)$ for a particular vibration mode can be different from zero.

Energetic balance between vibration modes

Despite the fact that operation of the lockable joints can cause increments of particular modal energies, the structure cannot be destabilised in free vibration. In Eq. (2.43), the damping matrix $\mathbf{C}$ is positive-definite and all matrices $\widetilde{\mathbf{C}}_k$ have a single nonzero eigenvalue $2c_{\max} > 0$, hence they are positive semi-definite. Thus, the sum of all these matrices remains positive-definite for any vector $\mathbf{u}(t) \in \{0,1\}^{N_k}$ and there is no negative damping introduced. A deeper understanding can be obtained by inspection of Eq. (2.70), from which one can derive that the sum of all modal energy transfer rates is close to zero (tends to zero as $c_{\max}$ approaches infinity):

$$\sum_{m=1}^{N_\mathrm{d}} \dot{W}_m(t) = \sum_{m=1}^{N_\mathrm{d}} \sum_{k=1}^{N_k} \Delta\dot{q}_k^{(m)}(t) f_k(t) = \sum_{k=1}^{N_k} f_k(t) \sum_{m=1}^{N_\mathrm{d}} \Delta\dot{q}_k^{(m)}(t) \approx 0. \tag{2.71}$$

In other words, when any k-th joint is locked the total work of the pair of self-equilibrated moments $f_k(t)$ (Fig. 2.11b) done over the structure is equal to zero because the opening angle between the corresponding rotational DOFs is constant due to the constraint (2.40). The exception applies only if rotational velocities of DOFs involved in the joint are different during the locking resulting in the inelastic collision. Then energy is shortly dissipated in the joint. However, after this transient state the energy transferred to any unlocked vibration mode is equal to the energy transferred out from the remaining unlocked vibration modes. In summary, the lockable joints aim at exchange of energy between coupled unlocked vibration modes but they intentionally do not perform any work nor change the overall amount of the structural energy.

Similarly, the amount of energy transferred to a certain subset of the unlocked vibration modes is equal to the energy transferred out from the all remaining unlocked vibration modes. Taking notation as in Eq. (2.65), the balance of the energy exchanged between monitored (lower-order) unlocked vibration modes and unmonitored (higher-order) ones can be written as follows:

$$\begin{aligned} \dot{W}_\mathrm{H}(t) \;&=\; -\dot{\boldsymbol{\eta}}_\mathrm{H}^\mathrm{T}(t) \sum_{k=1}^{N_k} u_k(t) \begin{bmatrix} \boldsymbol{\Gamma}_{\mathrm{HM}k} & \boldsymbol{\Gamma}_{\mathrm{HH}k} \end{bmatrix} \begin{bmatrix} \dot{\boldsymbol{\eta}}_\mathrm{M}(t) \\ \dot{\boldsymbol{\eta}}_\mathrm{H}(t) \end{bmatrix} \\ &\approx\; \dot{\boldsymbol{\eta}}_\mathrm{M}^\mathrm{T}(t) \sum_{k=1}^{N_k} u_k(t) \begin{bmatrix} \boldsymbol{\Gamma}_{\mathrm{MM}k} & \boldsymbol{\Gamma}_{\mathrm{MH}k} \end{bmatrix} \begin{bmatrix} \dot{\boldsymbol{\eta}}_\mathrm{M}(t) \\ \dot{\boldsymbol{\eta}}_\mathrm{H}(t) \end{bmatrix} = -\dot{W}_\mathrm{M}(t). \end{aligned} \tag{2.72}$$

This is very important observation, because it follows that to control the modal energy transfer to the higher-order vibration modes, it is sufficient to monitor only lower-order ones. The equation above can be written in equivalent form:

$$\dot{W}_\mathrm{H}(t) = \dot{\boldsymbol{\eta}}_\mathrm{H}^\mathrm{T}(t) \sum_{k=1}^{N_k} \boldsymbol{\Delta\phi}_{\mathrm{H}k} f_k(t) \approx -\dot{\boldsymbol{\eta}}_\mathrm{M}^\mathrm{T}(t) \sum_{k=1}^{N_k} \boldsymbol{\Delta\phi}_{\mathrm{M}k} f_k(t) = -\dot{W}_\mathrm{M}(t), \tag{2.73}$$

where:

$$\boldsymbol{\Delta\phi}_{\mathrm{M}k} = \left[\Delta\phi_k^{(1)} \;\; \Delta\phi_k^{(2)} \;\; \cdots \;\; \Delta\phi_k^{(N_p)}\right]^{\mathrm{T}} \tag{2.74}$$

for the first N_p monitored unlocked vibration modes and

$$\boldsymbol{\Delta\phi}_{\mathrm{H}k} = \left[\Delta\phi_k^{(N_p+1)} \;\; \Delta\phi_k^{(N_p+2)} \;\; \cdots \;\; \Delta\phi_k^{(N_\mathrm{d})}\right]^{\mathrm{T}}. \tag{2.75}$$

It also should be noticed that the energy transfer rate is the sum of energy transfer rates through each currently locked joint:

$$\dot{W}_{\mathrm{M}}(t) = \sum_{k=1}^{N_k} \dot{W}_{\mathrm{M}k}(t), \quad \dot{W}_{\mathrm{H}}(t) = \sum_{k=1}^{N_k} \dot{W}_{\mathrm{H}k}(t), \tag{2.76}$$

where $\dot{W}_{\mathrm{M}k}(t)$ and $\dot{W}_{\mathrm{H}k}(t)$ are energy transfer rates through the k-th lockable joint to monitored vibration modes and the higher order ones, respectively. $\dot{W}_{\mathrm{M}k}$ can be expressed as in equations below, whereas $\dot{W}_{\mathrm{H}k}(t)$ is defined analogously:

$$\dot{W}_{\mathrm{M}k}(t) = -u_k(t)\dot{\boldsymbol{\eta}}_{\mathrm{M}}^{\mathrm{T}}(t)\left[\boldsymbol{\Gamma}_{\mathrm{MM}k} \;\; \boldsymbol{\Gamma}_{\mathrm{MH}k}\right]\begin{bmatrix}\dot{\boldsymbol{\eta}}_{\mathrm{M}}(t)\\ \dot{\boldsymbol{\eta}}_{\mathrm{H}}(t)\end{bmatrix}, \tag{2.77}$$

$$\dot{W}_{\mathrm{M}k}(t) = \dot{\boldsymbol{\eta}}_{\mathrm{M}}^{\mathrm{T}}(t)\boldsymbol{\Delta\phi}_{\mathrm{M}k} f_k(t). \tag{2.78}$$

Illustrative summary

An illustrative example of the modal energy transfer typical of energy harvesting application is shown in Fig. 2.12. In this example energy is to be transferred from the excited unlocked vibration mode (free vibration) to the chosen unlocked mode to which energy harvester is designed. Both of them are monitored (lower-order) unlocked vibration modes. First, when the joint is in the unlocked state the excited vibration is mitigated only by the material damping and energy is

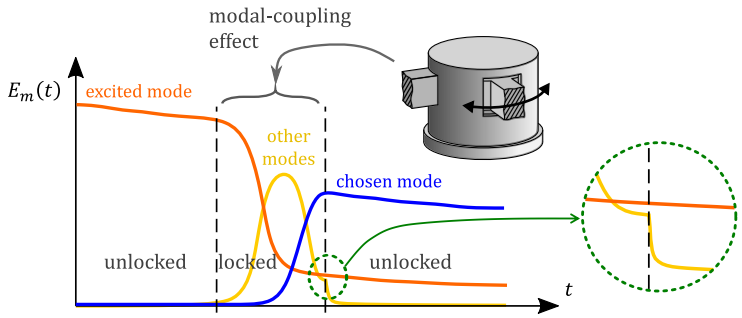

Fig. 2.12. Illustrative example of typical flow of modal energies in energy harvesting application.

not transferred between vibration modes. Later, when the joint becomes locked, modal coupling resulting in the modal energy transfer is provided. Due to the fact that matrices $\mathbf{\Gamma}_k$ are full it causes energy exchange between all unlocked vibration modes, including the higher-order ones. At this stage, the total structural energy is not dissipated quickly because the higher-order unlocked modes have mainly potential energy and become prestressed rather than vibrate freely. Finally, the joint is unlocked when the energy of the chosen vibration mode stops increasing. At the same time instance the higher-order modes that are yet prestressed start to vibrate freely and their modal energies are quickly dissipated in material damping (see: zoomed area on the right hand side of Fig. 2.12). This amount of energy is inevitably lost.

In the case of vibration damping application of the proposed methodology, such a quick energy dissipation is a desired phenomenon. Hence, the lockable joint could be dynamically unlocked, in the simplest case, at the instant when the higher-order modes (yellow line) reach their maximum energy, resulting in the largest sudden energy decrease (analogous to the zoomed area but of greater magnitude).

The appropriate control algorithm, along with the quantities to be measured and methods for the optimal placement of sensors and joints, is discussed in the next chapter.

3. Semi-active control strategy

This chapter describes a comprehensive methodology including the control law and control algorithm, the identified quantities required in measurement as well as methods for optimal placement of sensors and lockable joints. The semi-active control methodology is explicitly based on the derivations presented in the previous chapter. The control works in the feedback architecture. Its components are illustrated in the form of a block diagram shown in Fig. 3.1.

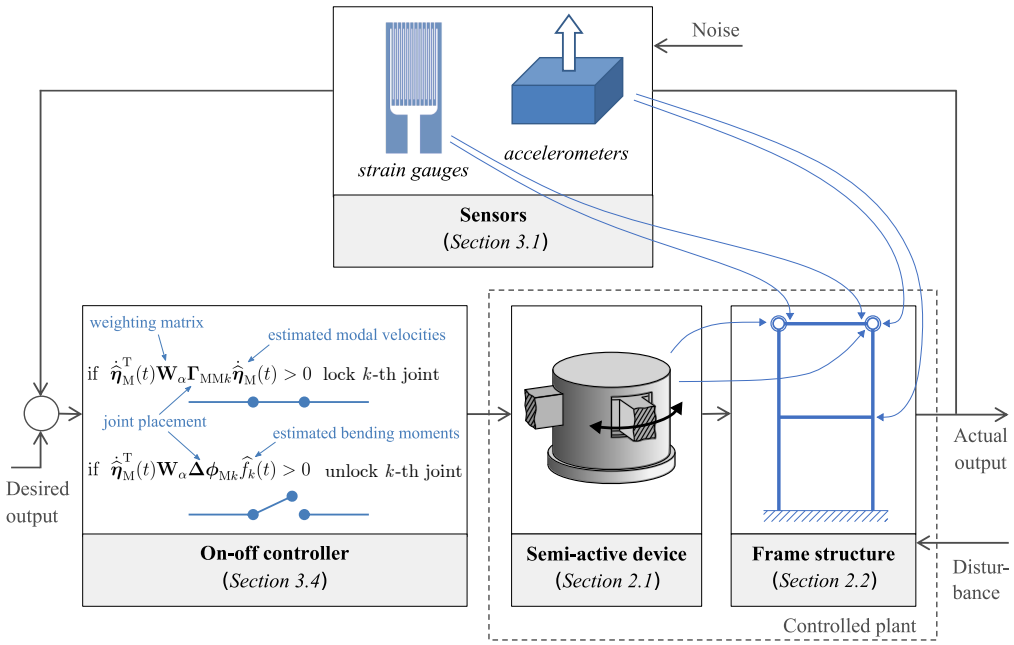

Fig. 3.1. Semi-active control methodology [144].

3.1. Quantities required to be measured and hierarchical feedback architecture

3.1.1. Issues to be addressed and selected measured quantities

The higher-order vibration modes are usually characterised by significant damping coefficients, thus their energy is quickly dissipated in free vibration.

However, in reconfigurable systems, the motion of higher-order unlocked vibration modes should not be regarded as free vibration when the joint is locked, as discussed at the end of Subsection 2.2.4. In this case, the structure is rather prestressed in these vibration modes until the joint is unlocked. Thus, the structural displacement is superposition of all unlocked vibration modes (including the higher-order ones) for the joints in the locked state, even if only several first locked vibration modes are induced. On the other hand, due to equipment limitations usually only lower-order unlocked vibration modes can be monitored. The main limitation is the restricted number of available sensors. Thus, the participation of the higher-order vibration modes in the structural motion and operation of the lockable joints are issues in the measurement technique that should be addressed.

As it is discussed in Section 3.4, the proposed control law for each joint requires estimation of the current modal energy transfer rate (Eqs. (2.77) and (2.78)) to make decision when the joint should be locked/unlocked. Regarding the above, first, the measurement of quantities required for this purpose is considered when the k-th joint is in the locked state. In this case, using Eq. (2.77) is impractical because $\dot{\boldsymbol{\eta}}_{\mathrm{H}}(t)$ is not measurable due to the equipment limitations. On the other hand, it cannot be omitted, as the higher-order unlocked vibration modes take significant participation in the structural response – especially in bending moments $f_k(t)$. Also, estimation of the whole vector $\dot{\boldsymbol{\eta}}_{\mathrm{H}}(t)$ using a state observer is too inaccurate when only the vector $\dot{\boldsymbol{\eta}}_{\mathrm{M}}(t)$ is available. These problems can be avoided using Eq. (2.78), where $\dot{\boldsymbol{\eta}}_{\mathrm{H}}(t)$ is not explicitly used. Here, both $\dot{\boldsymbol{\eta}}_{\mathrm{M}}(t)$ and $f_k(t)$ are required to be estimated to calculate $\dot{W}_{\mathrm{M}k}(t)$, however, the moment $f_k(t)$ can be easily obtained, e.g. via measurement of strains in the vicinity of the k-th lockable joint. Moments $f_k(t)$ contain sufficient information about the influence of the higher-order unlocked vibration modes on the modal energy transfer rate.

Next issue is that $f_k(t) = 0$ and $\dot{W}_{\mathrm{M}k}(t) = 0$ when the joint is unlocked. In this case Eq. (2.77) is used to estimate the eventual modal energy transfer rate that could occur when the k-th joint is dynamically locked at the time instant t by the substitution $u_k(t) = 1$. In this case, $\dot{W}_{\mathrm{M}k}(t)$ is estimated assuming that $\dot{\boldsymbol{\eta}}_{\mathrm{H}}(t) \approx \mathbf{0}$. It follows from the fact that the higher-order unlocked vibration modes are damped after previous unlocking of the lockable joint.

Summarising, both $\dot{\boldsymbol{\eta}}_{\mathrm{M}}(t)$ and $f_k(t)$ are required to be estimated to determine when the currently locked k-th joint should be unlocked and only $\dot{\boldsymbol{\eta}}_{\mathrm{M}}(t)$ is required when the currently unlocked joint state should be locked.

3.1.2. Realisation of measurement and its representation in the model

Taking into account the considerations above, the output vector $\mathbf{y}$, matrices $\mathbf{C}_{\mathrm{y}}$, $\mathbf{D}$ and the vector $\mathbf{v}(t)$ in Eq. (2.44) take the following form:

$$\mathbf{y}(t) = \begin{bmatrix} \boldsymbol{\varepsilon}_{\mathrm{M}}(t) \\ \dot{\mathbf{q}}_{\mathrm{M}}(t) \\ \mathbf{u}(t) \end{bmatrix}, \quad \mathbf{C}_{\mathrm{y}} = \begin{bmatrix} \mathbf{L}_{\varepsilon} & \mathbf{0} \\ \mathbf{0} & \mathbf{L}_{\mathrm{q}} \\ \mathbf{0} & \mathbf{0} \end{bmatrix}, \quad \mathbf{D} = \begin{bmatrix} \mathbf{0} \\ \mathbf{0} \\ \mathbf{I} \end{bmatrix}, \quad \mathbf{v}(t) = \begin{bmatrix} \mathbf{v}_{\varepsilon}(t) \\ \mathbf{v}_{\dot{\mathrm{q}}}(t) \\ \mathbf{0} \end{bmatrix}, \tag{3.1}$$

where $\boldsymbol{\varepsilon}_{\mathrm{M}}(t) = \begin{bmatrix} \varepsilon_{\mathrm{M}1}(t) & \varepsilon_{\mathrm{M}2}(t) & \cdots & \varepsilon_{\mathrm{M}N_k}(t) \end{bmatrix}^{\mathrm{T}} \in \mathbb{R}^{N_k}$ contains strains measured in the vicinity of each lockable joints, $\dot{\mathbf{q}}_{\mathrm{M}}(t) = \begin{bmatrix} \dot{q}_{\mathrm{M}1}(t) & \dot{q}_{\mathrm{M}2}(t) & \cdots & \dot{q}_{\mathrm{M}N_{\mathrm{s}}}(t) \end{bmatrix}^{\mathrm{T}} \in \mathbb{R}^{N_{\mathrm{s}}}$ is the vector containing measured velocities at N_{s} selected locations, $\mathbf{L}_{\varepsilon} \in \mathbb{R}^{N_k \times N_{\mathrm{d}}}$ is transformation matrix, $\mathbf{L}_{\mathrm{q}} \in \{0,1\}^{N_{\mathrm{s}} \times N_{\mathrm{d}}}$ is the Boolean matrix selecting appropriate DOFs of the structure. If sensors are located between FE mesh nodes, then $\mathbf{L}_{\mathrm{q}} \in \mathbb{R}^{N_{\mathrm{s}} \times N_{\mathrm{d}}}$ and it provides an estimate of the displacement at the sensor positions, computed from neighbouring nodal displacements using shape functions; $\mathbf{v}_{\varepsilon}(t)$ and $\mathbf{v}_{\dot{\mathrm{q}}}(t)$ represent measurement noise corresponding to measured strains and velocities, respectively; $\boldsymbol{\varepsilon}_{\mathrm{M}}(t)$, $\dot{\mathbf{q}}_{\mathrm{M}}(t)$ and $\mathbf{u}(t)$ are used to estimate $\mathbf{f}(t)$, $\dot{\boldsymbol{\eta}}_{\mathrm{M}}(t)$ and determine whether the joints are currently locked, respectively.

Estimation of the bending moments transmitted by the joint

The bending moment transmitted through this joint $f_k(t)$ can be estimated using the equation below:

$$\widehat{f}_k(t) = -\frac{2EI}{h}\varepsilon_{\mathrm{M}k}(t), \tag{3.2}$$

where: E, I and h are Young modulus, sectional moment of inertia and height of the cross-section of the beam connected to the k-th lockable joint, respectively, and

$$\varepsilon_{\mathrm{M}k}(t) = \frac{\varepsilon^{\mathrm{I}}_{\mathrm{M}k}(t) - \varepsilon^{\mathrm{II}}_{\mathrm{M}k}(t)}{2}, \tag{3.3}$$

where $\varepsilon^{\mathrm{I}}_{\mathrm{M}k}(t)$ and $\varepsilon^{\mathrm{II}}_{\mathrm{M}k}(t)$ are strains measured on both sides of the beam (elongated and compressed) in the vicinity of the k-th lockable joint. Difference of these two signals that usually are obtained with strain gauges ensures that $\varepsilon_{\mathrm{M}k}(t)$ contains only the strain component resulting from bending of the beam, whereas strains resulting from longitudinal loads are rejected.

The transformation matrix that describes strain-displacement relation is defined using shape functions of the beam elements:

$$\mathbf{L}_{\varepsilon} = \begin{bmatrix} (\boldsymbol{\Psi}_1\mathbf{R}_1)^{\mathrm{T}} & (\boldsymbol{\Psi}_2\mathbf{R}_2)^{\mathrm{T}} & \cdots & (\boldsymbol{\Psi}_{N_k}\mathbf{R}_{N_k})^{\mathrm{T}} \end{bmatrix}^{\mathrm{T}}, \tag{3.4}$$

where: $\mathbf{R}_k$ is matrix transforming displacement vector $\mathbf{q}(t)$ to a local coordinate system of the beam connected to the k-th lockable joint and $\boldsymbol{\Psi}_k$ is row matrix containing the first and second derivatives of the FE shape functions. If the

standard Euler–Bernoulli beam model is assumed, then the matrix $\mathbf{R}_k \in \mathbb{R}^{6\times N_\mathrm{d}}$ and

$$\boldsymbol{\Psi}_k = \left[\Psi_1'(\xi) \;\; -\frac{h}{2}\Psi_2''(\xi) \;\; -\frac{h}{2}\Psi_3''(\xi) \;\; \Psi_4'(\xi) \;\; -\frac{h}{2}\Psi_5''(\xi) \;\; -\frac{h}{2}\Psi_6''(\xi)\right]\Big|_{\xi=\xi_k}, \quad (3.5)$$

where $\Psi_i(\xi)$ are beam's shape functions and ξ_k is location of the pair of the strain gauges in the local coordinate system of the beam.

Estimation of the monitored modal velocities (modal filtering)

$\dot{\boldsymbol{\eta}}_\mathrm{M}(t)$ is estimated using the modal filtering technique. The estimate of $\dot{\boldsymbol{\eta}}(t)$ is calculated as

$$\dot{\widehat{\boldsymbol{\eta}}}_\mathrm{M}(t) = \mathbf{F}\dot{\mathbf{q}}_\mathrm{M}(t), \quad (3.6)$$

where

$$\mathbf{F} = (\mathbf{L}_\mathrm{q}\boldsymbol{\Phi}_\mathrm{M})^+ \in \mathbb{R}^{N_p\times N_\mathrm{s}} \quad (3.7)$$

is the modal filter and $(\cdot)^+$ is the Moore–Penrose inverse of the matrix; $\dot{\widehat{\boldsymbol{\eta}}}_\mathrm{M}(t)$ corresponds to the least-square estimate of the modal velocities using mode shapes at sensor locations. It is evident that the number of sensors N_s cannot be lower than the number of estimated modal velocities N_p. If $N_\mathrm{s} = N_p$, the modal filter is square matrix reciprocal to the matrix $\mathbf{L}_\mathrm{q}\boldsymbol{\Phi}_\mathrm{M}$.

An appropriate design of the modal filter $\mathbf{F}$, i.e. the selection of sensor locations described by the matrix $\mathbf{L}_\mathrm{q}$ and the selection of the vibration modes to be monitored, can significantly reduce the measurement spillover effect and the impact of the noise on estimation of the modal velocities. This topic is discussed in the next section.

Hierarchical feedback architecture

Modal velocities provide the information about global behaviour of the controlled structure, whereas bending moments depend on the local state of the structure in the vicinity of each lockable joint. It results in a hierarchical feedback architecture illustrated in Fig. 3.2. Each joint is controlled in a local collocated control loop independently of the remaining joints. Modal velocities are estimated from velocity measurement at various sensor locations on the structure. It can be illustrated as one global loop fed to each of the local collocated control loops. The possibility of making the control independent of each lockable joint results from the fact that total modal energy transfer rate to/from selected vibration modes is the sum of the particular transfers via each lockable joint (see: Eqs. (2.76)–(2.78)).

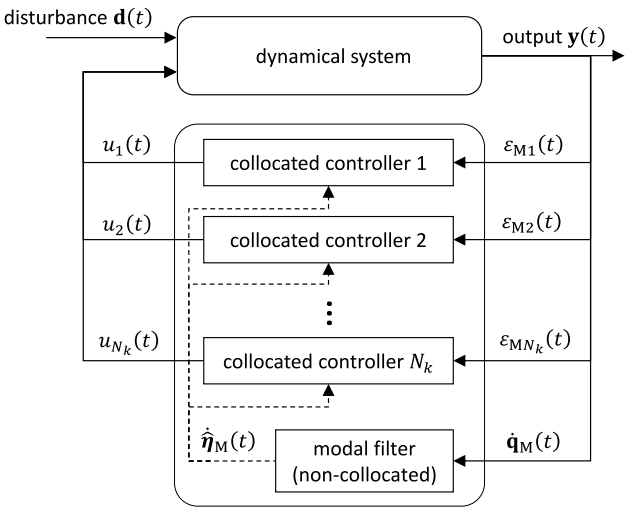

Fig. 3.2. Concept of hierarchical control architecture.

3.2. Optimal sensor placement

3.2.1. Error of the modal filter and its metrics

In this section, a method for selection of optimal sensor locations to ensure reliable estimation of $\dot{\boldsymbol{\eta}}_{\mathrm{M}}(t)$ is described. Rows in Eq. (3.1) related to the measured velocities can be rewritten into the following form:

$$\dot{\mathbf{q}}_{\mathrm{M}}(t) = \mathbf{L}_{\mathrm{q}} \begin{bmatrix} \boldsymbol{\Phi}_{\mathrm{M}} & \boldsymbol{\Phi}_{\mathrm{H}} \end{bmatrix} \begin{bmatrix} \dot{\boldsymbol{\eta}}_{\mathrm{M}}(t) \\ \dot{\boldsymbol{\eta}}_{\mathrm{H}}(t) \end{bmatrix} + \mathbf{v}_{\dot{\mathrm{q}}}(t). \tag{3.8}$$

It is assumed that $\mathbf{v}_{\dot{\mathrm{q}}}(t)$ is zero-mean and uncorrelated noise, and the standard deviation corresponding to each element of this vector is equal to σ_{q}. Seeking for the simplicity of further derivations let us denote by

$$\boldsymbol{\Phi}_{\mathrm{S}} = \mathbf{L}_{\mathrm{q}} \boldsymbol{\Phi}_{\mathrm{M}}, \tag{3.9}$$

the modal matrix truncated to the rows corresponding to measured DOFs and columns representing the monitored vibration modes.

Equations (3.6) and (3.7) describing modal filtering can be rewritten into the following form:

$$\begin{aligned} \hat{\dot{\boldsymbol{\eta}}}_{\mathrm{M}}(t) &= \boldsymbol{\Phi}_{\mathrm{S}}^{+} \dot{\mathbf{q}}_{\mathrm{M}}(t) \\ &= \dot{\boldsymbol{\eta}}_{\mathrm{M}}(t) + \boldsymbol{\Phi}_{\mathrm{S}}^{+} \underbrace{\mathbf{L}_{\mathrm{q}} \boldsymbol{\Phi}_{\mathrm{H}} \dot{\boldsymbol{\eta}}_{\mathrm{H}}(t)}_{\dot{\mathbf{q}}_{\mathrm{H}}(t)} + \boldsymbol{\Phi}_{\mathrm{S}}^{+} \mathbf{v}_{\dot{\mathrm{q}}}(t). \end{aligned} \tag{3.10}$$

In Eq. (3.10), the last two terms represent the influence of measurement spillover and measurement noise, respectively. Accordingly to the Gauss–Markov theorem the least-square estimator is unbiased and efficient if the error (here: $\dot{\mathbf{q}}_{\mathrm{H}}(t) + \mathbf{v}_{\dot{\mathrm{q}}}$) has a mean of zero and is uncorrelated. However, these assumptions may be invalid, as only $\mathbf{v}_{\dot{\mathrm{q}}}(t)$ is considered as a random zero-mean variable with uncorrelated elements. Due to the measurement spillover effect, the estimation error $\mathbf{e}_{\eta}(t)$, in general, does not have a zero expected value. The estimation error is given as:

$$\begin{aligned} \mathbf{e}_{\eta}(t) &= \dot{\widehat{\boldsymbol{\eta}}}_{\mathrm{M}}(t) - \dot{\boldsymbol{\eta}}_{\mathrm{M}}(t) \\ &= \boldsymbol{\Phi}_{\mathrm{S}}^{+} \left(\dot{\mathbf{q}}_{\mathrm{H}}(t) + \mathbf{v}_{\dot{\mathrm{q}}}(t) \right). \end{aligned} \tag{3.11}$$

As described at the beginning of Section 3.1 the higher-order unlocked vibration modes are quickly damped during their free vibration when the joints are unlocked, whereas they can significantly participate in the strain (potential) energy when joints are in the locked state. However, for the locked joints these vibration modes correspond to the quasi-static motion, since their current frequency of vibration is much smaller than their natural frequencies $\omega^{(m)}$, as summarized at the end of Chapter 2. Thus, the participation of these modes in structural velocities can be considered as negligible in further derivation, excepting only the short transient states after each joint unlock, when free high-frequency oscillations responsible for the error $\dot{\mathbf{q}}_{\mathrm{H}}(t)$ are present. Then, the control is stopped for corresponding selected time interval, as described in Section 3.4.

On the other hand, $\dot{\mathbf{q}}_{\mathrm{H}}(t)$ depends on the excitation case, kind of the controlled structure and selected algorithm parameters, hence it is difficult to estimate $\dot{\mathbf{q}}_{\mathrm{H}}(t)$ at this stage. Thus, calculation of the mean square error (MSE) of the estimator $\dot{\widehat{\boldsymbol{\eta}}}_{\mathrm{M}}(t)$, which quantifies the influence of the selected sensor locations on modal filtering, is challenging. The covariance matrix which provides information about deviation from the expected value (as opposed to MSE measure quantifying deviation from the true value $\dot{\boldsymbol{\eta}}_{\mathrm{M}}(t)$) could be used, since the higher-order unlocked vibration modes provide only a small estimator bias that can be neglected.

Taking the above considerations into account, a weaker formulation of the sensor placement problem, rather than explicit minimization of the MSE, can be adopted. MSE of the estimator cannot be lower than corresponding variance that, accordingly to the Cramér–Rao bound, cannot be lower than reciprocal of the Fisher information matrix (FIM):

$$\mathrm{MSE}(\mathbf{e}_{\eta}(t)) \geq \boldsymbol{\Sigma}_{\eta} \geq \boldsymbol{\mathfrak{I}}^{-1}, \tag{3.12}$$

where:

$$\mathrm{MSE}\left(\mathbf{e}_{\eta}(t)\right) = \mathrm{E}\left(\mathbf{e}_{\eta}(t)\mathbf{e}_{\eta}^{\mathrm{T}}(t)\right), \tag{3.13}$$

$\mathrm{E}(\cdot)$ is the expected value operator,

$$\begin{aligned}\boldsymbol{\Sigma}_\eta &= \mathrm{E}\left(\left[\mathbf{e}_\eta(t) - \mathrm{E}(\mathbf{e}_\eta(t))\right]\left[\mathbf{e}_\eta(t) - \mathrm{E}(\mathbf{e}_\eta(t))\right]^{\mathrm{T}}\right) \\ &= \mathrm{E}\left(\left[\mathbf{e}_\eta(t) - \boldsymbol{\Phi}_{\mathrm{S}}^{+}\dot{\mathbf{q}}_{\mathrm{H}}(t)\right]\left[\mathbf{e}_\eta(t) - \boldsymbol{\Phi}_{\mathrm{S}}^{+}\dot{\mathbf{q}}_{\mathrm{H}}(t)\right]^{\mathrm{T}}\right) \\ &= \sigma_{\mathrm{q}}^2\left(\boldsymbol{\Phi}_{\mathrm{S}}^{\mathrm{T}}\boldsymbol{\Phi}_{\mathrm{S}}\right)^{-1}, \end{aligned} \tag{3.14}$$

is the covariance matrix of estimator $\dot{\hat{\boldsymbol{\eta}}}_{\mathrm{M}}(t)$ and $\boldsymbol{\mathcal{I}}$ is FIM that in this particular case is equal to the reciprocal of the covariance matrix:

$$\boldsymbol{\mathcal{I}} = \sigma_{\mathrm{q}}^{-2}\left(\boldsymbol{\Phi}_{\mathrm{S}}^{\mathrm{T}}\boldsymbol{\Phi}_{\mathrm{S}}\right). \tag{3.15}$$

The inequality in Eq. (3.12) means that if $\mathbf{A} \geq \mathbf{B}$ then the matrix $\mathbf{A} - \mathbf{B}$ is positive semidefinite. As σ_{q} is constant it does not play the role in the optimisation procedure, hence FIM further is represented by the matrix $\boldsymbol{\mathcal{F}}$ written with the omitted σ_{q} term:

$$\boldsymbol{\mathcal{F}} = \boldsymbol{\Phi}_{\mathrm{S}}^{\mathrm{T}}\boldsymbol{\Phi}_{\mathrm{S}}. \tag{3.16}$$

3.2.2. Effective Independence concept

The covariance matrix $\boldsymbol{\Sigma}_\eta$ provides information about the expected measurement error, hence its various norms, e.g. its trace, could be used as the objective function to be minimised. However, calculation of the characteristics in dependence on the selected sensor locations (rows of $\boldsymbol{\Phi}_{\mathrm{M}}$ that form the matrix $\boldsymbol{\Phi}_{\mathrm{S}}$) is difficult. Hence, FIM is used in the optimisation process instead, as mentioned in Subsection 1.1.4. In this case, determinant of FIM $\det\boldsymbol{\mathcal{F}}$ is to be maximised during the optimisation procedure. It provides the trade-off between linear independence and norms of vectors formed from the mode shapes at sensor locations. One of methods searching for the near-optimal solution is the famous effective independence (EFI) proposed by Kammer [131]. The EFI method is introduced below, since a method used in this work is based on it.

In the EFI method the optimisation problem below is solved:

$$\begin{array}{ll} \text{find} & \mathbf{s} \in \{0,1\}^{N_{\mathrm{c}}} \\ \text{to maximise} & \det\boldsymbol{\mathcal{F}}(\mathbf{s}) \\ \text{subject to} & \displaystyle\sum_{i=1}^{N_{\mathrm{c}}} s_i = N_p, \end{array} \tag{3.17}$$

where $\mathbf{s}$ is the Boolean vector selecting DOFs to be sensor locations (corresponding rows of $\boldsymbol{\Phi}_{\mathrm{M}}$), N_{c} is the number of DOFs candidating to be sensor locations. In the simplest case $N_{\mathrm{c}} = N_{\mathrm{d}}$, however, in some cases the set of candidate sensor

locations may be restricted due to structural conditions, e.g. some locations can be not available for sensors. Here, it is assumed that rows of $\mathbf{\Phi}_{\mathrm{M}}$ corresponding to these locations are removed initially. The constraint pursued on the cardinality of sensor locations follows from the fact that N_p sensors are required to monitor N_p vibration modes.

Kammer proposed that starting from full vector $\mathbf{s}$ (containing only ones), sensor locations that contribute the least to $\det \mathcal{F}(\mathbf{s})$ are removed in an iterative manner. Then, the corresponding element of vector $\mathbf{s}$ is replaced with zero in each iteration step. The effective independence measure for all sensor locations is computed in the form of a vector:

$$\mathbf{r}(\mathbf{s}) = \operatorname{diag}\left(\mathbf{\Phi}_{\mathrm{S}}(\mathbf{s})\mathcal{F}^{-1}(\mathbf{s})\mathbf{\Phi}_{\mathrm{S}}^{\mathrm{T}}(\mathbf{s})\right) \tag{3.18}$$

before each sensor removal. If $r_i = 0$, then the i-th sensor location does not contribute to the $\det \mathcal{F}(\mathbf{s})$ representing the linear independence, whereas if $r_i = 1$, then removing this sensor causes that vectors in the reduced modal matrix $\mathbf{\Phi}_{\mathrm{S}}(\mathbf{s})$ are not linearly independent and the $\det \mathcal{F}(\mathbf{s}) = 0$. In other words, this sensor location is crucial and cannot be removed. Poston and Tolson showed that determinants of FIM before and after the removal of the i-th sensor are related as follows [145]:

$$\det \mathcal{F}(\mathbf{s}_{\mathrm{next}}) = (1 - r_i(\mathbf{s}_{\mathrm{current}})) \det \mathcal{F}(\mathbf{s}_{\mathrm{current}}). \tag{3.19}$$

Thus, the EFI method removes the candidate sensor locations in the way providing the smallest decreases (the smallest r_i is selected) of the determinant of FIM until N_p sensor locations are obtained. After each sensor removal the number of rows in $\mathbf{\Phi}_{\mathrm{S}}(\mathbf{s})$ is reduced by one. The matrix $\mathbf{\Phi}_{\mathrm{S}}(\mathbf{s})\mathcal{F}^{-1}(\mathbf{s})\mathbf{\Phi}_{\mathrm{S}}^{\mathrm{T}}(\mathbf{s})$ is idempotent, hence in each iteration step, the sum of elements of $\mathbf{r}(\mathbf{s})$ that is the trace of $\mathbf{\Phi}_{\mathrm{S}}(\mathbf{s})\mathcal{F}^{-1}(\mathbf{s})\mathbf{\Phi}_{\mathrm{S}}^{\mathrm{T}}(\mathbf{s})$ is equal to the number of monitored vibration modes:

$$\sum_{i=1}^{N_{\mathrm{c}}} r_i = N_p. \tag{3.20}$$

Thus, the vector $\mathbf{r}$ satisfies the constraint pursued on the vector $\mathbf{s}$ in the problem described in Eq. (3.17).

3.2.3. Convex relaxation approach for sensor layout optimisation

The EFI allows one to find a near-optimal solution of good quality without the need for an exhaustive search with all possible combinations of sensor locations which is not possible in practical applications due to the large N_{c}. However, the drawback of this method is that it performs $N_{\mathrm{c}} - N_p$ iterations to find sensor

locations. Thus, the convex relaxation (CR) method is proposed to reduce the computational burden.

In the CR-based method, instead of selecting the rows of $\boldsymbol{\Phi}_{\mathrm{S}}$ to be removed, the sensor density vector $\boldsymbol{\rho} \in [0,1]^{N_{\mathrm{c}}}$ provides relaxed Boolean constraints, as shown in Eq. (3.21):

$$\boldsymbol{\Phi}_{\rho} = \mathrm{diag}(\boldsymbol{\rho})\boldsymbol{\Phi}_{\mathrm{M}}. \tag{3.21}$$

In the equation above rows of the modal matrix $\boldsymbol{\Phi}_{\mathrm{M}}$ containing all candidate sensor locations are weighted by elements of the sensor density vector. On the other hand, elements ρ_i provide information how much the i-th candidate sensor location is relevant analogously to the vector $\mathbf{r}$ in Eq. (3.18).

Taking into account the considerations above, in the CR-based approach, a continuous optimisation problem (3.22) is solved, which is the relaxed counterpart of the discrete problem (3.17):

$$\begin{aligned} &\text{find} && \boldsymbol{\rho} \in [0,1]^{N_{\mathrm{c}}} \\ &\text{to maximise} && \det\left(\boldsymbol{\Phi}_{\rho}^{\mathrm{T}}\boldsymbol{\Phi}_{\rho}\right) \\ &\text{subject to} && \sum_{i=1}^{N_{\mathrm{c}}} \rho_i = N_p. \end{aligned} \tag{3.22}$$

The procedure that searches for a near-optimal solution to the problem (3.22) is shown in Algorithm 1 in the form of pseudo code. In this approach N_p elements of the vector $\boldsymbol{\rho}$ that contribute most to linear independence converge to ones at the expense of the remaining elements which converge to zeros, since the condition (3.20) is always satisfied also for the vector $\boldsymbol{\rho}$.

Algorithm 1 Pseudo code for CR-based sensor placement

Input: $\boldsymbol{\Phi}_{\mathrm{M}}$ related to monitored vibration modes and all candidate sensor locations and ϵ_{tol} for stop condition.
Output: indices i_{M} of DOFs to be measured.

$\boldsymbol{\rho} \leftarrow \frac{N_p}{N_{\mathrm{c}}}\mathbf{1}_{N_{\mathrm{c}}}$
Flag $\leftarrow 1$
while Flag **do**
    $\boldsymbol{\rho}_{\mathrm{prev}} \leftarrow \boldsymbol{\rho}$
    $\boldsymbol{\Phi}_{\rho} \leftarrow \mathrm{diag}(\boldsymbol{\rho})\boldsymbol{\Phi}_{\mathrm{M}}$
    $\boldsymbol{\rho} \leftarrow \mathrm{diag}\left(\boldsymbol{\Phi}_{\rho}\left(\boldsymbol{\Phi}_{\rho}^{\mathrm{T}}\boldsymbol{\Phi}_{\rho}\right)^{-1}\boldsymbol{\Phi}_{\rho}^{\mathrm{T}}\right)$
    if $\|\boldsymbol{\rho} - \boldsymbol{\rho}_{\mathrm{prev}}\| < \epsilon_{\mathrm{tol}}$ **then**
        Flag $\leftarrow 0$
    end if
end while
Select DOF indices i_{M} related to sensor densities close to 1, e.g. $\{i_{\mathrm{M}} : \rho_{i_{\mathrm{M}}} > 0.5\}$

3.3. Optimal placement of the lockable joints

3.3.1. Controllability in the control of modal energy transfer – issues

The controllability metrics discussed in the literature review such as the value of mode shape at the actuator location (as in the PBH test) and the controllability gramian are usually good measures of controllability of particular vibration modes when the controlled system is linear. Often, the structure contains a relatively small number of nonlinear structural members or devices, whereas its whole remaining part is linear. In such cases, it is common practice to treat the nonlinear forces generated by these components as external excitations and to apply controllability measures typically used for linear systems, as demonstrated, for example, in [107, 143]. Thanks to this simplification, it is possible to avoid the use of advanced mathematical formalism when determining the controllability of the system, e.g. Lie brackets [146]. Structures considered in this thesis fulfil these requirements. However, the aim of the proposed control methodology is to transfer the energy between unlocked vibration modes which interact with each other. These interactions are represented by the bilinear terms in the equations of motion, where the control forces do not depend only on the control signals but also directly on the current state of the structure. Thus, calculating the controllability metric for a single unlocked vibration mode may be insufficient.

For the considered control methodology, in the simplest case one could take elements γ_{kmn} of the matrix $\mathbf{\Gamma}_k$ as the metric of degree of coupling between the m-th and n-th unlocked vibration modes through the k lockable joint at its current location. Equation (2.63) shows that γ_{kmn}, analogously to the PBH test, is proportional to rotational displacements of the unlocked mode shapes at DOFs involved in the k-th lockable joint that are entries for the self-equilibrated pair of moments illustrated in Fig. 2.11b. However, similarly to the PBH test γ_{kmn} elements do not provide information about the amount of the energy that can be transferred from/to the monitored unlocked modes.

3.3.2. Proposed controllability metric

The proposed criterion is based on the assumption that locked mode shapes $\widetilde{\boldsymbol{\phi}}^{(m)}$ can be expressed in terms of a basis formed from the unlocked mode shapes $\boldsymbol{\phi}^{(m)}$, as discussed in Chapter 2. Here, for the purpose of optimal placement of the lockable joints mode shapes $\widetilde{\boldsymbol{\phi}}^{(m)}$ obtained for the structure with joints locked at $\Delta q_k = 0$ for all k are used (see Eq. (2.58)).

The ability of the lockable joints to transfer the energy between the m-th vibration mode and all remaining ones can be expressed as:

$$g_m = \frac{\Delta \widetilde{E}_{\mathrm{p}m}}{\widetilde{E}_{\mathrm{p}m}}, \tag{3.23}$$

where

$$\widetilde{E}_{\mathrm{p}m} = \frac{1}{2}\widetilde{\boldsymbol{\phi}}^{(m)\mathrm{T}}\widetilde{\mathbf{K}}\widetilde{\boldsymbol{\phi}}^{(m)} = \frac{1}{2}\widetilde{\omega}^{(m)2} \tag{3.24}$$

is strain (potential) energy related to the m-th locked vibration mode for the unit modal displacement $\widetilde{\eta}_m(t) = 1$ and $\Delta\widetilde{E}_{\mathrm{p}m}$ represents the amount of strain energy that will be released into vibration in unlocked vibration modes other than m-th one after sudden unlocking of the joints. It can be calculated as follows:

$$\begin{aligned}\Delta\widetilde{E}_{\mathrm{p}m} &= \widetilde{E}_{\mathrm{p}m} - E_{\mathrm{p}m} = \widetilde{E}_{\mathrm{p}m} - \frac{1}{2}\vartheta_{mm}^2\boldsymbol{\phi}^{(m)\mathrm{T}}\mathbf{K}\boldsymbol{\phi}^{(m)} \\ &= \frac{1}{2}\left(\widetilde{\omega}^{(m)2} - \vartheta_{mm}^2\omega^{(m)2}\right),\end{aligned} \tag{3.25}$$

where the coefficient ϑ_{mm} is the m-th diagonal element of the matrix $\boldsymbol{\Theta}$ that satisfies the equation

$$\mathbf{B}\widetilde{\boldsymbol{\Phi}} = \boldsymbol{\Phi}\boldsymbol{\Theta}, \tag{3.26}$$

where the matrix $\widetilde{\boldsymbol{\Phi}}$ collects locked mode shapes. $\boldsymbol{\Theta}$ is calculated simply as

$$\boldsymbol{\Theta} = \boldsymbol{\Phi}^{-1}\mathbf{B}\widetilde{\boldsymbol{\Phi}} \tag{3.27}$$

and contain information about participation of the unlocked mode shapes in structural deformation equal to the locked ones.

The greater the terms $\Delta\widetilde{E}_{\mathrm{p}m}$ are, the greater is the amount of energy distributed among all unlocked vibration modes when the structure vibrates in lower-order locked vibration modes. Thus, it is evident that the greater the value of $\Delta\widetilde{E}_{\mathrm{p}m}$, the better the ability to transfer energy between the m-th unlocked vibration mode and the remaining modes. Hence, g_m shown in Eq. (3.23) can be considered as the controllability of the m-th vibration mode in the sense of the energy transfer.

Usually only lower-order unlocked vibration modes are to be monitored. Their locked counterparts are less sensitive to local changes of the stiffness (e.g. unlocking the joints) than the higher-order ones, hence corresponding coefficients $\vartheta_{mm} \approx 1$. Thus, for many practical cases the controllability metric can be simplified to:

$$g_m = \frac{\widetilde{\omega}^{(m)2} - \vartheta_{mm}^2\omega^{(m)2}}{\widetilde{\omega}^{(m)2}} \approx \frac{\widetilde{\omega}^{(m)2} - \omega^{(m)2}}{\widetilde{\omega}^{(m)2}}. \tag{3.28}$$

Apart from reflecting the ability of the lockable joints at their current locations to transfer energy between vibration modes, the proposed controllability metric is also straightforward to compute. It requires only modal parameters of the structure with all locked and all unlocked joints.

3.3.3. Implementation for various applications

Aiming at efficient vibration damping, the controllability metrics g_m can be weighted by appropriate coefficients and summed to form a cumulative controllability metric:

$$G_1 = \sum_{p=1}^{N_p} \beta_p g_p, \tag{3.29}$$

where β_p are weights reflecting the priority of damping of the particular vibration modes in placement of the lockable joints. For example, weights selected as $\beta_p = 1/\omega^{(p)}$ or $\beta_p = 1/\omega^{(p)2}$ pursue higher priority to mitigate vibration of the lower-order unlocked vibration modes that have lower material damping and are associated with greater vibration amplitudes.

If it is demanded to keep all monitored unlocked modes controllable, then the lockable joints should be located in such a way that no g_p is close to zero. It applies to the energy harvesting application of the control methodology, in which the energy is to be transferred from all monitored vibration modes to the selected one. In this case, cumulative controllability is reflected better by the product of the controllabilities associated with particular vibration modes rather than their sum:

$$G_2 = \prod_{p=1}^{N_p} g_p. \tag{3.30}$$

In cases where the mass of the lockable joints is not negligible Eq. (3.29) or Eq. (3.30) is evaluated for each tested placement of the lockable joints. Then, the exhaustive search method is employed to find the solution of such a combinatorial problem. In cases where the mass of the lockable joint can be considered negligible compared to the mass of the structure, the following simplification may be applied to improve computational efficiency. Controllability metrics $\beta_p g_{ip}$ can be aggregated in the controllability matrix $\mathbf{G} \in \mathbb{R}_+^{N_{\mathrm{Jc}} \times N_p}$, where g_{ip} is a controllability metric of the p-th unlocked vibration mode for only one lockable joint placed at i-th subsequent pair of rotational DOFs and N_{Jc} is the number of candidate locations of the lockable joints. Subsequently, depending on the control objectives, N_k rows of $\mathbf{G}$ (corresponding to the N_k joints to be placed) are selected either based on the highest sum of their elements (analogous to the control metric G_1), or based on the highest product of their elements (analogous to the control metric G_2). In the later case weights β_p do not affect the selected locations.

3.4. Semi-active control – potential applications

As noted in [12], determining the control functions $u_k(t)$ that are optimal in the sense of Pontryagin's maximum principle is challenging for the semi-active

structure equipped with lockable joints. It is due to the fact that the costate equations contain negative damping. Hence, integration of the state and costate equations is not stable. However, Pontryagin's principle provided important information that optimal control is of the bang-bang type (fully locked/fully unlocked joint). Thus, previously proposed the PAR strategy represents simplification of the optimal approach (more details in Subsection 1.1.3). The PAR relies solely on strain information in the vicinity of the lockable joints and employs a feedback mechanism that can be visualised as collocated control loops only (see Fig. 3.2), omitting the modal filter. Methodology developed in this thesis additionally employs information about global state of the controlled system that is provided by modal velocities (an additional loop in Fig. 3.2). It allows for explicit formulation of instantaneously optimal control related to the modal energies associated with monitored unlocked vibration modes, as opposed to the PAR strategy which is the heuristic approach.

Derivation of the control law, control algorithm and its implementation in vibration attenuation is discussed in Subsection 3.4.1. Later, the control law is adopted for energy harvesting application by modifying algorithm parameters, as discussed in Subsection 3.4.2. Basic properties of the proposed control strategy are illustrated by three control scenarios employing the two-DOF system in Subsection 3.4.3. It aims to introduce the reader to the control strategy prior to the discussion of extensive numerical and experimental studies presented in the next two chapters.

3.4.1. Implementation for vibration suppression

Objective function and instantaneous optimality

Regarding Eqs. (2.72) and (2.73), the amount of the energy transferred to the higher-order unlocked vibration modes by operation of the lockable joints is equal to the energy transferred out from the monitored unlocked vibration modes. Hence, transferring the mechanical energy to the higher-order unlocked vibration modes is equivalent to pursuing energy transfer out from monitored unlocked modes only. Thus, in the case of the vibration attenuation, the Lyapunov function $V(t)$ is defined as the weighted sum of energies associated with monitored unlocked vibration modes:

$$V(t) = \sum_{p=1}^{N_p} \alpha_p E_p(t), \tag{3.31}$$

where α_p are weights that pursue priority in damping of particular vibration modes. In this subsection it is shown that instantaneous minimisation of $V(t)$ causes transfer of the energy to the higher-order unlocked vibration modes.

The selection of weights α_p is crucial for operation of the control algorithm. Since the lower-order unlocked modes usually are characterised by the lower inherent material damping and have the biggest participation in the structural motion, their energy should be transferred out into the higher-order modes with priority decreasing with the order of the monitored mode, e.g.:

$$\alpha_p = \frac{1}{\omega^{(p)2}}. \tag{3.32}$$

The control signals $\mathbf{u}(t)$ are sought aiming at providing the steepest descent of $V(t)$ at each time instant t. It can be formally written as the instantaneous optimisation problem:

$$\begin{aligned} &\text{for current } t \text{ find} && \mathbf{u}(t) \in \{0,1\}^{N_k} \\ &\text{to minimise} && \dot{V}(t). \end{aligned} \tag{3.33}$$

The optimisation problem above is formulated for the current time instant as opposed to the optimisation problems formulated a certain time interval (e.g. Pontryagin's maximum principle). In other words, the considered optimisation problem does not require variational calculus to be solved. Thus, no constraints in the form of state equations are used here. As shown further, despite the presence of derivatives with respect to time, only the algebraic problem is solved to optimise the control.

From Eq. (2.68) it follows that $\dot{V}(t)$ can be written as

$$\dot{V}(t) = \sum_{p=1}^{N_p} \alpha_p \left(\dot{W}_p(t) + \dot{E}_p^{\text{loss}}(t) + \dot{W}_p^{\text{ext}}(t) \right). \tag{3.34}$$

Only the modal energy transfer rates $\dot{W}_p(t)$ directly depend on control signals. Hence, an equivalent optimisation problem can be solved:

$$\begin{aligned} &\text{for current } t \text{ find} && \mathbf{u}(t) \in \{0,1\}^{N_k} \\ &\text{to minimise} && \dot{V}_W(t), \end{aligned} \tag{3.35}$$

where

$$\dot{V}_W(t) = \sum_{p=1}^{N_p} \alpha_p \dot{W}_p(t). \tag{3.36}$$

Taking into account that the modal energy transfer rate is the sum of the modal energy transfer rates provided by each lockable joint (see: Eqs. (2.69) and (2.76)), the calculations below are valid:

$$\dot{V}_W(t) = \sum_{p=1}^{N_p} \alpha_p \sum_{k=1}^{N_k} \dot{W}_{pk}(t) = \sum_{k=1}^{N_k} \sum_{p=1}^{N_p} \alpha_p \dot{W}_{pk}(t) = \sum_{k=1}^{N_k} \dot{V}_{Wk}(t). \tag{3.37}$$

$\dot{W}_{pk}(t)$ is the modal energy transfer rate to the p-th monitored unlocked vibration mode through the k-th lockable joint and $\dot{V}_{Wk}(t)$ represents the weighted modal energy transfer rate to all monitored vibration modes through the k-th lockable joint. It should be noticed that the negative sign of $\dot{V}_{Wk}(t)$ means the opposite direction of the energy flow, i.e. from the monitored vibration modes to the remaining ones.

It is evident that to minimise $\dot{V}_W(t)$ each k-th component of the sum above can be instantaneously minimised independently of other components, accordingly to earlier considerations that each joint can be controlled independently of the other ones. It is visualised in Fig. 3.2 as local control loops for each lockable joint.

Control law and control algorithm employing measured quantities

Let $\dot{\widehat{V}}_{Wk}(t)$ denote the estimated weighted modal energy transfer rate through the k-th joint after its locking. Then, taking into account the considerations above, the control law for each lockable joint

$$u_k = \begin{cases} 1 & \text{for } \dot{\widehat{V}}_{Wk}(t) < 0 \\ 0 & \text{otherwise} \end{cases} \tag{3.38}$$

is pursued. Regarding considerations in Section 3.1 $\dot{\widehat{V}}_{Wk}(t)$ can be estimated using estimated modal velocities when the k-th joint is currently unlocked or both modal velocities and k-th bending moment when the k-th joint is locked.

In the former case, making analogous calculations as in Eq. (2.77) but using estimated modal velocities and employing weights α_p we receive

$$\dot{\widehat{V}}_{Wk}(t) = -\dot{\widehat{\boldsymbol{\eta}}}_{\mathrm{M}}^{\mathrm{T}}(t)\mathbf{W}_{\alpha}\boldsymbol{\Gamma}_{\mathrm{MM}k}\dot{\widehat{\boldsymbol{\eta}}}_{\mathrm{M}}(t), \tag{3.39}$$

where

$$\mathbf{W}_{\alpha} = \operatorname{diag}\left([\alpha_1 \;\; \alpha_2 \;\; \cdots \;\; \alpha_{N_p}]^{\mathrm{T}}\right). \tag{3.40}$$

In Eq. (3.39), the value of $\dot{\widehat{V}}_{Wk}(t)$ that could occur after eventual sudden lock of the k-th joint is calculated. When it has the positive sign the joint is not locked yet but if $\dot{\widehat{V}}_{Wk}(t)$ changes its sign into a negative value then the joint is suddenly locked (see: Eq. (3.38)). Here, $\dot{\widehat{\boldsymbol{\eta}}}_{\mathrm{M}}$ is sufficient to calculate $\dot{\widehat{V}}_{Wk}(t)$ when the k-th joint is currently unlocked, as discussed in Subsection 3.1.1.

In the later case, i.e. when the joint is currently locked, calculations analogous to Eq. (2.78) but with employed weights α_p are performed on estimated quantities as follows:

$$\dot{\widehat{V}}_{Wk}(t) = \dot{\widehat{\boldsymbol{\eta}}}_{\mathrm{M}}^{\mathrm{T}}(t)\mathbf{W}_{\alpha}\boldsymbol{\Delta}\boldsymbol{\phi}_{\mathrm{M}k}\widehat{f}_k(t). \tag{3.41}$$

Here, the k-th joint is unlocked when the estimated weighted modal energy transfer rate becomes positive, i.e. the direction of the flow of mechanical energies associated with the monitored unlocked vibration modes becomes unprofitable. After the unlock of the k-th joint Eq. (3.39) is used again to check if the k-th joint should be locked.

A possible implementation of the control law is shown in the form of the pseudo code in Algorithm 2. This algorithm fulfils the scheme shown in Fig. 3.2; $\dot{\widehat{\boldsymbol{\eta}}}_{\mathrm{M}}(t)$ carries information about the global state of the structure, whereas iteration steps of the "for" loop correspond with the local collocated feedback loops for each lockable joint.

Algorithm 2 Pseudo code for implementation of the proposed semi-active modal control methodology

Input: selected modes to be monitored $p = 1, 2, \dots N_p$, weighting matrix $\mathbf{W}_\alpha$, modal filter $\mathbf{F}$, t_{unlock} and t_{lock}; calculated $\boldsymbol{\Gamma}_{\mathrm{MM}k}$ and $\boldsymbol{\Delta\phi}_{\mathrm{M}k}$, $k = 1, 2, \dots N_k$.
Measured quantities: velocities at sensor locations $\dot{\mathbf{q}}_{\mathrm{M}}(t)$, strains in vicinity of the lockable joints $\boldsymbol{\varepsilon}_{\mathrm{M}k}(t)$, $k = 1, 2, \dots N_k$.
Output: control signals $u_k(t)$, $k = 1, 2, \dots N_k$ for each lockable joint.

1: $\dot{\widehat{\boldsymbol{\eta}}}_{\mathrm{M}}(t) \leftarrow \mathbf{F}\dot{\mathbf{q}}_{\mathrm{M}}(t)$ ▷ Global feedback loop
2: **for** $k = 1, 2, \dots N_k$ **do** ▷ For each joint (local control loops)
3: $u_k^{\mathrm{prev}} \leftarrow u_k$
4: **if** $u_k(t) == 0$ **then** ▷ Is unlocked?
5: $\dot{\widehat{V}}_{Wk}(t) \leftarrow -\dot{\widehat{\boldsymbol{\eta}}}_{\mathrm{M}}^{\mathrm{T}}(t)\mathbf{W}_\alpha\boldsymbol{\Gamma}_{\mathrm{MM}k}\dot{\widehat{\boldsymbol{\eta}}}_{\mathrm{M}}(t)$
6: **if** $\dot{\widehat{V}}_{Wk}(t) < -\kappa_1$ **then**
7: $u_k(t) \leftarrow 1$ ▷ Lock k-th joint
8: **end if**
9: **else**
10: $\widehat{f}_k(t) \leftarrow -\frac{2EI}{h}\varepsilon_{\mathrm{M}k}(t)$
11: $\dot{\widehat{V}}_{Wk}(t) \leftarrow \dot{\widehat{\boldsymbol{\eta}}}_{\mathrm{M}}^{\mathrm{T}}(t)\mathbf{W}_\alpha\boldsymbol{\Delta\phi}_{\mathrm{M}k}\widehat{f}_k(t)$
12: **if** $\dot{\widehat{V}}_{Wk}(t) \geq \kappa_2$ **then**
13: $u_k(t) \leftarrow 0$ ▷ Unlock k-th joint
14: **end if**
15: **end if**
16: **end for**
17: **if** any($u_k^{\mathrm{prev}} == 1$ and $u_k == 0$) **then** ▷ Any joint unlocked
18: Wait t_{unlock} ▷ Wait until higher-order modes are not mitigated
19: **else if** any($u_k^{\mathrm{prev}} == 0$ and $u_k == 1$) **then** ▷ Any joint locked
20: Wait t_{lock} ▷ Wait until higher-order modes are not mitigated
21: **end if**
22: Return to line no. 1

Thresholds κ_1 and κ_2 (lines no. 6 and 12) that are preselected with the trial-and-error method prevent from redundant switches of the joint states (locking/unlocking) caused by measurement errors. Additionally, after any change in the state of the lockable joint, the algorithm waits for t_{lock} or t_{unlock}, as required for mitigation of the higher-order unlocked vibration modes that could cause the measurement spillover effect and, consequently, lead to redundant joint switches. Usually $t_{\text{unlock}} \geq t_{\text{lock}}$, hence unlocking is checked first (line no. 17). Apart enhancing reliability of the lockable joints, these simple modifications in the control algorithm based on the control law described by Eq. (3.38) significantly improve the control performance. Moreover, κ_1 and κ_2 are selected in such a way that allows to keep the joints locked if the vibration level (and thus possible weighted modal energy transfer rate) is below a certain value. In this situation joint operation is not required. If the structure is excited sufficiently, the joints will be unlocked at the profitable time instant (condition in line no. 12) and start to operate again to mitigate the vibration.

Jerking-preventing properties of the proposed control

The sudden lock of the joint can cause large transient accelerations. Such a behaviour is demonstrated using the two-DOF system in Section 2.1 (see: Fig. 2.8). However, Algorithm 2 implicitly prevents from jerking of the controlled structure.

The joint is to be locked when $\dot{\hat{V}}_{Wk}(t)$ crosses zero or a small threshold as shown in the 6th line of Algorithm 2. By substitution of Eqs. (2.63) and (2.74) into Eq. (3.39) we receive:

$$\dot{\hat{V}}_{Wk}(t) = -\underbrace{\dot{\hat{\boldsymbol{\eta}}}_{\text{M}}^{\text{T}}(t)\mathbf{W}_{\alpha}\overbrace{\boldsymbol{\Delta}\boldsymbol{\phi}_{\text{M}k}c_{\max}\boldsymbol{\Delta}\boldsymbol{\phi}_{\text{M}k}^{\text{T}}}^{\boldsymbol{\Gamma}_{kmn}}\dot{\hat{\boldsymbol{\eta}}}_{\text{M}}(t)}_{\delta_k^{\alpha}(t) \qquad\qquad c_{\max}\Delta\dot{q}_k^{N_p}(t)}, \tag{3.42}$$

where: $\Delta\dot{q}_k^{N_p}(t)$ is the relative velocity between rotational DOFs involved in the k-th lockable joint obtained from the superposition of the monitored modal velocities only, whereas $-c_{\max}\Delta\dot{q}_k^{N_p}(t)$ would be the bending moment transmitted by the k-th lockable joint if this joint is suddenly locked, and $\delta_k^{\alpha}(t)$ is a function of the monitored modal velocities (if all $\alpha_p = 1$ then $\delta_k^{\alpha}(t) = \Delta\dot{q}_k^{N_p}(t)$). As the higher-order unlocked vibration modes are naturally mitigated when the joints are in the unlocked state, one can assume that $\Delta\dot{q}_k^{N_p}(t) \approx \mathbf{l}_k^{\text{T}}\dot{\mathbf{q}}(t) = \dot{q}_i(t) - \dot{q}_j(t)$, $t \in (t_{\text{u}}, t_{\text{l}}]$. Thus, from the equation above it follows that Algorithm 2 locks the k-th joint only when the relative rotational velocity between adjacent beam ends $\dot{q}_i(t) - \dot{q}_j(t)$ or the term $\delta_k^{\alpha}(t)$ crosses zero (or is close to zero when $\kappa_1 \neq 0$ is selected in Algorithm 2). Passing zero by the function $\delta_k^{\alpha}(t)$ simultaneously when

$\dot{q}_i(t)$ and $\dot{q}_j(t)$ are significantly different is not expected during normal operation of the algorithm – the explanation is shown in Subsection 3.4.3. The property of locking joints only when $\dot{q}_i(t) \approx \dot{q}_j(t)$ avoids harmful transient accelerations, which are demonstrated using the two-DOF system in Fig. 2.8. It significantly reduces jerking of the structure and slipping of the frictional parts in the joints, resulting in enhanced reliability and durability of the system.

3.4.2. Implementation for energy harvesting

Objective function

In the application of the proposed control methodology for energy harvesting, the goal is to transfer the mechanical energy to the selected vibration mode r, to which the energy harvester is tuned. Thus, in the simplest case one could pursue the condition that the r-th modal energy transfer rate must be non-negative:

$$\dot{W}_r(t) \geq 0. \tag{3.43}$$

Then, the function $V(t)$ to be minimised is written with the negative sign of the modal energy:

$$V(t) = -E_r(t). \tag{3.44}$$

The above objective function cannot be called the Lyapunov function because now it is not positive. Moreover, the energy associated with the targeted vibration mode is to be maximised instead of its minimisation. However, the control cannot destabilise the controlled structure in free vibration, as described in Subsection 2.2.4, on page 89; the p-th modal energy can increase only at the expense of the remaining modal energies.

Adaptation of the objective function and control algorithm for energy harvesting application

The condition in (3.44) based only on the selected vibration mode is theoretically sufficient to formulate the control law. $\dot{W}_r(t)$ depends on the targeted modal velocity and other monitored modal velocities or bending moments, analogously to Eq. (2.69). However, in practice, this may be insufficient to ensure the efficient energy flow to the targeted vibration mode. Hence, conditions pursued also on the remaining monitored vibration modes, from which energy is to be transferred out, also are employed. It results in the methodology described in the previous subsection but with different weighting parameters in the matrix $\mathbf{W}_\alpha$. In this case, the weight corresponding to the selected vibration mode is negative:

$$\mathbf{W}_\alpha = \operatorname{diag}\left(\begin{bmatrix}\alpha_1 & \cdots & \alpha_r & \cdots & \alpha_{N_p}\end{bmatrix}^{\mathrm{T}}\right), \quad \alpha_r < 0, \quad \text{all } \alpha_p \geq 0. \tag{3.45}$$

Here, the control can be realised as shown in Algorithm 2 with the weighting matrix as in Eq. (3.45).

The modified weighting matrix $\mathbf{W}_\alpha$ does not change the jerk-limiting properties of the control algorithm. Equation (3.42) is still valid.

3.4.3. Illustrative example of control of the system with two degrees of freedom

In this subsection, several control scenarios of the two-DOF system, that is described in detail in Section 2.1, are discussed. Apart from the negligible amount of damping provided by the utilised model of the lockable joint the system is undamped. Equations of motion are integrated with the zero-order hold method (see: Eq. (2.45) in Subsection 2.2.2). The integration step $\Delta t = 0.1$ ms is selected. It is assumed that the full state of the system is known in all considered control scenarios. Thus, all unlocked vibration modes are monitored: $N_p = N_\mathrm{d} = 2$. As all the unlocked vibration modes are available for the control algorithm, both forms of the estimated weighted modal energy transfer rate (Eqs. (3.39) and (3.41) or lines 5 and 11 in Algorithm 2, respectively) are equivalent according to Eq. (2.69). Moreover, the estimated weighted modal energy transfer rate $\hat{\dot{V}}_W(t)$ is equal to its exact value $\dot{V}_W(t)$; κ_1, κ_2, t_lock and t_unlock are selected as equal to zero.

Modal energy transfer to the first unlocked vibration mode

The first considered scenario is free vibration with the initial condition: $\mathbf{q}_0 = 0.02\,\boldsymbol{\phi}^{(2)}$ and $\dot{\mathbf{q}}_0 = \mathbf{0}$. This means that the two-DOF system has potential energy in the second mode, which is released in free vibrations. The aim of the control is to transfer this energy to the first, targeted, unlocked vibration mode by locking and unlocking the joint in suitable time instances. To this end, the following weights are selected: $\alpha_1 = -1$ and $\alpha_2 = 0$ (see: Eq. (3.45)). By pursuing only one non-zero weight α_1 the minimised weighted modal energy transfer rate has the following form:

$$\dot{V}_W(t) = -\dot{\eta}_1(t)\alpha_1 \begin{bmatrix}\gamma_{11} & \gamma_{12}\end{bmatrix} \begin{bmatrix}\dot{\eta}_1(t) \\ \dot{\eta}_2(t)\end{bmatrix} = \dot{\eta}_1(t)\alpha_1 \Delta\phi^{(1)} f(t). \tag{3.46}$$

Results are shown in Fig. 3.3. It is evident that the locking effect of the joint causes modal coupling resulting in the energy flow between unlocked vibration modes (compare Figs. 3.3a and d). Due to the proposed control algorithm, the joint is locked when the modal energy transfer has the profitable direction, whereas it is unlocked when the sign of the modal energy transfer rate changes. It allows for monotonic change of the modal energies as opposed to results shown in Fig. 2.9d, where the joint once permanently locked allows only for repetitive and alternate energy transfer between the unlocked vibration modes.

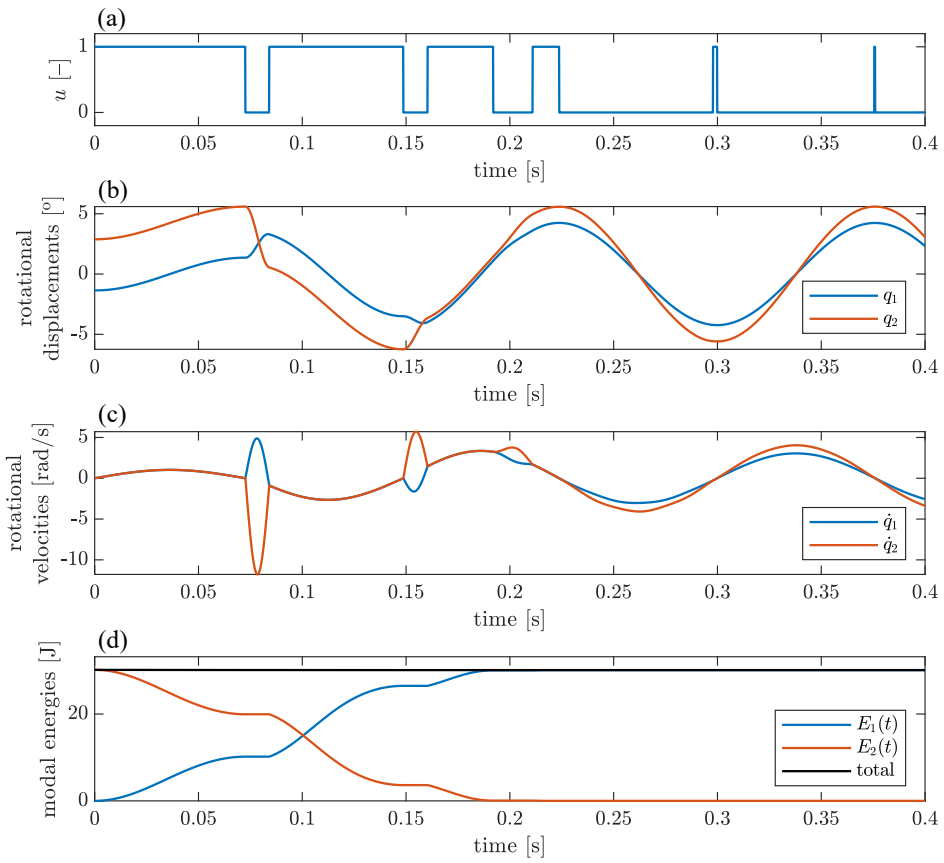

Fig. 3.3. Energy transfer from the second unlocked mode (initial, $\alpha_2 = 0$) of the two-DOF system to the first one (targeted, $\alpha_1 = -1$); time histories of: (a) control signal, (b) rotational displacements, (c) rotational velocities and (d) participation of the modal energies in mechanical energy of the system.

It is also evident that the algorithm locks the joint when rotational velocities have the same value (Fig. 3.3c). Thus, there is no energy loss in the lockable joint resulting from the ideally inelastic collision (compare with Figs. 2.8b and d), as mentioned at the end of Subsection 3.4.1.

It is worth to notice that the most of the mechanical energy is transferred to vibration in the first unlocked mode after two cycles (locking and unlocking) of the joint (Fig. 3.3d). It demonstrates the performance of the proposed control strategy.

Figure 3.4 provides a clearer understanding of the energy transfer phenomenon. The locking effect resulting in a quasi-constant Δq (quasi-constant due to the relaxed kinematic constraint) is especially visible in the time history of the second modal coordinate in Fig. 3.4b (compare with Fig. 3.3b).

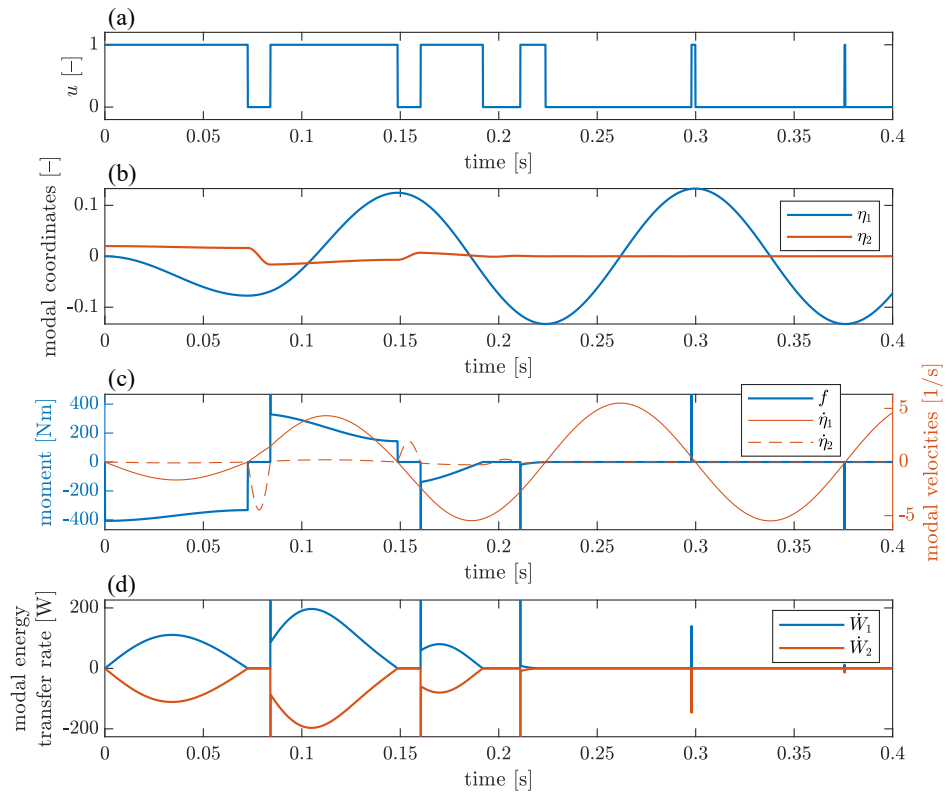

Fig. 3.4. Energy transfer from the second unlocked mode (initial, $\alpha_2 = 0$) of the two-DOF system to the first one (targeted, $\alpha_1 = -1$); time histories of: (a) control signal, (b) modal coordinates, (c) bending moment transmitted via lockable joint along with modal velocities (d) modal energy transfer rates for both unlocked vibration modes.

Figure 3.4c shows all "measured" quantities required for calculation of $\dot{V}_W(t)$ (see: Eq. (3.46)), whereas modal energy transfer rates to each particular vibration mode (see: Eq. (2.69)) also are shown in Fig. 3.4d. It is evident that $\dot{W}_1(t) \approx -\dot{W}_2(t) \geq 0$ (if $c_{\max}$ approaches infinity then $\dot{W}_1(t) = -\dot{W}_2(t)$ would be satisfied) analogously to Eqs. (2.72) and (2.73) despite the fact that only α_1 is selected nonzero.

Peak-like transient states, visible in Figs. (3.4)c and d, are the numerical side-effect of the selected step size in the numerical integration. The numerical procedure cannot perfectly hit the point where $\dot{q}_1(t) = \dot{q}_2(t)$. This effect can be reduced by changing the step size towards smaller values. However, step sizes smaller than currently selected do not affect remaining parts of time histories.

Results shown in Fig. 3.4c allow for better understanding why the control algorithm locks the joints when $\dot{q}_1(t) \approx \dot{q}_2(t)$. First, using an analogous derivation

as in Eq. (3.42) the weighted modal energy transfer rate for the two-DOF system in Eq. (3.46) can be rewritten into the form:

$$\dot{V}_W(t) = -\dot{\eta}_1(t)\alpha_1 c_{\max}\Delta\phi^{(1)} \underbrace{\left[\Delta\phi^{(1)} \;\; \Delta\phi^{(2)}\right]\begin{bmatrix}\dot{\eta}_1(t)\\ \dot{\eta}_2(t)\end{bmatrix}}_{\dot{q}_1(t)-\dot{q}_2(t)}. \tag{3.47}$$

The algorithm locks or unlocks the joint when the term above changes its sign. It takes place only when the targeted modal velocity $\dot{\eta}_1(t)$ or relative rotational velocity between rotational DOFs $\dot{q}_1(t) - \dot{q}_2(t)$ crosses zero. By comparing Figs. 3.3c and 3.4c one can see that only the former case occurs. The first case is possible but is not expected when the first modal velocity that corresponds to the nonzero weight participates significantly in the structural motion.

Step-like increments and decrements of the transmitted bending moment $f(t)$ result from the fact that the two-DOF system consists of two ideally rigid rods that are connected via rotational spring in parallel with the lockable joint (Fig. 2.2). If the joint is locked at the time instance when $\Delta q \neq 0$ then the moment $f(t)$ not only balances the inertia forces in the system but also the moment provided by the second rotational spring. This results in piece-wise constant components of the time history of $f(t)$, whereas the varying components relate to balancing the inertia forces. In the next chapter the transmitted bending moments represented by measured strains have not step-like character due to the fact that the considered structures do not contain any rotational spring connected in parallel to the lockable joint.

Modal energy transfer to the second unlocked vibration mode

Regarding the transfer of the energy in the opposite direction, i.e. from the first unlocked vibration mode to the second one, it is allowable to pursue weights: $\alpha_1 = 0$ and $\alpha_2 = -1$. It provides efficient energy flow analogously to the case described above. However, to show that it is possible to transfer the energy between two unlocked vibration modes in both directions by changing the sign of only the first weight, the following weights are selected: $\alpha_1 = 1$ and $\alpha_2 = 0$. In result, Eq. (3.46) refers also to current selection of weights. Other parameters of the algorithm remain unchanged. The two-DOF system vibrates freely, where initial conditions are: $\mathbf{q}_0 = 0.1\,\boldsymbol{\phi}^{(1)}$ and $\dot{\mathbf{q}}_0 = \mathbf{0}$. Results for this case are shown in Fig. 3.5.

It is evident that energy transfer from the first unlocked vibration mode to the second one is efficient until the third unlock of the joint (closely before $t = 0.2$ s). Within this time almost whole mechanical energy initially accumulated in the first unlocked vibration mode is transferred out from this mode (accordingly to $\alpha_1 > 0$) and directed to the second unlocked vibration mode.

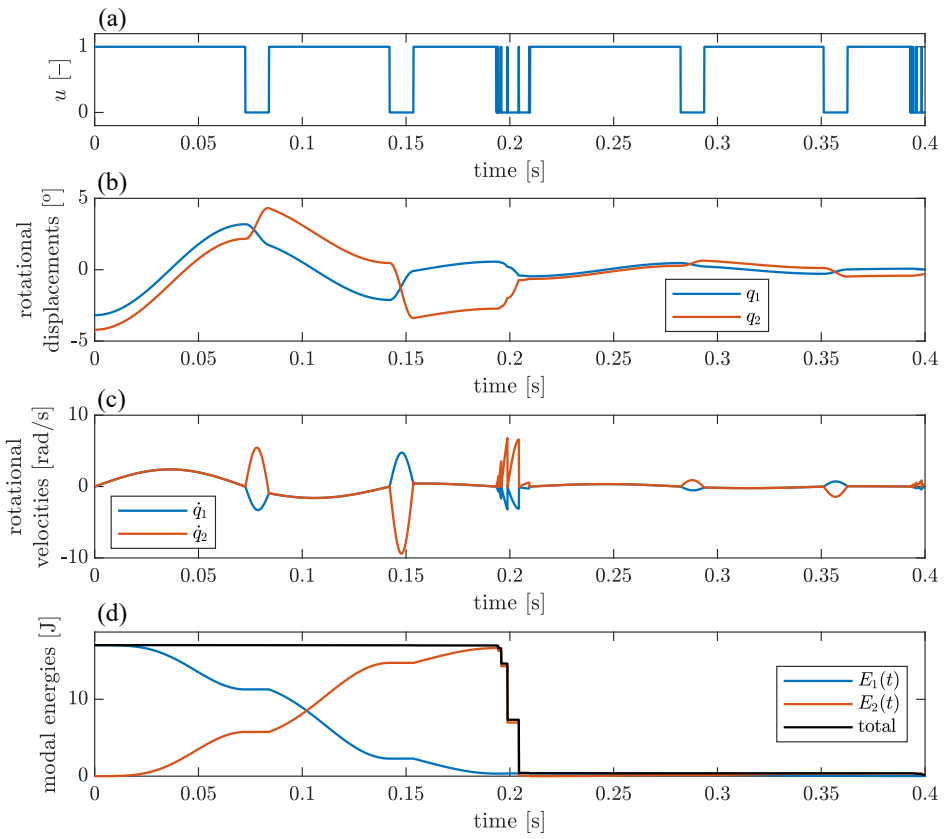

Fig. 3.5. Energy transfer from the first unlocked mode (initial, $\alpha_1 = 1$) of the two-DOF system to the second one (targeted, $\alpha_2 = 0$); time histories of: (a) control signal, (b) rotational displacements, (c) rotational velocities and (d) participation of the modal energies in mechanical energy of the system.

After the third joint unlock the control algorithm locks the joint at time instances when the structural members have significantly different rotational velocities (Fig. 3.5c). It results in the energy loss (Fig. 3.5d) in inelastic collisions at the lockable joint. This problem arises because the unlocked vibration mode related to weight α_1 participate negligibly in the structural motion when the most of its energy is transferred out to the second unlocked vibration mode that then becomes predominant. Hence, it is highly probable that the first modal velocity crosses zero $\dot{\eta}_1(t) = 0$ when $\dot{\eta}_2(t)$ is significantly different from zero. It results in the change of sign of $\dot{V}_W(t)$ when $\dot{q}_1(t) \neq \dot{q}_2(t)$. This phenomenon is visible in Fig. 3.6b (compare with Fig. 3.5c). Such a situation does not occur in the previous control scenario (transfer to the first unlocked mode) because the nonzero weight is assigned to the targeted mode that is becomes predominant, as opposed to the present control scenario (Figs. 3.4b and c).

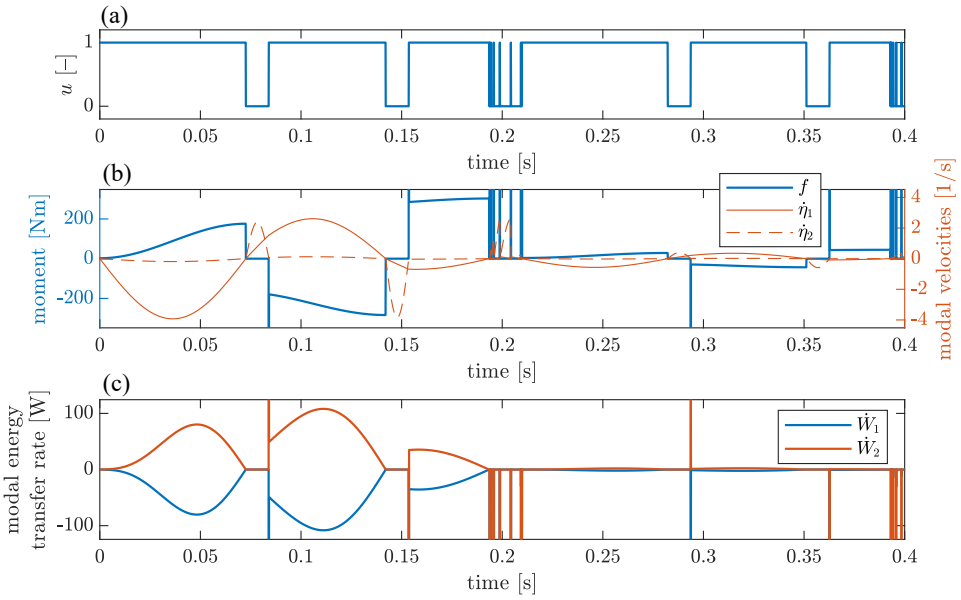

Fig. 3.6. Energy transfer from the first unlocked mode (initial, $\alpha_1 = 1$) of the two-DOF system to the second one (targeted, $\alpha_2 = 0$); time histories of: (a) control signal, (b) bending moment transmitted via lockable joint along with modal velocities and (c) modal energy transfer rates for both unlocked vibration modes.

When a significant amount of the energy is dissipated in the inelastic collisions, as shown in Fig. 3.5d, the modal energy transfer rates can be unbalanced (their sum differs from zero), as shown in Fig. 3.6d. The reason is that constraint in Eq. (2.40) is not satisfied during these collisions. It turns out that Eqs. (2.71)–(2.73), describing the balance of the modal energy transfer, also are not fulfilled.

The locking of the joint when $\dot{q}_1(t) \neq \dot{q}_2(t)$ can be overcome in several ways. The first is setting parameters κ_1, κ_2, t_{lock} and t_{unlock} different from zero, e.g. with the trial-and-error method. Also assigning the both weights nonzero, e.g. $\alpha_1 = 1$ and $\alpha_2 = -1$ allows for avoiding locking the joint when $\dot{q}_1(t) \neq \dot{q}_2(t)$, as shown in Fig. 3.7.

The problem of locking the joint when $\dot{q}_1(t) \neq \dot{q}_2(t)$ does not occur in MDOF structures when the control aims at vibration damping. In this case, similarly to the above considerations, the vibration energy is transferred out from the monitored lower-order unlocked vibration modes (that have nonzero weights) into the remaining, higher-order ones that are not monitored. However, due to the efficiency of the damping mechanism the high-frequency vibrations vanish after each joint unlock within the time usually shorter than preselected time interval t_{unlock} (see: line 18 in Algorithm 2). Thus, even if monitored modal velocities

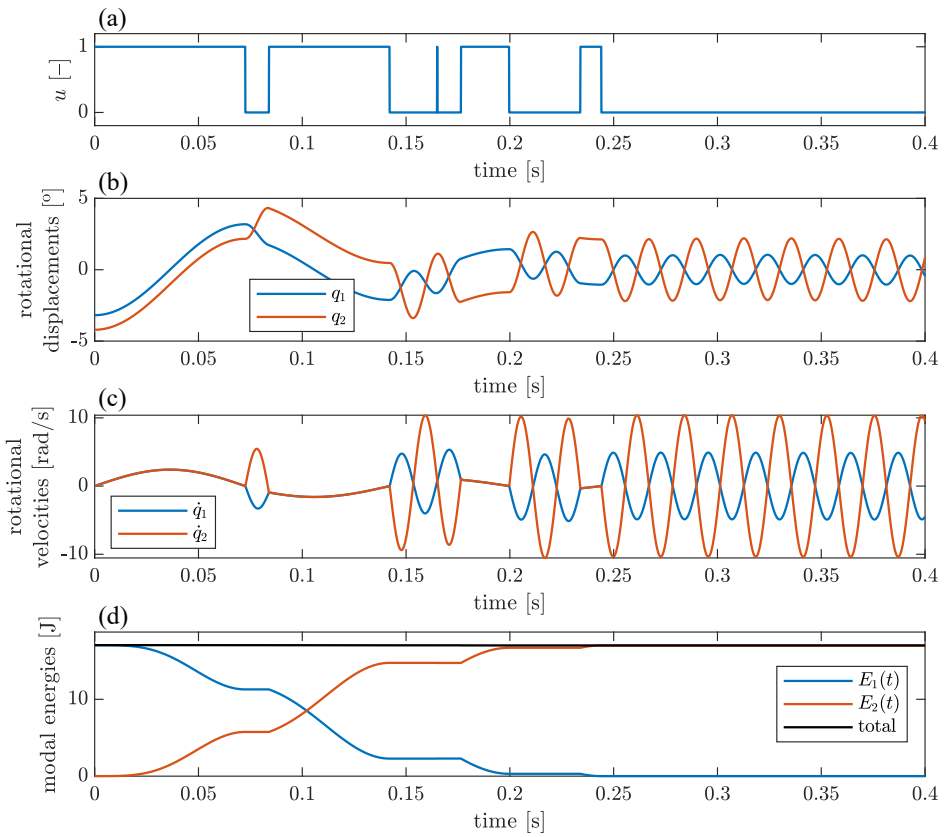

Fig. 3.7. Energy transfer from the first unlocked mode (initial, $\alpha_1 = 1$) of the two-DOF system to the second one (targeted, $\alpha_2 = -1$); time histories of: (a) control signal, (b) rotational displacements, (c) rotational velocities and (d) participation of the modal energies in mechanical energy of the system.

tend to zero in the vibration mitigation process the unmonitored modes do not affect the control, as demonstrated in Section 4.1.

4. Numerical study

The potential of the proposed methodology both in vibration attenuation and energy harvesting is illustrated in this chapter on various types of excitation. Section 4.1 compares performance of the proposed control in vibration damping with PAR for various placements of the lockable joints. Efficacy of the proposed control methodology in enhancing of the energy harvesting for two configurations of relatively smaller structure with attached EMEH is tested in Section 4.2. In all tests the full state of the controlled structure is not known. Instead, measurement data as described in Section 3.1 are employed for control algorithms proposed in Section 3.4. Methods for sensor and lockable joint placement (see: Sections 3.2 and 3.3) ensuring efficient operation of the control algorithm have also been adopted.

4.1. Vibration attenuation

For comparison purposes PAR control strategy, which is known as one providing efficient vibration damping by means of the lockable joints, is employed as a benchmark. This is described below. In the following subsections, both the proposed and PAR strategies are tested and compared on an eight-bay frame structure equipped with a single pair of lockable joints placed at two selected locations. In one case the pair of the lockable joints is placed optimally, demonstrating potential performance of both compared methods (Subsection 4.1.2). In the next case the placement of the lockable joints is non-optimal allowing assessment of the robustness of the vibration control approaches (Subsection 4.1.3). In both cases, the structure is subjected to various excitations.

4.1.1. Prestress accumulation–release (PAR) as a benchmark

In PAR control only strains $\boldsymbol{\varepsilon}_{\mathrm{M}}(t)$ are measured, as described in Subsection 3.1. Here, the lockable joints are kept mainly in the locked state. During the motion of the structure the measured strains $\boldsymbol{\varepsilon}_{\mathrm{M}}(t)$ increase which corresponds to an increase in potential energy. Some part of this energy is accumulated in the higher-order unlocked vibration modes. When the strains reach their maximum values the joints are unlocked for a short moment t_{unlock}. Then, strain energy is released in free vibration of higher-order unlocked vibration modes

and quickly dissipated in material damping. Simultaneously, strains are relaxed. After re-locking of the joints the whole procedure is repeated.

The k-th joint is unlocked if the condition below is satisfied.

$$\frac{\varepsilon^2_{\mathrm{M}k}(t) - \varepsilon^2_{\mathrm{M}k}(t-\Delta t)}{\Delta t} < -\kappa_\varepsilon, \tag{4.1}$$

Δt is an integration step or sampling period and κ_ε is the selected threshold; $\varepsilon^2_{\mathrm{M}k}(t)$ is assumed to be near-proportional to the strain energy accumulated in the higher-order unlocked vibration modes and the left hand side of Eq. (4.1) represents its derivative.

4.1.2. Eight-bay smart structure equipped with two optimally placed lockable joints

The considered frame structure that is to be controlled is shown in the scheme in Fig. 4.1a. Characteristic dimensions and physical properties are listed in Table 4.1. The FE model of the structure is shown in Fig. 4.1b. The structure is discretized with one beam-type FE per each bay side (24 FEs in total). FEs are based on the Euler–Bernoulli beam theory and have cubic shape functions. The beams are assumed to be non-extensible due to the fact that longitudinal vibration usually have a significantly smaller participation than transversal vibration of the beams for the structure of such dimensions. The FE model has $N_\mathrm{d} = 26$ DOFs. The viscous damping coefficient $c_{\max} = 3 \cdot 10^4$ Nms/rad has been selected for simulation of the locking effect.

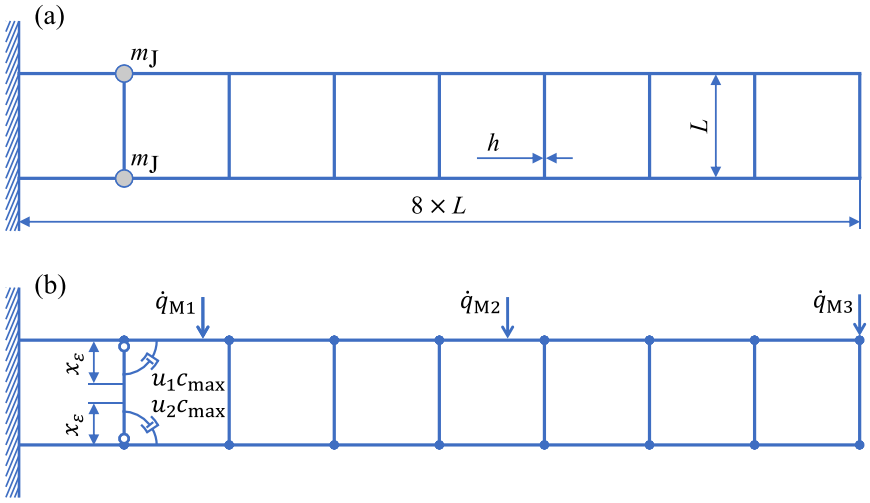

Fig. 4.1. Eight-bay structure equipped with two lockable joints: (a) scheme of the structure and (b) FE model with indicated sensor locations [144].

Table 4.1. Dimensions and properties of the eight-bay structure.

Quantity	Symbol	Unit	Value
Bay side length	L	mm	600
Offset of the strain gauges	x_ε	mm	50
Young modulus	E	Pa	$210 \cdot 10^9$
Material density	ρ	kg/m^3	7860
Cross-section: height × width	$h \times b$	mm	8×10
Mass of the lockable joint	m_J	kg	1.2

The first three unlocked vibration modes of the structure are selected to be monitored. The unlocked mode shapes are considered for the design of the controller. They are shown in Fig. 4.2 along with vibration modes obtained for the joints in the locked state.

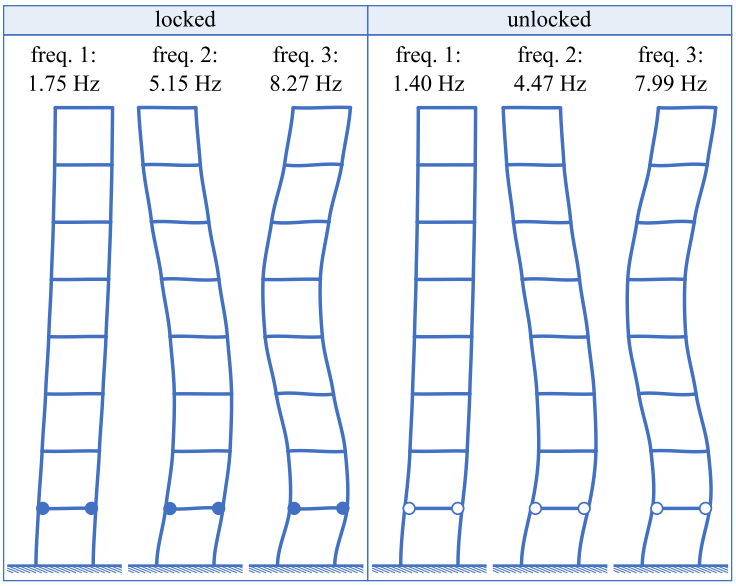

Fig. 4.2. First three vibration modes for both locked and unlocked lockable joints.

Three sensor locations for modal filtering (Fig. 4.1b) are selected using Algorithm 1 in Section 3.2. Measured strains at the distance x_ε from the joint axes are simulated from structural displacements with known shape functions of the FEs and dimensions of the beam cross-section.

Optimal locations of the lockable joints, visible in Fig. 4.1, have been selected according to the highest controllability metric G defined as in Eq. (3.29), where weights β_p are selected as the reciprocals to the natural frequencies. Figure 4.3 shows mode controllability metrics for each transversal beam potentially

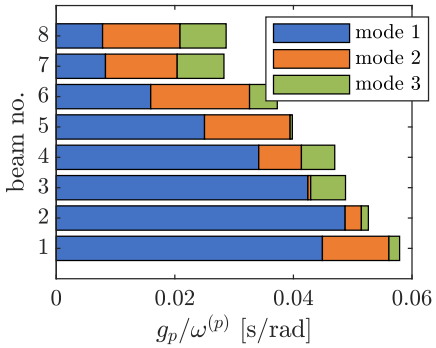

Fig. 4.3. Controllability metrics of the monitored unlocked vibration modes for particular locations of the pair of the lockable joints.

equipped with lockable joints (including the selected one). For each beam that could be equipped with the lockable joints the mode shapes and natural frequencies are obtained and then Eq. (3.29) is evaluated, since mass of the lockable joints in different locations affects dynamics of the structure.

Proportional material damping $\mathbf{C} = \alpha\mathbf{\Phi}^{\mathrm{T}}\mathbf{M}\mathbf{\Phi} + \gamma\mathbf{\Phi}^{\mathrm{T}}\mathbf{K}\mathbf{\Phi}$ is frequently used due to the property of keeping modes uncoupled. However, it is difficult to assign the suitable damping level both for lower-order modes and the higher-order ones using this model. Hence, model combining classical proportional material damping and equal modal damping is used according to the equation below:

$$\operatorname{diag}(2\omega^{(m)}\zeta^{(m)}) = \mathbf{\Phi}^{\mathrm{T}}\mathbf{C}\mathbf{\Phi} = \underbrace{\alpha\mathbf{I}}_{\alpha\mathbf{\Phi}^{\mathrm{T}}\mathbf{M}\mathbf{\Phi}} + \beta\mathbf{\Omega} + \underbrace{\gamma\mathbf{\Omega}^2}_{\gamma\mathbf{\Phi}^{\mathrm{T}}\mathbf{K}\mathbf{\Phi}} . \tag{4.2}$$

In this study $\alpha = 0$, $\beta = 0.015$ and $\gamma = 5.7278 \cdot 10^{-4}$ that results in modal damping ratios $\zeta^{(1)} = 1\,\%$, $\zeta^{(2)} = 1.55\,\%$, and $\zeta^{(3)} = 2.19\,\%$. The relation between modal damping ratios and natural frequencies is shown in Fig. 4.4.

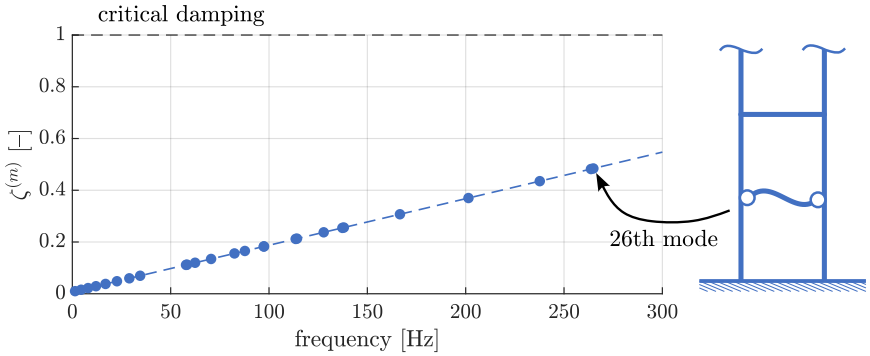

Fig. 4.4. Modal damping factors in dependence on the natural frequencies of the structure.

The structure described above is used to assess the proposed control methodology and compare it with PAR in three cases of excitation:

case 1: free vibration caused by a sudden stop of the support motion,

case 2: harmonic force excitation and

case 3: kinematic noise excitation.

In all cases of excitation of the structure with optimally placed lockable joints the following parameters are selected to be used with Algorithm 2: $\alpha_p = 1/\omega^{(p)2}$, $t_{\text{lock}} = t_{\text{unlock}} = 12$ ms, $\kappa_1 = 0.03$ W and $\kappa_2 = 0.0005$ W. Remaining required parameters are calculated from modal data and structural dimensions. The parameter $\kappa_\varepsilon = 30$ and the same time interval $t_{\text{unlock}} = 12$ ms for the PAR method are selected. Equations of motion are rewritten into the state equations and integrated as shown in Eq. (2.45) with a time step $\Delta t = 1$ ms.

Case 1

In this case, a sudden halt of the structural support is considered, while prior to this event, the support and the structure were undergoing transverse motion. This kind of excitation can represent operation of many flexible mechanical systems, especially deployment of light-weight space structures, which also are within the range of the potential control applications. The initial condition on velocities

$$\dot{\mathbf{q}}_0 = -\mathbf{l}_{\text{x}} v_0, \tag{4.3}$$

where $\mathbf{l}_{\text{x}}$ is a Boolean vector selecting DOFs representing horizontal displacements and v_0 is the support velocity before the sudden stop, is applied; $v_0 = 0.5$ m/s is selected. Results of simulation with the proposed modal control are shown in Fig. 4.5.

Lockable joints are controlled symmetrically (Fig. 4.5a) due to the fact that unlocked mode shapes have the same relative opening angles between beams connected via left and right lockable joints (see: Fig. 4.2, "unlocked") and the fact that measured strains are also symmetric for this kind of excitation (Fig. 4.5c).

It is evident that when joints become locked ($u_k = 1$) modal energies of the monitored unlocked modes change their value due to the introduced modal coupling (Fig. 4.5b). Two following observations should be noticed. First, their energy is transferred to the higher-order unlocked vibration modes. The measured strains are then increasing, as shown in Fig. 4.5c. It confirms that the higher-order unlocked vibration modes accumulate mainly the potential energy. When the total energy of the higher-order unlocked vibration modes has a significant value (but not necessary in the maximum), the joints are unlocked and the strain energy is released into free vibration of the structure in the higher-order unlocked vibration modes. Significant damping coefficients of these modes and their high frequencies cause quick dissipation of their energy and a sudden decrease in the measured strains. The second observation is that energy is

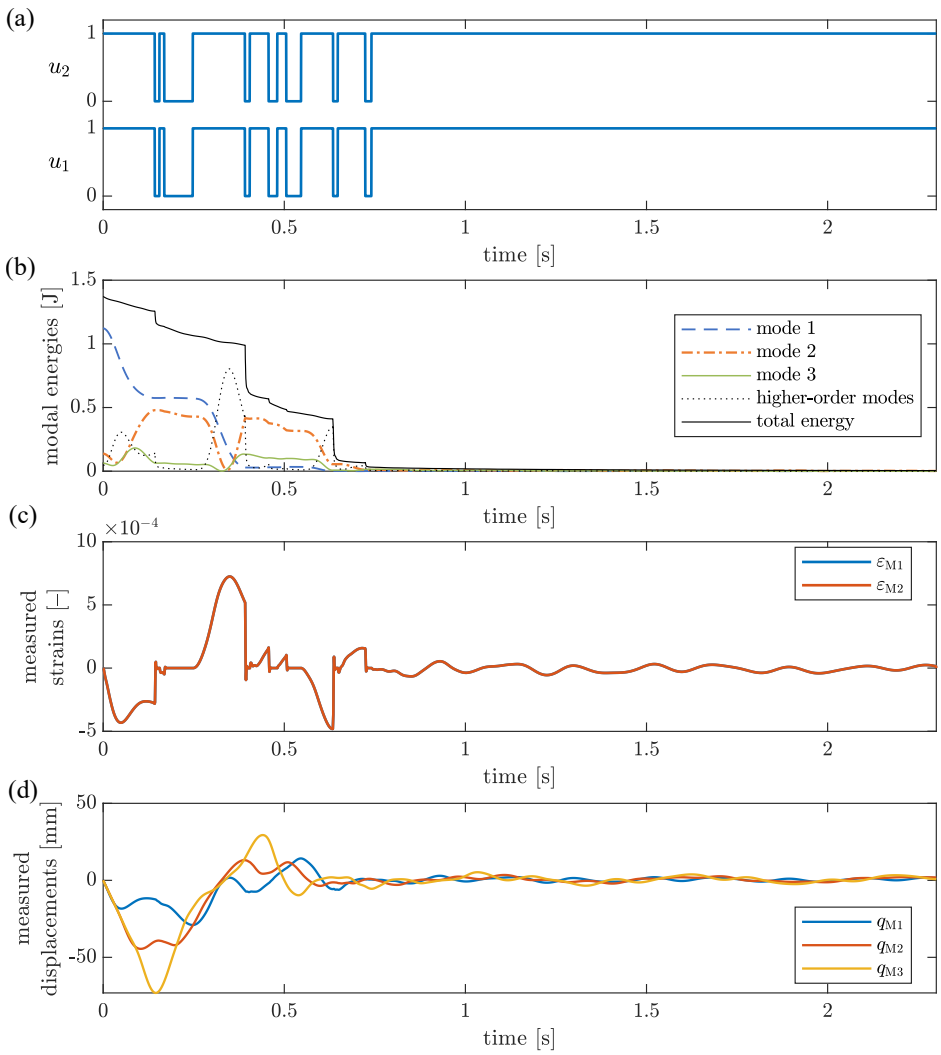

Fig. 4.5. Time histories of: (a) control signals, (b) modal energies of the structure, (c) measured strains and (d) structural displacements at sensor locations for case 1 of excitation and modal control approach.

also transferred within monitored unlocked vibration modes from lower-order to higher-order ones (e.g. from the first to the second one) due to the weights α_p decreasing with the mode order. Thus, it is evident that weights α_p allow for imposing the priority of particular vibration modes to be damped.

It is worth to notice that quick decrements of the structural energy occur only after the joint unlock due to the mechanism described above. There is no any significant loss of the kinetic energy during the joint lock, since the control algorithm locks the joints when rotational velocities of the adjacent beam ends

are equal or very close, as commented in Subsection 3.4.1 (see: comments to Eq. (3.42)). Hence, jerking of the structure during locking the joint is avoided.

Due to the selected weights α_p pursuing the highest priority of damping of the lowest-order unlocked vibration mode (according to the comments to Eq. (3.32)), effective mitigation of a structural response has been obtained, as shown in Fig. 4.5d. Finally, such a selection of the weights results in fewer switches of the lockable joints due to the lower natural frequencies of lower-order unlocked vibration modes.

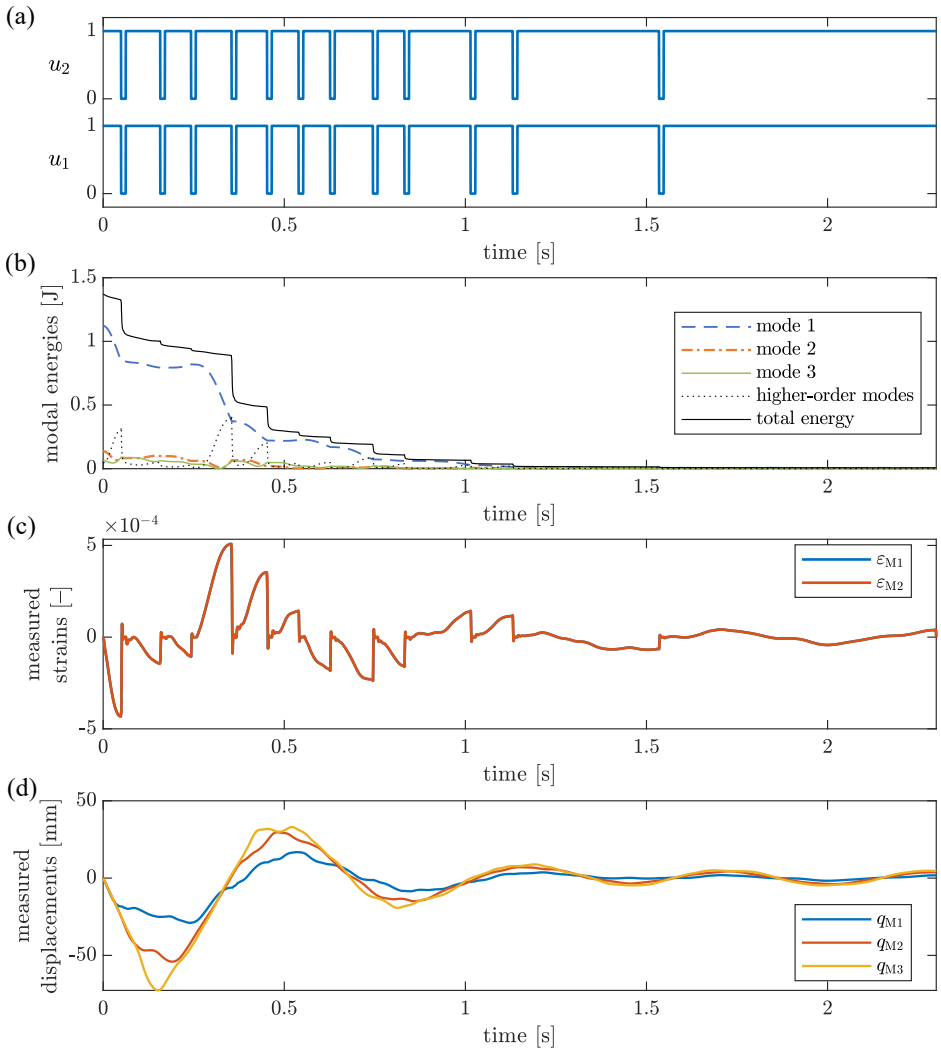

Fig. 4.6. Time histories of: (a) control signals, (b) modal energies of the structure, (c) measured strains and (d) structural displacements at sensor locations for case 1 of excitation and PAR control approach.

Analogous results for PAR control strategy are shown in Fig. 4.6. Here, a response of the lockable joints is also symmetric due to symmetrically measured strains (Figs. 4.6a and c).

Despite the fact that the control law is not based explicitly on the energy transfer phenomenon, PAR control also causes energy flow between unlocked vibration modes due to the modal coupling effect introduced by the lockable joints (Fig. 4.6b). However, PAR algorithm unlocks the joints in each local extreme of measured strains. As opposed to the modal approach, the PAR algorithm does not use information about the global state of the structure in the form of modal velocities as well as does not use any weights assigned to particular unlocked vibration modes. It makes the PAR approach simpler but also more sensitive to local strain maxima resulting in a greater number of redundant joint unlocks. Additionally, due to the predominant participation of the first unlocked vibration mode in the overall vibration mitigation process, the displacements are greater in the PAR approach despite a similar total energy level.

Comparison of the modal and PAR approaches is shown in Fig. 4.7 and in Table 4.2. The quantities in Table 4.2 are: RMS($q_{\mathrm{M}s}$) – root-mean-square value of the displacement, $\overline{E}$ – mean structural energy and n_{J} – total number of switches of both lockable joints.

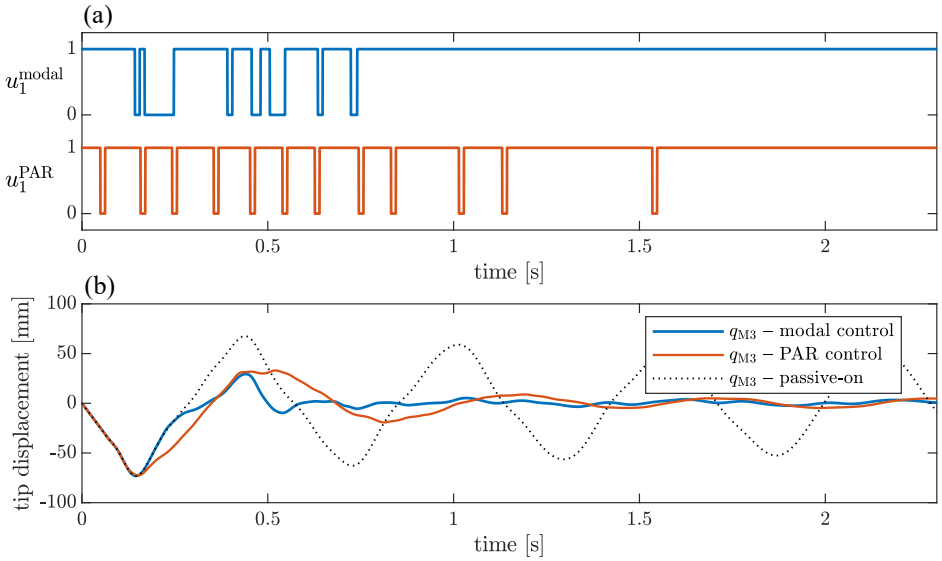

Fig. 4.7. Comparison of modal and PAR control strategies for excitation case 1: (a) control signals and (b) structural tip displacements accompanied with the structure with locked joints.

It is evident that both methods compared effectively mitigate the vibration (Fig. 4.7b). The modal control achieves slightly greater mean energy of the structure (Table 4.2), but displacement RMSes are significantly lower. It confirms

Table 4.2. Comparison of various metrics of the control performance for modal and PAR approaches, and passively locked joints for the excitation case 1.

Control type	RMS(q_{M1}) [mm]	RMS(q_{M2}) [mm]	RMS(q_{M3}) [mm]	$\overline{E}$ [J]	n_J [–]
Modal	7.36	12.51	16.13	0.260	28
PAR	9.53	17.07	20.47	0.227	48
Passive-on	11.54	29.59	38.54	0.896	0

that additional insight into the structural state in the form of modal velocities and assigning the higher weights α_p to the lower-order unlocked vibration modes allows for better reduction of the low-frequency oscillations that usually are characterised by the biggest displacements. Moreover, due to these additional information used by the modal control it requires near two times less joint switches to mitigate vibration than the PAR approach.

Case 2

In this case harmonic force excitation

$$f_{\text{exc}}(t) = A_f \sin \Omega_f t, \tag{4.4}$$

acts on the structure at the point shown in Fig. 4.8. This location allows for excitation of all three monitored unlocked vibration modes (see: Fig. 4.2), since it is not the node of any of these modes.

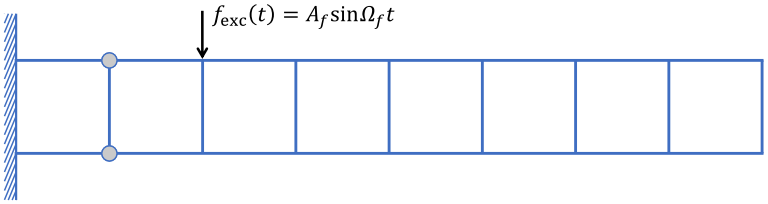

Fig. 4.8. Location of the harmonic force excitation.

In this test the structure controlled with modal and PAR approaches, and with passively locked joints are excited in various excitation frequencies within the range $\Omega_f \in 2\pi[1, 10]$ rad/s. The excitation amplitude $A_f = 4$ N. For each excitation frequency the vibration duration was calculated as

$$T(\Omega_f) = 45 \text{ s} \cdot \widetilde{\omega}^{(1)}/\Omega_f. \tag{4.5}$$

Such a selection of the duration time is adopted due to the faster stabilisation of the vibration amplitude for higher excitation frequencies. The duration time

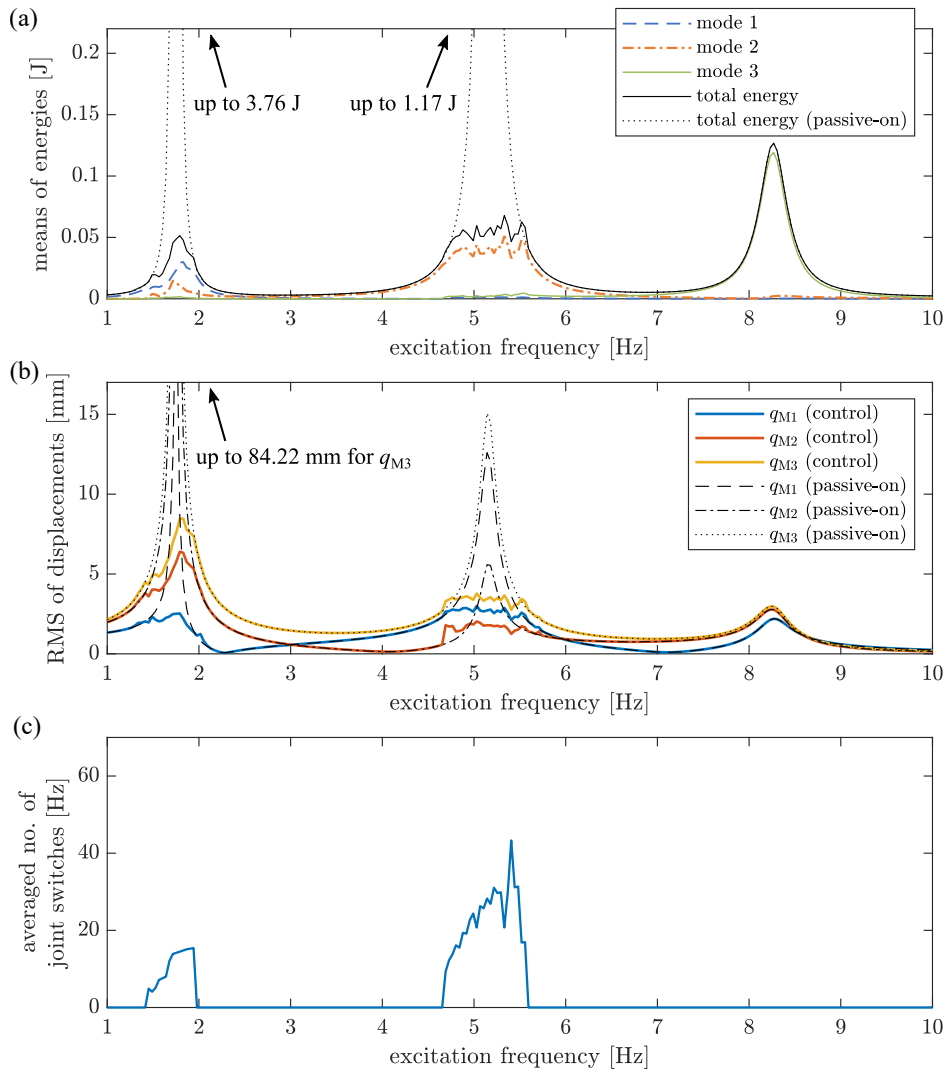

Fig. 4.9. Various metrics of performance calculated for modal control in dependence on the excitation frequency (excitation case 2): (a) mean modal energies, (b) RMS displacement values and (c) mean number of joint switches per second.

$T(\Omega_f)$ is selected in such a way that the steady-state vibration of the structure with passively locked joints cover the time interval:

$$\mathbf{T}_{\text{steady}}(\Omega_f) = \big[2/3 \cdot T(\Omega_f),\ T(\Omega_f)\big], \tag{4.6}$$

whereas the operation of the controlled structure becomes near-steady much earlier. Only the time interval $\mathbf{T}_{\text{steady}}(\Omega_f)$ is considered in calculation of results

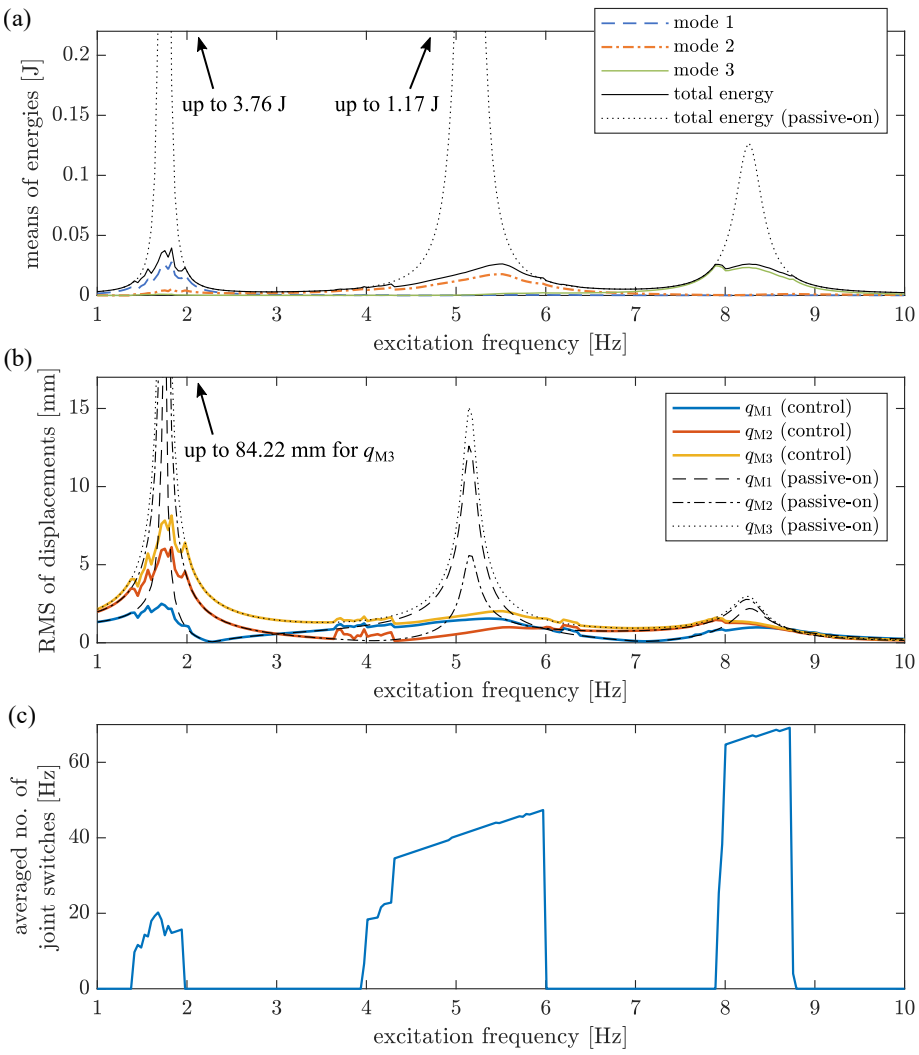

Fig. 4.10. Various metrics of performance calculated for PAR control in dependence on the excitation frequency (excitation case 2): (a) mean modal energies, (b) RMS displacement values and (c) mean number of joint switches per second.

for modal and PAR approaches that are shown in Figs. 4.9 and 4.10, respectively. The averaged number of joint switches (Figs. 4.9c and 4.10c) is calculated as:

$$\overline{n}_{\mathrm{J}}^{\mathrm{steady}} = n_{\mathrm{J}}^{\mathrm{steady}} / T_{\mathrm{steady}}(\Omega_f), \tag{4.7}$$

where: $n_{\mathrm{J}}^{\mathrm{steady}}$ is the sum of all joint switches within the time interval $\mathbf{T}_{\mathrm{steady}}(\Omega_f)$ and $T_{\mathrm{steady}}(\Omega_f)$ is its length. Such a metric gives information about the expected mean frequency of joint switches.

Modal control has similar efficiency in damping vibration at the first resonance as the PAR approach (Figs. 4.9a, b and 4.10a, b). The averaged number of switches $\overline{n}_{\mathrm{J}}^{\mathrm{steady}}$ for the PAR control at the first resonance is slightly higher than for the modal control. The second unlocked mode is better damped with the PAR approach due to the fact that weights α_p in the modal control are selected to mitigate mainly the first unlocked vibration mode. It results in worse but still satisfactory performance of the modal approach at the second resonance. More importantly, the modal control achieves a significantly lower average number of joint switches and a narrower frequency range in which they operate. At the third resonance, the modal control does not mitigate the vibration because possible level of the energy transfer rate from the third unlocked vibration mode weighted by the selected small α_3 is lower than the selected thresholds κ_1 and κ_2 for the present level of excitation. The PAR control mitigates the third unlocked mode efficiently. However, in the passive-on (joints locked) state the third resonance corresponds with 30 times lower vibration energy for the employed excitation than the first resonance and requires the highest averaged number of joint switches – near to 65 Hz for the PAR approach. Thus, the current selection of weights α_p in the modal approach can be regarded as one possible way to enhance the durability of the lockable joints, provided that damping of the third mode is not required. If it is, the weights could be adjusted even online, during the operation of the control algorithm.

Despite the fact that the modal controller is designed using the unlocked modal parameters it efficiently damps also locked vibration modes as shown in Figs. 4.9a and b. Hence, the difference in locked and unlocked natural frequencies (see: Fig. 4.2) does not affect efficiency of the proposed modal approach or its operational bandwidth in any way. It is due to the fact the control algorithm is based on the energy transfer rates which do not depend explicitly on natural frequencies. Instead, it depends on monitored modal velocities, bending moments transmitted by the lockable joints and parameters based on the unlocked mode shapes which can be considered as components of structural displacement also when the joints are currently locked.

Case 3

The last excitation considered in this subsection simulates random motion of the support. The acceleration of the support has a Gaussian distribution in each time step. It results in substitution of a vector of external disturbances $\mathbf{d}(t)$ in Eq. (2.41) with the inertia force

$$\mathbf{d}(t) = -\mathbf{M}\mathbf{l}_{\mathrm{x}}\sigma_a a_{\mathcal{N}(0,1)}, \tag{4.8}$$

where $a_{\mathcal{N}(0,1)}$ is the random acceleration with a normalised Gaussian distribution and σ_a is its magnitude (also standard deviation of the acceleration).

For simulation purposes $\sigma_a = 9$ m/s^2 and duration time of vibration 40 s are selected. 1000 simulations with random accelerations are performed for calculation of various averaged performance metrics. The performance metrics are calculated for each particular simulation analogously to case 2 but using the data from the time interval $\mathbf{T} = [15, 40]$ s. Comparison of the modal control and PAR strategy accompanied with results for the structure with passively locked joints are shown in Fig. 4.11 and listed in Table 4.3; $\overline{n}_{\mathrm{J}}$ is the number of switches averaged in the time interval $\mathbf{T}$:

$$\overline{n}_{\mathrm{J}} = n_{\mathrm{J}}/T, \tag{4.9}$$

where T is length of $\mathbf{T}$.

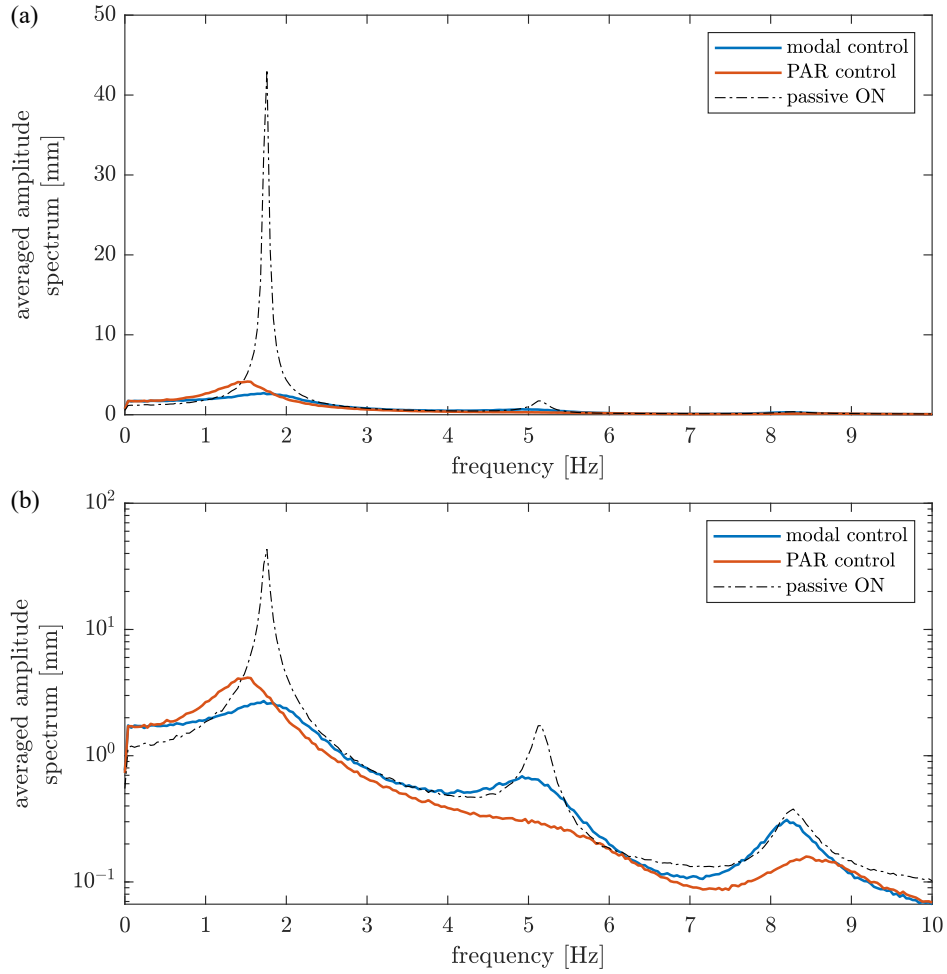

Fig. 4.11. Averaged amplitude spectra of structural tip end ($q_{\mathrm{M3}}(t)$) in (a) linear and (b) semilog-y scales for the excitation case 3.

Table 4.3. Comparison of various metrics of the control performance for modal PAR approaches and passively locked joints for the excitation case 3 averaged from 1000 simulations.

Control type	RMS(q_{M1}) [mm]	RMS(q_{M2}) [mm]	RMS(q_{M3}) [mm]	$\overline{E}$ [J]	$\overline{n}_J$ [Hz]
Modal	5.83	10.71	13.73	0.169	27.82
PAR	7.37	13.45	16.28	0.155	39.65
Passive-on	15.10	39.62	51.46	1.580	0

Once again, due to the selected weights α_p, the proposed modal approach mitigates the first unlocked vibration mode more effectively at the expense of damping effectiveness of the remaining modes, comparing to the PAR control. It results in lower RMS values of the structural displacements at sensor locations despite slightly greater mean vibration energy. Also the lower averaged number of joint switches for the modal control is achieved. The PAR approach shifts the first resonance peak towards lower frequencies, whereas the modal control only mitigates it, without its shifting.

4.1.3. Eight-bay smart structure with two non-optimally placed lockable joints

Candidate locations for optimal placement of actuators or semi-active devices in many situations can be restricted due to possible technical limitations, e.g. limited space for the device, availability of the power supply, safety reasons, etc. Thus, in this subsection performance of the modal and PAR approaches obtained for non-optimal joint locations is assessed and compared.

The structure under investigation is the same as in the previous subsection (Fig. 4.1) but with lockable joints placed at the ends of the fourth transversal beam. The first one is then connected with longitudinal beams as remaining transversal beams. The first three vibration modes calculated for the new arrangement of the lockable joints (both in the locked and unlocked states) are shown in Fig. 4.12. The optimal sensor locations corresponding to the unlocked modes are shown in Fig. 4.13. Strain gauges are located on the beam equipped with lockable joints analogously to Subsection 4.1.2.

The comparison of the proposed methodology and the PAR approach is conduced using the same test excitations as introduced in Subsection 4.1.2 (cases 1–3). Due to the non-optimally placed lockable joints thresholds $\kappa_1 = 7.5 \cdot 10^{-4}$ W and $\kappa_2 = 0.5$ W are selected, whereas the remaining algorithm parameters keep the same values as for optimally placed lockable joints (Subsection 4.1.2). In the case of the PAR approach $\kappa_\varepsilon = 50$. These parameters are selected with the trial-and-error method.

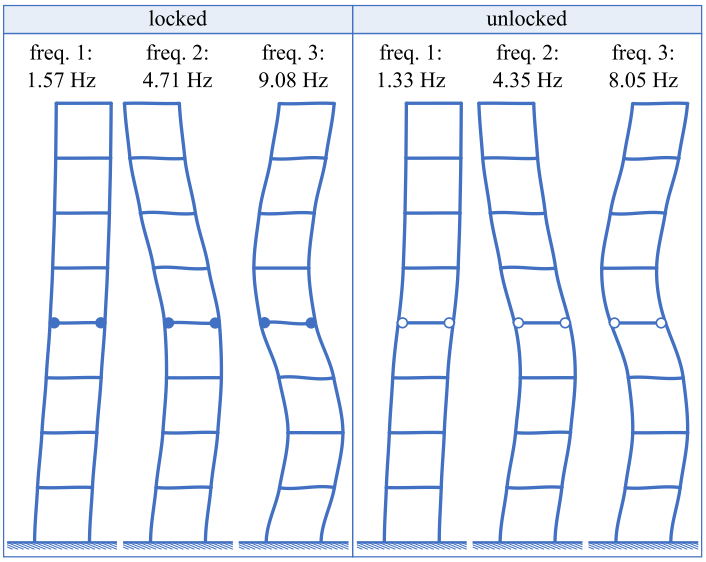

Fig. 4.12. Structure with non-optimally placed lockable joints: first three vibration modes for both locked and unlocked joints.

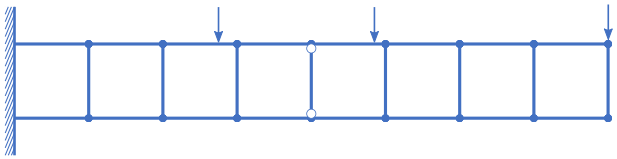

Fig. 4.13. FE mesh with optimal sensor locations obtained for structure with non-optimally located lockable joints.

Case 1

Simulation results of structural vibration damped with the modal approach, obtained for sudden stop of the ground motion (Eq. (4.3)) are shown in Fig. 4.14. Non-optimal placement of the lockable joints results in a greater number of the local extreme values both of the measured strain signals and the energy associated with the higher-order (not monitored) unlocked vibration modes in relation to optimal joint placement (Figs. 4.14b and c; compare with Figs. 4.5b and c). For the lockable joints placed at the ends of the fourth transversal beam the controllability of the third unlocked mode is greater in relation to the first unlocked vibration mode than for the previous joint arrangement (see: Fig. 4.3). Thus, the lock of the joints causes relatively more effective interaction between the third monitored unlocked vibration mode and the higher-order ones. In this case, the more frequent local extreme values of measured strains and energy related to the higher-order unlocked vibration modes are related to the greater natural frequency of the third unlocked vibration mode. However, due to the

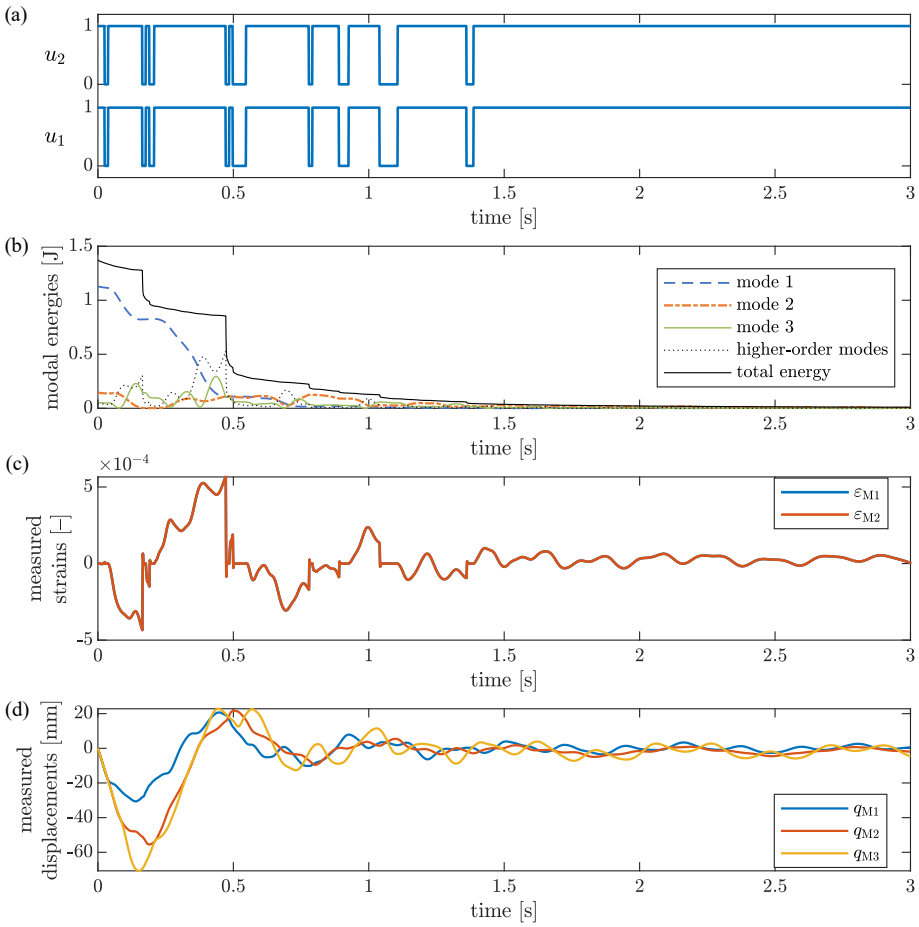

Fig. 4.14. Time histories of: (a) control signals, (b) modal energies of the structure, (c) measured strains and (d) structural displacements at sensor locations for case 1 of excitation of the structure with non-optimally placed lockable joints controlled by the modal control algorithm.

information about the global state of the system carried by the estimated modal velocities the control algorithm is robust with respect to these local extremes. Due to the selected weights α_p lockable joints are unlocked mainly in time instants then energy of the first unlocked vibration mode stops decreasing (compare Figs. 4.14a and b). The operation of the algorithm accordingly to the pursued priority in mitigating of the monitored unlocked vibration modes results in quick reduction of the main component of the structural displacements that is associated with the first unlocked vibration mode as shown in Fig. 4.14d. After transferring majority of the energy from the first unlocked vibration mode, later from the second and third ones, only residual vibration is visible due to the selected thresholds κ_1 and κ_2.

Results obtained for non-optimally placed lockable joints controlled with the PAR strategy and case 1 of excitation are shown in Fig. 4.15. As opposed to the modal control, in the PAR approach the lockable joints are unlocked each time when the measured strain signal goes through its extreme value, resulting in relatively frequent joint switches (compare: Figs. 4.15a and c). Then, mitigation of the first unlocked vibration mode is slower than in the modal control (see: Figs. 4.15b and d).

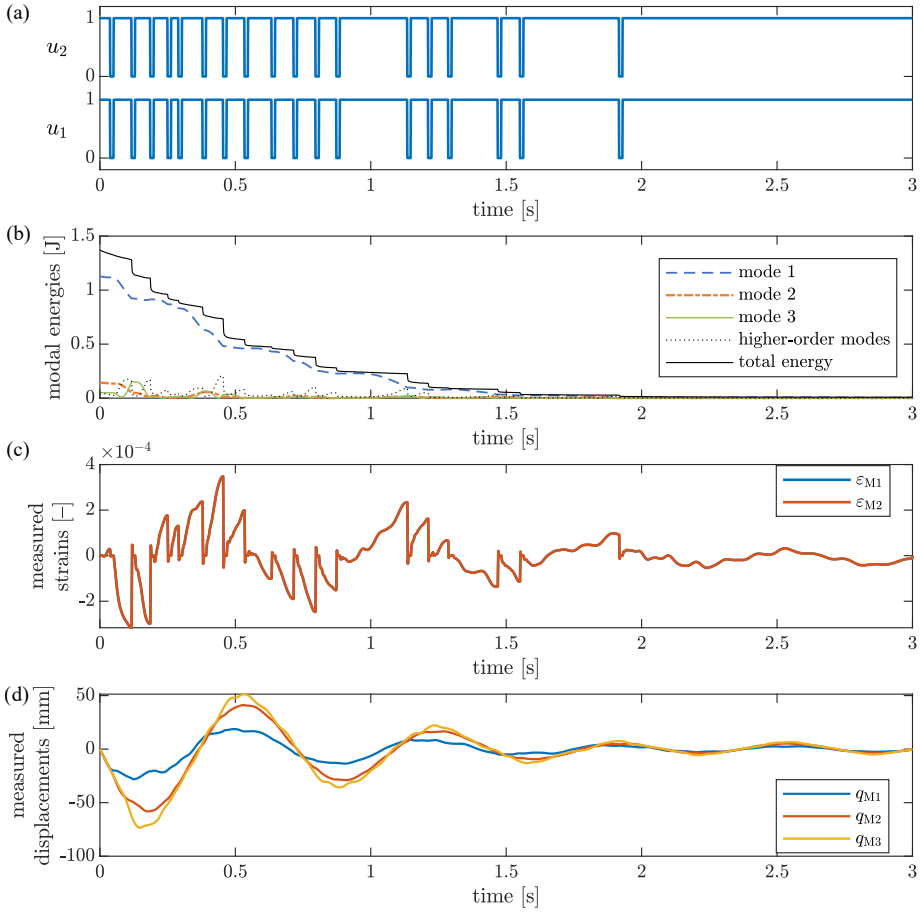

Fig. 4.15. Time histories of: (a) control signals, (b) modal energies of the structure, (c) measured strains and (d) structural displacements at sensor locations for case 1 of excitation of the structure with non-optimally placed lockable joints controlled by the PAR algorithm.

Comparison of the control signals and structural tip displacements for the modal control, PAR strategy and passive-on case (locked joints) is shown in Fig. 4.16. Even for non-optimal lockable joint placement, both vibration damping strategies still achieve satisfactory performance and allows for quick dissi-

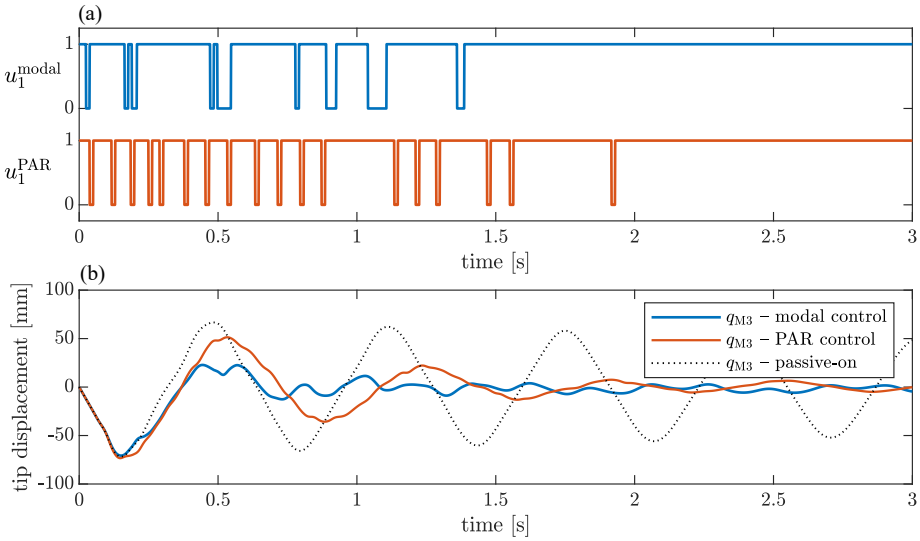

Fig. 4.16. Comparison of modal and PAR control strategies for excitation case 1 and non-optimal placement of the lockable joints: (a) control signals and (b) structural tip displacements accompanied with the passive-on case.

pation of the structural energy. However, the PAR strategy exhibits its greater sensitivity to the joint placement than the modal approach. It is visible as an increased number of cycles of the first unlocked vibration mode until it is mitigated, and a greater number of the joint switches. Decrement in the efficiency of the proposed modal control strategy is not as distinguishable as in the case of the PAR approach. This is also reflected in results listed in Table 4.4. The increment of the number of joint switches for the modal control in relation to optimally placed lockable joints is below 30 %, whereas for the PAR control it is 50 % (compare with Table 4.2). For both control methods the RMS values of displacements are slightly higher than for the optimally placed lockable joints. However, the mean energy decreased for the modal control as opposed to the PAR approach. In summary, for the non-optimally placed lockable joints the modal control provides the lower level of displacements, lower mean energy and smaller number of the joint switches in mitigation of free structural vibration.

Table 4.4. Comparison of various metrics of the control performance for modal and PAR approaches, and passively locked joints for their non-optimal locations in case 1 of excitation.

Control type	RMS(q_{M1}) [mm]	RMS(q_{M2}) [mm]	RMS(q_{M3}) [mm]	$\overline{E}$ [J]	n_J [–]
Modal	8.06	13.96	16.91	0.226	36
PAR	9.20	19.41	23.15	0.257	72
Passive-on	19.95	32.91	40.08	0.949	0

Case 2

In this case the structure with non-optimally placed lockable joints is excited according to the case 2 of excitation (Eq. (4.4) in Subsection 4.1.2). Results obtained with the modal control are shown in Fig. 4.17. The averaged number of joint switches is smaller at first two resonances (especially the second one) at the expense of slightly higher amplitudes of motion, as comparing to the case with optimally placed lockable joints. The lockable joints also operate in narrower fre-

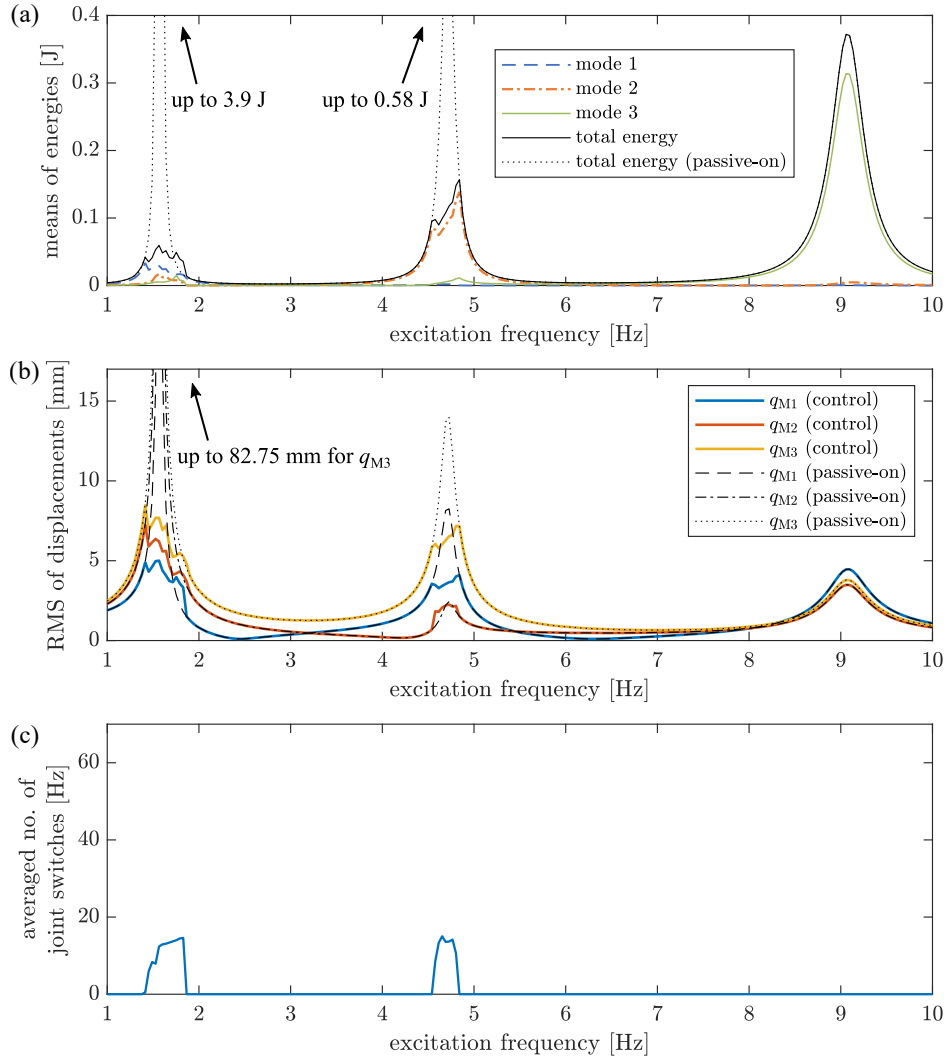

Fig. 4.17. Various metrics of performance calculated for modal control depending on the excitation frequency (excitation case 2) for non-optimal placement of the lockable joints: (a) mean modal energies, (b) RMS displacement values and (c) mean number of joint switches per second.

quency ranges. Similarly to the structure with optimally placed lockable joints, the third resonance is not mitigated because selected thresholds κ_1 and κ_2 are higher than the possible energy transfer rate related to the third unlocked vibration mode rate multiplied by α_3 for the current level of the excitation.

Analogous results for the PAR strategy are shown in Fig. 4.18. Due to the higher selected threshold κ_ε the PAR control also switches the lockable joints in narrower frequency ranges than for optimally located joints, excepting the third resonance. This behaviour is caused by the placement of the lockable joints pro-

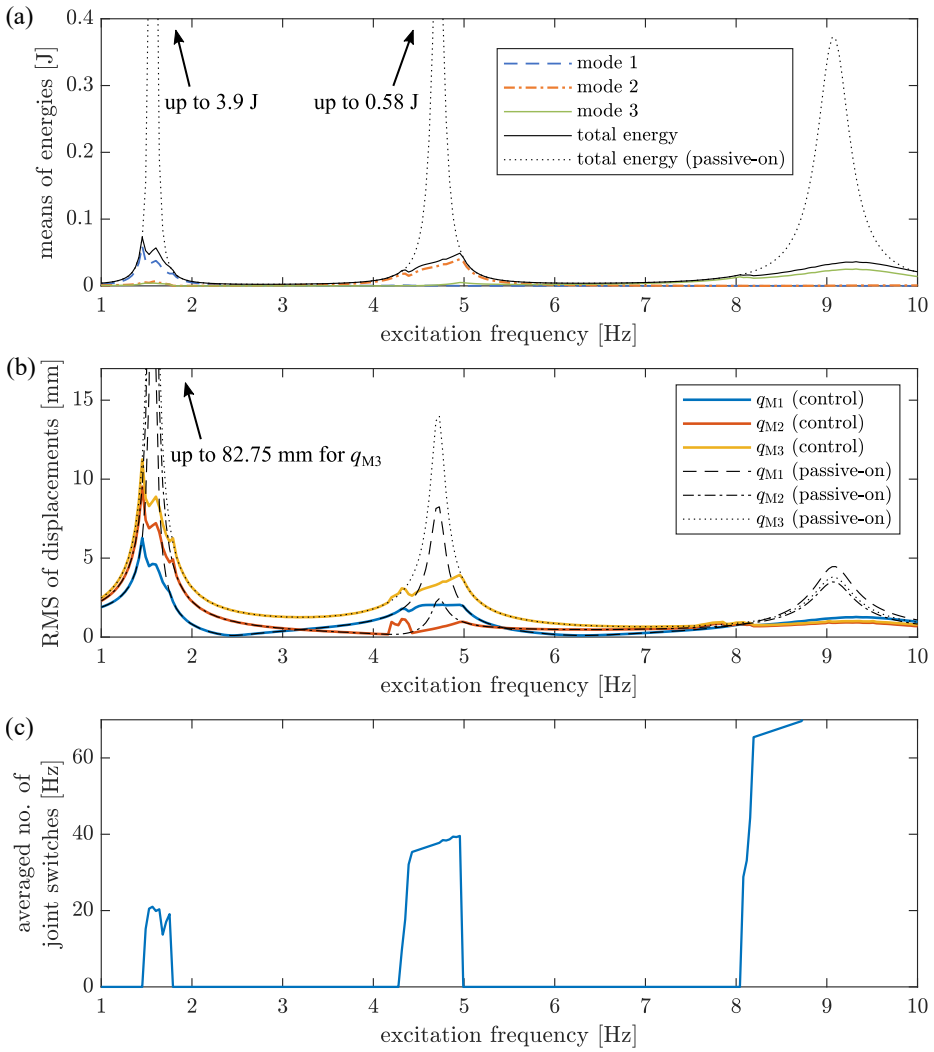

Fig. 4.18. Various metrics of performance calculated for PAR control depending on the excitation frequency (excitation case 2) for non-optimal placement of the lockable joints: (a) mean modal energies, (b) RMS displacement values and (c) mean number of joint switches per second.

viding higher controllability of the third unlocked vibration mode than for the optimal joint placement (see: Fig. 4.3, beam no. 1 vs beam no. 4). The higher modal controllability, the greater strains that can be accumulated in the transversal beam equipped with a pair of lockable joints. Hence, also more potential energy is released during the joint unlock in high-frequency vibrations.

PAR mitigates the first resonance, providing still satisfactory but slightly lower effectiveness than the modal approach and requiring more joint switches. The PAR approach does not allow for assigning weights to particular vibration modes, hence it mitigates vibration in all resonances at the expense of a significantly higher number of joint switches.

Case 3

In the present case, the structure with non-optimally placed lockable joints is excited by random base motion as described in Subsection 4.1.2, case 3 (see: Eq. (4.8)). The results are shown in Fig. 4.19.

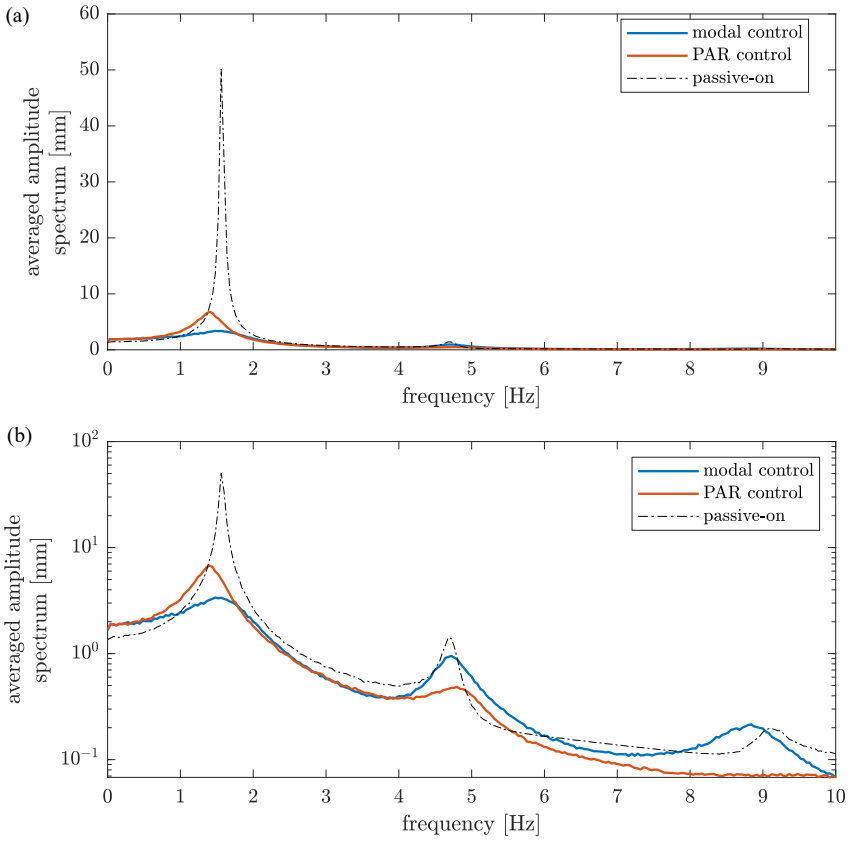

Fig. 4.19. Averaged amplitude spectra of structure tip end ($q_{M3}(t)$) in (a) linear and (b) semilog-y scales for the excitation case 3 and non-optimally placed lockable joints.

It is well demonstrated that the PAR strategy mitigates vibration at the second and third resonance better than the modal control at the expense of the first resonance. All metrics of control performance listed in Table 4.5 are better for the modal control, including the averaged number of joint switches. It is mainly due to the fact that the first unlocked vibration mode, which is suppressed by the modal approach with greater effectiveness, takes predominant participation in the structural motion. These results reveal that the possibility of weighing particular vibration modes by weights α_p in the proposed control allows for focusing of the efforts on the most harmful vibration modes, as opposed to PAR whose performance depends mainly on the location of the lockable joints. Once again the PAR approach shifts the first mitigated resonance peak towards lower frequencies, whereas in this case the modal approach shifts the third resonance peak without its suppression. Also its very small increase is noticeable as a result of decrease in the effective stiffness provided by unlocking of the joints. The second resonance peak is shifted towards the higher frequencies in the case of the PAR approach.

Table 4.5. Comparison of various metrics of the control performance for modal and PAR approaches, and passively locked joints for the excitation case 3 and non-optimally placed lockable joints averaged from 1000 simulations.

Control type	RMS(q_{M1}) [mm]	RMS(q_{M2}) [mm]	RMS(q_{M3}) [mm]	$\overline{E}$ [J]	$\overline{n}_{\mathrm{J}}$ [Hz]
Modal	7.86	12.55	15.32	0.20	24.42
PAR	8.59	17.28	20.67	0.23	39.52
Passive-on	28.25	46.70	56.84	2.00	0

4.2. Energy harvesting

The proposed control methodology is able not only to transfer mechanical energy from weakly damped vibration modes allowing for efficient mitigation of structural vibration, but also can be used for the directed energy transfer to the preselected unlocked vibration mode. In this section numerical results that present the use of this property to enhance the energy harvesting process are described and discussed. First, a small structure equipped with lockable joints that is to be controlled is described in the subsection below. This structure is a primary structure to which the energy harvester (EH) is attached as a secondary structure. The EH is tuned to one of the unlocked vibration modes of the controlled structure. This mode is referred to as the targeted mode to which the vibration energy is to be transferred. It provides that the EH works under resonance conditions even if external excitation of the primary structure is

away from the resonance range of the EH. In Subsection 4.2.2 an electromagnetic energy harvester (EMEH) and its model are discussed. The assembly and mechanical interaction between the EH and the primary structure are described in Subsection 4.2.3. The location of the EMEH depending on the targeted mode is also indicated in Subsection 4.2.4. Further, numerical study of the effectiveness of the proposed modal control and enhancement of the energy harvesting process for various excitations is described and discussed in Subsection 4.2.5.

4.2.1. Smart structure enhancing energy harvesting process

A scheme of the controlled (primary) frame structure is shown in Fig. 4.20a, whereas its FE model is shown in Fig. 4.20b. This two-bay structure is fixed in the ground. The lower transversal beam is connected to the longitudinal columns via joints providing rigid (uncontrolled) connections. The upper transversal beam is connected to the longitudinal beams via lockable (controlled) joints. Both controlled and rigid joints have non-negligible mass that allows for vibration of the structure in the two predominant low-frequency unlocked vibration modes. This facilitates control of these vibration modes and the energy exchange between them. Dimensions and properties of the structure shown in Fig. 4.20 are listed in Table 4.6.

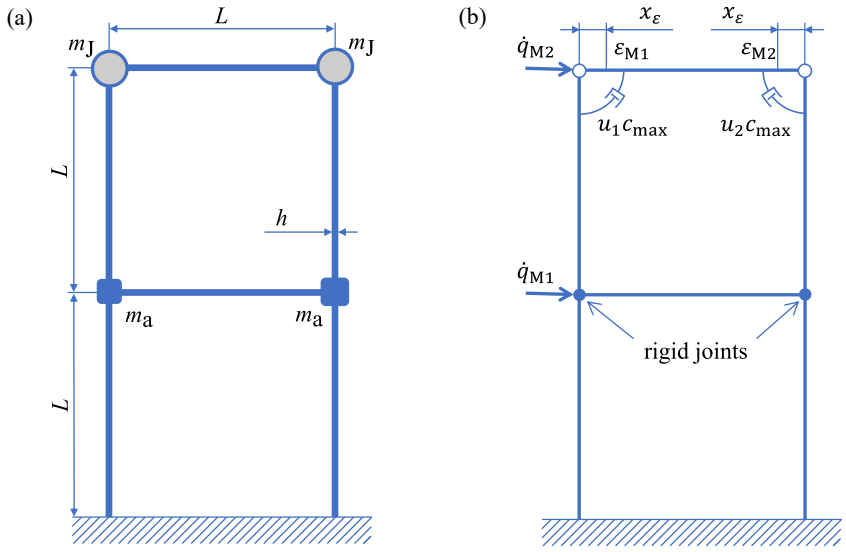

Fig. 4.20. Frame structure equipped with two lockable joints: (a) scheme of the structure, (b) finite element mesh and placement of sensors [144].

The FE model of the structure has 6 beam FEs based on the Euler–Bernoulli beam theory. Each beam FE is non-stretchable and has cubic shape functions. The FE model has 8 DOFs.

Table 4.6. Parameters of the two-story frame structure.

Quantity	Symbol	Units	Value
Length	L	[mm]	400
Offset of the strain gauges from semi-active joint	x_ε	[mm]	50
Young modulus (steel)	E	[Pa]	$210 \cdot 10^9$
Material density (steel)	ρ	[kg/m^3]	7860
Dimensions of the cross-section (height $\times$ width)	$h \times b$	[mm]	8×10
Mass of the semi-active joint	m_J	[kg]	1.0
Mass of the rigid connection	m_a	[kg]	0.4

Locations of two sensors for estimation of the first two modal velocities are shown in Fig. 4.20b along with locations of the strain gauges. The measured strains are calculated using FE shape functions as described in Section 3.1.

All eight unlocked vibration modes of the structure and the first two locked ones are shown in Fig. 4.21. It is visible that the third and higher-order unlocked modes shapes involve mainly local curvatures as opposed to the first two unlocked vibration modes involving significant displacements of horizontal beams along with massive, both lockable and rigid, joints.

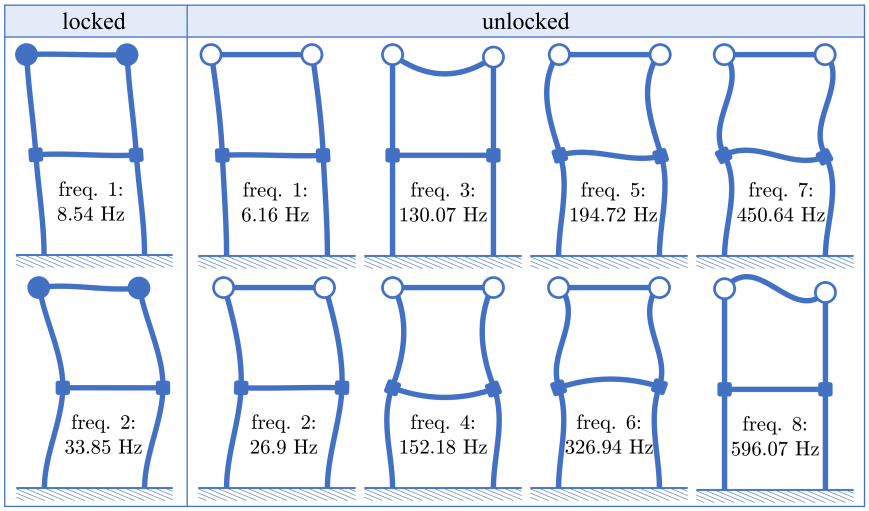

Fig. 4.21. Vibration modes of the controlled two-bay structure obtained for unlocked joints accompanied with the first two vibration modes obtained for joints locked at 90° between connected beams.

Aiming at the control of the first two unlocked vibration modes the lockable joints are located at the ends of the upper transversal beam instead of the lower one. Controllability of the monitored unlocked vibration modes in dependence

on the joint locations is shown in Fig. 4.22. In the case of energy harvesting application of the proposed methodology, all unlocked vibration modes have to be controllable. If the lockable joints are placed at the ends of first transversal beam the second unlocked vibration mode would be controlled with poor efficiency. Thus, the energy transfer to/from this vibration mode would be not effective. It is due to the fact that the first transversal beam almost does not accumulate strains in the second locked vibration mode (it is not significantly deflected, as shown in Fig. 4.21), hence the joints do not transmit any significant bending moment.

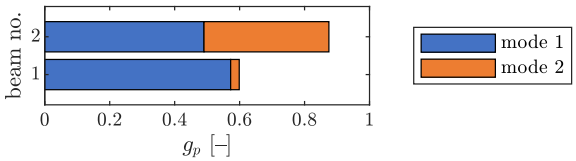

Fig. 4.22. Controllability of the monitored unlocked vibration modes for lockable joints placed at the ends of the first and second transversal beam of the structure.

Despite the fact that non-simplified form of Eq. (3.28) is employed to obtain results shown in Fig. 4.22 the simplified form would give similar results, since for the first two vibration of the considered structure: $\vartheta_{11} = 0.9897$ and $\vartheta_{22} = 0.987$ have values close to ones. It follows that the simplification proposed in Eq. (3.28) remains valid even for relatively small structures, provided that the set of monitored vibration modes is properly selected.

Material damping model is described by modal damping factors analogously to Eq. (4.2). For this structure coefficients $\alpha = 0$, $\beta = 0.012$ and $\gamma = 2.0785 \cdot 10^{-4}$ are selected. Corresponding modal damping factors in dependence on the natural frequencies are shown in Fig. 4.23. The first two modal damping factors are: $\zeta^{(1)} = 1$ % and $\zeta^{(2)} = 2.35$ %.

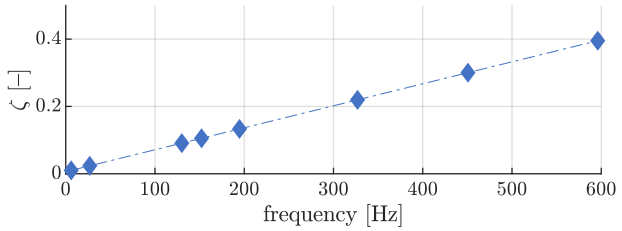

Fig. 4.23. Modal damping factors characterising material damping of the two-bay structure in dependence on the natural frequency.

4.2.2. Model of electromagnetic energy harvester

The electromagnetic energy harvester (EMEH) is selected, since EMEHs have relative low frequencies of operation that is desired in demonstrated application

example. The scheme of the EMEH is shown in Fig. 4.24a. The considered EMEH consists of the magnet having mass m attached to the spring having stiffness k inside a casing. The casing is covered by an electromagnetic coil. It is assumed that magnet of the EMEH is excited kinematically by displacement $x_{\mathrm{c}}(t)$ of the casing that is mounted to the vibrating structure (more details in the next subsection).

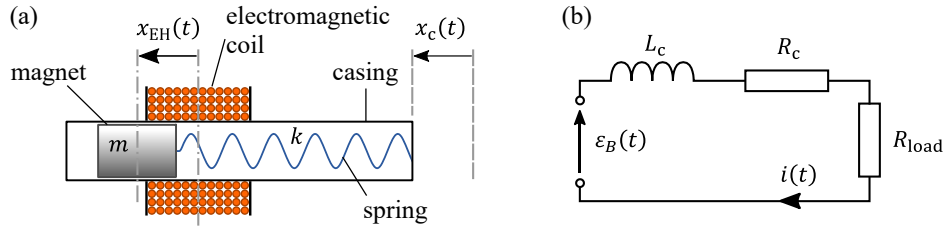

Fig. 4.24. EMEH device: (a) scheme of the mechanical part and (b) scheme of the electrical circuit [144].

Motion of the magnet inside the electromagnetic coil induces the electromotive force according to Faraday's law. The electromotive force generally depends nonlinearly on displacement of the magnet with respect to the coil $x_{\mathrm{EH}}(t)$ and linearly on the relative velocity $\dot{x}_{\mathrm{EH}}(t)$ (Fig. 4.24a). These nonlinearities have strong influence on the dynamics of the electrical circuit when displacements of the magnet with respect to the coil are large in relation to the coil dimensions, as investigated in [18]. However, for relatively small amplitude of the vibration of the magnet, the electromotive force $\varepsilon_B(t)$ can be considered as proportional to the relative magnet velocity:

$$\varepsilon_B(t) = \kappa_B \dot{x}_{\mathrm{EH}}(t), \tag{4.10}$$

where κ_B is called electromechanical coupling. Then, after proper selection of κ_B, EMEH behaviour is similar to that obtained from the rigorous nonlinear model, as investigated in [147].

The scheme of the electrical circuit of EMEH is shown in Fig. 4.24b, where L_{c} and R_{c} are inductance (also assumed to be constant) and resistance of the electromagnetic coil, respectively, R_{load} is resistance of the resistor considered as the energy receiver and $i(t)$ is electrical current. Behaviour of the considered EMEH is described by the following equation:

$$\begin{cases} m\ddot{x}_{\mathrm{EH}}(t) + c\dot{x}_{\mathrm{EH}}(t) + kx_{\mathrm{EH}}(t) = -\kappa_B i(t) - m\ddot{x}_{\mathrm{c}}(t), \\ L_{\mathrm{c}}\dot{i}(t) + (R_{\mathrm{c}} + R_{\mathrm{load}})\, i(t) = \kappa_B \dot{x}_{\mathrm{EH}}(t). \end{cases} \tag{4.11}$$

Since $x_{\mathrm{EH}}(t)$ is the displacement of the magnet with respect to the coil, it is also the displacement in a non-inertial reference frame associated with the moving EMEH casing (Fig. 4.24a); $x_{\mathrm{EH}}(t)$ is equal to the change in the spring length.

For the present study, values of parameters describing EMEH properties that are contained in Eq. (4.11) are shown in Table 4.7. They are similar to data describing EMEH researched in [147–149]. Stiffness of the model is linearized with respect to the equilibrium point (at zero displacement). Stiffness k is tuned to the targeted vibration mode of the two-bay primary structure (see: Subsection 4.2.4).

Table 4.7. Properties of EMEH adopted in present study [144, 147–149].

Quantity	Symbol	Units	Value
Mass of the magnet	m	[kg]	$90 \cdot 10^{-3}$
Damping coefficient	c	[Ns/m]	0.1
Electromechanical coupling	κ_B	[Vs/m]	60
Coil inductance	L_c	[H]	1.463
Coil resistance	R_c	[Ω]	1200
Magnet diameter × magnet height	$D_\mathrm{m} \times H_\mathrm{m}$	[m]	$20 \cdot 10^{-3} \times 35 \cdot 10^{-3}$
Coil wire diameter	D_w	[m]	$0.14 \cdot 10^{-3}$
Turns of winding	N_turns	[–]	12 740

Power produced by the EMEH device is calculated as

$$P(t) = R_\mathrm{load} i^2(t). \tag{4.12}$$

Power $P(t)$ changes with the frequency equal to twice of EMEH vibration frequency. Thus, it is more informative to use the mean value of the power produced by the EMEH:

$$\overline{P} = \frac{1}{T} \int_{t_0}^{t_0+T} P(t)\mathrm{d}t. \tag{4.13}$$

4.2.3. Interaction between the energy harvester and the structure

Displacement of EMEH casing attached to the structure in the inertial reference frame is described by the following formula

$$x_\mathrm{c}(t) = \mathbf{l}_\mathrm{EH}^\mathrm{T} \mathbf{q}(t) + q_\mathrm{g}(t). \tag{4.14}$$

In the equation above $\mathbf{l}_\mathrm{EH}$ is the Boolean vector selecting structural DOF to which EMEH is attached, $\mathbf{q}(t)$ is the structural displacement vector with respect to the ground and $q_\mathrm{g}(t)$ is the displacement of the ground (treated later as the non-inertial reference frame). The ground (or support) motion simulates vibration of the structure on which the whole energy harvesting system (controlled primary structure with attached EMEH) can be mounted.

EMEH acts on the structure with force

$$\mathbf{d}_{\mathrm{EH}}(t) = \mathbf{l}_{\mathrm{EH}} \left(\kappa_B i(t) + c\dot{x}_{\mathrm{EH}}(t) + k x_{\mathrm{EH}}(t) \right). \tag{4.15}$$

In the equation above, force $\mathbf{d}_{\mathrm{EH}}(t)$ is equal to the sum of: (1) the Lorentz force $\mathbf{l}_{\mathrm{EH}}\kappa_B i(t)$ that acts on the electromagnetic coil (fixed to the structure through the casing), (2) viscous damping force $\mathbf{l}_{\mathrm{EH}}c\dot{x}_{\mathrm{EH}}(t)$ and (3) the stiffness force $\mathbf{l}_{\mathrm{EH}}k x_{\mathrm{EH}}(t)$ generated by the spring deformed.

The EMEH and the controlled structure can be also considered as the assembled system using primal assembly formulation [150, 151]. The subsystems to be assembled, EMEH and structure, are shown in Fig. 4.25. i-th DOF of the component 1 (controlled structure) is indicated by the vector $\mathbf{l}_{\mathrm{EH}}$. In this figure the location of the EMEH on the structure is only the example.

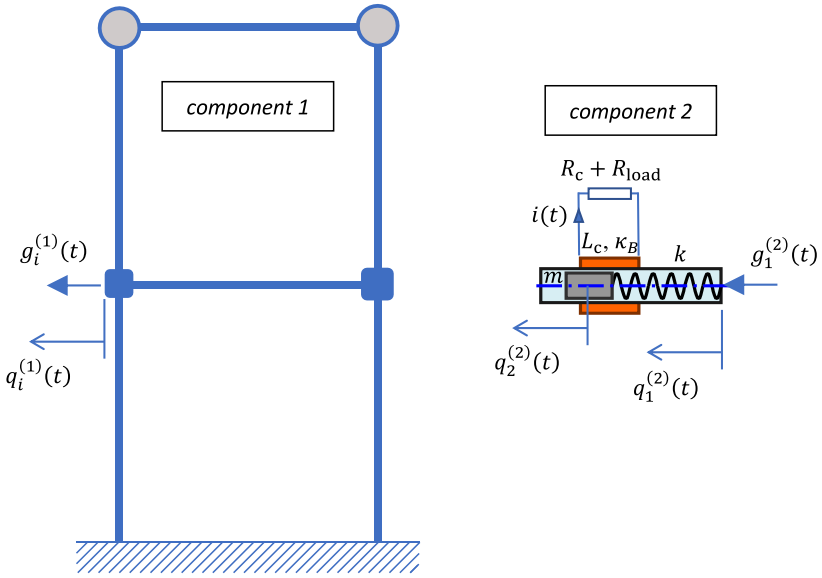

Fig. 4.25. Components (controlled structure and EMEH) for primal assembly.

Behaviour of the structure and the attached EMEH is described by the following equation:

$$\begin{cases} \mathbf{M}^{(1)}\ddot{\mathbf{q}}^{(1)}(t) + \mathbf{C}^{(1)}(\mathbf{u})\dot{\mathbf{q}}^{(1)}(t) + \mathbf{K}^{(1)}\mathbf{q}^{(1)}(t) = \mathbf{d}^{(1)}(t) + \mathbf{g}^{(1)}(t), \\ \mathbf{M}^{(2)}\ddot{\mathbf{q}}^{(2)}(t) + \mathbf{C}^{(2)}\dot{\mathbf{q}}^{(2)}(t) + \mathbf{K}^{(2)}\mathbf{q}^{(2)}(t) = \mathbf{d}^{(2)}(t) + \mathbf{g}^{(2)}(t), \\ \mathbf{l}_{\mathrm{EH}}^{\mathrm{T}}\mathbf{q}^{(1)}(t) - q_1^{(2)}(t) = 0, \\ \mathbf{l}_{\mathrm{EH}}^{\mathrm{T}}\mathbf{g}^{(1)}(t) + g_1^{(2)}(t) = 0. \end{cases} \tag{4.16}$$

Superscripts (1) and (2) refer to the component 1 and component 2 in Fig. 4.25, respectively, $\mathbf{M}^{(1)} = \mathbf{M}$, $\mathbf{C}^{(1)}(\mathbf{u}) = \mathbf{C} + \sum_{k=1}^{N_k} u_k(t)\widetilde{\mathbf{C}}_k$ (see: Eq. (2.43)), $\mathbf{K}^{(1)} = \mathbf{K}$, $\mathbf{q}^{(2)}(t) \in \mathbb{R}^3$,

$$\mathbf{M}^{(2)} = \begin{bmatrix} 0 & 0 & 0 \\ 0 & m & 0 \\ 0 & 0 & L_\mathrm{c} \end{bmatrix}, \quad \mathbf{C}^{(2)} = \begin{bmatrix} c & -c & -\kappa_B \\ -c & c & \kappa_B \\ \kappa_B & -\kappa_B & R_\mathrm{c} + R_\mathrm{load} \end{bmatrix}, \quad \mathbf{K}^{(2)} = \begin{bmatrix} k & -k & 0 \\ -k & k & 0 \\ 0 & 0 & 0 \end{bmatrix},$$

vectors $\mathbf{g}^{(1)}(t)$ and $\mathbf{g}^{(2)}(t)$ are the interface forces that stay in equilibrium ($\mathbf{g}^{(1)}(t)$ is equal to $\mathbf{d}_\mathrm{EH}(t)$ in Eq. (4.15)); $q_3^{(2)}(t)$ represents electrical charge, whereas its time derivative is equal to the electrical current $i(t)$.

Equations describing interfaces can be rewritten into the following form:

$$\mathbf{L}_\mathrm{EH} \begin{bmatrix} \mathbf{q}^{(1)}(t) \\ \mathbf{q}^{(2)}(t) \end{bmatrix} = \mathbf{0}, \qquad \mathbf{L}_\mathrm{N}^\mathrm{T} \begin{bmatrix} \mathbf{g}^{(1)}(t) \\ \mathbf{g}^{(2)}(t) \end{bmatrix} = \mathbf{0}, \tag{4.17}$$

where: $\mathbf{L}_\mathrm{EH} = \begin{bmatrix} \mathbf{L}_\mathrm{EH}^{(1)} & \mathbf{L}_\mathrm{EH}^{(2)} \end{bmatrix}$, $\mathbf{L}_\mathrm{EH}^{(1)} = \mathbf{l}_\mathrm{EH}^\mathrm{T}$, $\mathbf{L}_\mathrm{EH}^{(2)} = \begin{bmatrix} -1 & 0 & 0 \end{bmatrix}$ and $\mathbf{L}_\mathrm{N}$ is defined as the null space of the matrix $\mathbf{L}_\mathrm{EH}$. Substituting

$$\begin{bmatrix} \mathbf{q}^{(1)}(t) \\ \mathbf{q}^{(2)}(t) \end{bmatrix} = \mathbf{L}_\mathrm{N} \mathbf{q}_\mathrm{u}(t), \tag{4.18}$$

where $\mathbf{q}_\mathrm{u}(t)$ describes unique DOFs for the total structure, into Eq. (4.16) and left-multiplying by $\mathbf{L}_\mathrm{N}^\mathrm{T}$ we receive the following equation of motion

$$\underbrace{\mathbf{L}_\mathrm{N}^\mathrm{T} \begin{bmatrix} \mathbf{M}^{(1)} & \mathbf{0} \\ \mathbf{0} & \mathbf{M}^{(2)} \end{bmatrix} \mathbf{L}_\mathrm{N}}_{\mathbf{M}_\mathrm{u}} \ddot{\mathbf{q}}_\mathrm{u}(t) + \underbrace{\mathbf{L}_\mathrm{N}^\mathrm{T} \begin{bmatrix} \mathbf{C}^{(1)}(\mathbf{u}) & \mathbf{0} \\ \mathbf{0} & \mathbf{C}^{(2)} \end{bmatrix} \mathbf{L}_\mathrm{N}}_{\mathbf{C}_\mathrm{u}(\mathbf{u})} \dot{\mathbf{q}}_\mathrm{u}(t)$$

$$+ \underbrace{\mathbf{L}_\mathrm{N}^\mathrm{T} \begin{bmatrix} \mathbf{K}^{(1)} & \mathbf{0} \\ \mathbf{0} & \mathbf{K}^{(2)} \end{bmatrix} \mathbf{L}_\mathrm{N}}_{\mathbf{K}_\mathrm{u}} \mathbf{q}_\mathrm{u}(t) = \underbrace{\mathbf{L}_\mathrm{N}^\mathrm{T} \begin{bmatrix} \mathbf{d}^{(1)}(t) \\ \mathbf{d}^{(2)}(t) \end{bmatrix}}_{\mathbf{d}_\mathrm{u}(t)} + \underbrace{\mathbf{L}_\mathrm{N}^\mathrm{T} \begin{bmatrix} \mathbf{g}^{(1)}(t) \\ \mathbf{g}^{(2)}(t) \end{bmatrix}}_{\mathbf{0}}. \tag{4.19}$$

The equation of motion above represents the controlled structure and EMEH as one total system (including the state of the electrical circuit of the EMEH).

The assembly of the system components into one total system allows for simulation of the system behaviour by integration of one equation set. Then, Eq. (4.19) is integrated as described at the end of Subsection 2.2.2 (see: Eqs. (2.44) and (2.45)). The time step $\Delta t = 5 \cdot 10^{-5}$ s is selected for simulations of the behaviour of the EMEH and controlled structure.

4.2.4. Optimal EMEH placement and tuning for preselected targeted unlocked vibration mode

Seeking for the highest efficiency of the energy harvesting system, EMEH should be located at the DOF of the biggest displacement value corresponding to the targeted unlocked mode shape. This DOF is selected by the vector $\mathbf{l}^{\star}_{\mathrm{EH}}(r) = \begin{bmatrix} 0 & \cdots & 0 & 1 & 0 & \cdots & 0 \end{bmatrix}^{\mathrm{T}}$ such that

$$\mathbf{l}^{\star\mathrm{T}}_{\mathrm{EH}}(r)\boldsymbol{\phi}^{(r)} = \max_{i \in S_{\mathrm{EH}}} \left| \phi_i^{(r)} \right|, \tag{4.20}$$

where: r is index of the targeted unlocked vibration mode and S_{EH} is set of structural DOFs candidate to be EMEH location.

EMEH should be also tuned to the targeted vibration mode. The stiffness of the EMEH spring is selected that EMEH has the same natural frequency as the targeted mode:

$$\frac{k(r)}{m} = \omega^{(r)2}. \tag{4.21}$$

In the present study, the energy harvesting system is tested for both the first and the second controlled unlocked vibration mode selected as the targeted one. EMEH placements for both these modes and tuned stiffness k of the spring are shown in Fig. 4.26. In the further part of this thesis the system configuration shown in Fig. 4.26a is called "configuration 1", whereas one shown in Fig. 4.26b is called "configuration 2".

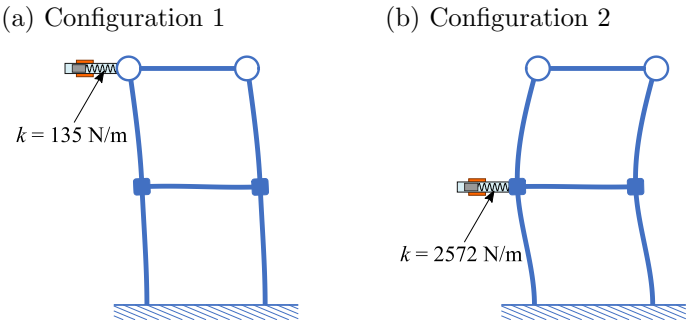

Fig. 4.26. Selected EMEH location when tuned to (a) the first and (b) the second unlocked vibration mode, selected as the targeted one.

4.2.5. Modal energy transfer for enhancement of the energy harvesting process

In this subsection three cases of the kinematic excitations are considered:

case 1: short modulated harmonic ground motion causing transient vibration of the structure,

case 2: harmonic excitation and

case 3: noise excitation.

Case 1

Modulated horizontal ground motion serving as the kinematic excitation is expressed as

$$q_{\mathrm{g}}(t) = A_{\mathrm{g}}(t) \sin \Omega_{\mathrm{g}} t, \tag{4.22}$$

where: $A_{\mathrm{g}}(t)$ is the motion amplitude depending on the time and Ω_{g} is the excitation frequency. The resulting inertia force acting on the structure integrated with the EMEH (see: Eq. (4.19)) is as follows:

$$\mathbf{d}_{\mathrm{u}}(t) = -\mathbf{M}_{\mathrm{u}} \mathbf{l}_{\mathrm{xu}} \ddot{q}_{\mathrm{g}}(t), \tag{4.23}$$

where the Boolean vector $\mathbf{l}_{\mathrm{xu}}$ selects translational DOFs analogously as $\mathbf{l}_{\mathrm{x}}$ but includes also the motion of the magnet in EMEH.

The ability of the control to transfer the vibration energy to the first unlocked mode (see Fig. 4.26a) is tested first. The test kinematic excitation is modulated and has the same frequency as the second unlocked vibration mode of the structure, as shown in Fig. 4.27a. This sub-case of the excitation is further called "**case 1-1**". Later, the mechanical energy is to be transferred from the currently excited, the second, unlocked vibration mode of the structure to the first, targeted, unlocked one, as illustrated in Fig. 4.27b. Finally, the EMEH tuned to the targeted vibration mode recovers the vibration energy.

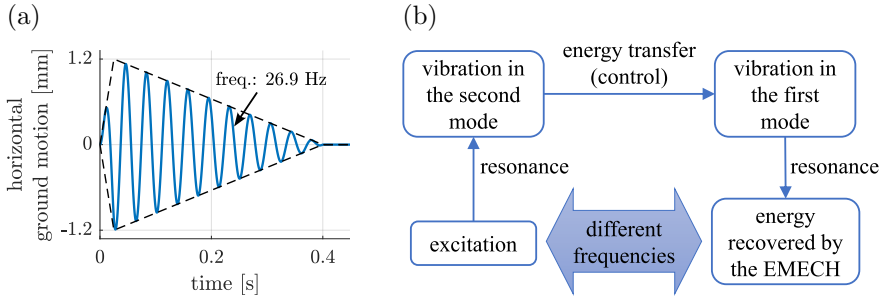

Fig. 4.27. (a) Time history of kinematic excitation (horizontal ground motion) providing resonance of the second structural unlocked mode and (b) flowchart of the desired energy flow in the system for the configuration 1.

The algorithm parameters (see: Algorithm 2) have been selected with the trial-and-error method as follows: $\alpha_1 = -1$, $\alpha_2 = 0$, $t_{\mathrm{lock}} = t_{\mathrm{unlock}} = 0$, $\kappa_1 = 300$ W and $\kappa_2 = 0$. Only the first weight selected nonzero is sufficient and provides satisfactory results.

Results are shown in Fig. 4.28. It can be seen that the second unlocked mode has predominant energy at the beginning due to the resonance with the kinematic

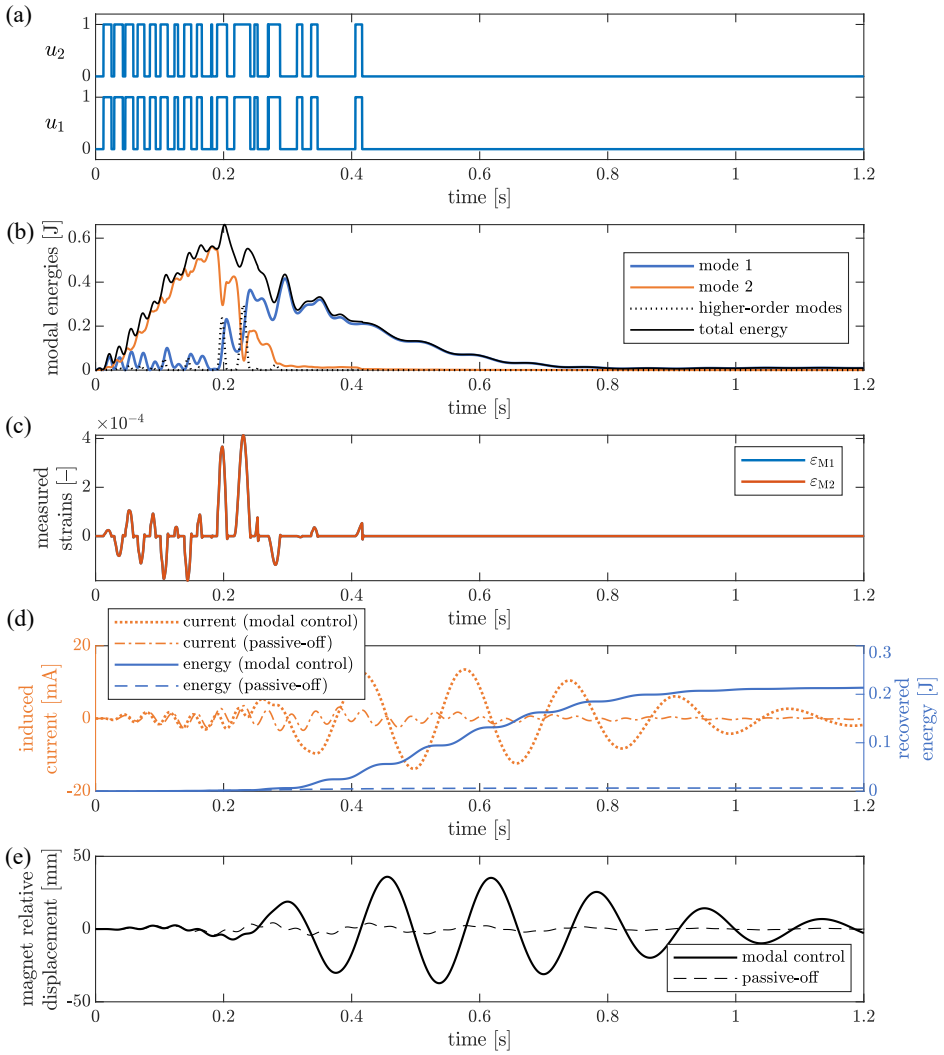

Fig. 4.28. Time histories of: (a) control signals, (b) modal energies of the structure, (c) measured strains, (d) electrical current and energy produced by the EMEH displacements compared with passive-off case and (e) relative magnet displacement compared with the passive-off case for case 1-1 of excitation and configuration 1 of the system.

excitation (Fig. 4.28b). However, operation of the lockable joints (Fig. 4.28a) causes that the energy is effectively transferred to the first unlocked vibration mode.

In this case the joints are unlocked in time instances when the potential energy of the higher-order unlocked vibration modes is near to zero (dotted line in Fig. 4.28b). It corresponds to near-zero measured strains in Fig. 4.28c. Due

to that, neither the step-like decrements in the structural energy nor measured strains are visible after the joint unlocking (compare with the results for vibration attenuation application shown in Section 4.1). In the present case, the strain energy provided by the bending moments transmitted by the lockable joints is transferred back to the targeted mode before the joint unlock, instead of being released in the high-frequency vibration. As a result, this mechanical energy is not wasted but kept to be finally recovered by EMEH. The opposite case of the system behaviour could be considered as a result of control spillover, as opposed to the vibration attenuation application of the control, where dissipation of the energy in the material damping is a desired phenomenon.

The energy transferred to the first unlocked vibration mode quickly decreases due to the operation of the EMEH that acts on the controlled structure as TMD. This results in a significantly increased amplitude of the magnet relative displacement in comparison to the passive-off case, when the joints are passively unlocked (see: Fig. 4.28e). In consequence, the produced electrical current and energy also are significantly higher in relation to the corresponding quantities obtained for the passive-off case (Fig. 4.28d). In the passive-off case, the energy is not transferred to the first unlocked vibration mode, thus EMEH is not in resonance and produces almost no energy.

This numerical example shows that the mechanical energy can be effectively transferred to the first unlocked vibration mode from the second one. Here, the energy flow is opposite to the case in which vibration is to be mitigated. It suggest that the proposed control methodology has potential to be used to precisely manage the distribution of mechanical energy among the unlocked vibration modes.

The ability of the proposed control strategy to transfer the energy to the second unlocked vibration mode is investigated below employing configuration 2 of the system (Fig. 4.26b). In this case, the kinematic excitation is of the same type but has a frequency equal to the natural frequency of the first unlocked vibration mode of the structure and has a bigger amplitude. In relation to case 1-1 the amplitude is multiplied by the ratio $\omega^{(2)}/\omega^{(1)}$ that provides the same energy level of the excitation accordingly to the rule

$$A_{\mathrm{g}}^2(t = t_i)\Omega_{\mathrm{g}}^2 = \mathrm{const}, \tag{4.24}$$

where: $A_{\mathrm{g}}(t = t_i)$ is the amplitude of the ground motion for any fixed time instant t_i and Ω_{g} is its frequency (here: $\Omega_{\mathrm{g}} = \omega^{(2)}$). This sub-case of excitation is called "**case 1-2**" in the further part of this thesis. The test excitation is shown in Fig. 4.29a, whereas the desired energy flow is shown in Fig. 4.29b.

The algorithm parameters (see: Algorithm 2) have been selected with the trial-and-error method differently from the previous system configuration: $\alpha_1 = 1.5$, $\alpha_2 = -1$, $t_{\mathrm{lock}} = t_{\mathrm{unlock}} = 0$, $\kappa_1 = 800$ W and $\kappa_2 = 0$. In this case the control algorithm checks the weighted sum of current modal energy transfer rates both

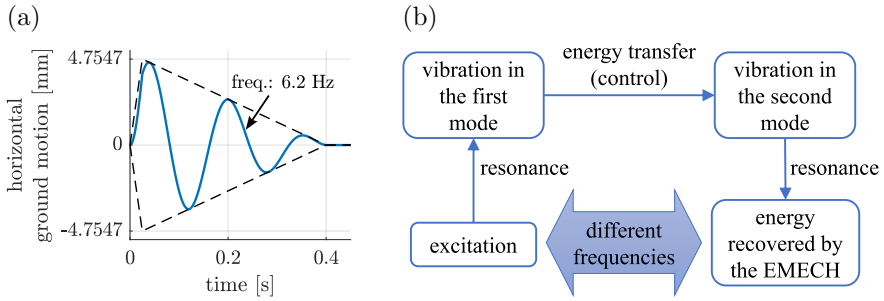

Fig. 4.29. (a) Time history of kinematic excitation (horizontal ground motion) providing resonance of the first structural unlocked mode and (b) flowchart of the desired energy flow in the system for the configuration 2.

from the first unlocked vibration mode (the positive first weight) and to the targeted mode (the negative second weight). The reason is explained as follows. The second unlocked modal velocity changes its sign more frequently than the first one in the free vibration according to their natural frequencies. In result, if only α_2 is selected nonzero the eventual weighted modal energy transfer rate estimated from Eq. (3.39) also would change its sign more frequently. Such a selection of weights could result in more frequent and less effective switches of the lockable joints. Selecting both weights nonzero allows for decrease in the redundant sign changes. In consequence, it reduces the number of redundant and less effective joint switches.

The results corresponding to case 1-2 of excitation are shown in Fig. 4.30. The first unlocked vibration mode enters resonance with the modulated kinematic excitation. Due to the operation of the lockable joints, the energy is transferred to the second, targeted, unlocked vibration mode (see: Figs. 4.30a and b). However, in this case, the joints mainly are unlocked at time instances characterised by nonzero strain values resulting in quick drops of the measured strain signal (Fig. 4.30c), as opposed to case 1-1. It is due to the fact that the targeted mode has bigger natural frequency than the currently excited unlocked mode, from which energy is transferred. In this situation, the targeted mode and remaining higher-order unlocked ones vibrate with frequency lower than their natural frequencies. Thus, the energy transferred to the second and higher-order unlocked vibration modes is accumulated mostly as the strain (potential) energy. This structural behaviour is similar to the vibration attenuation (see: Section 4.1), where the energy also is transferred from the lower-order unlocked vibration modes to the higher-order ones. However, in this case due to the negative second weight α_2, the second modal energy usually has a predominant participation in the total strain energy to be released after the joint unlock.

Similarly to the case 1-1, the modal energy transfer to the targeted mode causes an increase in: the relative magnet displacement amplitude, the level of the

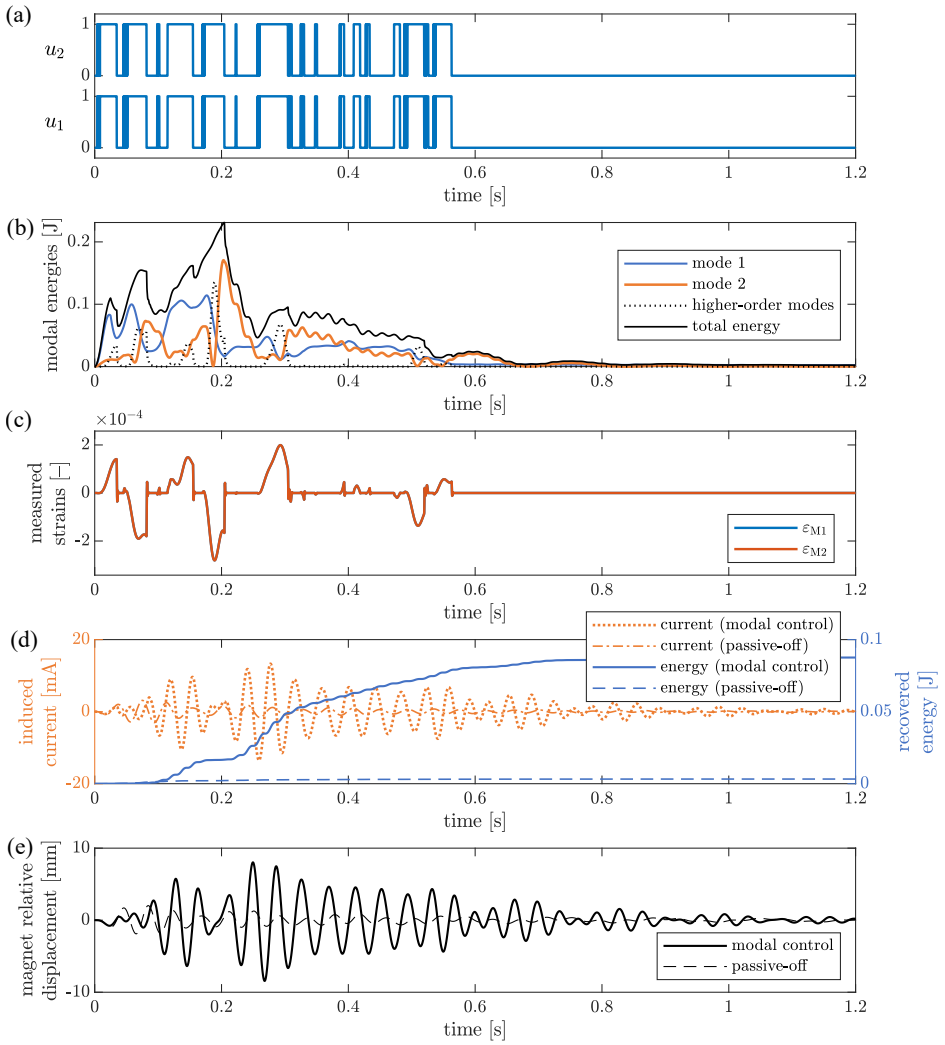

Fig. 4.30. Time histories of: (a) control signals, (b) modal energies of the structure, (c) measured strains, (d) electrical current and energy produced by the EMEH displacements compared with passive-off case and (e) relative magnet displacement compared with the passive-off case for case 1-2 of excitation and configuration 2 of the system.

produced electrical current and recovered energy in relation to the passive-off case (Figs. 4.30d and e). However, the produced energy is more than two times smaller than in the case 1-1 despite the same level of the excitation energy in the sense of Eq. (4.24). The control spillover effect is the first reason. Apart from the targeted vibration mode, some part of the strain energy is released in the free vibration of the higher-order vibration modes after the joint unlock and later quickly dissipated in the material damping (Figs. 4.30a and b). The second

reason is that the second unlocked vibration mode has greater damping than the first one, hence its energy is dissipated slightly quicker. Then, the less amount of the energy can be recovered by EMEH.

Case 2

In this case, kinematic excitation with the amplitude constant over time is considered. However, the amplitude depends on the frequency that provides the constant energy level of the excitation in the sense of Eq. (4.24). The horizontal ground displacement is thus described by the equation below

$$q_{\mathrm{g}}(t) = \frac{A_0}{\Omega_{\mathrm{g}}} \sin \Omega_{\mathrm{g}} t. \tag{4.25}$$

Excitation with the selected $A_0 = 0.03$ sm/rad is used for both configurations of the system – see: Fig. 4.26. The excitation frequencies from range from 1 to 45 Hz is selected. For each frequency of excitation the vibration in the duration time of 10 s is simulated. All results shown in this case are obtained from the last second of this duration in which steady-state of the system is provided.

For both system configurations the algorithm parameters remain the same as for case 1 of the excitation.

Comparison of the results obtained both for controlled and passive-off cases for the configuration 1 of the system is shown in Fig. 4.31. The two resonance peaks of the structural motion for each sensor location (Fig. 4.20b) are visible near to the natural frequency of the first (targeted) unlocked vibration mode (Fig 4.31a). It is due to the fact that the attached EMEH provides the additional mechanical DOF and is tuned to the first unlocked vibration mode. Due to the damping in the system and small mass of the magnet in the EMEH these peaks are not well-separated. In this case, the control does not switch the joint state (Fig. 4.31d) and does not transfer energy between unlocked vibration modes, since the targeted mode is naturally excited. Thus, response of the controlled structure is the same as in the uncontrolled case.

For the excitation frequencies in the vicinity of the second unlocked natural frequency of the structure, the amplitude of q_{M1} is greater than q_{M2} for the passive case. It corresponds with the second unlocked mode shape and is in opposite to structural behaviour in the vicinity of the first natural frequency of the structure. However, for the controlled structure, the amplitude of q_{M1} is lower than that of q_{M2}, as it is the case for the first unlocked structural vibration mode. It is evident that the controlled structure vibrates mainly in the first unlocked vibration mode despite the excitation frequency near to the second unlocked natural frequency. This is the result of energy transfer to the first unlocked vibration mode from the second one.

The phenomenon of the energy transfer is visible also in behaviour of the magnet in EMEH (Fig. 4.31b). In the vicinity of the second natural frequency of the

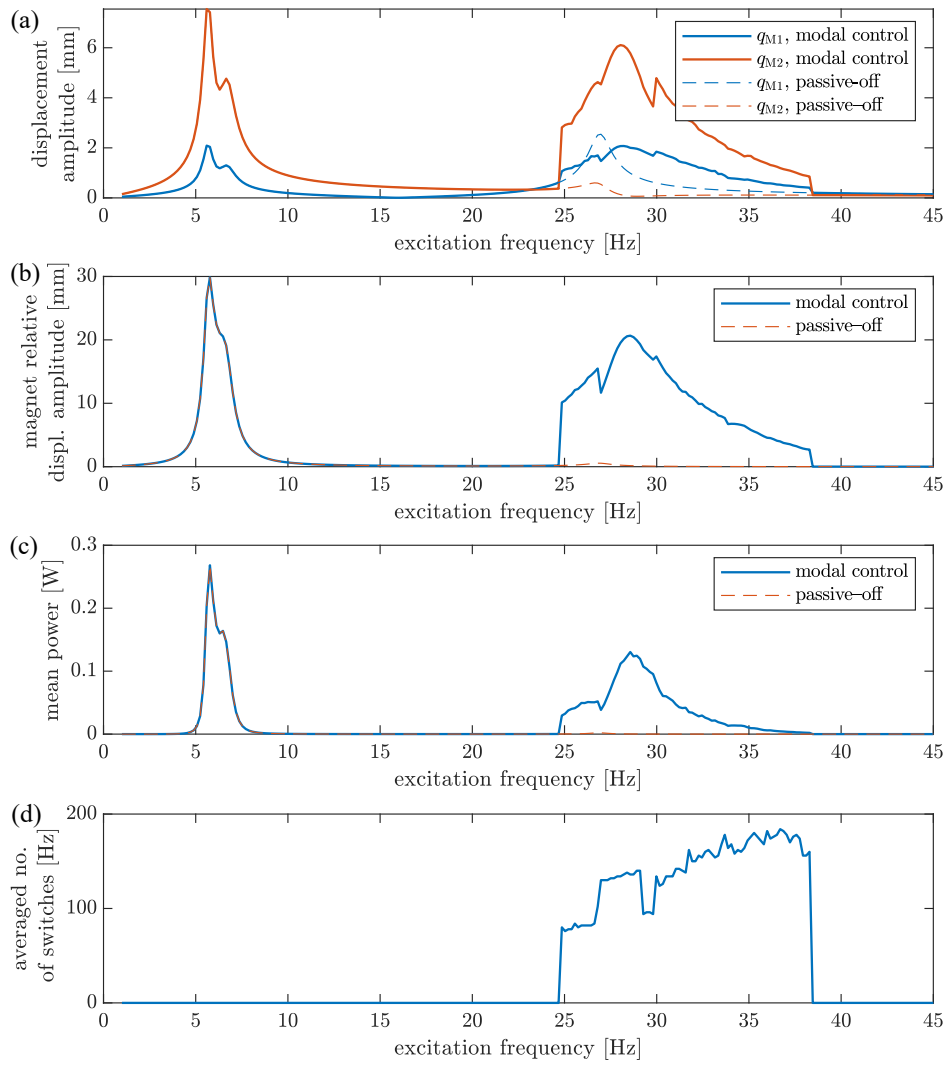

Fig. 4.31. Various quantities characterising steady-state system behaviour in dependence on the frequency of kinematic excitation (case 2) obtained for both controlled and passive-off system in configuration 1: (a) amplitudes of structural displacements at sensor locations, (b) amplitude of the relative magnet motion, (c) mean power produced by the EMEH and (d) averaged number of joint switches $\overline{n}_{\mathrm{J}}$.

structure the magnet reaches an amplitude equal to 2/3 of the amplitude at the first resonance, whereas in the passive-off case it is close to zero. Due to the controlled energy transfer, the generated power in this region is also significantly greater than in the passive-off case, for which almost no energy is recovered (Fig. 4.31c). In the controlled case, the maximum mean power produced by EMEH when the energy is transferred from the second unlocked vibration mode to the

first one is near to half of the maximum average power obtained for the first resonance peak. The power peak related to the modal energy transfer has broadened the frequency range both in relation to the first power peak and to the frequency range of the second unlocked vibration mode.

It is visible that for the frequency range in which modal energy transfer occurs the state of lockable joints is switched with a mean frequency below 200 Hz. This quantity increases with the excitation frequency, which is typical behaviour. Joints suddenly stop their operation below 25 Hz and above 38 Hz of the excitation frequency. It is due to the selected threshold κ_1 preventing from the frequent joint switches when energy transfer rates are small due to small vibration amplitudes.

Results for the configuration 2 of the system are shown in Fig. 4.32. The first observation is that the operation of the lockable joints caused a significant reduction (near to 10 times) in the vibration amplitude near the first resonance (Fig. 4.32a). The first reason is that the joints are unlocked at time instances when strains are not equal to zero. Then, some part of energy is released in the higher-order unlocked vibration modes and the vibration is mitigated, as described in case 1-2. The second reason is that the amplitude of vibration in the second unlocked vibration mode, to which energy is transferred, is significantly smaller than in the first one for the same level of the mechanical energy. As contrary to the results shown in Fig. 4.31a, after the transfer of the energy to the targeted mode the amplitudes of structural displacements at particular sensor locations do not change their order. It is due to the smaller amplitude of the second, targeted, unlocked vibration mode and still non-negligible participation of the first unlocked mode in the structural vibration.

The two resonance peaks in the vicinity of the second natural frequency of the structure (visible from 20 to 35 Hz) are the result of the influence of EMEH on structural dynamics. Here, EMEH tuned to the second unlocked vibration mode behaves similarly to TMD, analogously to the results for configuration 1 of the system. However, the two new peaks are well-separated for EMEH tuned to the second unlocked vibration mode. The main reason is the increased stiffness of the EMEH spring aiming at tuning of the EMEH to the second unlocked vibration mode.

The amplitude of the relative magnet displacement in the controlled case is significantly increased with respect to the passive case in the vicinity of the first natural frequency of the structure (Fig. 4.32b). It confirms that energy is transferred to the second unlocked vibration mode, to which EMEH is tuned. The amplitude of the relative magnet displacement resulting from the modal energy transfer to the targeted mode is near to half of the maximal amplitude that is achieved in the resonance at 24 Hz.

Regarding the power generated by the EMEH device, the peak efficiency is slightly smaller than for the previous system configuration but the corresponding

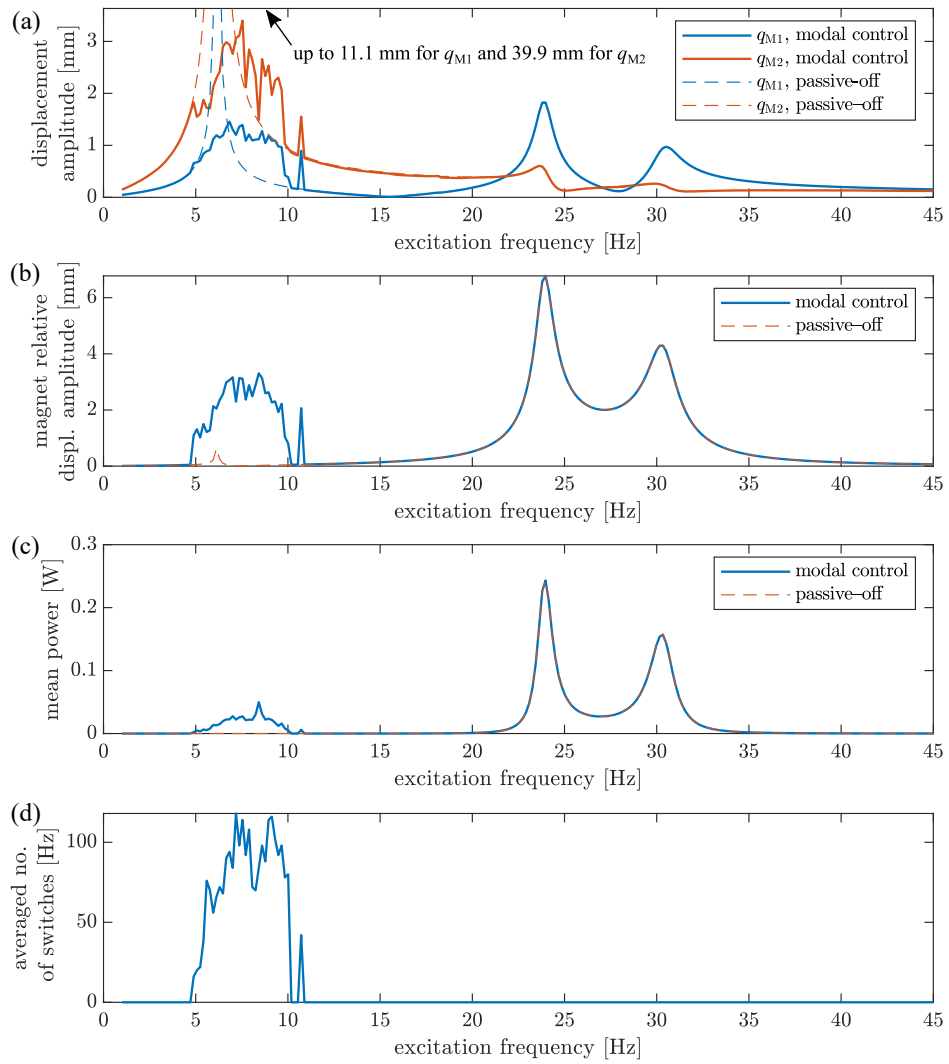

Fig. 4.32. Various quantities characterising steady-state system behaviour in dependence on the frequency of kinematic excitation (case 2) obtained for both controlled and passive-off system in configuration 2: (a) amplitudes of structural displacements at sensor locations, (b) amplitude of the relative magnet motion, (c) mean power produced by the EMEH and (d) averaged number of joint switches $\overline{n}_{\mathrm{J}}$.

operational frequency bandwidth is wider (compare: Fig. 4.31c and Fig. 4.32c). However, both the bandwidth and level of the generated power for the configuration 2 of the system when energy is transferred from the first unlocked vibration mode are significantly smaller than for configuration 1 when energy is transferred from the second unlocked vibration mode to the first one. The

corresponding bandwidth is 2.5 times narrower and the corresponding generated power level is near to 3 times smaller.

The frequency range in which the modal energy transfer occurs corresponds to the range in which the lockable joints are switched (Fig. 4.32d), analogously to the previous system configuration. Here, the averaged number of switches achieves the level around 100 Hz or is below. It is lower than in the previous system configuration due to the fact that in the present system configuration the joints operate for lower frequencies of excitation aiming at transferring energy in the reversed direction (from the first to the second unlocked mode).

Case 3

In this case the system is excited by the inertia force described analogously to Eq. (4.8) but the additional DOF related to the EMEH magnet motion is taken into account ($\mathbf{M}_{\mathrm{u}}$ and $\mathbf{l}_{\mathrm{xu}}$ are considered instead of $\mathbf{M}$ and $\mathbf{l}_{\mathrm{x}}$, respectively). Here, the noise magnitude (standard deviation) $\sigma_a = 75$ m/s^2. Results discussed in this case are averaged from 1000 simulations. In each such a simulation, the duration time is 30 s, where the last 20 s is taken for calculations of the results. In such a way the two structure configurations are tested to assess the ability

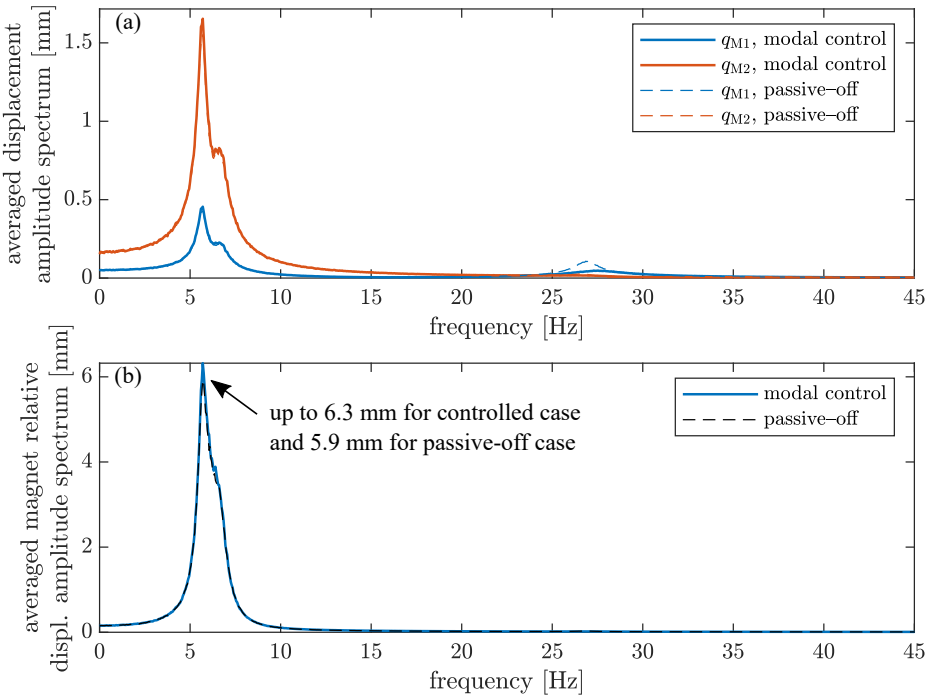

Fig. 4.33. Averaged amplitude spectra of: (a) structural displacement at sensor locations and (b) magnet relative displacement obtained for the configuration 1 and excitation case 3, compared with results obtained for uncontrolled structure (passive-off).

of the control algorithm to transfer the energy to the first and second unlocked vibration mode. For both system configurations algorithm parameters remain the same as for the case 1 of excitation.

Performance metrics for the configuration 1 of the system are shown in Fig. 4.33. In this case the noise kinematic excitation causes vibration mainly in the first unlocked vibration mode (targeted one). Thus, the amount of the energy transferred to this mode is negligible. It is visible in Fig. 4.33a, where resonance peaks of the amplitude spectra corresponding to controlled and passive-off case almost overlap in the vicinity of the first structural natural frequency. The modal energy transfer is visible in these metrics due to a reduction in the resonance peak corresponding to the second structural unlocked vibration mode. Energy from this mode is transferred to the first one that results in small increment of the amplitude of the magnet relative displacement (Fig. 4.33b).

Corresponding performance metrics obtained for the configuration 2 of the system are shown in Fig. 4.34. Here, similarly to the case 2 of the excitation, the amplitude spectra for the first structural unlocked vibration mode are significantly reduced (Fig. 4.34a). The first reason is the control spillover effect. The energy is undesirably transferred to the higher-order unlocked vibration modes

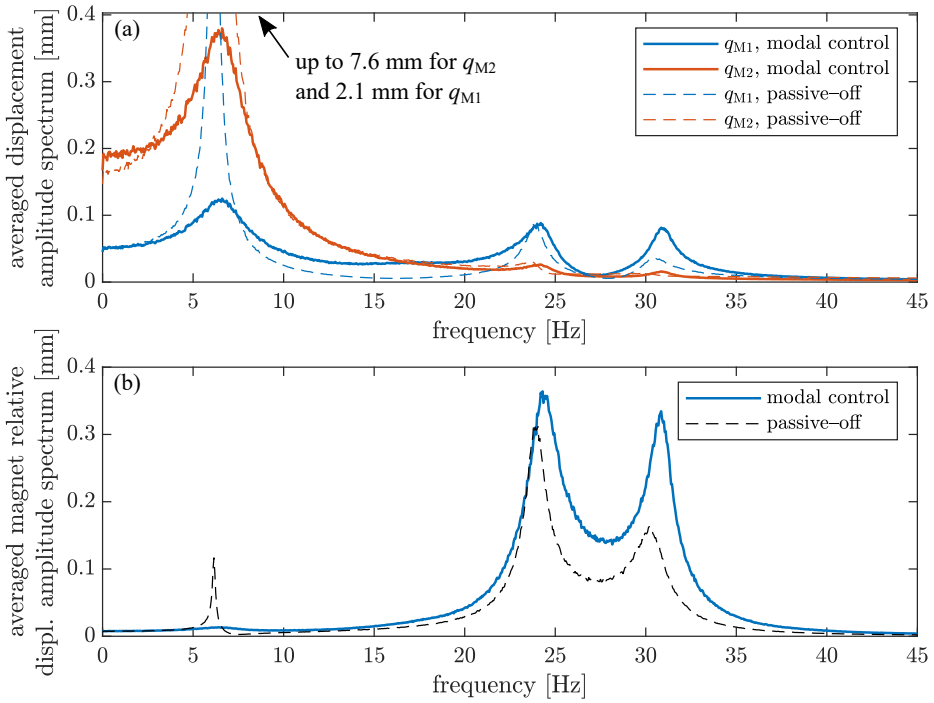

Fig. 4.34. Averaged amplitude spectra of: (a) structural displacement at sensor locations and (b) magnet relative displacement obtained for the configuration 2 and excitation case 3, compared with results obtained for uncontrolled structure (passive-off).

and dissipated in the material damping. It is described in detail in case 1-2. The second reason is, as mentioned in the case 2, disproportion between modal energy and corresponding structural displacement amplitudes for subsequent mode orders. Thus, relatively small but noticeable increment of the amplitude spectra near to the second natural frequency of the structure is achieved at the expense of the large decrement in the first resonance peak due to the modal energy transfer provided by operation of the lockable joints.

Operation of the control algorithm results in the increment of the relative magnet displacement amplitude spectrum in the vicinity of the second structural unlocked vibration mode (Fig. 4.34b). It is visible for both resonance peaks related to the operation of the EMEH but the second one is characterised by the greater increment than the first one. A small peak corresponding to the first structural unlocked vibration mode is present in the passive-off case due to the relatively big amplitude of the structural vibration. For the controlled case the vibration in this mode is significantly reduced and the resonance peak is not distinguishable.

Table 4.8 summarizes effectiveness of the control for both system configurations. $\delta\overline{P}$ is relative increment of the mean power produced by the EMEH (Eq. (4.13)) defined by the following equation:

$$\delta\overline{P} = \frac{\overline{P}_{\mathrm{c}} - \overline{P}_{\mathrm{off}}}{\overline{P}_{\mathrm{off}}}, \tag{4.26}$$

where subscripts “c” and “off” refer to the controlled and passive-off case, respectively.

Table 4.8. Comparison of performance metrics of the energy harvesting systems in configuration 1 and 2 the case 3 of excitation, averaged from 1000 simulations.

System configuration	Control state	$\overline{P}$ [mW]	$\delta\overline{P}$ [%]	$\overline{n}_{\mathrm{J}}$ [Hz]
Configuration 1	controlled	283.0	6.3	79.2
	passive-off	266.2		–
Configuration 2	controlled	88.8	169	134.1
	passive-off	33.0		–

It is evident that the mean power produced by EMEH in the controlled case is near three times greater for the configuration 1 of the system than for the configuration 2. It is due to the fact that the first unlocked vibration mode (the targeted one in the configuration 1) of the controlled structure is more sensitive to the kinematic excitation. After substitution of Eq. (4.8) into Eq. (2.60) we can see that modal forces for the first and second unlocked vibration mode are

proportional to: $|\boldsymbol{\phi}^{(1)\mathrm{T}}\mathbf{M}\mathbf{l}_{\mathrm{x}}| = 1.81$ and $|\boldsymbol{\phi}^{(2)\mathrm{T}}\mathbf{M}\mathbf{l}_{\mathrm{x}}| = 0.85$, respectively. Amplitudes referring to the inertia force have greater participation in the first unlocked mode shape than in the second one. Moreover, the first unlocked vibration mode is less damped than the second one (Fig. 4.23). Thus, despite the fact that for the configuration 2 the 169 % increment of the generated power is achieved, the configuration 1 provides significantly better performance of the system even without energy transfer, as in the passive-off case.

The averaged number of joint switches presented in Table 4.8 is calculated analogously as in Eq. (4.9) and averaged from 1000 simulations. It is greater for the configuration 2 than for the configuration 1, as opposed to case 2 of excitation. Case 2 is affected by the excitation frequency for which the transfer occurs (Figs. 4.31d and 4.32d), however, in the present case excitation for both configurations is of random type. Hence, in this case, the other influencing factor is the natural frequency of the targeted mode. The second monitored modal velocity typically changes its sign more frequently than the first one (e.g., during free vibration), and therefore the corresponding estimated weighted modal energy transfer rates cross the selected thresholds in Algorithm 2 more often. In the results, Algorithm 2 switches the joint state more frequently for configuration 2.

From the numerical study discussed in this subsection it follows that the energy harvesting system should be designed in such a way that the targeted mode is the most sensitive to expected excitations and is within their frequency range. Energy transfer from other unlocked vibration modes should be treated as additional possibility for expanding of the operational frequency bandwidth. Moreover, it is also desired that the targeted mode has lower natural frequency than other unlocked vibration modes within the considered frequency range. It is due to the control spillover effect, which occurs when the targeted unlocked vibration mode has greater order than the currently excited ones, resulting in undesirable transfer of the mechanical energy to the unmonitored (higher-order) vibration modes. Moreover, lower-order unlocked vibration modes are usually less damped which is also an advantage when selecting the target mode. However, if the control system is installed on the structure for both vibration mitigation and energy recovery, then these recommendations are not the most suitable. Here, the one of the highest-order unlocked vibration modes among the monitored ones should be selected as the targeted mode. Numerical results obtained for configuration 2 of the system demonstrate that simultaneous vibration mitigation and additional vibration recovery are possible. Vibration mitigation in this configuration occurs even if it is not the purpose of the control. Moreover, weights α_p can be switched on-line during the operation of the control algorithm giving greater flexibility and its adaptation to the current operation purposes or emergency situations, in which the damping has the biggest priority.

5. Experimental verification

In this chapter, a laboratory-scale frame demonstrator equipped with six lockable joints first is introduced and described (Section 5.1) along with its locked vibration modes (the reason of using the locked vibration modes also is explained). Later, in Section 5.2, the FE model of the structure is presented, followed by a model updating procedure based on modal data obtained for locked joints. Equipment limitations, hardware control loop and preparation of the control algorithm is described in Section 5.3. In Section 5.4, experimental results of vibration attenuation are analysed and compared with those obtained from numerical simulations using the updated FE model. Both free and forced vibrations are considered. A similar comparison of the energy transfer to a preselected vibration mode is discussed in Section 5.5.

5.1. Experimental setup

5.1.1. Smart structure equipped with 6 semi-active joints

A smart structure under consideration is the laboratory-scale frame equipped with six lockable joints. Its scheme and dimensions are shown in Fig. 5.1a, while

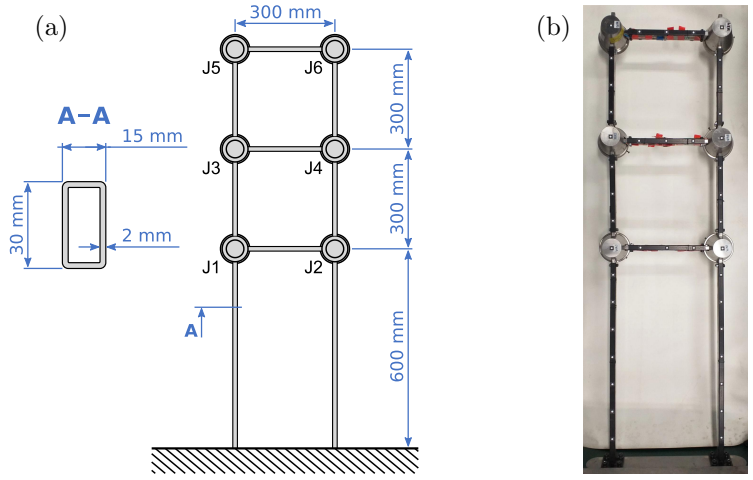

Fig. 5.1. Laboratory frame structure: (a) scheme with structural dimensions and numeration of the lockable joints, and (b) its photograph [152].

its photo is presented in Fig. 5.1b. The locking effect in the joints is achieved by a clamping force sufficient to prevent relative rotation between the frictional contact surfaces. The working principle of the joint and structure is similar to one shown in Fig. 2.10b but in the employed real lockable joint, the friction interface is conical in shape. Beams are connected to the friction parts in such a way that rotations of ends of transversal beams can be coupled or decoupled with rotation of longitudinal beams at corresponding locations if the joints are currently locked or unlocked, respectively. The lockable joints always transmit a bending moment between longitudinal beams, independently of the control signals. This also can be deduced from details shown in Fig. 5.2, where both adjacent longitudinal beams are connected to one casing, whereas transversal beam is connected to inner part of the joint that can rotate relative to the casing (when the joint is unlocked).

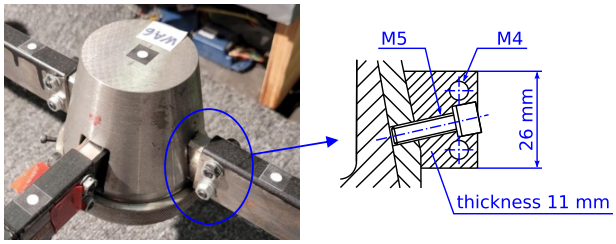

Fig. 5.2. Details of the bolted connection between lockable joint and beam [153].

The lockable joints utilized for the experimental verification are designed in such a way that when they are not supplied with any voltage they are locked by the inner springs providing a clamping force between the friction parts. When the appropriate voltage is supplied then the piezo stack unlocks the joint. This action does not change the adopted convention of description of the control signal. Still, $u_k(t) = 0$ denotes that the joint is unlocked, whereas $u_k(t) = 1$ denotes the locked state of the joint. The delay in unlocking the joint relative to the change in the control signal is 3 ms. The delay in locking is not known precisely but it is assumed to have a similar value. The maximal operational frequency of the lockable joints is 300 Hz.

The clamping force provided by the inner springs is sufficient to prevent the sliding between friction parts if the assumed maximal transmitted bending moment $f_k^{\mathrm{l}\max}$ is not exceeded. Unfortunately, when the joint is in the unlocked state the friction parts are not completely detached. It results in residual friction between friction parts. Thus, for a sufficiently small level of vibration the bending moment transmitted by the lockable joint does not exceed the maximal value $f_k^{\mathrm{u}\max}$ corresponding to the maximal value of residual static friction between friction surfaces. In this scenario, there is no difference in behaviour of the unlocked and locked state of the joint. The maximal bending moments

$f_k^{\mathrm{l\,max}}$ and $f_k^{\mathrm{u\,max}}$ that can be transmitted by the lockable joints in the locked and unlocked state, respectively, without the sliding effect are listed in Table 5.1. Numeration of the lockable joints is consistent with Fig. 5.1a. The discrepancies in the transmitted bending moments of particular lockable joints result not only from the operational wear but also from the fact that various generations of the joint prototypes are employed.

Table 5.1. Maximal bending moments transmitted by the lockable joints corresponding to their locked and unlocked states.

Joint no.	J1	J2	J3	J4	J5	J6
$f_k^{\mathrm{u\,max}}$ [Nm]	2	2.2	1.5	1.5	2	2
$f_k^{\mathrm{l\,max}}$ [Nm]	16	16	38	31	31	37

The lockable joints are connected with the beams via bolted connections. Details of such a connection are shown in Fig. 5.2. The bolted connection should not be modeled as ideally rigid, as this would lead to significant discrepancies in natural frequencies and mode shapes compared to the actual structure, as demonstrated in [152]. Section 5.2 discusses modelling and parametric identification of the stiffness of the bolted connection aiming at reproduction of the structural behaviour by the FE model. To this end, the modal data (natural frequencies and mode shapes) of the frame structure are used. These data are described in the subsection below.

5.1.2. Experimental modal analysis

Modal data from the frequency range 0–960 Hz are extracted via modal analysis. To this end, four three-directional accelerometers are used. A dense mesh of measurement points distributed with the spatial resolution 75 mm along structural members is achieved with the roving accelerometer technique. It results in 41 sensor locations and 123 measured outputs. The structure is excited using a modal hammer. Hardness of the modal hammer tip is increased for subsequent frequency sub-ranges that are: 0–25 Hz, 25–150 Hz, 150–280 Hz, 280–360 Hz, 360–450 Hz, 450–660 Hz and 660–960 Hz. Measurement data are collected and analysed with the aid of the LMS SCADAS system integrated with LMS Test.Lab software. The stochastic subspace identification method is used.

Due to the fact that lockable joints keep a residual clamping force in the unlocked state they introduce a certain friction-based bending moment resulting in nonlinearities and strongly non-proportional damping of the system. Therefore, experimental modal analysis is conducted exclusively with the joints in the locked state to avoid the aforementioned undesired effects. The FE model is updated solely by changing the stiffness of the bolted connections. Thus, it can also

be updated with joints in the locked state and after unlocking the stiffness of the bolted connections will be preserved.

25 three-dimensional locked mode shapes, natural frequencies and modal damping factors are extracted. They are shown in Appendix A[1]. As described in the appendix, 10 in-plane (IP) vibration modes are selected for the model updating purposes, since out-of-plane vibration modes are not controllable by the lockable joints. The selected IP modes are shown in Fig. 5.3.

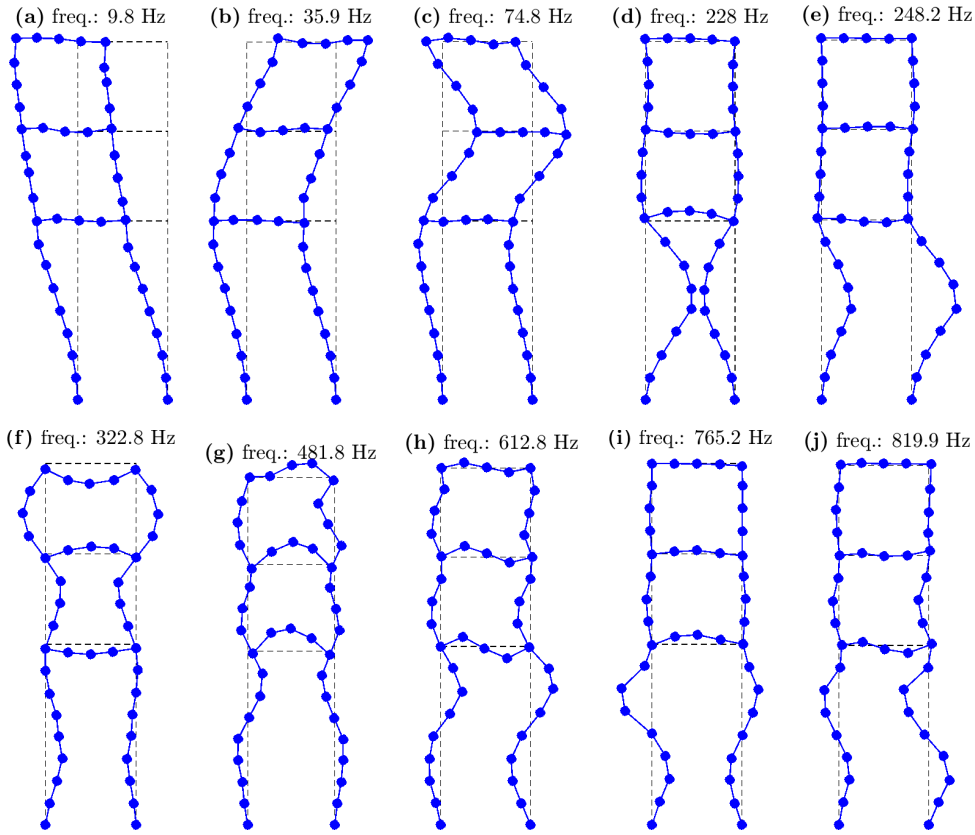

Fig. 5.3. Measured locked vibration modes selected for the model updating.

Mode shapes shown in Fig. 5.3 contain many shape deviations including asymmetry. It shows that bolted connections (Fig. 5.2) are highly uncertain due to the operational wear of the structure and assembly discrepancies.

[1]The identified modal parameters are slightly different from those shown in [152] due to the fact that the frame has been disassembled, renovated, and reassembled again before modal analysis described in this thesis.

5.2. Numerical model of the real structure

5.2.1. Initial finite element model

As mentioned in Subsection 5.1.2, the FE model is to be updated using experimental modal data obtained for the joints in the locked state. Hence, the locked vibration modes obtained from the FE model are also used for comparison. To this end, the locking effect is obtained by pursuing an exact kinematic constraint on DOFs involved in the lockable joints (Eq. (2.37)). The resulting model is reduced by six DOFs (one rotational DOF per lockable joint).

A FE model $(\widetilde{\mathbf{M}}, \widetilde{\mathbf{K}}(\boldsymbol{\theta}))$ of class $\mathcal{C}$ is considered for model updating. Matrices $\widetilde{\mathbf{M}}$ and $\widetilde{\mathbf{K}}(\boldsymbol{\theta})$ refer to the FE model with locked joints and can be obtained with transformation as in Eq. (2.58). $\widetilde{\mathbf{M}}$ is assumed to be known, whereas $\widetilde{\mathbf{K}}(\boldsymbol{\theta})$ depends on the unknown parameter vector $\boldsymbol{\theta} = \begin{bmatrix}\theta_1 & \theta_2 & \cdots & \theta_{N_\theta}\end{bmatrix}^{\mathrm{T}}$ as follows:

$$\widetilde{\mathbf{K}}(\boldsymbol{\theta}) = \widetilde{\mathbf{K}}_0 + \sum_{t=1}^{N_\theta} \theta_t \widetilde{\mathbf{K}}_t, \tag{5.1}$$

where: $\widetilde{\mathbf{K}}_0$ is matrix representing stiffness of well-known components of the structure, θ_t is unknown parameter scaling matrix $\widetilde{\mathbf{K}}_t$ associated with the components of the structure with uncertain stiffness.

The FE model of the structure is shown in Fig. 5.4a. Behaviour of the bolted connection is reproduced by nominal rotational stiffness k_{R} scaled by an unknown

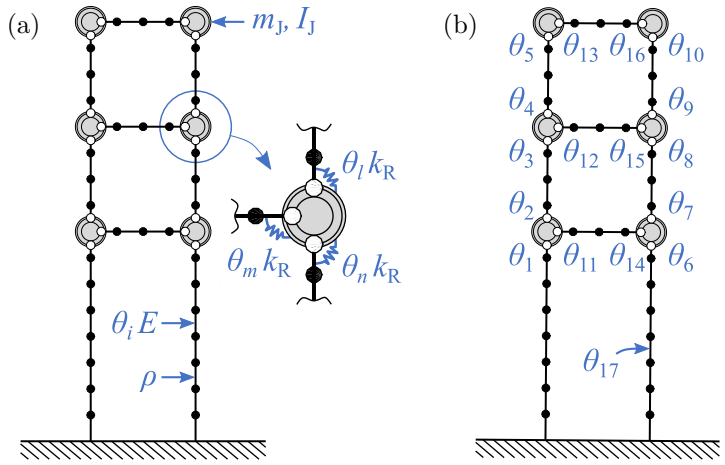

Fig. 5.4. Structural FE model to be updated [152]: (a) FE mesh with assigned physical properties and (b) assigning of the unknown parameters to the bolted connections and Young modulus of the beams.

parameter θ_t as shown in the zoomed area. For the t-th bolted connection matrix $\widetilde{\mathbf{K}}_t$ is defined as follows:

$$\widetilde{\mathbf{K}}_t = k_{\mathrm{R}} \widetilde{\mathbf{b}}_t \widetilde{\mathbf{b}}_t^{\mathrm{T}}, \tag{5.2}$$

where the vector

$$\widetilde{\mathbf{b}}_t = [0 \ \cdots \ 0 \ 1 \ 0 \ \cdots \ 0 \ -1 \ 0 \ \cdots \ 0]^{\mathrm{T}}$$

selects DOFs involved in t-th bolted connection (that differ from DOFs selected by the vector $\mathbf{l}_k$ described in Subsection 2.2.2).

Additionally, the Young modulus of the material of beams is also scaled by the unknown parameter. Finally, the structure is parameterized with 17 unknown parameters: 16 for all bolted connections (each bolted connection is parameterized independently) and one for stiffness of all beams by scaling the Young modulus (a common parameter for all beams), as shown in Fig. 5.4b.

Physical properties are listed in Table 5.2 along with FE model parameters. Due to the fact that joints are kept in the locked state they are treated as rigid bodies with mass m_{J} and inertia moment I_{J}. Beam structural members are represented by beam FEs based on the Euler–Bernoulli beam theory. Each beam FE has 6 DOFs (in-plane motion). Its transversal motion is described by cubic shape functions, whereas longitudinal deformation by linear shape functions. FE mesh nodes on the beams are consistent with accelerometer locations, excepting beam ends (compare Figs. 5.4 and 5.3). Then, a length of particular FEs belonging to one structural beam is not constant. However, bending moments transmitted by the beams connected to the locked joints are usually greatest at their ends, thus it is desirable to use the denser FE mesh in these regions.

Table 5.2. Properties of the FE model of the structure.

Quantity	Symbol	Units	Value
Young modulus (steel)	E	[Pa]	$210 \cdot 10^9$
Material density (steel)	ρ	[kg/m^3]	7840
Geometric moment inertia of the beam cross-section	I	[mm^4]	5554
Area of the cross-section of the beam	A	[mm^2]	164
Total mass of the semi-active joint	m_{J}	[kg]	1.86
Total mass moment of inertia of the locked joint	I_{J}	[kg $\cdot$ mm^4]	$1.55 \cdot 10^9$
Nominal rotational stiffness of the bolted connection	k_{R}	[Nm/rad]	10^4
Total no. of DOFs (unlocked joints)	N_{d}	[–]	145
Reduced no. of DOFs (locked joints)	$N_{\mathrm{d}} - N_k$	[–]	139

The selected value of the nominal rotational stiffness k_{R} (Table 5.2) is within the highest sensitivity range of the numerical modal parameters to the changes of the rotational stiffness of the bolted connections (when $\theta_t = 1$, $t = 1, 2, ..., 17$).

It improves estimation accuracy of the unknown parameters (see Subsection 5.2.2). k_{R} much below of the selected value could cause behaviour of the bolted connection similar to the hinge, whereas too big k_{R} could cause that the bolted connection behaves as a semi-rigid joint. In both cases, sensitivity of the numerical modal parameters to the stiffness of the bolted connection is too low to provide reliable model updating [154]. The sensitivity range and selection of the nominal rotational stiffness for the structure under consideration in this thesis is investigated in [152].

After the stage of model updating, when the FE model is used for the controller design and simulation, the joint can be unlocked and, in consequence, the total mass moment of inertia of the locked joint I_{J} (see Table 5.2) is divided into moment of inertia $I_{\mathrm{J1}} = 1.21 \cdot 10^9$ kg $\cdot$ mm^4 related to the rotational DOF belonging to the longitudinal beams and $I_{\mathrm{J2}} = 3.41 \cdot 10^8$ kg $\cdot$ mm^4 related to the end of transversal beam. The total mass of the lockable joint m_{J} does not have to be divided, since translational DOFs are not decoupled when the joint is unlocked.

5.2.2. Model updating

Classical model updating methods can be divided into two groups according to the type of model that is to be updated and the way they find the updated model [155]: direct methods and iterative methods. Direct methods are faster but have many significant disadvantages. They usually tend to exactly reproduce the measurement data, including the measurement noise. Thus, high-accuracy of measurement is a prerequisite. The direct methods often operate on entire matrices representing the updated model, e.g. mass and stiffness matrices. Thus, they require extrapolation of the measurement data from the measurement locations to the configuration space of the FE model or reduction of the FE model to the configuration space related to sensor locations. Moreover, the physical meaning provided by the updated mass and stiffness matrices is limited and the updated model often reproduces only the data to which was calibrated, whereas it may be not able to reproduce behaviour of the real system in any other scenario. There is also a possibility to introduce the spurious modes. As opposed, the iterative methods operate on the parametric model, whose example is described in Section 5.2, which enables selection of the parameters that are to be updated. These parameters are physically meaningful. Iterative methods demand higher computational burden and require a physical insight to select updated parameters; however, they avoid disadvantages of the direct methods.

Among iterative methods of model updating based on the experimental modal data the two ones are widely accepted: mode matching and the Bayesian approach proposed by Yuen *et al.* Mode matching is based on sensitivity of the modal parameters with respect to $\boldsymbol{\theta}$. It minimises a norm of error between nu-

merical and experimental modal data [155, 156]. However, measured modal data can be incomplete (missing some of subsequent modes) and, in addition, numerical vibration modes obtained from the FE model may have an order different from the experimental ones. Moreover, the order of numerical vibration modes can be switched during the model updating procedure due to changing unknown parameters representing structural properties. Thus, each iteration step requires matching of the numerical modal data with the corresponding experimental data which allows for proper calculation of the error norm and its derivatives. It is reflected in the name of the method. Usually, experimental and numerical modes are matched according to the highest MAC value. Mode matching problem can be avoided using the Bayesian probabilistic framework for parametric identification of the structural stiffness proposed by Yuen *et al.* [157, 158]. However, identified modal parameters shown in Fig. 5.3 have sufficient number of sensor locations for calculation of MAC between experimental modes and their numerical counterparts allowing for reliable mode matching. Moreover, a comprehensive comparison provided by Ostrowski *et al.* [152] demonstrates that the method proposed by Yuen *et al.*, despite its advantages, should not be recommended for identification of rotational stiffness of the structural members. For the considered class of problems, this method is characterised by very slow convergence, resulting in tremendous computational burden required to find stiffness parameter values. The method also creates numerical problems resulting in unreliable estimation of parameter variances. Mode matching is devoid of these disadvantages: it finds stiffness parameters quickly (tens of iterations vs. hundreds of thousands of iterations) and allows for reliable estimation of variances. Due to its performance in estimation of rotational stiffness parameters, mode matching is adopted, in this thesis, to update of the considered FE model.

Mode matching: optimization problem

The mode matching method solves the optimization problem:

$$\begin{array}{ll} \text{Find} & \boldsymbol{\theta} \in \mathbb{R}_{+}^{N_\theta} \\ \text{to minimise} & \varepsilon(\boldsymbol{\theta}), \end{array} \tag{5.3}$$

where:

$$\varepsilon(\boldsymbol{\theta}) = \mathbf{e}^{\mathrm{T}}(\boldsymbol{\theta}) \mathbf{W}_{\mathrm{e}} \mathbf{e}(\boldsymbol{\theta}), \tag{5.4}$$

is the objective function representing the weighted square error between numerical and experimental vibration modes. Such a weighted norm is a widely accepted measure of error for a model updating engineering structures [153, 155, 156, 159–162]. In the equation above $\mathbf{W}_{\mathrm{e}}$ is the selected weighting matrix and the vector $\mathbf{e}(\boldsymbol{\theta})$ collects errors between modal parameters including both locked eigenvalues (squares of corresponding natural frequencies) and locked mode shapes:

$$\mathbf{e}(\boldsymbol{\theta}) = \begin{bmatrix} \widetilde{\boldsymbol{\lambda}}_{\mathrm{exp}} \\ \widetilde{\boldsymbol{\psi}}_{\mathrm{exp}} \end{bmatrix} - \begin{bmatrix} \widetilde{\boldsymbol{\lambda}}(\boldsymbol{\theta}) \\ \mathbf{L}_{\mathrm{o}} \widetilde{\boldsymbol{\phi}}(\boldsymbol{\theta}) \end{bmatrix}, \tag{5.5}$$

where: vectors $\widetilde{\boldsymbol{\lambda}}_{\mathrm{exp}} = \begin{bmatrix} \widetilde{\lambda}_{\mathrm{exp}}^{(1)} & \cdots & \widetilde{\lambda}_{\mathrm{exp}}^{(N_{\mathrm{M}})} \end{bmatrix}^{\mathrm{T}} \in \mathbb{R}^{N_{\mathrm{M}}}$, $\widetilde{\lambda}_{\mathrm{exp}}^{(1)} = \widetilde{\omega}^{(m)2}$, and $\widetilde{\boldsymbol{\psi}}_{\mathrm{exp}} = \begin{bmatrix} \widetilde{\boldsymbol{\psi}}_{\mathrm{exp}}^{(1)\mathrm{T}} & \cdots & \widetilde{\boldsymbol{\psi}}_{\mathrm{exp}}^{(N_{\mathrm{M}})\mathrm{T}} \end{bmatrix}^{\mathrm{T}} \in \mathbb{R}^{N_{\mathrm{M}} N_{\mathrm{o}}}$ involve N_{M} experimental locked eigenvalues and experimental locked mode shapes, respectively, N_{o} is the number of measured outputs. Analogously, vectors $\widetilde{\boldsymbol{\lambda}}(\boldsymbol{\theta}) \in \mathbb{R}^{N_{\mathrm{M}}}$ and $\widetilde{\boldsymbol{\phi}}(\boldsymbol{\theta}) \in \mathbb{R}^{N_{\mathrm{M}} N_{\mathrm{d}}}$ contain matched numerical locked eigenvalues $\widetilde{\lambda}^{(k_m)}(\boldsymbol{\theta})$ and scaled numerical locked mode shapes $c_m \widetilde{\boldsymbol{\phi}}^{(k_m)}(\boldsymbol{\theta}) \in \mathbb{R}^{N_{\mathrm{d}}}$, where c_m is the modal scale factor

$$c_m = \frac{\widetilde{\boldsymbol{\psi}}_{\mathrm{exp}}^{(m)\mathrm{T}} \mathbf{D} \widetilde{\boldsymbol{\phi}}^{(k_m)}}{\left\| \mathbf{D} \widetilde{\boldsymbol{\phi}}^{(k_m)} \right\|^2}. \tag{5.6}$$

Usually, $\mathbf{D} \in \{0,1\}^{N_{\mathrm{o}} \times N_{\mathrm{d}}}$ is the Boolean matrix selecting the measured DOFs from numerical mode shapes but as mentioned earlier the FE mesh is not consistent with all measured locations. Thus, in this case, $\mathbf{D} \in \mathbb{R}^{N_{\mathrm{o}} \times N_{\mathrm{d}}}$ is the sparse transformation matrix. $\mathbf{L}_{\mathrm{o}} \in \mathbb{R}^{N_{\mathrm{M}} N_{\mathrm{o}} \times N_{\mathrm{M}} N_{\mathrm{d}}}$ in Eq. (5.5) is a block-diagonal matrix composed of matrices $\mathbf{D}$. Numerical vibration modes are matched (paired) to the experimental modes according to the highest MAC value. For each m-th experimental vibration mode, the index k_m of the numerical vibration mode is obtained as follows:

$$k_m = \arg\max_{k} \left[\mathrm{MAC}\left(\widetilde{\boldsymbol{\psi}}_{\mathrm{exp}}^{(m)}, \mathbf{D} \widetilde{\boldsymbol{\phi}}^{(k)}(\boldsymbol{\theta}) \right) \right]. \tag{5.7}$$

Seeking simplification of notation, indices k_m of the numerical locked vibration modes are replaced with indices of the corresponding experimental locked modes m in the further part of the thesis.

It is recommended to select the weighting matrix as reciprocal to the measurement covariance matrix $\boldsymbol{\Sigma}_{\mathrm{M}} \in \mathbb{R}^{N_{\mathrm{M}}(N_{\mathrm{o}}+1) \times N_{\mathrm{M}}(N_{\mathrm{o}}+1)}$ describing uncertainties of measured modal parameters (both eigenvalues and mode shapes). If $\boldsymbol{\Sigma}_{\mathrm{M}}$ is not known one can assume the following form of the weighting matrix:

$$\mathbf{W} = \mathrm{diag}\left(\begin{bmatrix} \dfrac{1}{\widetilde{\lambda}_{\mathrm{exp}}^{(1)2}}, & \cdots & \dfrac{1}{\widetilde{\lambda}_{\mathrm{exp}}^{(N_{\mathrm{M}})2}}, & \dfrac{w_\psi}{\left\| \widetilde{\boldsymbol{\psi}}_{\mathrm{exp}}^{(1)} \right\|^2} \mathbf{1}_{\mathrm{o}}^{\mathrm{T}}, & \cdots & d \dfrac{w_\psi}{\left\| \widetilde{\boldsymbol{\psi}}_{\mathrm{exp}}^{(N_{\mathrm{M}})} \right\|^2} \mathbf{1}_{\mathrm{o}}^{\mathrm{T}} \end{bmatrix}^{\mathrm{T}} \right), \tag{5.8}$$

where: w_ψ is the selected coefficient reflecting level of the measurement discrepancies of the mode shapes and $\mathbf{1}_{\mathrm{o}}$ is the vector containing N_{o} ones. Such a form of the matrix relates to the fact that variances of eigenvalues are near-proportional to their squared expected values.

Gauss-Newton minimisation for model updating

The optimisation problem shown in Eq. (5.3) is the weighted nonlinear least square problem. The nonlinearities result from the nonlinear dependence of the numerical modal parameters in Eq. (5.5) on the unknown parameter vector $\boldsymbol{\theta}$. Thus, the Gauss–Newton method, which is widely accepted for minimisation of such objective functions, is selected [163]. Friswell and Mottershead adopted this method for various model updating problems discussed in [155]. For the considered case, modal parameters in Eq. (5.5) are locally linearized with respect to unknown parameters. It results in the following function that is to be minimised with respect to increment of the unknown parameter vector $\boldsymbol{\Delta\theta}$ in each iteration step of the optimisation process:

$$J_\varepsilon(\boldsymbol{\Delta\theta}) = \left(\mathbf{S}(\boldsymbol{\theta})\boldsymbol{\Delta\theta} - \mathbf{e}(\boldsymbol{\theta})\right)^{\mathrm{T}} \mathbf{W} \left(\mathbf{S}(\boldsymbol{\theta})\boldsymbol{\Delta\theta} - \mathbf{e}(\boldsymbol{\theta})\right), \tag{5.9}$$

where the matrix

$$\mathbf{S}(\boldsymbol{\theta}) = \begin{bmatrix} \dfrac{\partial\widetilde{\lambda}^{(1)}}{\partial\theta_1} & \cdots & \dfrac{\partial\widetilde{\lambda}^{(1)}}{\partial\theta_{N_\theta}} \\ \vdots & & \vdots \\ \dfrac{\partial\widetilde{\lambda}^{(N_{\mathrm{M}})}}{\partial\theta_1} & \cdots & \dfrac{\partial\widetilde{\lambda}^{(N_{\mathrm{M}})}}{\partial\theta_{N_\theta}} \\ c_1\mathbf{D}\dfrac{\partial\widetilde{\boldsymbol{\phi}}^{(1)}}{\partial\theta_1} & \cdots & c_1\mathbf{D}\dfrac{\partial\widetilde{\boldsymbol{\phi}}^{(1)}}{\partial\theta_{N_\theta}} \\ \vdots & & \vdots \\ c_{N_{\mathrm{M}}}\mathbf{D}\dfrac{\partial\widetilde{\boldsymbol{\phi}}^{(N_{\mathrm{M}})}}{\partial\theta_1} & \cdots & c_{N_{\mathrm{M}}}\mathbf{D}\dfrac{\partial\widetilde{\boldsymbol{\phi}}^{(N_{\mathrm{M}})}}{\partial\theta_{N_\theta}} \end{bmatrix} \tag{5.10}$$

represents modal sensitivities to the unknown parameters. In this thesis eigenvalue derivatives $\frac{\partial\widetilde{\lambda}^{(1)}}{\partial\theta_t}$ are calculated using the method proposed in [164], whereas eigenvector derivatives $\frac{\partial\widetilde{\boldsymbol{\phi}}^{(m)}}{\partial\theta_t}$ are obtained as described in [165]. $J_\varepsilon(\boldsymbol{\Delta\theta})$ is minimised in the current iteration step by pursuing $\nabla J_\varepsilon(\boldsymbol{\Delta\theta}) = \mathbf{0}$. Then we have the following equation representing the weighted least square problem:

$$\mathbf{S}^{\mathrm{T}}(\boldsymbol{\theta})\mathbf{W}\mathbf{S}(\boldsymbol{\theta})\boldsymbol{\Delta\theta} = \mathbf{S}^{\mathrm{T}}(\boldsymbol{\theta})\mathbf{W}\mathbf{e}(\boldsymbol{\theta}), \tag{5.11}$$

that is to be solved with respect to $\boldsymbol{\Delta\theta}$. Finally, for the s-th iteration step the unknown parameter vector is updated:

$$\begin{aligned} \boldsymbol{\theta}[s+1] &= \boldsymbol{\theta}[s] + \kappa_\theta \Delta\boldsymbol{\theta}[s] \\ &= \boldsymbol{\theta}[s] + \kappa_\theta \left(\mathbf{S}^{\mathrm{T}}(\boldsymbol{\theta}[s])\mathbf{W}\mathbf{S}(\boldsymbol{\theta}[s])\right)^{-1} \mathbf{S}^{\mathrm{T}}(\boldsymbol{\theta}[s])\mathbf{W}\mathbf{e}(\boldsymbol{\theta}[s]), \end{aligned} \tag{5.12}$$

where κ_θ is the scaling factor that is selected with the trial-and-error method.

Updating of the FE model using identified modal parameters

Experimental modal data described in Subsection 5.1.2 are used for updating of the FE model shown in Subsection 5.2.1 with initial parameter values $\boldsymbol{\theta}_0 = \begin{bmatrix} 1 & 1 & \cdots & 1 \end{bmatrix}^{\mathrm{T}}$. The covariance matrix $\boldsymbol{\Sigma}_{\mathrm{M}}$ describing measurement uncertainties is not available. Thus, weighting matrix is constructed in accordance to Eq. (5.8). The coefficient $w_\psi = 0.01$ is selected, as the coefficient of variation of the measured mode shapes is typically one order of magnitude greater than that of the natural frequencies [152, 155]; $\kappa_\theta = 0.5$ is selected. The stop condition is selected in such a way that all unknown parameters must have absolute relative increment $\frac{|\Delta\theta_t[s]|}{\theta_t[s]} < 10^{-5}$, $t = 1, 2, \ldots, N_\theta$.

The convergence of unknown parameters and error metrics of modal parameters is shown in Fig. 5.5. Mode matching finds unknown parameters in 36 iteration steps.

Evolution of the relative natural frequency error (Fig. 5.5d) shows that natural frequencies are closely reproduced. Absolute values of this error for all vibration modes are below 0.5 %, whereas the absolute value of initial relative error was near to 20 %. Similarly, MAC between experimental and numerical locked mode shapes is significantly improved during model updating. At the initial iteration step the worse MAC is near to 0.6. All MAC values are above 0.8 for the updated model and most of them are above 0.9 that is a satisfactory result. It allows for reproduction of asymmetries and other distortions of experimental mode shapes as demonstrated in Fig. 5.6. It is visible especially for mode shapes shown in Figs. 5.6d, e, g, i and j. Even high-frequency vibration modes that are characterised by local curvatures in the mode shapes are reproduced by the updated FE model.

Such accurate reproduction of experimental locked mode shapes is possible due to independent parameterization for each bolted connection. Unknown parameters related to bolted connections the right-hand side of the structure are different from the corresponding parameters related to the left-hand side (Figs. 5.5a, b and 5.4b). Moreover, final values of the unknown parameters are strongly scattered around their initial values. It reveals assembly discrepancies of the bolted connections which affects the mode shapes.

An unknown parameter describing the Young modulus of the beams changes significantly less than parameters related to the bolted connections (compare Fig. 5.5c with Figs. 5.4a and b). It is in agreement with expectations, since the Young modulus of the beam is the parameter characterised by much lower uncertainty than stiffness of bolted connection whose actual value can be affected by many local effects.

The accurate calibration of the FE model of the controlled frame not only allows for accurate calculation of quantities required by the controller but also improves reliability of the simulation within a broad frequency range. It is valuable

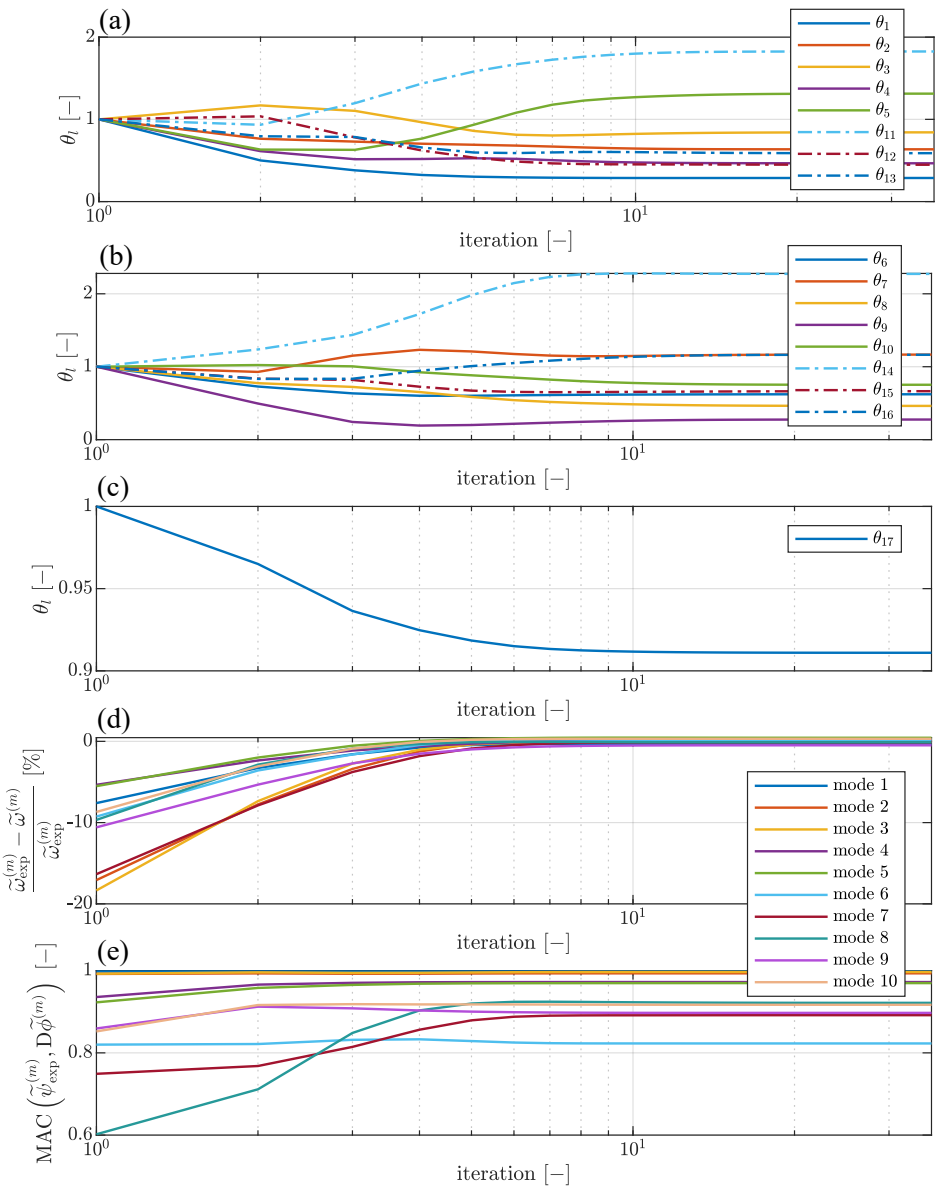

Fig. 5.5. Evolution of various parameters during model updating: (a) unknown parameters characterising stiffness of the bolted connections on the left-hand side of the structure, (b) analogous parameters for the right-hand side of the structure, (c) unknown parameter characterising the Young modulus of the beams, (d) relative error of the locked natural frequency and (e) MAC between locked experimental and locked numerical mode shapes.

property of the updated model, since higher-order vibration modes are induced due to operation of the lockable joints.

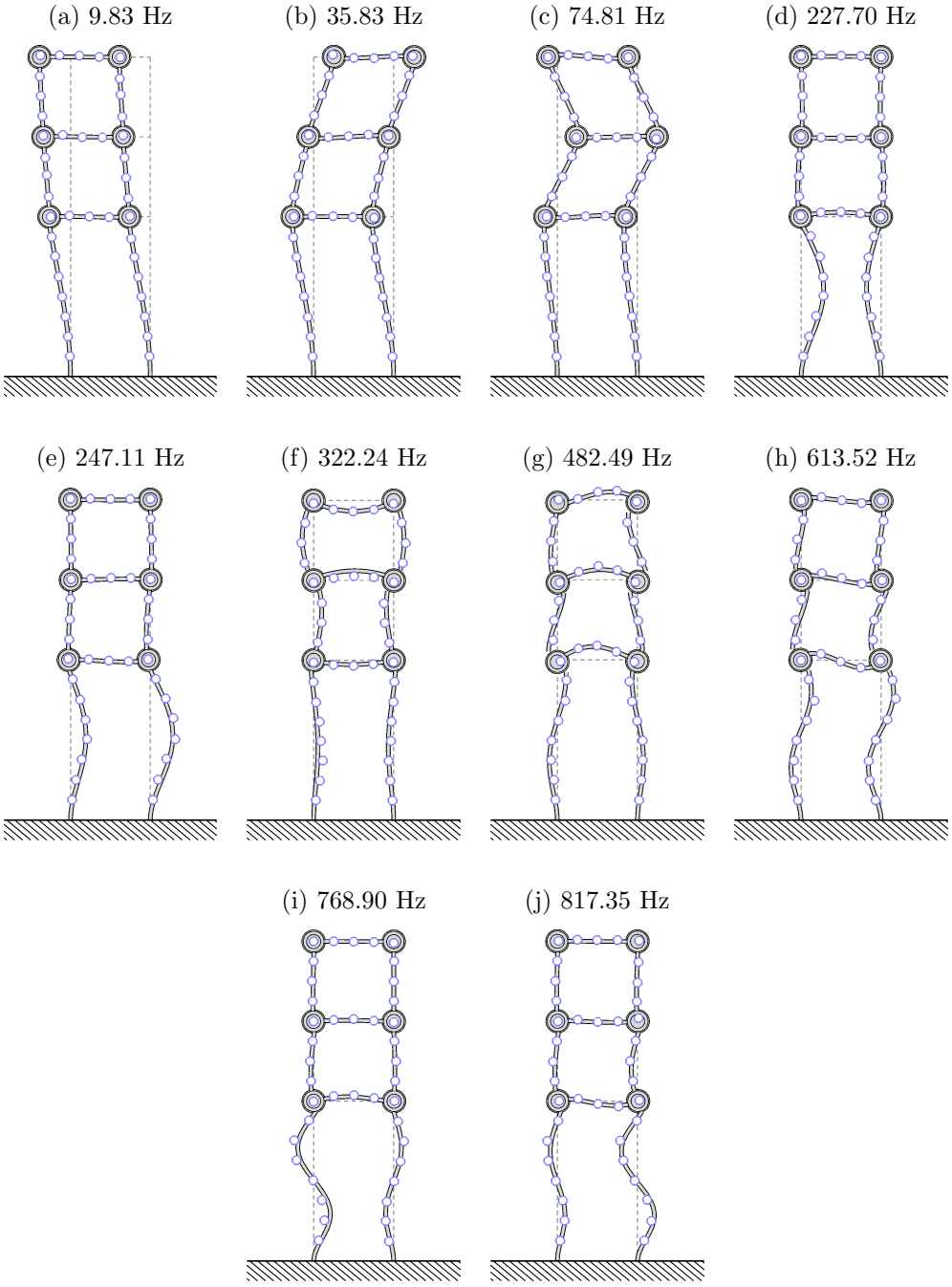

Fig. 5.6. Numerical locked mode shapes $\boldsymbol{\phi}^{(m)}(\boldsymbol{\theta})$ obtained from the updated FE model (gray solid lines), accompanied with corresponding numerical natural frequencies, compared with experimental locked mode shapes $\boldsymbol{\psi}^{(m)}$ (blue points at sensor locations).

5.2.3. Material damping

Due to the fact that estimation of the modal damping ratios is highly uncertain, the material damping model is analogous to one adopted in Chapter 4. The following values of coefficients in Eq. (4.2) are selected with the trial-and-error method: $\alpha = 0$, $\beta = 0.016$ and $\gamma = 3 \cdot 10^{-5}$. These coefficients are valid for all cases considered in the next section. As indicated in Section 5.3 unlocked vibration modes change depending on the lockable joints selected to be controlled (whereas the remaining ones are passively locked), however, the dependence of the modal damping ratios on natural frequency (Eq. (4.2)) is invariant with respect to the lockable joints selected to be controlled. It means that for various lockable joints selected to be controlled the modal damping rations corresponding to the unlocked vibration modes will be slightly different but always will be placed on the same curve $\zeta(\omega)$ indicated by β and γ.

5.3. Hardware control loop

5.3.1. Equipment and its limitations

The control algorithm is realised by the embedded real-time controller cRIO-9014 combined with cRIO-9114 CompactRIO Chassis that is based on the field-programmable gate array (FPGA)-based processor Virtex-5 LX50. This real-time controller is further called "FPGA controller". Unfortunately, the FPGA controller utilised in the present research has a limited memory, thus also the uploaded algorithm is subject to some restrictions.

The main restriction is that the controller is able to produce only one control signal $u(t)$. On the other hand, as shown in Chapter 4 the lockable joints are usually controlled symmetrically (see e.g. Figs. 4.5, 4.14, 4.28 and 4.30) due to the symmetry of the structure. Moreover, it has been demonstrated that a single pair of lockable joints is sufficient to yield satisfactory results. Thus, the available control signal can be used to control selected pair of the lockable joints. During the experiments it has been assumed that one pair of the lockable joints among three available ones can be controlled at the ends of:

- the first (bottom, joints J1 and J2) transversal beam (see Fig. 5.1a),
- the second (middle, joints J3 and J4) and
- the third (top, joints J5 and J6) one.

The lockable joints that are not selected to be controlled always are passively locked at an angle 90° between adjacent beams ($\Delta q = 0$). The voltage, determined by the control signal $u(t)$, is supplied to both selected lockable joints to be controlled. The selected pair can be changed for various control scenarios.

Since the pair of the lockable joints is controlled by a single signal $u(t)$ it is theoretically sufficient to measure strains in the vicinity of only one lockable joint

by the pair of strain gauges according to Eq. (3.3). It is confirmed by the simulation results in Figs. 4.5, 4.14, 4.28 and 4.30 where due to structural symmetry and character of the excitations the signals of measured strain are the same for the joint on the left-hand side and right-hand side of the structure. However, during the experimental validation the quality of the strain measurement is improved by calculation of the mean strain signal from two particular pairs of the strain gauges located in the vicinity of both controlled joints:

$$\varepsilon_{\mathrm{M}}(t) = \frac{1}{2}\left(\varepsilon_{\mathrm{M1}}(t) + \varepsilon_{\mathrm{M2}}(t)\right). \tag{5.13}$$

Each pair of the strain gauges is mounted 7.5 cm from the rotational axis of the corresponding lockable joint. During control of the structure, only strain gauges corresponding to the controlled joints are used. Signals $\varepsilon_{\mathrm{M1}}(t)$ and $\varepsilon_{\mathrm{M2}}(t)$ are measured in a half-bridge configuration dedicated to bending measurements. These signals are filtered and conditioned.

First three unlocked vibration modes are selected to be monitored, since they are related to the motion of transversal beams along with the lockable joints (similarly to the locked vibration modes shown in Figs. 5.6a–c), whereas any higher-order mode shapes are related to the local curvatures and their natural frequencies are well-separated from the selected ones. This property is valid independently of the state of the lockable joints (locked or unlocked). The third monitored unlocked vibration mode is controlled with poor effectiveness due to the delay of the lockable joints (3 ms) that is near to 1/4 of the mode period. Thus, this mode is only monitored but not controlled in this research ($\alpha_3 = 0$). The FPGA controller updates a signal $u(t)$ with the frequency 10 kHz which is independent of the delay of the lockable joint caused by its mechanical properties.

Three laser displacement sensors (LDSes) Baumer OADM-2016 characterized with 10 µm linear resolution are adopted for estimation of first three modal velocities according to Eq. (3.10). Velocities $\dot{\mathbf{q}}_{\mathrm{M}}(t)$ are obtained by differentiation of the displacement signal provided by LDSes. Before differentiation the signal is conditioned and filtered.

5.3.2. Modal filtering and unlocked vibration modes

The modal filter matrix $\mathbf{\Phi}^{+}$ depends both on unlocked mode shapes of the structure and sensor locations. Here, unlocked mode shapes refer to the modes obtained for an unlocked controlled pair of the lockable joints, whereas the remaining ones are in the locked state. Thus, the unlocked mode shapes are different for each pair of lockable joints selected to be controlled. However, sensor locations are selected once and are not changed during experiments. Fortunately, the first three unlocked mode shapes are well correlated with their locked counterpart for each controlled pair of the lockable joints. All MAC values between unlocked

and locked vibration modes are above 0.9. Thus, the locked mode shapes can be used for selection of the sensor locations. The set of candidate sensor locations coincides with all measurement locations selected to identify locked mode shapes before the model updating procedure (Fig. 5.3). Sensor locations indicated with Algorithm 1 are shown in Fig. 5.7a.

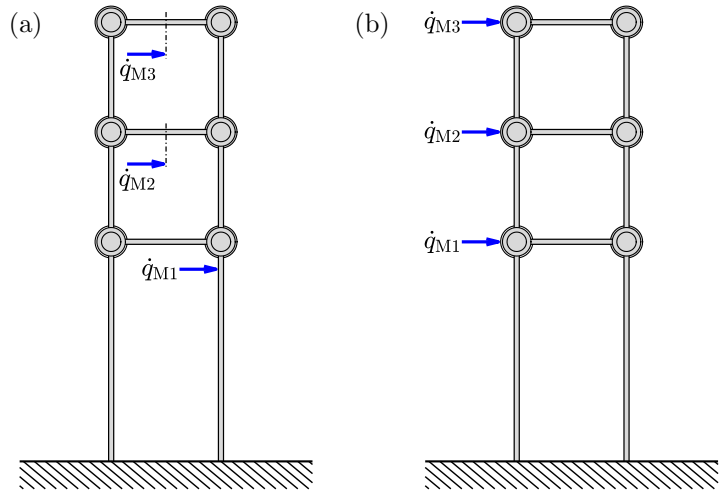

Fig. 5.7. Selected sensor locations for modal filtering of first three modal velocities: (a) indicated by CR-based approach and (b) modified which are adopted in experiments.

Sensor locations shown in Fig. 5.7a maximize the determinant of FIM, however, such a sensor layout has some drawbacks. First, LDSes require surfaces for reflection of the laser beam. Thus, locations at the middle of a transversal beam require mounting additional surfaces reflecting the laser beam. Another drawback is that sensor location $\dot{q}_{M1}(t)$ is not the best choice regarding contamination of the measurement signal by higher-order unlocked vibration modes. It is due to the fact that higher-order vibration modes involve local curvatures of the beams connected to the lockable joints and have lower amplitudes at locations related to heavy parts of the structure such as lockable joints along with whole transversal beams. Thus, new near-optimal sensor locations are proposed for experiments, as shown in Fig. 5.7b, which are devoid of these drawbacks and provide similar information about modal velocities.

5.3.3. Preparation of the control algorithm

The updated FE model is employed to obtain parameters required by Algorithm 2. Due to the fact that only one control signal is available for any selected pair of the lockable joints, the resulting matrix representing the locking effect

(see Eq. (2.43)) can be calculated as the sum of matrices corresponding to controlled joints:

$$\widetilde{\mathbf{C}} = \widetilde{\mathbf{C}}_1 + \widetilde{\mathbf{C}}_2. \tag{5.14}$$

The resulting matrix is not indexed, since indices k in Eq. (2.43) denote particular joints among all controlled ones, whereas here always only one pair (described by one matrix $\widetilde{\mathbf{C}}$) of lockable joints is available to be locked in a particular control scenario. Hence, providing any index depending on the selected pair of the controlled joints could be misleading.

From Eq. (5.14) it follows that when $u(t) = 1$ the resulting modal energy transfer rate to the monitored unlocked vibration modes is the sum of particular modal energy transfer rates caused by locking of both joints, according to Eq. (2.76). Using Eqs. (2.77) and (2.78), the resultant modal energy transfer rate to the monitored unlocked vibration modes can be written as follows:

$$\begin{aligned}\dot{W}_{\mathrm{M}} &= \dot{W}_{\mathrm{M1}} + \dot{W}_{\mathrm{M2}} \\ &= -u(t)\dot{\boldsymbol{\eta}}_{\mathrm{M}}^{\mathrm{T}}(t)\left(\begin{bmatrix}\boldsymbol{\Gamma}_{\mathrm{MM1}} & \boldsymbol{\Gamma}_{\mathrm{MH1}}\end{bmatrix} + \begin{bmatrix}\boldsymbol{\Gamma}_{\mathrm{MM2}} & \boldsymbol{\Gamma}_{\mathrm{MH2}}\end{bmatrix}\right)\begin{bmatrix}\dot{\boldsymbol{\eta}}_{\mathrm{M}}(t) \\ \dot{\boldsymbol{\eta}}_{\mathrm{H}}(t)\end{bmatrix} \\ &= \dot{\boldsymbol{\eta}}_{\mathrm{M}}^{\mathrm{T}}(t)\left(\boldsymbol{\Delta\phi}_{\mathrm{M1}} f_1(t) + \boldsymbol{\Delta\phi}_{\mathrm{M2}} f_2(t)\right).\end{aligned} \tag{5.15}$$

Finally, by taking into account the equations above, the estimated weighted modal energy transfer rates used in lines 5 and 11 of control Algorithm 2 (Eqs. (3.39) and (3.41), respectively) can be calculated as:

$$\dot{\hat{V}}_W(t) = -\dot{\hat{\boldsymbol{\eta}}}_{\mathrm{M}}^{\mathrm{T}}(t)\mathbf{W}_\alpha\boldsymbol{\Gamma}_{\mathrm{MM}}\dot{\hat{\boldsymbol{\eta}}}_{\mathrm{M}}(t), \tag{5.16}$$

where

$$\boldsymbol{\Gamma}_{\mathrm{MM}} = \boldsymbol{\Gamma}_{\mathrm{MM1}} + \boldsymbol{\Gamma}_{\mathrm{MM2}},$$

and

$$\dot{\hat{V}}_W(t) = \dot{\hat{\boldsymbol{\eta}}}_{\mathrm{M}}^{\mathrm{T}}(t)\mathbf{W}_\alpha\boldsymbol{\Delta\phi}_{\mathrm{M}}\widehat{f}(t), \tag{5.17}$$

where:

$$\boldsymbol{\Delta\phi}_{\mathrm{M}} = \boldsymbol{\Delta\phi}_{\mathrm{M1}} + \boldsymbol{\Delta\phi}_{\mathrm{M2}},$$

and $\widehat{f}(t)$ is calculated from the mean strain signal (Eq. (5.13)) analogously to Eq. (3.2):

$$\widehat{f}(t) = -\frac{2EI}{h}\varepsilon_{\mathrm{M}}(t). \tag{5.18}$$

In this case, the number of iterations of the "for" loop $N_k = 1$ (line 2 of the algorithm).

Similarly to the modal filter matrix, $\boldsymbol{\Gamma}_{\mathrm{MM}}$ and $\boldsymbol{\Delta\phi}_{\mathrm{M}}$ also are different depending on the selected pair of the lockable joints to be controlled. Hence, for

each pair of the lockable joint selected to be controlled, the control algorithm has different parameters based on modal data.

Thresholds κ_1 and κ_2 are selected with the trial-and-error method during each experiment. For each comparison between experimental and simulation results presented in this chapter, the simulation algorithm parameters are selected to mirror those used in the respective experiments. Due to the fact that measured signals are conditioned, the simulation algorithm parameters are recalculated to values corresponding to the measured quantities adopted in Algorithm 2. Time integration step $\Delta t = 0.1$ ms (Eq. (2.45)) is selected for the numerical simulation. It corresponds to the sampling frequency of the hardware control loop.

5.4. Vibration attenuation

This section focuses on experimental validation of the proposed control strategy in vibration attenuation. First, controllability of the monitored unlocked vibration modes for various pairs of the lockable joints is evaluated using the updated FE model in the following subsection. In Subsection 5.4.2, vibration attenuation is tested for free vibration, employing two different pairs of the lockable joints selected to be controlled. Each time experimental results are compared with the simulation. Comparison of experimental and simulation results of forced-vibration attenuation for two different pairs of the lockable joints selected to be controlled is discussed in Subsection 5.4.3. Here, vibration was excited by frequency sweeps provided with modal shaker and later analysed mainly in the frequency domain.

5.4.1. Modal controllability by various pairs of lockable joints

Selection of the pair of the controlled lockable joints depends on the priority of damping of particular unlocked vibration modes. Therefore, controllability metrics for particular monitored unlocked vibration modes with weights $\beta_p = 1/\omega^{(p)}$ (see Eq. (3.29)) is calculated for each pair of potentially controlled lockable joints and shown in Fig. 5.8. It is obtained using actual unlocked vibration modes for each selection of the lockable joints to be controlled.

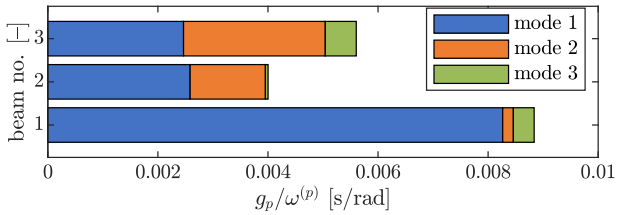

Fig. 5.8. Controllability of the monitored unlocked vibration modes for lockable joints placed at the ends of particular transversal beams (from the bottom to the top).

It is evident that the first unlocked vibration mode is controllable for each pair of lockable joints. However, lockable joints at the ends of the first (bottom) transversal beam cannot control the second unlocked vibration mode effectively. It is in agreement with the observation that this beam accumulates almost no strains for the second locked mode shape. It can be seen in Fig. 5.6b, where the first transversal beam almost does not deform and longitudinal beams are not inclined at the corresponding height due to their maximal transversal displacement. Similarly, the third unlocked vibration mode is almost not-controllable by the lockable joints at the ends of the second (middle) transversal beam.

The agreement between the controllability metrics and modal energy transfer rates achieved during vibration attenuation of the first vibration mode is demonstrated for each pair of the lockable joints selected to be controlled. To this end, the initial condition that the structure is prestressed in the first unlocked vibration mode, achieving 1 J of potential energy, is pursued. Thus, for each tested pair of the lockable joints: $\mathbf{q}_0 = \frac{1}{\omega^{(1)}}\boldsymbol{\phi}^{(1)}$, $\dot{\mathbf{q}}_0 = \mathbf{0}$ and the following parameters

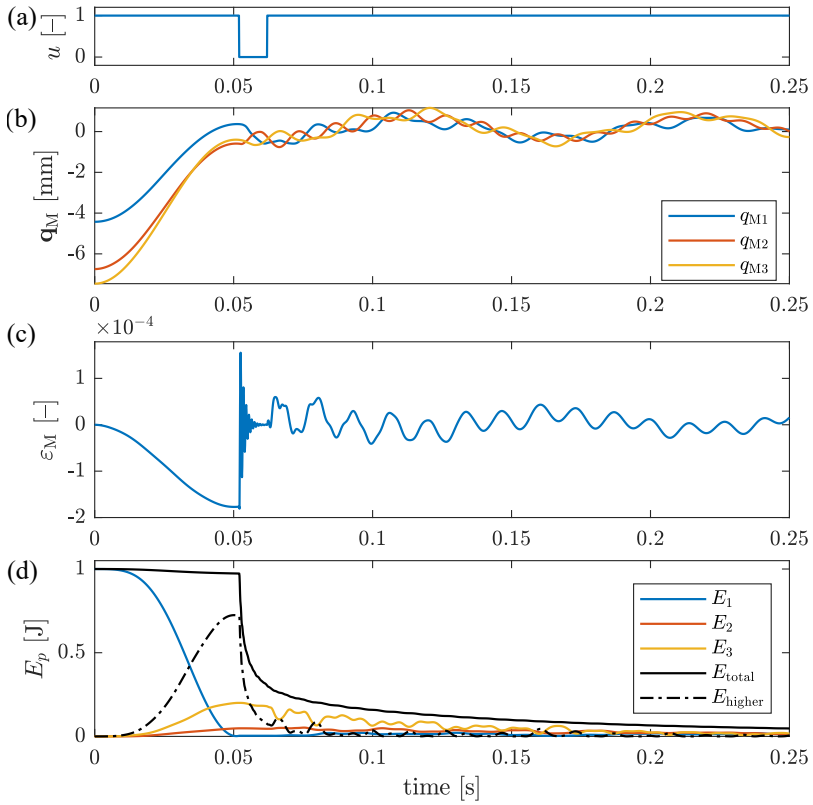

Fig. 5.9. Simulation test of the controllability of the first unlocked vibration mode by the lockable joints placed at the first (bottom) transversal beam; time histories of: (a) control signal, (b) measured displacements, (c) measured strain and (d) modal energies of the structure.

of the control algorithm are selected: $\alpha_1 = 1$, $\alpha_2 = \alpha_3 = 0$, $t_{\text{unlock}} = 10$ ms, $t_{\text{lock}} = 5$ ms, $\kappa_1 = 100$ W and $\kappa_2 = 1$ W. Results for controlled lockable joints at the ends of first, second and third transversal beams of the structure are shown in Figs. 5.9, 5.10 and 5.11, respectively.

It is evident that for the first transversal beam almost whole energy associated with the first unlocked vibration mode is transferred out and directed to the remaining vibration modes within one time interval when the controlled joints are locked (Figs. 5.9a and d). Vibration of the first unlocked vibration mode is suppressed within 0.05 s until the first unlock of the currently selected lockable joints which is near to half of the first-mode period (Fig. 5.9b). The strain measured in the vicinity of the controlled lockable joints is accumulated monotonically and after the joint unlock high-frequency unlocked vibration modes are demonstrated in the strain signal within a short time interval. It is evident that controllability of the first unlocked vibration mode by the currently selected lockable joints is very satisfactory and agrees with results shown in Fig. 5.8.

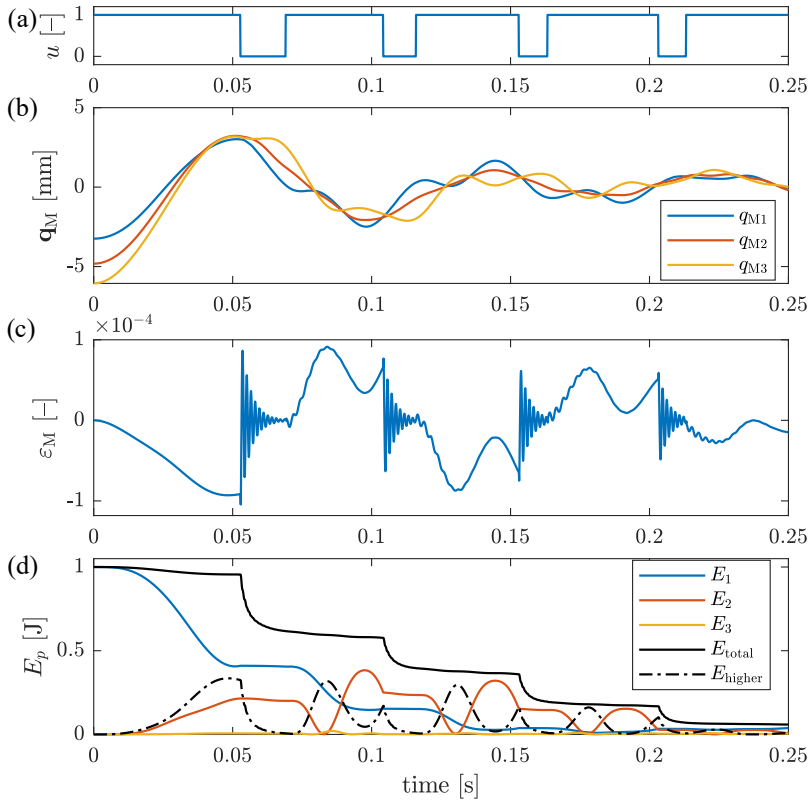

Fig. 5.10. Simulation test of the controllability of the first unlocked vibration mode by the lockable joints placed at the second (middle) transversal beam; time histories of: (a) control signal, (b) measured displacements, (c) measured strain and (d) modal energies of the structure.

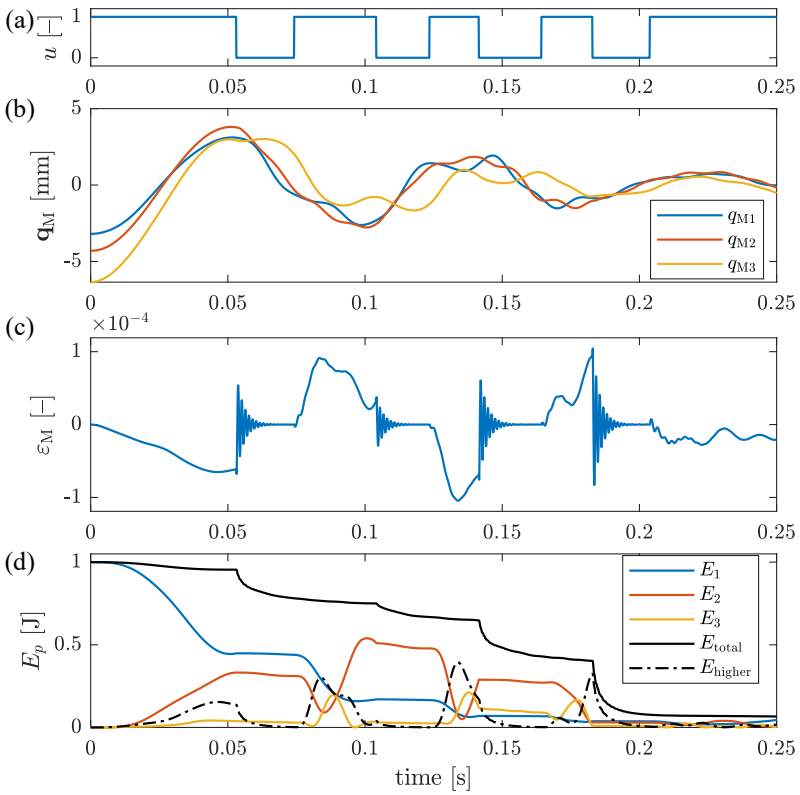

Fig. 5.11. Simulation test of the controllability of the first unlocked vibration mode by the lockable joints placed at the third (top) transversal beam; time histories of: (a) control signal, (b) measured displacements, (c) measured strain and (d) modal energies of the structure.

Controllability metrics of the first unlocked vibration mode for the joints belonging to the second and third transversal beams are almost equal and are smaller than for the first transversal beam (Fig. 5.8). This observation is in good agreement with behaviour of the structure controlled by the lockable joints located at the ends of the second and third transversal beam that is presented in Figs. 5.10 and 5.11, respectively. In both these cases the time history of the first modal energy is very similar (Figs. 5.10d and 5.11d) corresponding to the controllability metrics. The lockable joints are unlocked after 0.05 s, in the first tested case (Fig. 5.9). However, for the second and third transversal beams energy decreases to the value close to 0.5 J as opposed to the first transversal one, where almost whole energy is transferred out from the first unlocked vibration mode before the first joint unlock.

Additional observation is that energy transferred from the first vibration mode is partially transferred to other monitored vibration modes near-proportionally to the controllability metrics presented in Fig. 5.8. In Fig. 5.9d, the second vi-

bration mode is almost not-excited due to its poor controllability by the lockable joints belonging to the first transversal beam. For the third transversal beam (Fig. 5.11), the second modal energy achieves values above 0.5 J, whereas for the second one (Fig. 5.10) slightly below. Similar observations on the controllability of the third monitored vibration mode can be noticed.

Lower values of measured strains for the case of the controlled lockable joints belonging to the second and third transversal beams in relation to the first one can be observed. It is due to lower amount of the transferred energy from the first unlocked vibration mode that results in smaller deformations of the structure occurring during a single time period when joints are in the locked state. However, high-frequency vibration demonstrated in the measured strain is more noticeable than for the first test of modal controllability. It results from the fact that for various lockable joints selected to be controlled the different higher-order unlocked vibration modes are excited predominantly. Moreover, the same high-frequency modes can be demonstrated differently depending on the location of the strain gauges that changes along with the selected pair of the lockable joints to be controlled.

Although it is not shown in this thesis, a good agreement of the proposed controllability metric with the structural behaviour can be obtained also when the energy is to be transferred out from the modes other than the first unlocked one. However, in the case of experiments the proposed metric of controllability of particular vibration modes does not reflect structural behaviour as relevantly as for simulations using the updated FE model. The reason is that currently used lockable joints are imperfect and do not unlock completely (see Table 5.1). It causes that some amount of the potential energy that could be released in high-frequency free vibration is still kept in strains. This phenomenon especially affects operation of the joints J5 and J6 belonging to the top transversal beam. They are less effective than one could expect from the proposed controllability metrics, thus only the first and second transversal beams are selected to be controlled in the further part of this chapter.

5.4.2. Mitigation of free structural vibration

Two various scenarios of mitigation of free vibrations are investigated and described below. The structure is pre-stressed with the aid of a manual hook attached to the end tip of the structure. Later, the structural free vibration is caused by the release of the hook. The hook is shown in Fig. 5.12. All joints are in the locked state when the hook is released. This method of starting up the structure is also simulated with the aid of the FE model by applying the following initial conditions:

$$\mathbf{q}_0 = \mathbf{B}\widetilde{\mathbf{K}}^{-1}\mathbf{d}_\mathrm{h}, \qquad \dot{\mathbf{q}}_0 = \mathbf{0}, \tag{5.19}$$

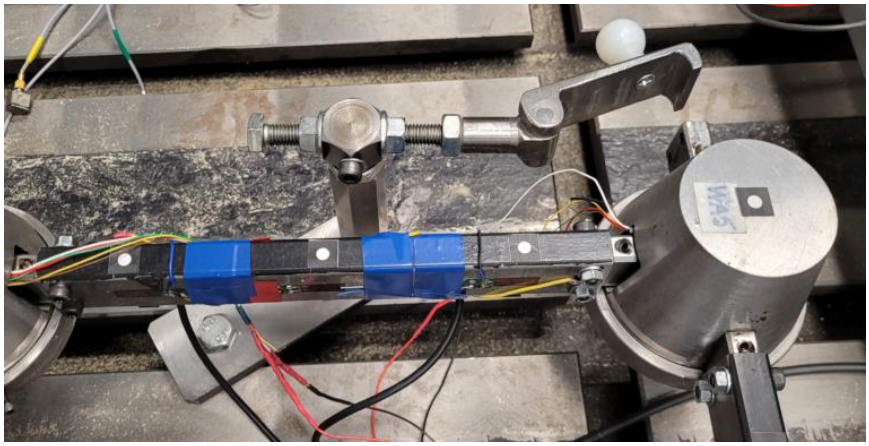

Fig. 5.12. Manual hook used in free-vibration testing.

where $\mathbf{d}_{\mathrm{h}} = \begin{bmatrix} 0 & \cdots & 0 & d_{\mathrm{h}} & 0 & \cdots & 0 \end{bmatrix}^{\mathrm{T}}$ is the force vector representing prestress of the structure by the hook and has nonzero element at DOF representing the location of the hook. The value d_{h} is selected in such a way that $\mathbf{q}_0$ at the appropriate location is equal to the structural tip displacement imposed by the hook that is 6 mm. Here, matrices $\widetilde{\mathbf{K}}$ and $\mathbf{B}$ are obtained separately for each pair of the controlled joints. The remaining (not controlled) joints are passively locked and treated as regular structural components.

The algorithm controlling the real structure starts working when a structural tip passes the preselected displacement value q_{ON}: $|q_{\mathrm{ON}}| = 5$ mm. It allows avoiding operation of the algorithm when the hook has not yet been released. The same condition is adopted in the simulation.

The two cases of free-vibration mitigation are investigated in this subsection:

case 1: joints J1 and J2 are controlled (the first transversal beam) and

case 2: joints J3 and J4 are controlled (the second transversal beam).

They differ also in the selected thresholds κ_1 and κ_2. As mentioned, remaining (uncontrolled) joints are passively locked in each control scenario. Parameters of Algorithm 2 that are common for these two cases are: $\alpha_1 = 1$, $\alpha_2 = \alpha_3 = 0$ and $t_{\mathrm{lock}} = t_{\mathrm{unlock}} = 15$ ms. The selection of weights α_p corresponds to the fact that mainly the first vibration mode is excited with the manual hook.

Case 1

The thresholds $\kappa_1 = 0.38$ W and $\kappa_2 = 4.2 \cdot 10^{-4}$ W are selected.

Results of the experiment comparing a structural response at the tip of the controlled and uncontrolled (locked joints) structure along with a control signal are shown in Fig. 5.13a, whereas analogous results obtained with simulation employing the updated FE model are shown in Fig. 5.13b. The experimental results

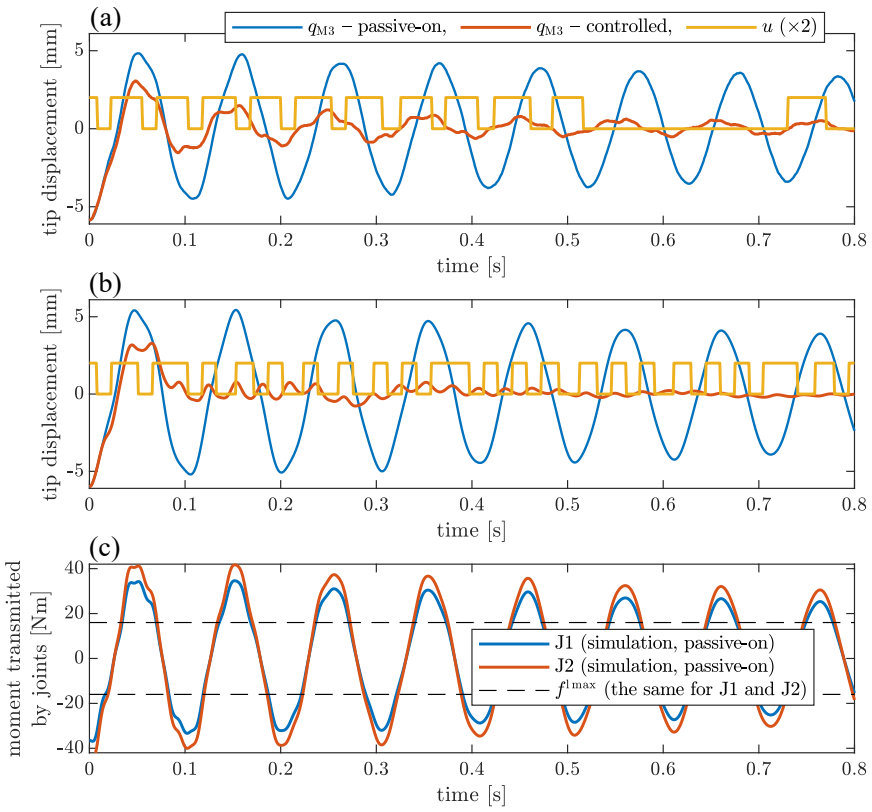

Fig. 5.13. Case 1 of free vibration attenuation: structural tip displacement for uncontrolled (passive-on) and controlled structure along with the control signal for: (a) experiment, (b) corresponding simulation, and (c) bending moments transmitted by the passively locked joints obtained from the updated FE model compared with maximal bending moments transmitted by the real joints.

demonstrate satisfactory performance of the control but noticeably worse in relation to the simulation. The displacement of the structural tip decays slower in the experiment. In simulation structural displacement related to the first unlocked vibration mode is mitigated quickly whereas the second unlocked vibration mode is mitigated very slowly. It is due to the selected weights α_p and small controllability of the second unlocked vibration mode (see Fig. 5.8). The second unlocked vibration mode also does not decay in experimental results.

Relatively frequent switches of the lockable joints demonstrated in Fig. 5.13b follows from high participation of the second unlocked vibration mode in relation to quickly mitigated first one. It affects the operation of the control algorithm, despite the fact that weights $\alpha_2 = \alpha_3 = 0$. Such a sensitivity to the second unlocked vibration mode is caused by the thresholds κ_1 and κ_2 that are selected for the best algorithm operation in the experiment, where the first unlocked vibra-

tion mode participates significantly in the structural motion within the whole investigated time interval.

The differences in behaviour of the controlled structure in the simulation and experiment follows from the fact that the lockable joints are prototypes and are imperfect. Fig. 5.13c shows bending moments transmitted by the joints J1 and J2 corresponding to the passive-on response shown in Fig. 5.13b, which are compared with the maximal transmitted bending moments by real lockable joints (see Table 5.1). These bending moments are not estimated from the strain gauges but calculated using Eq. (2.39). It is evident that they exceed maximal transmitted bending moments $f_{\mathrm{J1}}^{\mathrm{l\,max}} = f_{\mathrm{J2}}^{\mathrm{l\,max}}$ characterising the real joints. It follows that friction parts in real joints can slide against each other providing dry friction, as opposed to the situation when $f^{\mathrm{l\,max}}$ is not reached. When $f^{\mathrm{l\,max}}$ is exceeded Eq. (2.70) and thus Eq. (2.73) are not valid. Here, the decrease in the energy corresponding to the monitored unlocked vibration modes (that are to be damped) is limited by $f^{\mathrm{l\,max}}$, as follows:

$$\left|\dot{W}_{\mathrm{M}}(t)\right| \leq \left|\dot{\boldsymbol{\eta}}_{\mathrm{M}}^{\mathrm{T}}(t) \sum_{k=1}^{N_k} \boldsymbol{\Delta}\boldsymbol{\phi}_{\mathrm{M}k} f_k^{\mathrm{l\,max}}\right|, \tag{5.20}$$

and then the energy transferred to the higher-order unlocked vibration modes W_{H} is additionally decreased by the energy dissipated in dry fiction between the sliding friction surfaces inside the joints. Despite the fact that $f^{\mathrm{l\,max}}$ limits the transmitted bending moment even two times, the proposed control still has satisfactory effectiveness. It demonstrates that the proposed control is robust with respect to considerable differences between behaviour of the employed prototypes of real lockable joints and the model.

Apart from the influence of dry friction in the lockable joints on the control performance, it can cause two more phenomena that should be commented. First, locked natural frequencies are decreased, since sliding of the friction surfaces in the lockable joints not only provides additional damping to the structure but also has similar influence on the structural dynamics as reduction of the stiffness. The change of the locked natural frequency is visible in of the phase shift between displacement of the structural tip for the experiment and simulation (passive-on), which is especially visible at the end of the considered time interval (Figs. 5.13a and b). This difference probably follows from the fact that the FE model is updated using experimental modal data obtained for lower amplitudes of motion for which $f^{\mathrm{l\,max}}$ is not exceeded. The second phenomenon is additional nonlinearity related to dry friction. However, its exact influence on structural dynamics is unclear at this stage of the research. Coherence for the passively locked joints shown in Figs. 5.18b and 5.19b that is discussed in Subsection 5.4.3 suggests that the structure behaves near-linearly. This issue is outside of the scope of this thesis focusing on the control strategy being developed. It seems to be interesting topic for the future research.

The bending moment transmitted by the lockable joint J2 achieves greater values than the joint J1 due to the fact that the bolted connection coupling the bottom horizontal beam with the lockable joint J2 is stiffer than one coupling this beam with the joint J1. It is shown in Figs. 5.5a and b, where the stiffness unknown parameter θ_{14} is greater than θ_{11} (see Fig. 5.4b).

Case 2

In the second case of free vibration testing the lockable joints belonging to the second transversal beam (J3 and J4) are selected to be controlled. The thresholds $\kappa_1 = 0.38$ and $\kappa_2 = 5.3 \cdot 10^{-4}$ are selected. Corresponding results for the experiment and simulation are shown in Figs. 5.14a and b, respectively.

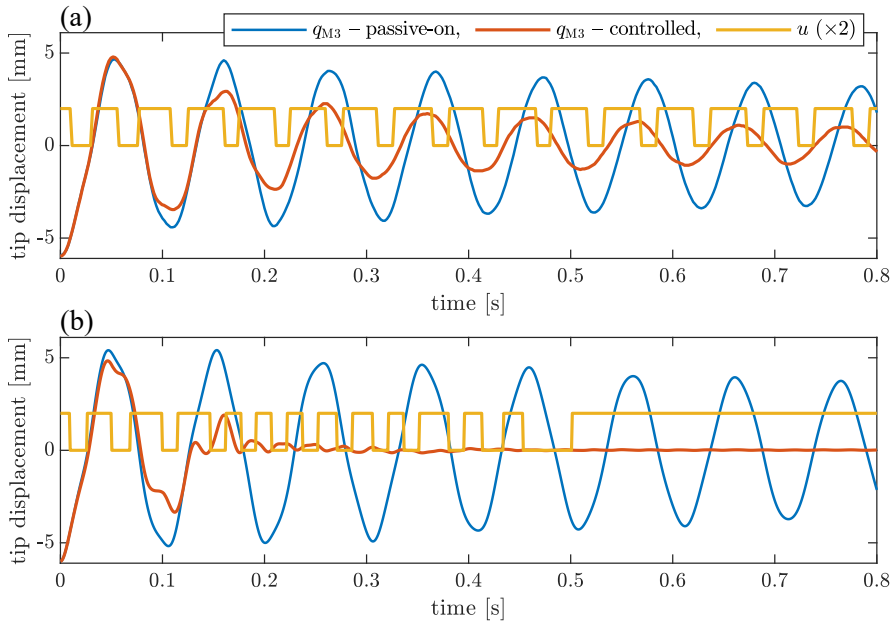

Fig. 5.14. Structural tip displacement for uncontrolled (passive-on) and controlled structure along with control signal in case 2 of free vibration attenuation for: (a) experimental results and (b) corresponding simulation ones.

Due to location of the controlled lockable joints the effectiveness of the damping of the first unlocked vibration mode is slightly smaller than in case 1 both for the experiment and simulation. It agrees with controllability metrics shown in Fig. 5.8. Due to the selected weights α_p the first vibration mode is mitigated first. The second vibration mode is mitigated due to the fact that joint locking/unlocking intended to suppress vibration in the first unlocked mode also acts on the second one. Greater controllability metric for the second unlocked vibration mode than in case 1 causes that this non-intentional mitigation of the

second vibration mode is relatively more efficient in simulation results (compare with Fig. 5.13b).

Similarly to case 1, the control achieves worse performance in the experiment than in the simulation. In this case bending moments transmitted by the lockable joints do not reach $f^{\mathrm{l\,max}}$, since the second transversal beam accumulates lower strains than the first one when the joints are in the locked state. Conversely, joint efficiency is degraded by residual dry friction present in the unlocked state because the friction surfaces are not effectively detached. For a sufficiently small vibration amplitude the unlocking of the joint provides a little or even no effect. This situation occurs for the real controlled structure at the end of the time duration shown in Fig. 5.14a, where the structural tip displacement has an amplitude lower than 1 mm. An additional simulation with the aid of the updated FE model, aiming at comparison of the expected level of transmitted bending moments and maximal transmitted bending moments $f^{\mathrm{u\,max}}$ of the real joints in the unlocked state, is provided. In this simulation all joints are passively locked and an initial displacement imposed by the hook is reduced to 1 mm. Corresponding results are shown in Fig. 5.15. It is evident that for such an amplitude of vibration the bending moments transmitted by the lockable joints only slightly

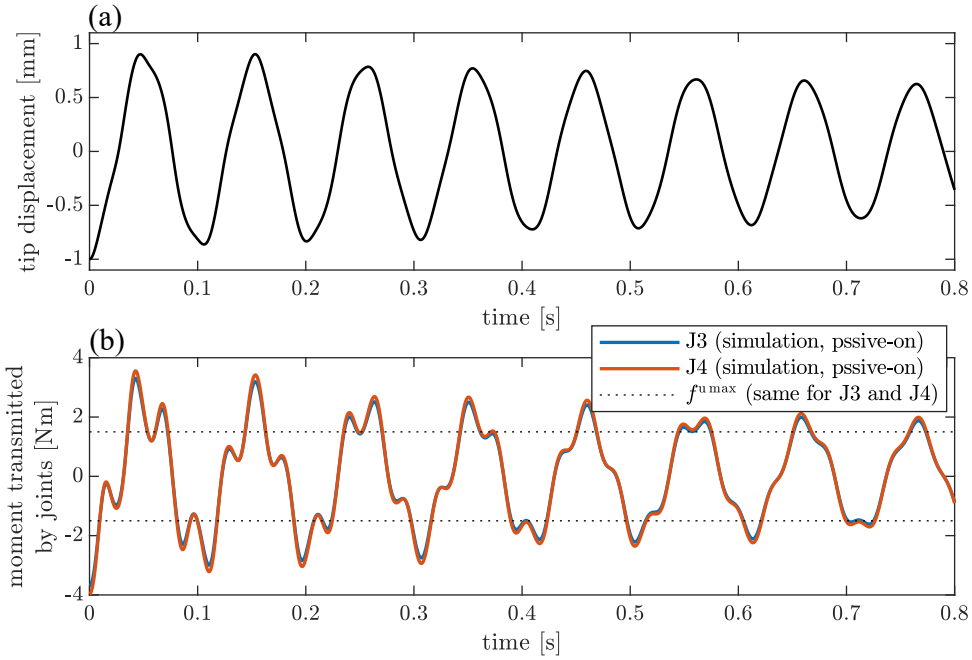

Fig. 5.15. Time histories of: (a) structural tip displacement joints in the locked state obtained from the numerical simulation for reduced initial displacement and (b) corresponding bending moments compared with the maximal bending moments transmitted by the real joint in the unlocked state.

exceed $f^{\mathrm{u\,max}}$. Hence, the only a little amount of the strain energy is released in high-frequency free vibrations, whereas the remaining part is still kept in the accumulated strains.

Despite the decrease in the control performance in the experiment it still mitigates the structural response until the the described above imperfectness of the lockable joints does not dominate their behaviour. It confirms the robustness of the proposed control methodology.

5.4.3. Mitigation of the forced structural vibration

The controlled structure is excited by the modal shaker attached to the structure at the location shown in Fig. 5.16. The time history of the excitation force provided by the modal shaker is measured with a force sensor located at the end of the stinger. The amplitude of force produced by the modal shaker depends on the current structural response. Thus, uncontrolled and controlled structural responses are obtained for different amplitudes of the excitation force due to their different vibration amplitude levels. Hence, frequency response functions (FRFs) are utilised to avoid this problem. They allow to assess the level of the structural response with respect to the level of the excitation.

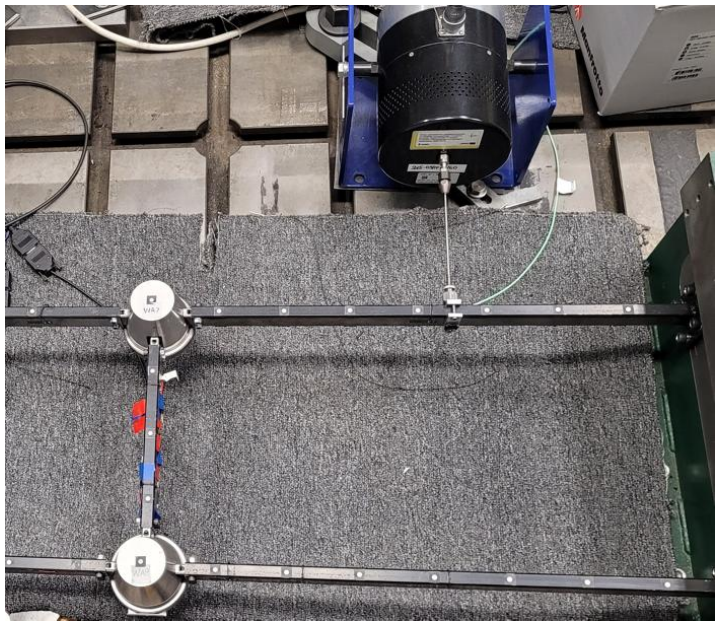

Fig. 5.16. Location of the stinger of the modal shaker exciting the structure.

Aiming at validation of the control performance in vibration attenuation frequency sweeps are performed. Each time the frequency range from 4 to 100 Hz

is swept by the modal shaker with the logarithmic increment of the frequency. The duration of each frequency sweep is 32 s. Data demonstrated in frequency domain: power spectral density (PSD), frequency response function (FRF) and coherence function are calculated as the mean value from the corresponding frequency-domain data obtained from 10 frequency sweeps. FRF is calculated using the H1 estimator.

In numerical simulation the excitation force is assumed to have a constant amplitude $A_\mathrm{d} = 85$ N. The force in a single frequency sweep is described by the equation:

$$\mathbf{d}(t) = \mathbf{L}_\mathrm{d}\boldsymbol{\Xi}(s_\mathrm{d})A_\mathrm{d}\sin F(t), \tag{5.21}$$

where: $\boldsymbol{\Xi}(s_\mathrm{d})$ is column matrix containing values of FE shape functions at the location of the excitation force s_d, with the exception of the longitudinal motion, since the force has a direction transversal to the beam; $\mathbf{L}_\mathrm{d}$ is the transformation matrix,

$$F(t) = \frac{\Omega_0 T}{\ln\left(\frac{\Omega_1}{\Omega_0}\right)}\left(\frac{\Omega_1}{\Omega_0}\right)^{\frac{t}{T}}, \tag{5.22}$$

$\Omega_0/2/\pi = 4$ Hz, $\Omega_1/2/\pi = 100$ Hz and $T = 32$ s. The function of time $F(t)$ satisfies the condition that the frequency

$$\Omega_\mathrm{d}(t) = \frac{\mathrm{d}F(t)}{\mathrm{d}t} = \Omega_0\left(\frac{\Omega_1}{\Omega_0}\right)^{\frac{t}{T}} \tag{5.23}$$

grows exponentially from Ω_0 to Ω_1 in time T.

Similarly to free vibration testing, two cases of the mitigation of forced vibrations are investigated in this subsection:

case 1: lockable joints belonging to the first transversal beam (J1 and J2) are controlled and

case 2: lockable joints belonging to the second transversal beam (J3 and J4) are controlled.

The algorithm parameters $t_\mathrm{unlock} = t_\mathrm{lock} = 15$ ms are common for both cases discussed in this subsection, whereas α_p, $p = 1, 2, 3$, κ_1 and κ_2 are selected separately for each case.

Case 1

In this case lockable joints J1 and J2 are selected to be controlled. Weights $\alpha_1 = 1$, $\alpha_2 = \alpha_3 = 0$ and thresholds $\kappa_1 = 0.384$, $\kappa_2 = 0.0011$ are selected.

Time histories of the structural tip displacement and force produced by the modal shaker obtained in single experimental frequency sweeps both for the controlled and uncontrolled structure are shown in Fig. 5.17. As the frequency of excitation increases and crosses the three locked natural frequencies of the

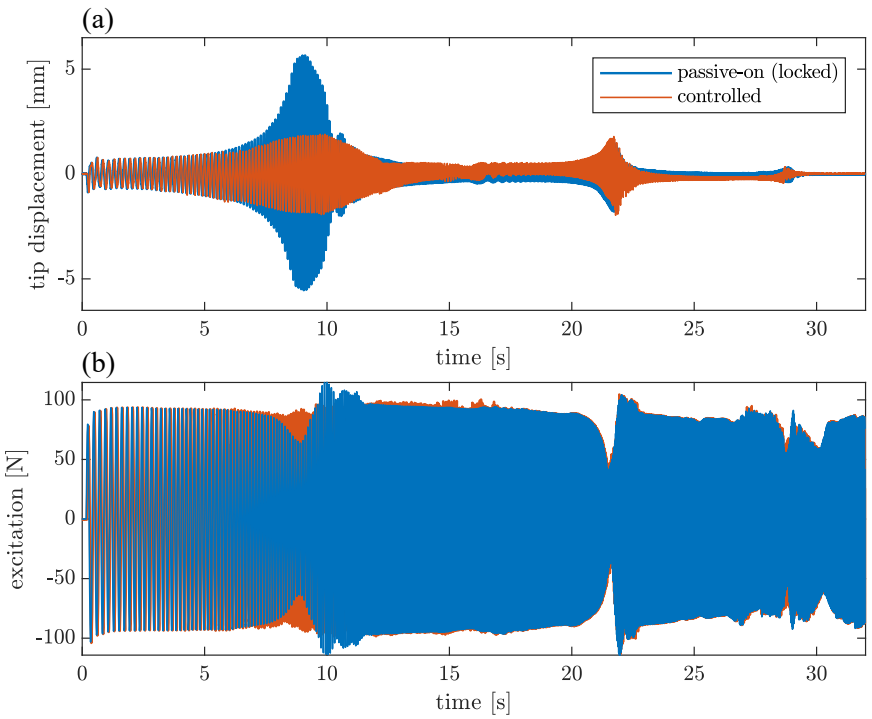

Fig. 5.17. Time history of the tip displacement of laboratory frame demonstrator and excitation force of controlled (case 1) and uncontrolled (passively locked) structure obtained from the single frequency sweep.

structure, three corresponding resonances can be distinguished in the structural displacement (Fig. 5.17a). The amplitude of the structural displacement is significantly reduced for the controlled structure. It is worth to notice that the force amplitude decreases when the structural vibration achieves a greater amplitude. Hence, the controlled structure is excited with greater force values than uncontrolled one in the region of the first resonance (Fig. 5.17b). Thus, damping introduced by the proposed control is greater in reality than presented in Fig. 5.17a. Due to the selected weights in the algorithm only the first resonance is intentionally mitigated by the control.

A comparison of frequency response functions $\mathrm{FRF}_{\mathrm{dis}}$ characterising the dependence on the structural tip displacement on the excitation force for the uncontrolled and controlled laboratory structure is shown in Fig. 5.18a. Analogous results obtained from the simulation are shown in Fig. 5.18c. As mentioned in a previous paragraph, the control mitigates only the first resonance peak due to the selected weights in the control algorithm. Similarly to free-vibration tests the control performance in the experiment is worse than in the simulation but still satisfactory. The reason of the worse performance is again the imperfect-

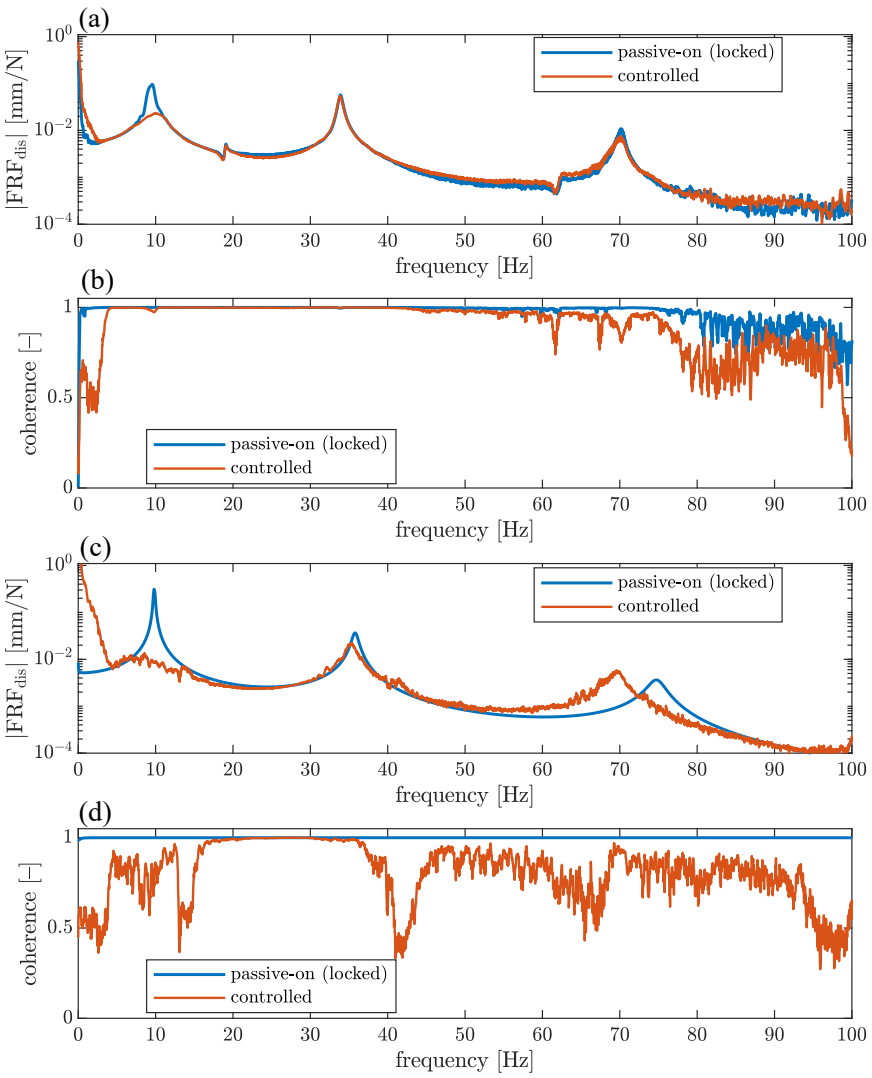

Fig. 5.18. Comparison of various frequency-domain characteristics of vibration of controlled (case 1) and uncontrolled (passively locked) structure: (a) experimental FRF for structural tip displacement, (b) corresponding experimental coherence, (c) numerical FRF for structural tip displacement and (d) corresponding numerical coherence.

ness of the lockable joints and the fact that the level of the transmitted bending moments reaches the maximal values, since the displacement amplitude at the first resonance is comparable to the previously tested free vibration (compare Figs. 5.17a and 5.13a, c). Then, dry friction introduces additional damping into the structure even for the locked joints. This results in the fact that $\mathrm{FRF}_{\mathrm{dis}}$ obtained from the simulation with uncontrolled structure contains bigger the first

resonance peak, whereas for the corresponding controlled case is smaller than in the experimental case.

Despite the nonlinear character of dry friction introduced by real lockable joints the coherence functions obtained for the laboratory structure with both the passively locked and controlled joints are mainly close to one. Only decreases and noise in the region close to the upper limit of the excitation bandwidth and near to zero frequency that is outside the excitation bandwidth (4–100 Hz) are noticeable. FRFs for the controlled structure demonstrated in Figs. 5.18a and c achieve large values for frequencies close to zero. Due to the excitation frequency starting from 4 Hz these values can be overestimated corresponding to the decreased coherence functions.

A very interesting observation is that the coherence function obtained from the simulation involving the updated FE model (Fig. 5.18d) has lower values than one obtained from the experiment (Fig. 5.18b). The reason is that the updated FE model is described by the piece-wise linear equation of motion (e.g. Eqs. (2.43) and (2.44)). This piece-wise linear character relates to the capability of the joints to be fully locked or fully unlocked. Due to the fact that the lockable joints in the FE model have no such limitations as the real joints, the simulated structure can accumulate and release more energy in the higher-order unlocked vibration modes. This behaviour is visible when comparing the experimental and numerical structural response in free-vibration tests, e.g. in Figs. 5.14a and b. The numerical structural response is more distorted than the experimental response which decays more gently. Also behaviour of the FE model is more sensitive to the time instant of the joint unlock. It results in more non-coherent structural response signals than for the experimental case, despite the nonlinearity resulting form the dry friction in real joints.

The third resonance peak in simulation results (Fig. 5.18c) is not mitigated but is shifted towards lower frequencies. As $\alpha_3 = 0$, the third vibration mode is not mitigated. However, relatively small thresholds κ_1 and κ_2 result in additional joint switches. As the structural stiffness is lower when the joint is unlocked, the third resonance peak is shifted to the frequency near to 70 Hz that is between unlocked and locked natural frequency of the structure, 66.4 and 74.8 Hz, respectively.

The observations aforementioned are relevant also for FRFs calculated for accelerations of the structural tip and corresponding coherence functions presented in Fig. 5.19.

Experimental PSDs of structural tip displacements and accelerations are shown in Figs. 5.20a and b, respectively. Despite the fact that the level of the force produced by the modal shaker is relatively greater for the controlled structure than in the passively locked case near the first resonance (see Fig. 5.17), PSD of the structural tip displacement is reduced by 90 % at the first resonance peak.

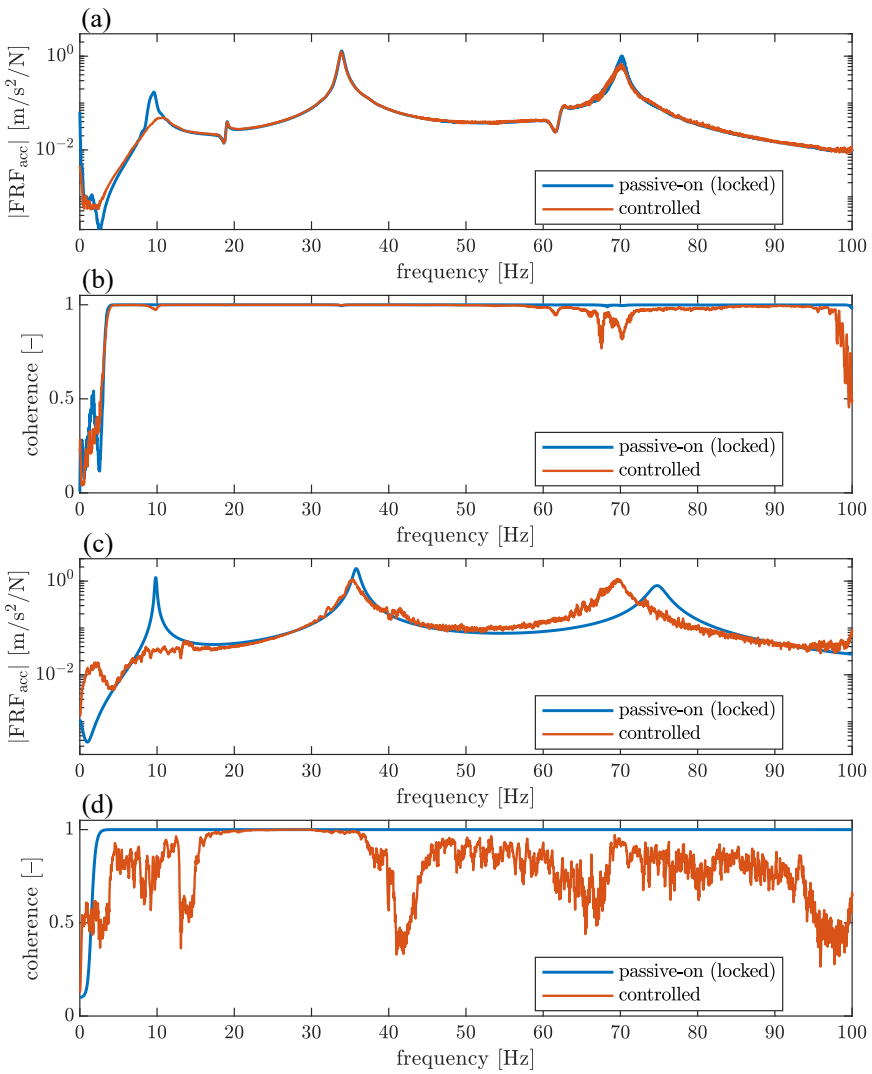

Fig. 5.19. Comparison of various frequency-domain characteristics of vibration of controlled (case 1) and uncontrolled (passively locked) structure: (a) experimental FRF for structural tip acceleration, (b) corresponding experimental coherence, (c) numerical FRF for structural tip acceleration and (d) corresponding numerical coherence.

PSD of structural tip accelerations reveals the phenomenon of the modal energy transfer from the first unlocked vibration mode into the higher-order vibration modes that are outside the frequency range of the excitation (4–100 Hz). It is the essential observation in the conduced experimental validation, since despite the significant imperfectness of the lockable joints utilised in the laboratory frame demonstrator the proposed control algorithm still operates in agreement

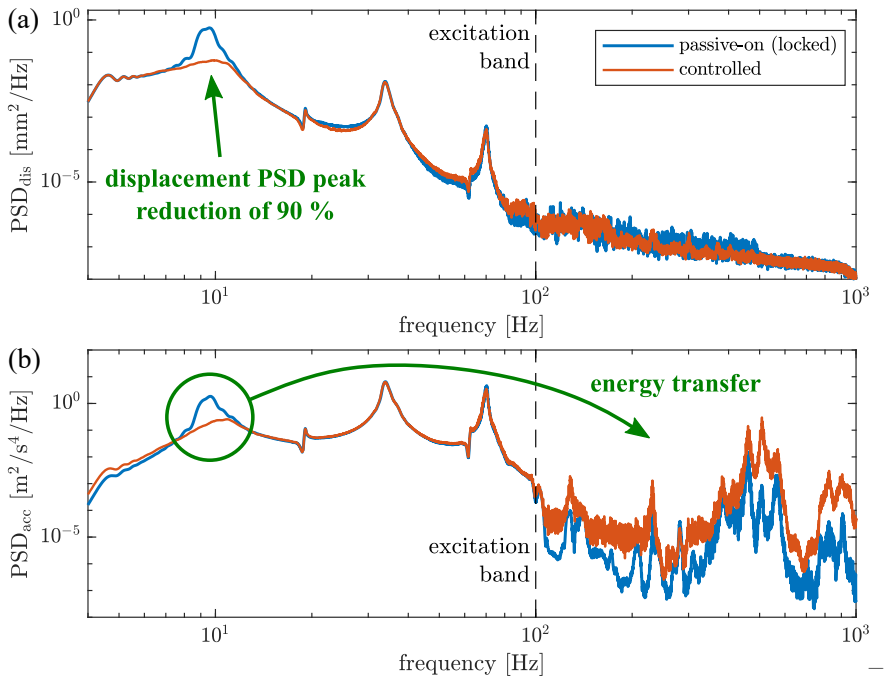

Fig. 5.20. Experimental power spectral densities of structural tip (a) displacement and (b) acceleration obtained for case 1.

with the stated thesis. PSD of the structural tip accelerations for the controlled structure is increased at the higher frequencies (outside the excitation bandwidth) at the expense of the first resonance peak in accordance with the selected weights. It is despite the fact that a certain amount of mechanical energy is dissipated in the dry friction in the lockable joints due to the limited clamping force.

Case 2

In this case, lockable joints J3 and J4 are selected to be controlled. The thresholds and weights are selected as follows: $\alpha_1 = 1$, $\alpha_2 = 0.05$, $\alpha_3 = 0$, $\kappa_1 = 0.384$ W and $\kappa_2 = 5.3 \cdot 10^{-4}$ W.

Experimental and numerical FRFs accompanied with corresponding coherence functions are presented in Fig. 5.21. FRFs depicted in Figs. 5.21a and c are additionally plotted in a linear scale in Fig. 5.22, in order to show more details in vicinity of the resonance peaks. Here, not only the first resonance is damped but also the second one. It is interesting that the first resonance peak is reduced significantly more efficiently in the numerical simulation than in the experiment, whereas the control algorithm mitigates the second resonance peak effectively both for the experiment and the simulation. The reason of this phe-

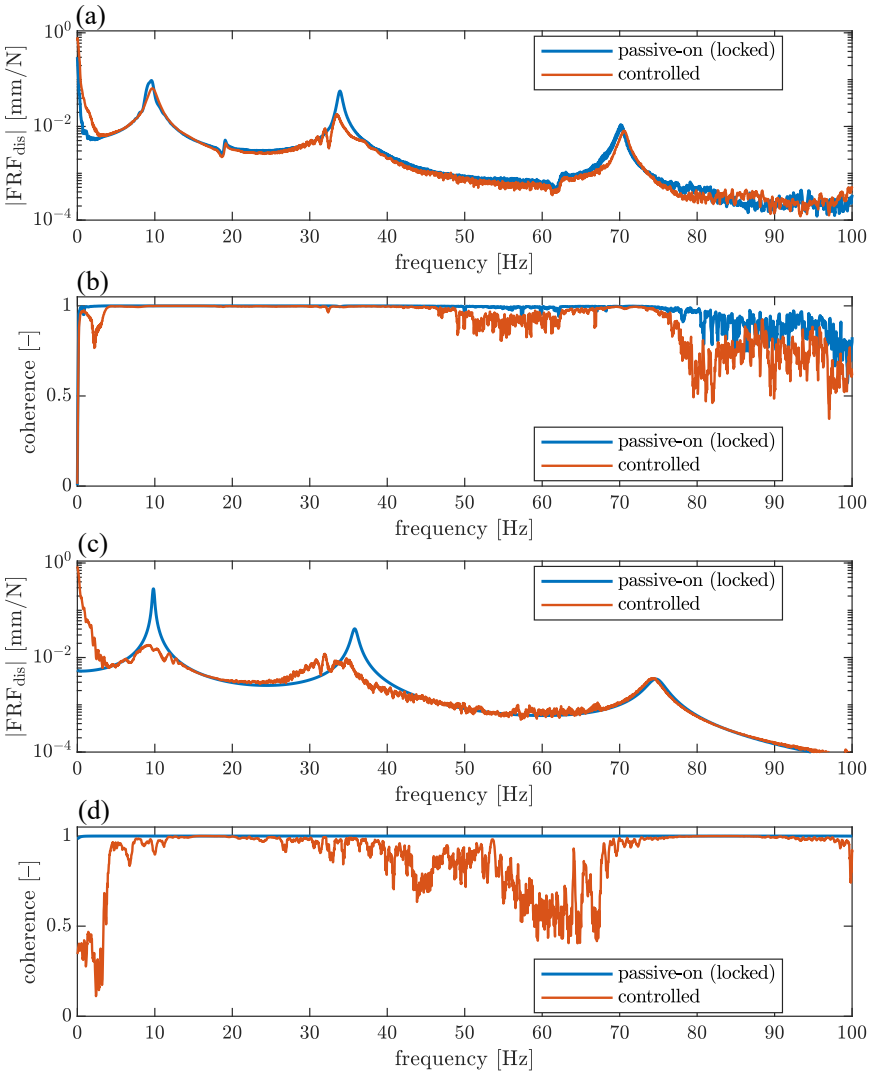

Fig. 5.21. Comparison of various frequency-domain characteristics of vibration of controlled (case 2) and uncontrolled (passively locked) structure: (a) experimental FRF for structural tip displacement, (b) corresponding experimental coherence, (c) numerical FRF for structural tip displacement and (d) corresponding numerical coherence.

nomenon can be explained by returning to the considerations on case 2 of the free vibration, where the same pair of joints is controlled (J3 and J4). Case 2 of free vibration tests reveals that significant amount of the strain energy accumulated in higher-order unlocked vibration modes is not released in the free vibration when the joint is being unlocked. It is due to the residual clamping force in the real lockable joints. As the release of the manual hook excites vibration mainly in the

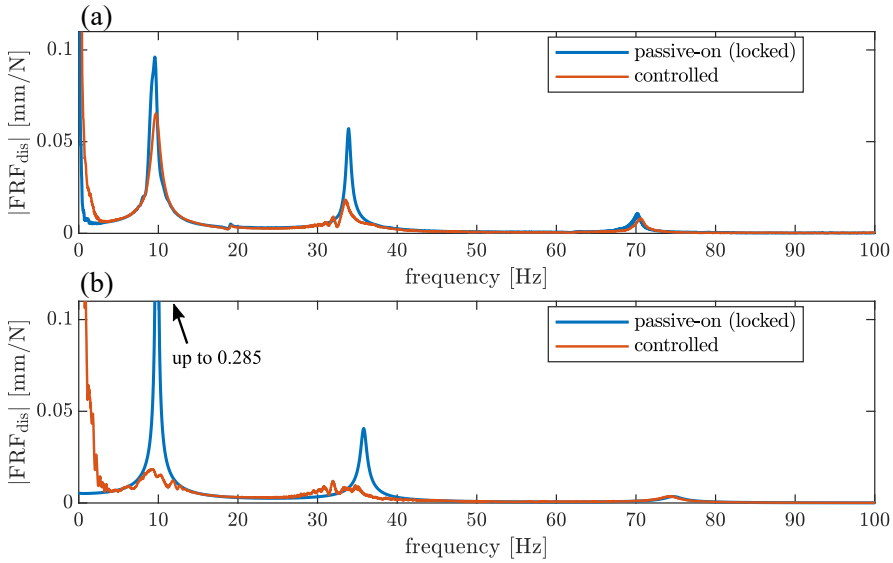

Fig. 5.22. Comparison of FRFs for structural tip displacement in linear scale for controlled (case 2) and uncontrolled (passively locked) structure obtained from: (a) experiment and (b) numerical simulation.

first vibration mode, this observation is relevant also for the first resonance peak in the present case of the forced vibration. However, the second peak is efficiently mitigated even in the experimental case due to the fact that the pair of joints J3 and J4 transmits greater bending moments when modal shaker sweeps the second resonance peak. This is illustrated in Fig. 5.23 by using the updated FE model with passively locked joints. The greater level of the transmitted bending moments in relation to the moment $f^{\mathrm{u\,max}}$ results in ability to release more strain energy in the free vibration. The structural tip displacement obtained with the updated FE model is significantly greater than the corresponding displacement obtained experimentally for the passively locked joints (compare Figs. 5.17a and 5.23a) due to the additional friction-based damping in real joints, whereas joints in numerical simulations are locked without slipping. It is worth to notice, that despite the fact that the joints J1 and J2 are not controlled in this case (passively locked), slipping between their friction parts still cannot be avoided.

In the present case of the forced vibration testing once again experimental coherence is close to one despite the nonlinearity provided by the dry friction (Fig. 5.21b). Coherence has lower values only for frequencies above the third resonance peak and below 4 Hz, which is a lower limit of the excitation bandwidth. Numerical coherence (Fig. 5.21d) obtained for the controlled structure tends to be smaller than experimental one at frequencies below 70 Hz. It is consistent with results discussed in case 1.

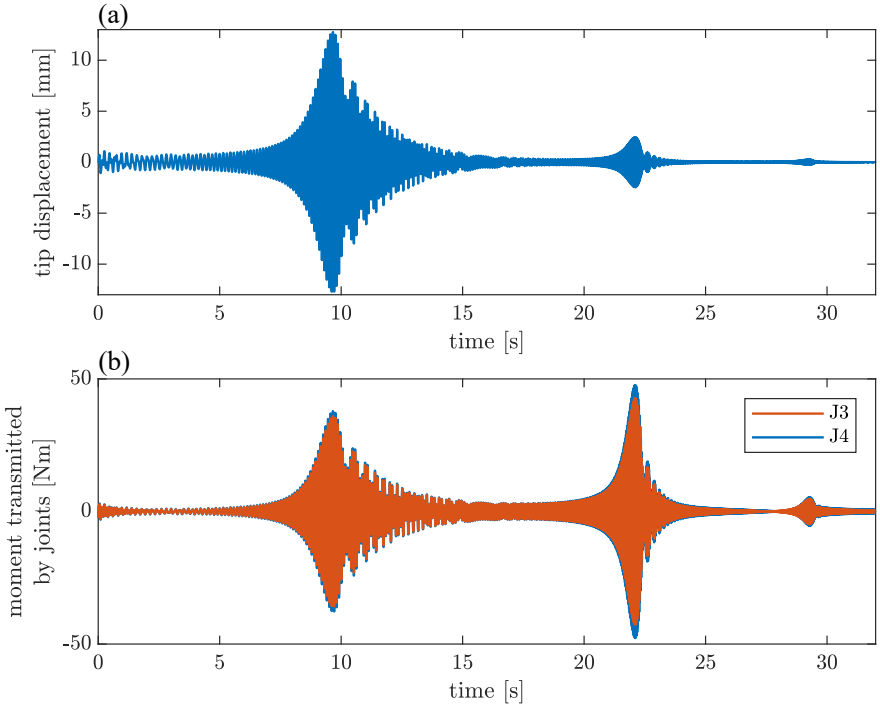

Fig. 5.23. Time history of (a) tip displacement obtained with the updated FE model with passively locked joints and (b) corresponding bending moments transmitted by the joints J3 and J4 for a single frequency sweep.

Experimental PSDs of the structural response both for the controlled and uncontrolled case are compared in Fig. 5.24. Similarly to FRFs, the PSDs of the structural response are reduced more effectively for the second resonance peak (displacement PSD peak reduction of 73 %) than for the first one (reduction of only 45 %). A comparison of the PSD of the structural tip acceleration (Fig. 5.24b) demonstrates that mechanical energy is transferred from the first and second unlocked vibration mode into the higher-order vibration modes. The PSD level of the structural tip acceleration for the controlled structure outside the excitation frequency range is visibly greater than one obtained for the passively locked joints. This difference is greater than in case 1 (compare with Fig. 5.20b). The first possible reason is that the energy is transferred out from the two controlled unlocked vibration modes, unlike in case 1 where only the first resonance peak is reduced. Additionally, the second resonance peak corresponds with the greater bending moments transmitted by the lockable joints J3 and J4 (see Fig. 5.23). Another reason is that the operation of the pair of lockable joints J3 and J4 provides better accumulation of the strain energy than in the case of the joints J1 and J2 due to higher maximal bending moments $f_k^{\mathrm{l\,max}}$ (see Table 5.1).

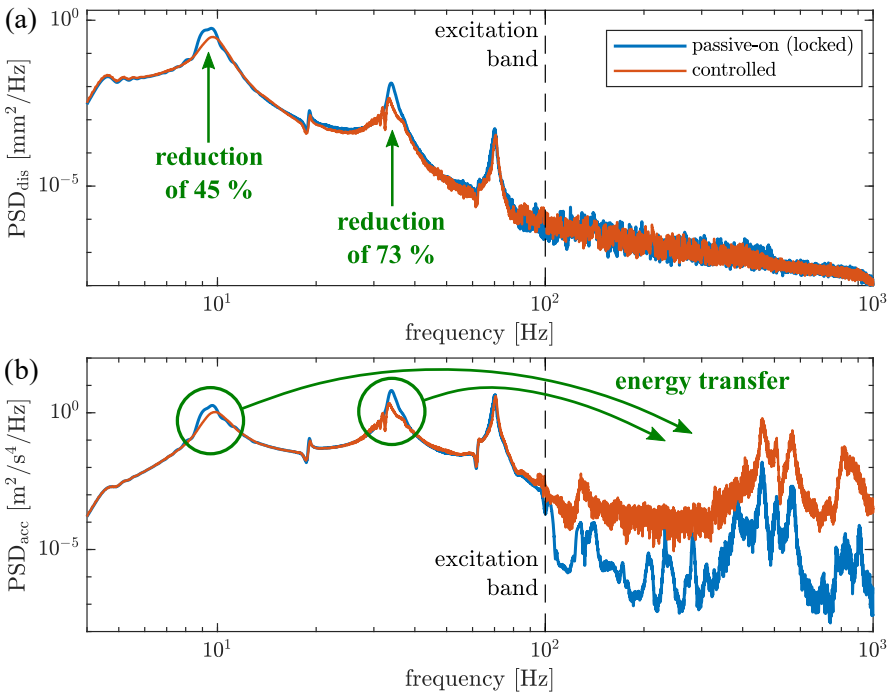

Fig. 5.24. Experimental power spectral densities of structural tip (a) displacement and (b) acceleration obtained for case 2.

5.5. Energy transfer to the targeted mode

In this section, the ability of the proposed control strategy to transfer the mechanical energy from the currently excited unlocked vibration modes into the preselected one is verified experimentally. Experimental results are compared with ones obtained with the aid of the updated FE model. The use of a manual hook is insufficient in examination of the control strategy in transferring the mechanical energy in various directions. The manual hook excites mainly the first vibration mode, whereas the ability to excite various vibration modes is desired. Thus, only the forced vibration are tested. Each time the preselected unlocked vibration mode is outside the frequency bandwidth of the excitation aiming at demonstration of the modal energy transfer phenomenon.

The excitation force is provided by the modal shaker whose stinger is connected at the same location as when testing the control performance in vibration attenuation (see Fig. 5.16). The modal shaker sweeps frequency with logarithmic frequency increments over time, analogously to tests of the vibration mitigation. The difference lies in the frequency range, which varies depending on the particular control case and is described below. The frequency sweeps of time duration

32 s are performed. Results discussed below are averaged from five particular frequency sweeps. Excitation in numerical simulation is reproduced analogously to vibration attenuation tests, however, new frequency limits from the cases discussed below are substituted into Eq. (5.22) and the amplitude $A_\mathrm{d} = 70$ N is adopted in Eq. (5.21).

Two control scenarios are considered:

case 1: the first unlocked vibration mode is targeted, whereas only the second and third unlocked vibration modes are within excitation frequency range and

case 2: the second unlocked vibration mode is targeted, whereas only the first one is within the excitation frequency range.

Lockable joints J3 and J4 (belonging to the second transversal beam) are selected to be controlled in both control cases. These lockable joints provide good controllability both for the first and second monitored vibration mode. Similarly to vibration attenuation, Algorithm 2 is adopted according to Subsection 5.3.3. Algorithm parameters $t_\mathrm{lock} = t_\mathrm{unlock} = 15$ ms, $\kappa_1 = 0.384$ W, and $\kappa_2 = 5.25{\cdot}10^{-4}$ W are common for both control cases, whereas the weights α_p are selected separately with the trial-and-error method.

Due to the fact that that energy is transferred to the unlocked vibration mode outside the frequency bandwidth of the excitation, FRFs are not used in this subsection. Only PSD functions are utilised to analyse the structural behaviour in the frequency domain.

Case 1

In this case the first unlocked vibration mode is selected as the targeted one. The first unlocked natural frequency of the updated FE model is $f^{(1)} = 8.98$ Hz, whereas its locked counterpart is $\widetilde{f}^{(1)} = 9.83$ Hz. Both of these frequencies are outside the frequency bandwidth of excitation that is 20–100 Hz. The following algorithm weights are selected: $\alpha_1 = -1$, $\alpha_2 = \alpha_3 = 0$.

PSD of structural displacement at the tip for controlled and passively locked joints obtained from the experiment is shown in log-log and log-lin scales in Figs. 5.25a and b, respectively. Figure 5.25b demonstrates the increase in the vibration amplitude after transferring the energy into the first unlocked vibration mode, whereas Fig. 5.25a demonstrates the structural response in all monitored unlocked vibration modes and higher-order ones up to 1 kHz.

It is evident that a significant amount of the energy is transferred from the second unlocked vibration mode into the first, targeted, one that is outside the excitation frequency range. It results in the significant increment of the vibration amplitude, since it is natural that lower-order vibration modes require less energy to be excited with the same amplitude than the higher-order ones.

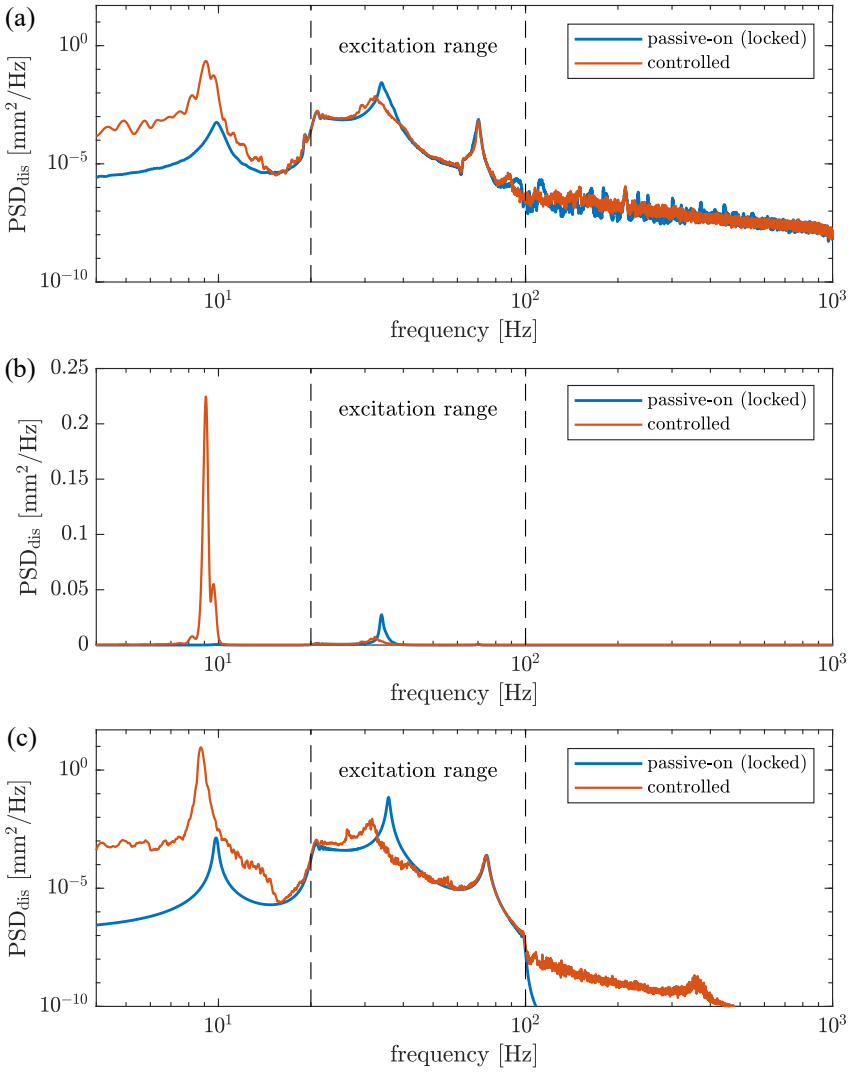

Fig. 5.25. Comparison of power spectral densities of structural tip displacements for the passively locked and controlled (case 1) lockable joints J3 and J4 obtained from: (a) experiment, shown in log-log scale, (b) experiment, shown in log-lin scale and (c) numerical simulation, shown in log-log scale.

As $\alpha_3 = 0$, the third resonance peak is not affected by the lockable joints. Additionally, controllability of this mode by the currently controlled pair of the lockable joints is very crude (see Fig. 5.8).

Analogous results obtained from the numerical simulation are shown in Fig. 5.25c. Here the observation that energy is transferred from the second unlocked vibration mode to the first one is also relevant. Due to the fact that

the lockable joints in the simulation are not subjected to the slip effect, the energy transfer is more efficient and results in the greater PSD value for the targeted unlocked vibration mode.

A comparison of PSD of structural tip accelerations for passively locked and controlled joints is shown in Fig. 5.26 both for experiment and numerical simulation. Here, the effect of directed energy flow into the first vibration mode from the second one also is clearly demonstrated both for the experiment and numerical simulation. A certain amount of the structural energy is unintentionally transferred into the higher-order unlocked vibration modes that is demonstrated by the increment of the PSD values for the controlled structure at frequencies above the excitation range. This can be considered as the control spillover effect, as in the energy harvesting application it is an undesired phenomenon. The increment of PSD for the controlled case corresponding to the targeted vibration mode and the higher-order vibration modes is greater for the numerical simulation due to mentioned limitation of the real lockable joints.

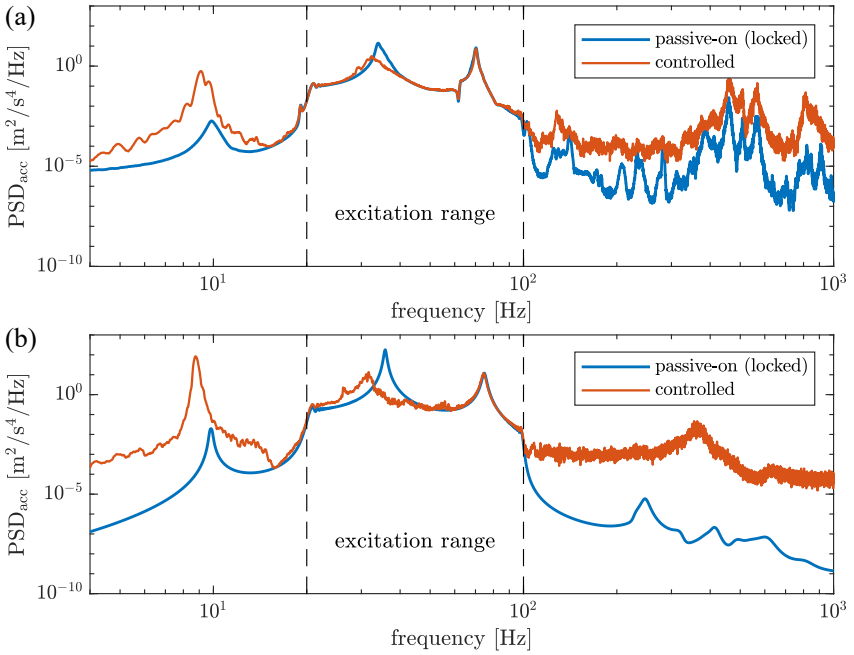

Fig. 5.26. Comparison of power spectral densities of structural tip accelerations for the passively locked and controlled (case 1) lockable joints J3 and J4 obtained from: (a) experiment and (b) numerical simulation.

The time history of the structural tip displacement obtained from a single experimental frequency sweep for uncontrolled (passive-on) and controlled joints J3 and J4 is depicted in Fig. 5.27. Two resonance regions visible in Fig. 5.27a relate

to the excitation frequency range omitting the first (both locked and unlocked) vibration mode. Results shown the zoomed area (Fig. 5.27b) demonstrate the sudden change of the predominant vibration frequency accompanied with the increase in the amplitude. These phenomena result from the operation of the joints which starts closely before the zoomed area, where the vibration amplitude of the controlled structure gently increases. This change of character of structural vibration confirms that the proposed control causes the modal energy transfer from the second to the first unlocked vibration mode. It is despite the significant imperfectness of the real lockable joints.

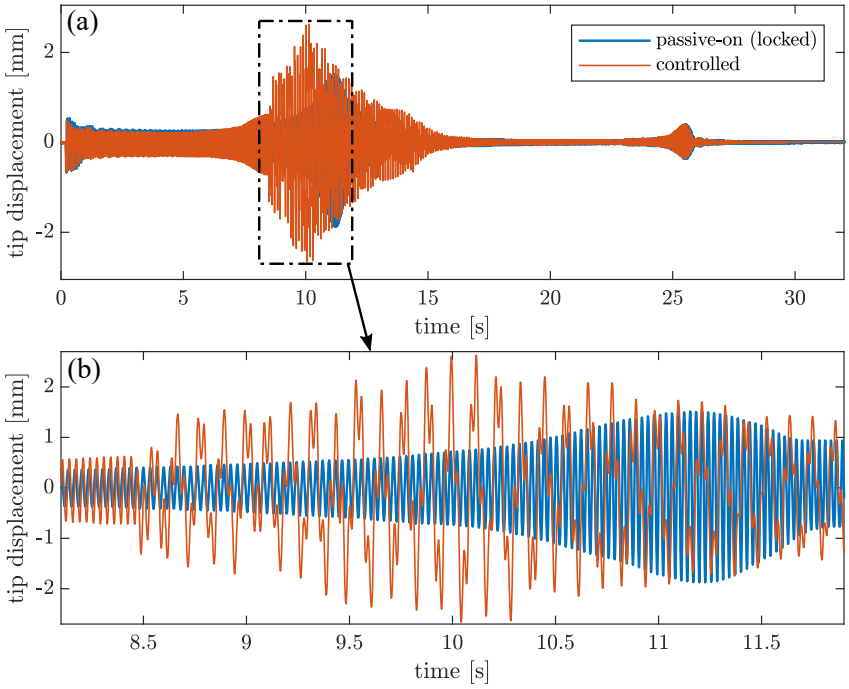

Fig. 5.27. Comparison of time histories of structural response on single frequency sweep for the uncontrolled and controlled (case 1) laboratory frame demonstrator: (a) whole duration and (b) zoomed region.

Case 2

In this case the energy is transferred into the second unlocked vibration mode, whose natural frequency is $f^{(2)} = 28.91$ Hz, whereas the second locked natural frequency is $\widetilde{f}^{(2)} = 35.83$ Hz. Both of these frequencies are outside the excitation frequency range that is 4–20 Hz. Algorithm weights $\alpha_1 = 0.5$, $\alpha_2 = -1$ and $\alpha_3 = 0$ are selected.

A comparison of PSD of structural tip displacements obtained for passively locked and controlled lockable joints both for the experiment and simulation are

shown in Fig. 5.28. It is evident that the second, targeted, unlocked vibration mode has greater participation in the structural motion at the expense of the currently excited, the first one. It is visible both in the experiment and numerical simulation. The second frequency peak obtained for the controlled structure is placed between the second locked and unlocked natural frequency, $f^{(2)}$ and $\widetilde{f}^{(2)}$, respectively. It is difficult to assess whether the doubled peak related to the targeted mode of the controlled case in the numerical results (Fig. 5.28b) relates to locked and unlocked vibration modes shifted in the frequency domain or it is the result of the leakage effect.

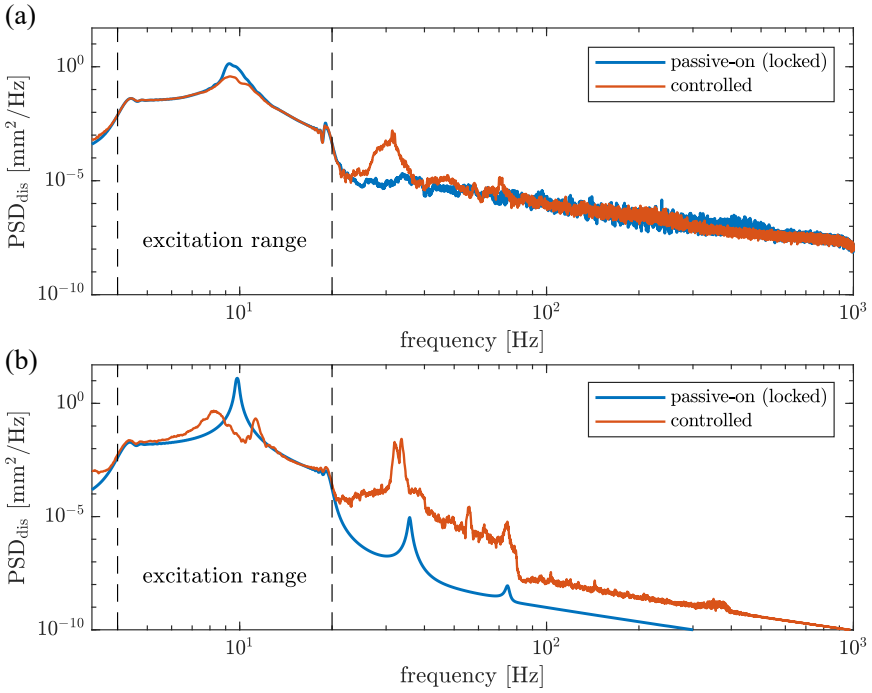

Fig. 5.28. Comparison of power spectral densities of structural tip displacement for the passively locked and controlled (case 2) lockable joints J3 and J4 obtained from: (a) experiment and (b) numerical simulation.

The experimental results once again demonstrate reduced effectiveness of the proposed control strategy compared to numerical simulations, attributed to the imperfect behaviour of the lockable joints. A lower value of the first resonance peak for the passive-on case in the experiment in relation to the corresponding one obtained in the numerical simulation is the result of both the decreased force provided by the modal shaker when the structure is in resonance and additional nonlinear damping provided by the dry friction in real lockable joints (joints J1 and J2, even if they are not controlled).

PSD functions of structural tip acceleration corresponding to results discussed above are shown in Fig. 5.29. The modal energy transfer from the first vibration mode to the second one is clearly demonstrated. PSD of accelerations at frequencies above the second unlocked vibration mode are increased for the controlled structure both in the experiment and numerical simulation. It shows that a certain amount of the energy is unintentionally transferred into the higher-order unlocked vibration modes. Here, this effect seems more pronounced than in case 1 due to the lower level of high-frequency accelerations of passive structure. However, the level of the high-frequency accelerations of the controlled structure is similar as in case 1 (compare with Fig. 5.26). The reason is explained in case 1–2 of the numerical study on energy harvesting applications in Subsection 4.2.5. As explained, when the mechanical energy is to be transferred from the currently excited unlocked vibration mode to the targeted one whose the unlocked natural frequency is relatively greater the joints are unlocked at time instances when measured strains are nonzero (see e.g. Fig. 4.30c). In this case usually some amount of the energy is not only released in the free vibration of the targeted unlocked vibration mode but also in the higher-order ones. However, the negative weight of the targeted mode allows for the reduction of the energy escape into high-frequency oscillations.

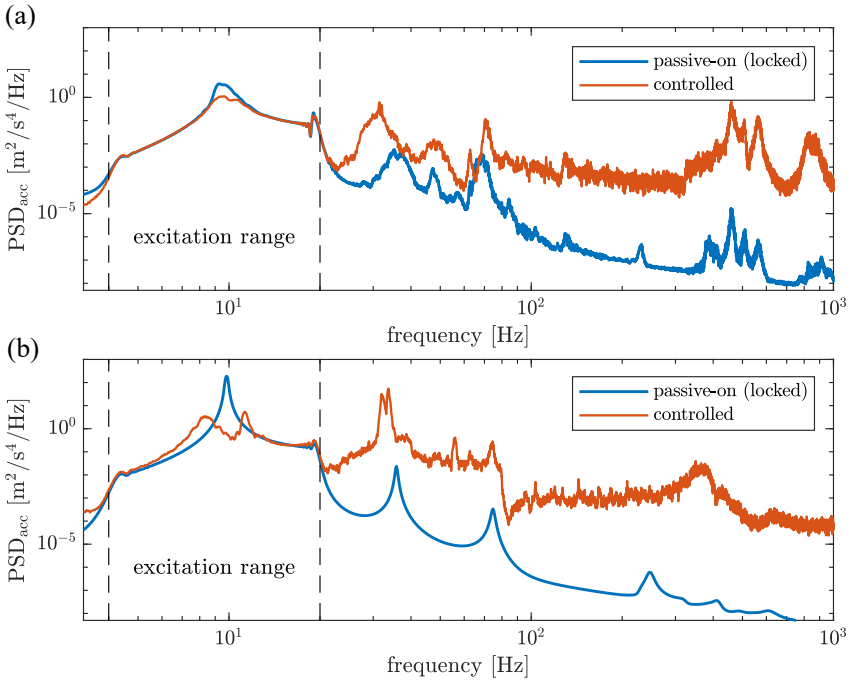

Fig. 5.29. Comparison of power spectral densities of structural tip acceleration for the passively locked and controlled (case 2) lockable joints J3 and J4 obtained from: (a) experiment and (b) numerical simulation.

6. Conclusions

In the present thesis, the new semi-active control methodology for energy transfer between structural vibration modes has been proposed. Such a transfer is realised by locking or unlocking the structural joints that provides or removes the modal coupling effect resulting in the energy flow. The proposed control methodology includes novel: control law and control algorithm as well as methods for optimal placement of sensors and lockable joints.

The control strategy is explicitly based on thorough analytical derivations, as opposed to previously proposed semi-active control strategies inducing the energy transfer between vibration modes that are heuristic. In Chapter 2, it has been shown that locking and unlocking of the joint causes a system reconfiguration that changes: number of structural DOFs, local stiffness properties of the structure, modal basis and its dimension. It has been demonstrated that it is possible to express structural displacement in the single unlocked modal basis (obtained for all joints in the unlocked state) even if the joints are currently locked. The use of the locked modal basis (obtained for joints locked) is insufficient due to its lower dimension. It has been shown that the constraint describing the joint lock can be relaxed by employing large viscous damping between locked rotational DOFs. It significantly simplifies the numerical simulation of the structural behaviour and further analytical derivations.

In Chapter 3, the control strategy has been proposed, taking into account the equipment limitations. The quantities to be estimated from measurements for the proper operation of the proposed control have been identified: the modal velocities (obtained using the modal filtering technique) and the bending moments transmitted by the lockable joints (estimated from strain measurements taken in the vicinity of each lockable joint).

The adopted method of sensor layout optimisation for modal filtering purposes is straightforward in the code implementation and enables proper operation of the control algorithm both in simulations and during experimental tests in presence of real measurement noise. The new criterion for optimal placement of the lockable joints, dedicated for the developed control methodology, also has been proposed. It describes the amount of energy that can be distributed among various unlocked vibration modes by unlocking the joint at its current location. The measure of the modal controllability can be approximated using only the locked and unlocked natural frequencies.

The novel control law, explicitly based on the derivation describing modal energy transfer, has been proposed. It provides the steepest descent of weighted sum of the energies associated with monitored vibration modes. For vibration attenuation application all weights are selected as positive, resulting in the energy transfer from the monitored unlocked vibration modes to the higher-order ones that are highly damped. Then, mechanical energy is effectively dissipated in the structural volume. For the energy harvesting application, the weight associated with the targeted mode is selected to be negative. It imposes the energy flow from currently excited monitored vibration modes to the targeted mode tuned to the energy harvester mounted on the controlled structure. It ensures the resonance of the energy harvester. Moreover, it has been shown that the proposed control algorithm locks the joints at time instances when structural jerking is avoided or reduced.

Benchmark tests in numerical study described in Chapter 4 demonstrate that the proposed control methodology achieves better performance of vibration attenuation with a lower number of joint switches (locking/unlocking) than the PAR method. Moreover, the modal approach allows for mitigation of particular unlocked vibration modes with priorities pursued by the selected algorithm weights, as opposed to the PAR approach. The proposed control strategy is also less sensitive to non-optimal placement of the lockable joints (e.g. due to construction limitations). Regarding the energy transfer to the targeted unlocked vibration mode, the ability of the control to effectively transfer the energy to the targeted vibration mode has been demonstrated. It allows operation of the energy harvester in resonance independently of the currently excited vibration mode of the structure. It has been also concluded that if the targeted vibration mode has greater order than currently excited ones the vibration is mitigated due to undesired energy scattering into higher-order (unmonitored) vibration modes. This phenomenon does not take place when the energy is transferred in the opposed direction. Thus, if the aim of the system is only the energy harvesting, then one of the lowest order unlocked vibration modes should be the targeted one. However, if the control is applied to mitigate vibrations with additional simultaneous energy harvesting, then one of the highest-order monitored vibration modes can be the targeted one, providing both effective vibration damping and possibility of the energy recovery from the broadened frequency range of excitations.

Finally, the proposed control methodology has been verified experimentally in Chapter 5, using the laboratory-scale frame demonstrator equipped with six lockable joints. As the lockable joints used are still prototypes, the control strategy has been tested in the presence of significant imperfections, resulting in residual friction and sliding between their friction surfaces. The FE model updated by identification of 17 uncertain stiffness parameters has been employed to design the control algorithm (calculation of required modal parameters) and numerical simulations for the comparison with the experiment.

Free-vibration tests on the updated FE model demonstrate that the proposed controllability metric precisely reflects the ability of the joints at particular locations to transfer the mechanical energy between the vibration modes. In experiment the agreement between controllability metric and structural behaviour is not guaranteed due to the imperfectness of the real joints.

The control performance in transferring energy from excited monitored vibration modes to higher frequencies outside the external excitation range has been demonstrated experimentally during vibration-attenuation tests. For the energy harvesting application, precise energy transfer to the targeted mode outside the external excitation range can be achieved in both scenarios: whether the targeted frequency is lower or higher than the excitation frequency.

The thesis stated in Section 1.2 has been proven comprehensively: from theoretical considerations and analytical calculations to numerical and experimental validation. The proposed semi-active modal control methodology not only meets the expectations set for it but also is accompanied with the deepened theoretical foundation. This allows for a better understanding of the modal energy transfer in semi-actively controlled systems, the further development of the proposed methodology as well as its adoption to other kinds of structures.

The issues that are not investigated or resolved in this thesis, but are considered interesting and worthy of future research, are:

- an experimental investigation of the proposed control methodology using improved prototypes of the lockable joints, or a rearrangement of the currently employed ones so that the joints capable of transmitting the highest bending moments will be placed closest to the structural support,
- an experimental verification of the control with energy harvester and/or with especially designed primary (controlled) structure,
- maximisation of harvested energy and operational frequency bandwidth through primary-structure design,
- testing an analogous semi-active control strategy in three dimensional truss-like structures, in which translational DOFs are locked (lockable truss member) instead of rotational ones (lockable joint).

Appendix A. Three dimensional mode shapes of the laboratory-scale frame

In this appendix, all identified three-dimensional (3D) mode shapes of the structure described in Subsection 5.1.1 are shown in Figs. A.1–A.25. They are obtained for the joints in the locked state. The method of identification is described in Subsection 5.1.2.

Due to the fact that only in in-plane (IP) vibration modes are controllable by the lockable joints, the 3D vibration modes are divided into IP vibration modes and out-of-plane (OoP) vibration modes. IP vibration modes are used to update the FE model which reproduces only in-plane vibration. IP vibration modes are selected based on visual inspection of 3D mode shapes. Moreover, mode shapes that are strongly distorted are suspected to be spurious modes, highly contaminated by measurement error or error resulting from some nonlinearities. Thus, such vibration modes also are rejected. They could affect the quality of the updated model. The selected IP modes are: 2th, 5th, 7th, 10th, 11th, 13th, 18th, 22th, 23th and 24th one. The fifth 3D mode shape is similar to the fourth one and their natural frequencies also are not well-separated. They are almost orthogonal modes. However, due to the fact that the fifth vibration mode has a lower OoP displacement component in relation to the IP displacement component than the fourth vibration mode, only the fifth vibration mode is selected for the model updating procedure.

Seeking for the simplicity, after the selection of the IP vibration modes they are numerated from 1 to 10 in this thesis.

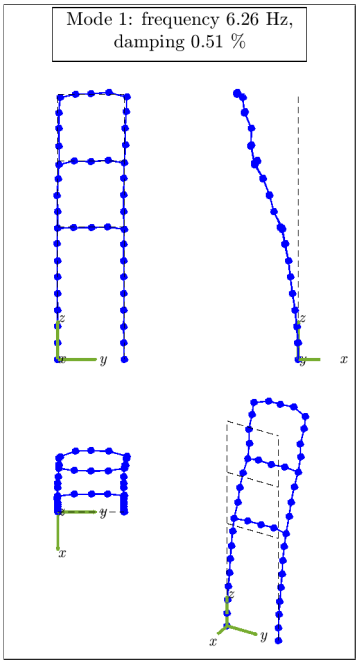

Fig. A.1. 3D mode 1.

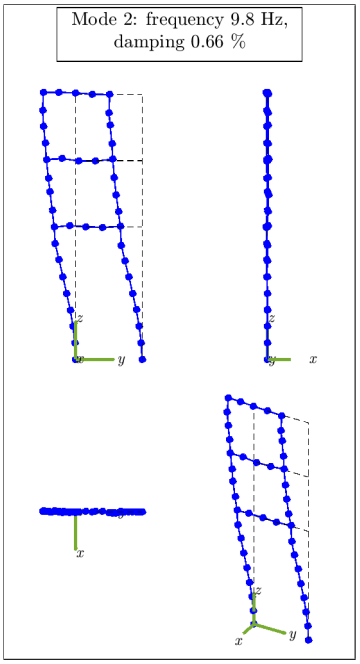

Fig. A.2. 3D mode 2.

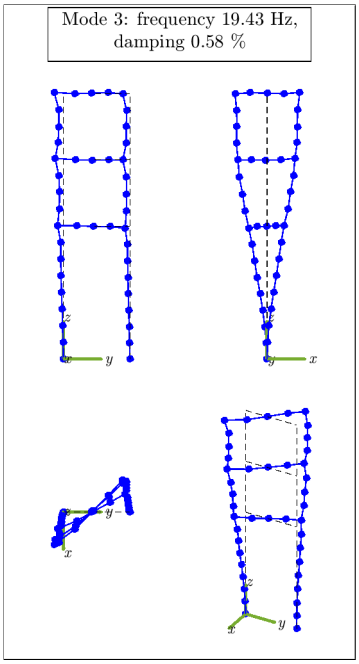

Fig. A.3. 3D mode 3.

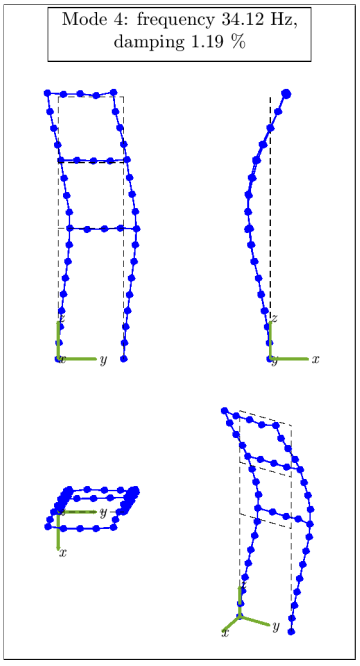

Fig. A.4. 3D mode 4.

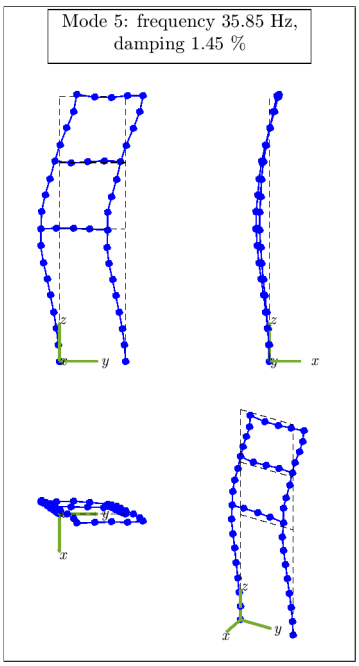

Fig. A.5. 3D mode 5.

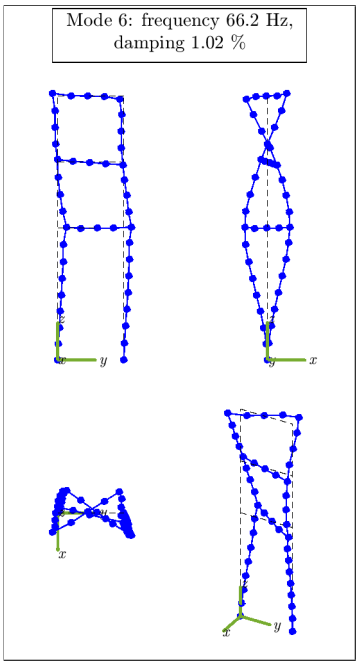

Fig. A.6. 3D mode 6.

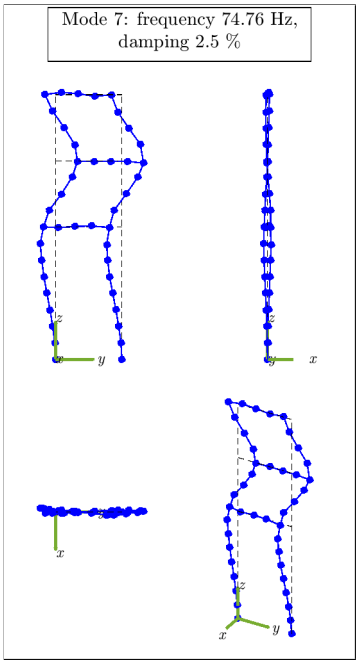

Fig. A.7. 3D mode 7.

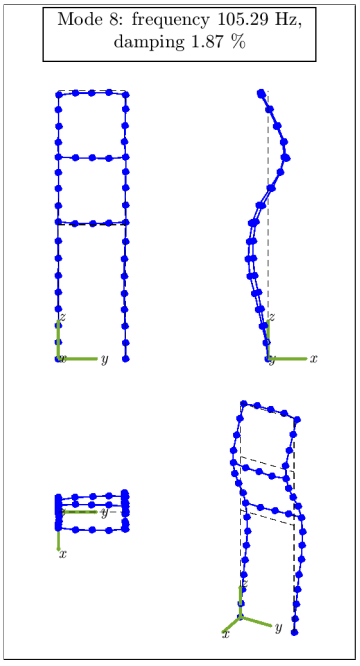

Fig. A.8. 3D mode 8.

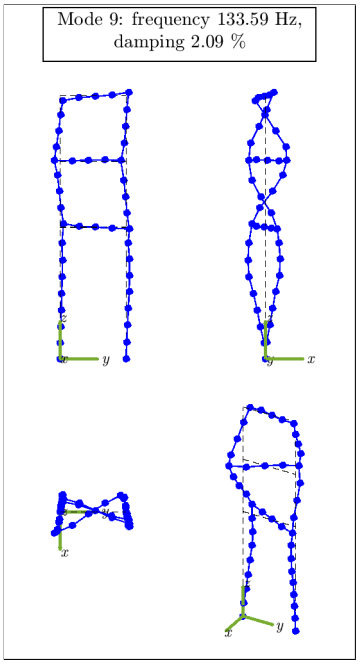

Fig. A.9. 3D mode 9.

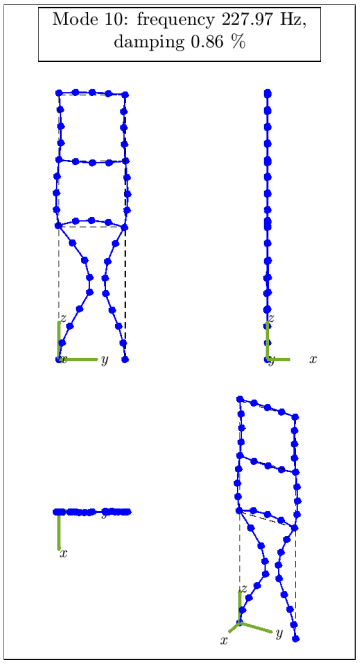

Fig. A.10. 3D mode 10.

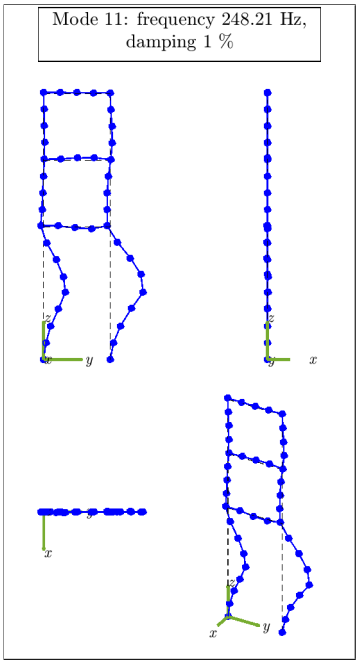

Fig. A.11. 3D mode 11.

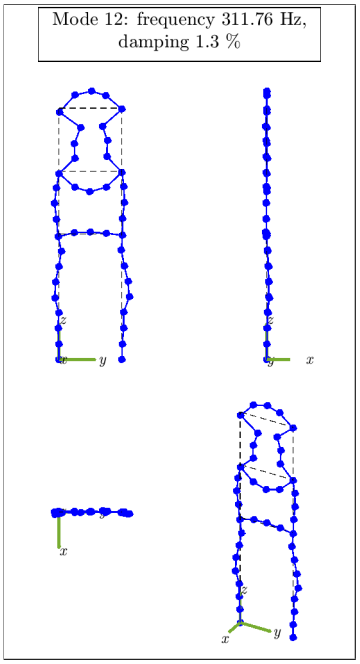

Fig. A.12. 3D mode 12.

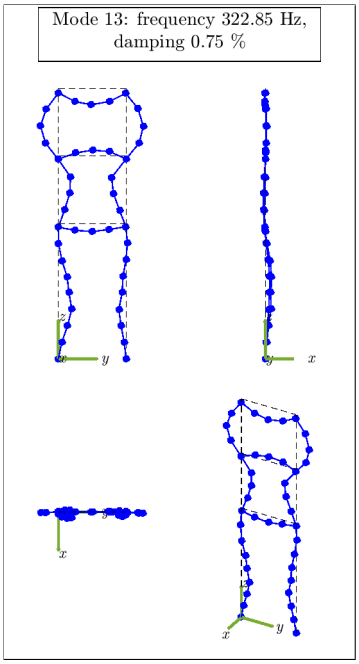

Fig. A.13. 3D mode 13.

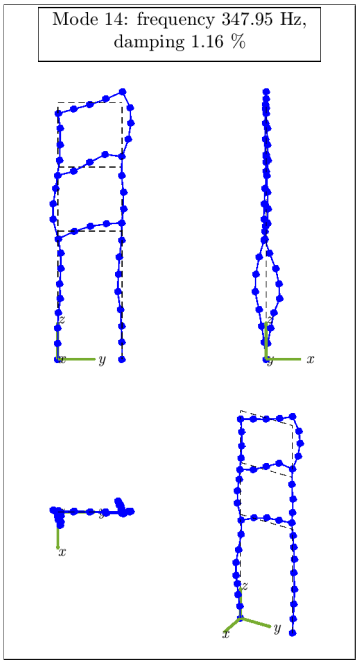

Fig. A.14. 3D mode 14.

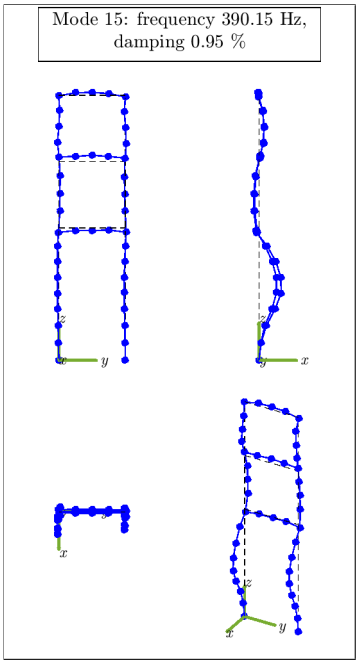

Fig. A.15. 3D mode 15.

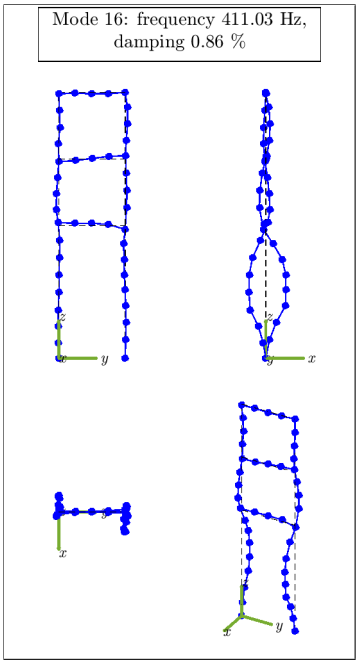

Fig. A.16. 3D mode 16.

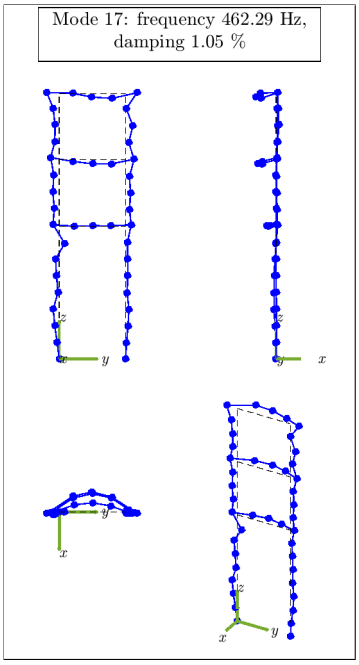

Fig. A.17. 3D mode 17.

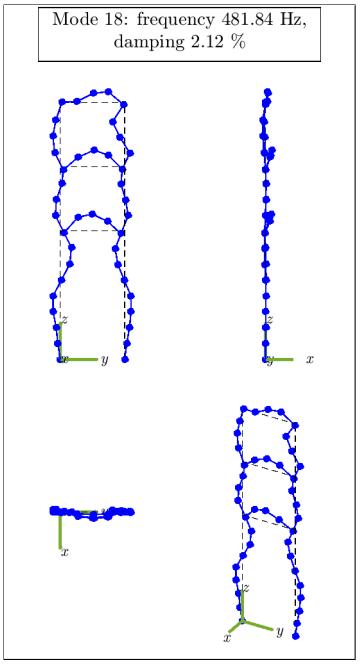

Fig. A.18. 3D mode 18.

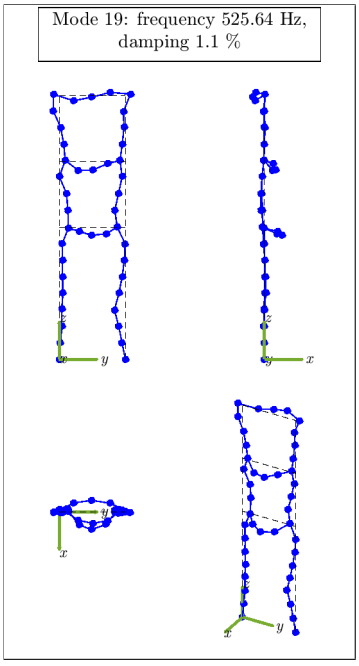

Fig. A.19. 3D mode 19.

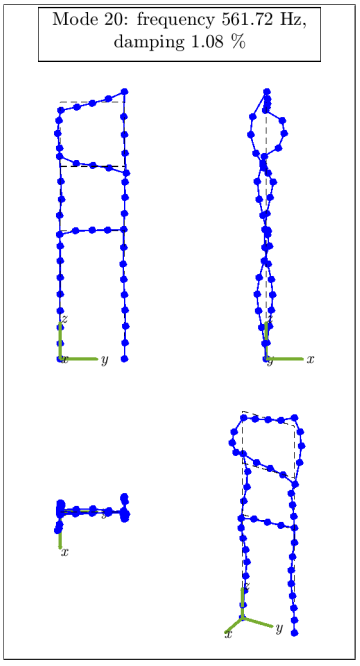

Fig. A.20. 3D mode 20.

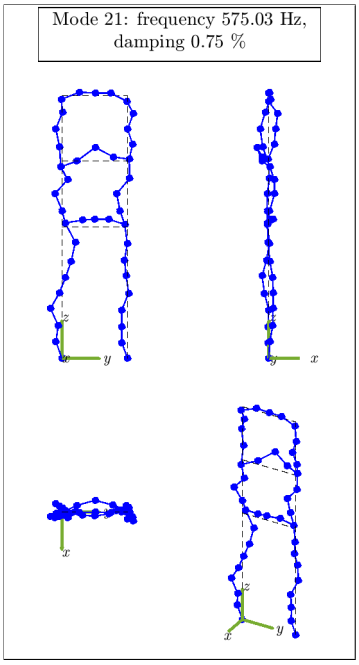

Fig. A.21. 3D mode 21.

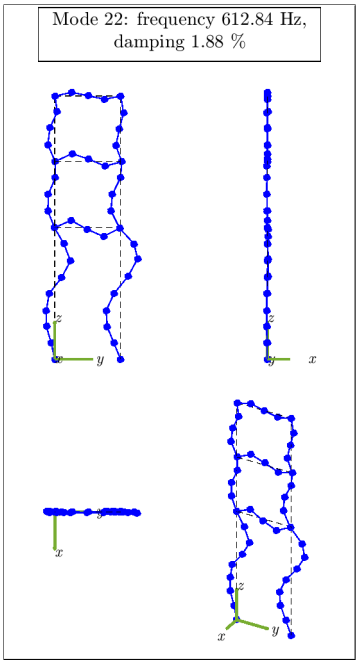

Fig. A.22. 3D mode 22.

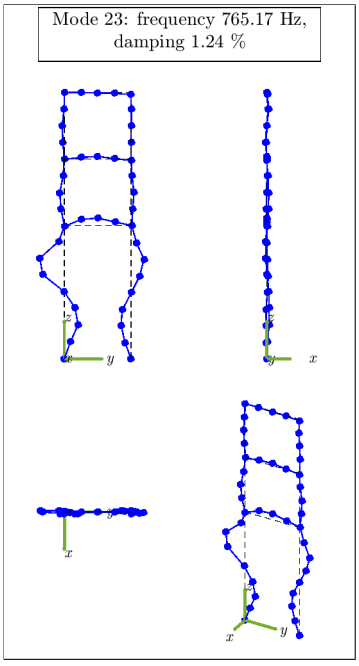

Fig. A.23. 3D mode 23.

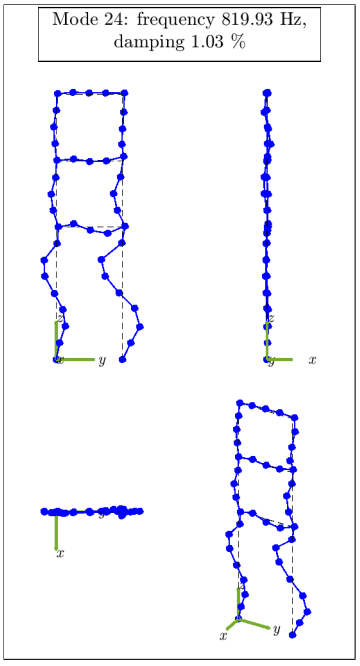

Fig. A.24. 3D mode 24

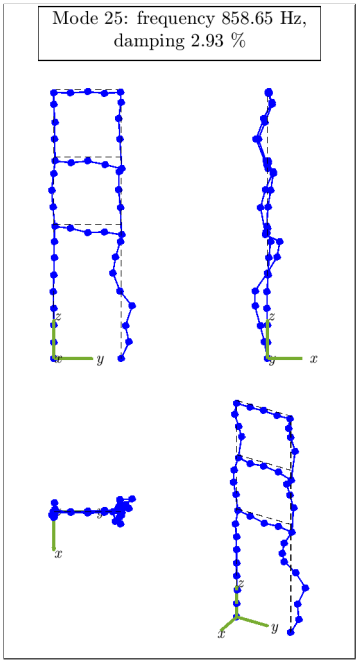

Fig. A.25. 3D mode 25.

Bibliography

1. K. Ghaedi, Z. Ibrahim, H. Adeli, A. Javanmardi, Invited review: Recent developments in vibration control of building and bridge structures, *Journal of Vibroengineering*, 19(5): 3564–3580, 2017, https://doi.org/10.21595/jve.2017.18900.
2. C. Wei, X. Jing, A comprehensive review on vibration energy harvesting: Modelling and realization, *Renewable and Sustainable Energy Reviews*, 74: 1–18, 2017, https://doi.org/10.1016/j.rser.2017.01.073.
3. W. Li, N.E. Wierschem, X. Li, T. Yang, On the energy transfer mechanism of the single-sided vibro-impact nonlinear energy sink, *Journal of Sound and Vibration*, 437: 166–179, 2018, https://doi.org/10.1016/j.jsv.2018.08.057.
4. T. Theurich, J. Gross, M. Krack, Effects of modal energy scattering and friction on the resonance mitigation with an impact absorber, *Journal of Sound and Vibration*, 442: 71–89, 2019, https://doi.org/10.1016/j.jsv.2018.10.055.
5. B. Fang, T. Theurich, M. Krack, L.A. Bergman, A.F. Vakakis, Vibration suppression and modal energy transfers in a linear beam with attached vibro-impact nonlinear energy sinks, *Communications in Nonlinear Science and Numerical Simulation*, 91: 105415, 2020, https://doi.org/10.1016/j.cnsns.2020.105415.
6. X. Li, A. Mojahed, L.Q. Chen, L.A. Bergman, A.F. Vakakis, Shock response mitigation of a large-scale structure by modal energy redistribution facilitated by a strongly nonlinear absorber, *Acta Mechanica Sinica*, 38: 121464, 2022, https://doi.org/10.1007/s10409-022-09023-x.
7. Z. Lu, M. Zhou, J. Zhang, Z. Huang, S.F. Masri, A semi-active impact damper for multi-modal vibration control under earthquake excitations, *Mechanical Systems and Signal Processing*, 210: 111182, 2024, https://doi.org/10.1016/j.ymssp.2024.111182.
8. J. Onoda, T. Endo, H. Tamaoki, N. Watanabe, Vibration suppression by variable-stiffness members, *AIAA Journal*, 29(6): 977–983, 1991, https://doi.org/10.2514/3.59943.
9. J.E. Holnicki-Szulc, Z. Marzec, New technique of vibration control, In: *Lecture Notes 1*, J.E. Holnicki-Szulc, ed., Centre of Excellence for Advanced Materials and Structures, IPPT, Warsaw, 2001, https://rcin.org.pl/dlibra/publication/24998/edition/35913/content?ref=L3B1YmxpY2F0aW9uLzI0OTkwL2VkaXRpb24vMzU5MTI.
10. A. Mróz, A. Orłowska, J. Holnicki-Szulc, Semi-active damping of vibrations. Prestress accumulation-release strategy development, *Shock and Vibration*, 17: 126402, 2010, https://doi.org/10.3233/SAV-2010-0502.

11. A. Mróz, J. Holnicki-Szulc, J. Biczyk, Prestress accumulation-release technique for damping of impact-born vibrations: Application to self-deployable structures, *Mathematical Problems in Engineering*, 2015: 720236, 2015, https://doi.org/10.1155/2015/720236.

12. B. Popławski, G. Mikułowski, A. Mróz, Ł. Jankowski, Decentralized semi-active damping of free structural vibrations by means of structural nodes with an on/off ability to transmit moments, *Mechanical Systems and Signal Processing*, 100: 926–939, 2018, https://doi.org/10.1016/j.ymssp.2017.08.012.

13. B. Popławski, G. Mikułowski, R. Wiszowaty, Ł. Jankowski, Mitigation of forced vibrations by semi-active control of local transfer of moments, *Mechanical Systems and Signal Processing*, 157: 107733, 2021, https://doi.org/10.1016/j.ymssp.2021.107733.

14. A. Orłowska, A. Gałęzia, A. Świercz, Ł. Jankowski, Mitigation of vibrations in sandwich-type structures by a controllable constrained layer, *Journal of Vibration and Control*, 27(13-14): 1595–1605, 2021, https://doi.org/10.1177/1077546320946130.

15. H. Zhang, L.R. Corr, T. Ma, Issues in vibration energy harvesting, *Journal of Sound and Vibration*, 421: 79–90, 2018, https://doi.org/10.1016/j.jsv.2018.01.057.

16. F. Cottone, R. Frizzell, S. Goyal, G. Kelly, J. Punch, Enhanced vibrational energy harvester based on velocity amplification, *Journal of Intelligent Material Systems and Structures*, 25: 443–451, 2014, https://doi.org/10.1177/1045389X13498316.

17. M.A. Halim, H. Cho, J.Y. Park, Design and experiment of a human-limb driven, frequency up-converted electromagnetic energy harvester, *Energy Conversion and Management*, 106: 393–404, 2015, https://doi.org/10.1016/j.enconman.2015.09.065.

18. M. Ostrowski, B. Błachowski, M. Bocheński, D. Piernikarski, P. Filipek, W. Janicki, Design of nonlinear electromagnetic energy harvester equipped with mechanical amplifier and spring bumpers, *Bulletin of the Polish Academy of Sciences: Technical Sciences*, 2020, 68(6): 1373–1383, 2020, https://doi.org/10.24425/bpasts.2020.135384.

19. M.M.R. El-Hebeary, M.H. Arafa, S.M. Megahed, Modeling and experimental verification of multi-modal vibration energy harvesting from plate structures, *Sensors and Actuators A: Physical*, 193: 35–47, 2013, https://doi.org/10.1016/j.sna.2013.01.006.

20. L.Q. Chen, Y. Fan, Internal resonance vibration-based energy harvesting, *Nonlinear Dynamics*, 111: 11703–11727, 2023, https://doi.org/10.1007/s11071-023-08464-0.

21. B. Błachowski, A. Świercz, M. Ostrowski, P. Tauzowski, P. Olaszek, Ł. Jankowski, Convex relaxation for efficient sensor layout optimization in large-scale structures subjected to moving loads, *Computer-Aided Civil and Infrastructure Engineering*, 35(10): 1085–1100, 2020, https://doi.org/10.1111/mice.12553.

22. G.W. Housner, L.A. Bergman, T.K. Caughey, A.G. Chassiakos, R.O. Claus, S.F. Masri, R.E. Skelton, T.T. Soong, B.F. Spencer, J.T.P. Yao, Structural control: Past, present, and future, *Journal of Engineering Mechanics*, 123(9): 897–971, 1997, https://doi.org/10.1061/(ASCE)0733-9399(1997)123:9(897).

23. B.L. Zhang, Q.L. Han, X.M. Zhang, Recent advances in vibration control of offshore platforms, *Nonlinear Dynamics*, 89: 755–771, 2017, https://doi.org/10.1007/s11071-017-3503-4.

24. S. Hurlebaus, L. Gaul, Smart structure dynamics, *Mechanical Systems and Signal Processing*, 20(2): 255–281, 2006, https://doi.org/10.1016/j.ymssp.2005.08.025.

25. C.D. Johnson, Design of passive damping systems, *Journal of Vibration and Acoustics*, 117(B): 171–176, 1995, https://doi.org/10.1115/1.2838659.

26. S. Elias, V. Matsagar, Research developments in vibration control of structures using passive tuned mass dampers, *Annual Reviews in Control*, 44: 129–156, 2017, https://doi.org/10.1016/j.arcontrol.2017.09.015.

27. T.T. Soong, B.F. Spencer, Supplemental energy dissipation: state-of-the-art and state-of-the-practice, *Engineering Structures*, 24(3): 243–259, 2002, https://doi.org/10.1016/S0141-0296(01)00092-X.

28. GERB, Tuned Mass Dampers for Bridges, Buildings and Other Tall Structures, Brochure, GERB Schwingungsisolierungen, Berlin, 2012.

29. A. Pavic, M. Willford, P. Reynolds, J.R. Wright, Key results of modal testing of the Millennium Bridge, London, In: *International Conference on the Design and Dynamic Behaviour of Footbridges*, pp. 225–233, 2002, http://vibration.ex.ac.uk/doc/4393_56.pdf.

30. M. Sacks, J. Swallow, Tuned mass dampers for towers and buildings, In: *Structural Engineering in Natural Hazards Mitigation: Proceedings of Papers Presented at the Structures Congress '93*, American Society of Civil Engineers, pp. 640–645, 1993.

31. P. Watts, On a method of reducing the rolling of ships at sea, In: *Transactions of the Institution of Naval Architects*, 26, pp. 165–190, 1883.

32. H. Frahm, Device for Damping Vibrations of Bodies, US Patent US 989958A, 1909.

33. G. Gatti, Fundamental insight on the performance of a nonlinear tuned mass damper, *Meccanica*, 53(1): 111–123, 2018, https://doi.org/10.1007/s11012-017-0723-0.

34. A.Y. Pisal, R.S. Jangid, Dynamic response of structure with tuned mass friction damper, *International Journal of Advanced Structural Engineering*, 8(4): 363–377, 2016, https://doi.org/10.1007/ s40091-016-0136-7.

35. M.H. Alkmim, A.T. Fabro, M.V.G. de Morais, Optimization of a tuned liquid column damper subject to an arbitrary stochastic wind, *Journal of the Brazilian Society of Mechanical Sciences and Engineering*, 40(11): 551, 2018, https://doi.org/10.1007/s40430-018-1471-3.

36. T.P. Sapsis, D. Dane Quinn, A.F. Vakakis, L.A. Bergman, Effective stiffening and damping enhancement of structures with strongly nonlinear local attachments, *Journal of Vibration and Acoustics*, 134(1): 011016, 2012, https://doi.org/10.1115/1.4005005.

37. S.L. Folkman, J.G. Bingham, J.R. Crookston, J.D. Dutson, B.D. Ferney, G.D. Ferney, E.A. Rowsell, *The Joint Damping Experiment (JDX)*, NASA Contractor Report 4781, 1997, https://ntrs.nasa.gov/api/citations/19970021575/downloads/19970021575.pdf.

38. E. Motato, A. Haris, S. Theodossiades, M. Mohammadpour, H. Rahnejat, P. Kelly, A.F. Vakakis, D.M. McFarland, L.A. Bergman, Targeted energy transfer and modal energy redistribution in automotive drivetrains, *Nonlinear Dynamics*, 87(1): 169–190, 2017, https://doi.org/10.1007/s11071-016-3034-4.

39. R.L. Forward, Electronic damping of vibrations in optical structures, *Applied Optics*, 18(5): 690–697, 1979, https://doi.org/10.1364/AO.18.000690.

40. R. Edwards, R. Miyakawa, *Large Structure Damping Task Report*, Hughes Aircraft Co Report (4132.22/1408), 1980.

41. N.W. Hagood, A. von Flotow, Damping of structural vibrations with piezoelectric materials and passive electrical networks, *Journal of Sound and Vibration*, 146(2): 243–268, 1991, https://doi.org/10.1016/0022-460X(91)90762-9.

42. B. Lossouarn, J.F. Deü, G. Kerschen, A fully passive nonlinear piezoelectric vibration absorber, *Philosophical Transactions of the Royal Society A: Mathematical, Physical and Engineering Sciences*, 376(2127): 20170142, 2018, https://doi.org/10.1098/rsta.2017.0142.

43. R. Darleux, B. Lossouarn, J.F. Deü, Passive self-tuning inductor for piezoelectric shunt damping considering temperature variations, *Journal of Sound and Vibration*, 432: 105–118, 2018, https://doi.org/10.1016/j.jsv.2018.06.017.

44. T.P. Sales, D.A. Rade, L.C.G. de Souza, Passive vibration control of flexible spacecraft using shunted piezoelectric transducers, *Aerospace Science and Technology*, 29(1): 403–412, 2013, https://doi.org/10.1016/j.ast.2013.05.001.

45. M.H. Tehrani, P.S. Harvey Jr, Enhanced passive control of dual-mode systems under extreme seismic loading: An optimal control approach, *Structural Control and Health Monitoring*, 26(7): e2367, 2019, https://doi.org/10.1002/stc.2367.

46. C.S. Tsai, T.C. Chiang, B.J. Chen, Finite element formulations and theoretical study for variable curvature friction pendulum system, *Engineering Structures*, 25(14): 1719–1730, 2003, https://doi.org/10.1016/S0141-0296(03)00151-2.

47. P. Shahbazi, T. Taghikhany, Sensitivity analysis of variable curvature friction pendulum isolator under near-fault ground motions, *Smart Structures and Systems*, 20(1): 23–33, 2017, https://doi.org/10.12989/sss.2017.20.1.023.

48. C.J. Swigert, R.L. Forward, Electronic damping of orthogonal bending modes in a cylindrical mast – Theory, *Journal of Spacecraft and Rockets*, 18(1): 5–10, 1981, https://doi.org/10.2514/3.28047.

49. C.R. Fuller, S.J. Elliott, P.A. Nelson, eds., *Active Control of Vibration*, Academic Press, London, 1996, https://doi.org/10.1016/B978-012269440-0/50000-5.

50. R. Alkhatib, M. Golnaraghi, Active structural vibration control: A review, *The Shock and Vibration Digest*, 35: 367–383, 2003.

51. A. Preumont, *Vibration Control of Active Structures,* Springer, 2011, https://doi.org/10.1007/978-94-007-2033-6.

52. Y. Zhang, L. Li, Y. Guo, X. Zhang, Bidirectional wind response control of 76-story benchmark building using active mass damper with a rotating actuator, *Structural Control and Health Monitoring*, 25(10): e2216, 2018, https://doi.org/10.1002/stc.2216.

53. J.N. Yang, A.K. Agrawal, B. Samali, J.C. Wu, Benchmark problem for response control of wind-excited tall buildings, *Journal of Engineering Mechanics*, 130(4): 437–446, 2004, https://doi.org/10.1061/(ASCE)0733-9399(2004)130:4(437).

54. D. Bruijnen, N. van Dijk, Combined input shaping and feedforward control for flexible motion systems, In: *2012 American Control Conference (ACC)*, pp. 2473–2478, 2012, https://doi.org/10.1109/ACC.2012.6315055.

55. A. Dhanda, J. Vaughan, W. Singhose, Vibration reduction using near time-optimal commands for systems with nonzero initial conditions, *Journal of Dynamic Systems, Measurement, and Control*, 138(4): 041006, 2016, https://doi.org/10.1115/1.4032064.

56. M. Wasilewski, D. Pisarski, C.I. Bajer, Adaptive optimal control for seismically excited structures, *Automation in Construction*, 106: 102885, 2019, https://doi.org/10.1016/j.autcon.2019.102885.

57. I. Chopra, Review of state of art of smart structures and integrated systems, *AIAA Journal*, 40(11): 2145–2187, 2002, https://doi.org/10.2514/2.1561.

58. J.N. Juang, K.B. Lim, J.L. Junkins, Robust eigensystem assignment for flexible structures, *Journal of Guidance, Control, and Dynamics*, 12(3): 381–387, 1989, https://doi.org/10.2514/3.20419.

59. M. Ghandchi Tehrani, J.E. Mottershead, A.T. Shenton, Y.M. Ram, Robust pole placement in structures by the method of receptances, *Mechanical Systems and Signal Processing*, 25(1): 112–122, 2011, https://doi.org/10.1016/j.ymssp.2010.04.005.

60. N. Wang, H. Adeli, Algorithms for chattering reduction in system control, *Journal of the Franklin Institute*, 349(8): 2687–2703, 2012, https://doi.org/10.1016/j.jfranklin.2012.06.001.

61. G. Gatti, M.J. Brennan, P. Gardonio, Active damping of a beam using a physically collocated accelerometer and piezoelectric patch actuator, *Journal of Sound and Vibration*, 303(3): 798–813, 2007, https://doi.org/10.1016/j.jsv.2007.02.006.

62. F. Casciati, G. Magonette, F. Marazzi, *Technology of Semiactive Devices and Applications in Vibration Mitigation*, John Wiley & Sons, 2006, https://doi.org/10.1002/0470022914.

63. D. Pisarski, R. Konowrocki, Ł. Jankowski, Scalable distributed optimal control of vibrating modular structures, *Structural Control and Health Monitoring*, 27(4): e2502, 2020, https://doi.org/10.1002/stc.2502.

64. M.U. Saeed, Z. Sun, S. Elias, Research developments in adaptive intelligent vibration control of smart civil structures, *Journal of Low Frequency Noise, Vibration and Active Control*, 41(1): 292–329, 2022, https://doi.org/10.1177/14613484211032758.

65. B. Błachowski, N. Pnevmatikos, Neural network based vibration control of seismically excited civil structures, *Periodica Polytechnica Civil Engineering*, 62(3):620–628, 2018, https://pp.bme.hu/ci/article/view/11601.

66. X. Jiang, H. Adeli, Dynamic fuzzy wavelet neuroemulator for non-linear control of irregular building structures, *International Journal for Numerical Methods in Engineering*, 74(7): 1045–1066, 2008, https://doi.org/10.1002/nme.2195.

67. N.D. Zorić, A.M. Tomović, A.M. Obradović, R.D. Radulović, G.R. Petrović, Active vibration control of smart composite plates using optimized self-tuning fuzzy logic controller with optimization of placement, sizing and orientation of PFRC actuators, *Journal of Sound and Vibration*, 456: 173–198, 2019, https://doi.org/10.1016/j.jsv.2019.05.035.

68. D. Cong Le, J. Zhang, Y. Pang, A novel pipelined neural FIR architecture for nonlinear adaptive filter, *Neurocomputing*, 440: 220–229, 2021, https://doi.org/10.1016/j.neucom.2020.11.036.

69. D. Karnopp, M.J. Crosby, R.A. Harwood, Vibration control using semi-active force generators, *Journal of Engineering for Industry*, 96(2): 619–626, 1974, https://doi.org/ 10.1115/1.3438373.

70. M.D. Symans, M.C. Constantinou, Semi-active control systems for seismic protection of structures: A state-of-the-art review, *Engineering Structures*, 21(6): 469–487, 1999, https://doi.org/10.1016/S0141-0296(97)00225-3.

71. F. Casciati, J. Rodellar, U. Yildirim, Active and semi-active control of structures – Theory and applications: A review of recent advances, *Journal of Intelligent Material Systems and Structures*, 23(11): 1181–1195, 2012, https://doi.org/10.1177/1045389X12445029.

72. P.S. Harvey Jr, H.P. Gavin, J.T. Scruggs, J.M. Rinker, Determining the physical limits on semi-active control performance: A tutorial, *Structural Control and Health Monitoring*, 21(5): 803–816, 2014, https://doi.org/10.1002/stc.1602.

73. B.F. Spencer, S.J. Dyke, M.K. Sain, J.D. Carlson, Phenomenological model for magnetorheological dampers, *Journal of Engineering Mechanics*, 123(3): 230–238, 1997, https://doi.org/10.1061/(ASCE)0733-9399(1997)123:3(230).

74. H. Du, K.Y. Sze, J. Lam, Semi-active H_∞ control of vehicle suspension with magneto-rheological dampers, *Journal of Sound and Vibration*, 283(3): 981–996, 2005, https://doi.org/10.1016/j.jsv.2004.05.030.

75. J. Yang, D. Ning, S.S. Sun, J. Zheng, H. Lu, M. Nakano, S. Zhang, H. Du, W.H. Li, A semi-active suspension using a magnetorheological damper with nonlinear negative-stiffness component, *Mechanical Systems and Signal Processing*, 147: 107071, 2021, https://doi.org/10.1016/j.ymssp.2020.107071.

76. M. Michajłow, Ł. Jankowski, T. Szolc, R. Konowrocki, Semi-active reduction of vibrations in the mechanical system driven by an electric motor, *Optimal Control Applications and Methods*, 38(6): 922–933, 2017, https://doi.org/10.1002/oca.2297.

77. Y. Li, J. Li, B. Samali, J. Wang, Design considerations and experimental studies on semi-active smart pin joint, *Frontiers of Mechanical Engineering in China*, 4(4): 363, 2009, https://doi.org/10.1007/s11465-009-0074-1.

78. Y. Li, J. Li, Dynamic characteristics of a magnetorheological pin joint for civil structures, *Frontiers of Mechanical Engineering*, 9(1): 15–33, 2014, https://doi.org/10.1007/s11465-014-0283-0.

79. S.J. Dyke, B.F. Spencer, M.K. Sain, J.D. Carlson, Modeling and control of magnetorheological dampers for seismic response reduction, *Smart Materials and Structures*, 5(5): 565–575, 1996, https://doi.org/10.1088/0964-1726/5/5/006.

80. Q.P. Ha, N.M. Kwok, M.T. Nguyen, J. Li, B. Samali, Mitigation of seismic responses on building structures using MR dampers with Lyapunov-based control, *Structural Control and Health Monitoring*, 15(4): 604–621, 2008, https://doi.org/10.1002/stc.218.

81. N.M. Kwok, Q.P. Ha, M.T. Nguyen, J. Li, B. Samali, A novel hysteretic model for magnetorheological fluid dampers and parameter identification using particle swarm optimization, *Sensors and Actuators A: Physical*, 132(2): 441–451, 2006, https://doi.org/10.1016/j.sna.2006.03.015.

82. R. Bogacz, C. Bajer, Active control of beams under a moving load, *Journal of Theoretical and Applied Mechanics*, 38(3): 523–530, 2000, https://www.ptmts.org.pl/jtam/index.php/jtam/article/download/v38n3p523/779.

83. M. Wasilewski, D. Pisarski, Adaptive semi-active control of a beam structure subjected to a moving load traversing with time-varying velocity, *Journal of Sound and Vibration*, 481: 115404, 2020, https://doi.org/10.1016/j.jsv.2020.115404.

84. H. Kurino, J. Tagami, K. Shimizu, T. Kobori, Switching oil damper with built-in controller for structural control, *Journal of Structural Engineering*, 129(7): 895–904, 2003, https://doi.org/10.1061/(ASCE)0733-9445(2003)129:7(895).

85. Y. Ikeda, Active and semi-active vibration control of buildings in Japan — Practical applications and verification, *Structural Control and Health Monitoring*, 16: 703–723, 2009, https://doi.org/10.1002/stc.315.

86. M.Q. Feng, M. Shinozuka, S. Fujii, Friction-controllable sliding isolation system, *Journal of Engineering Mechanics,* 119(9): 1845–1864, 1993, https://doi.org/10.1061/(ASCE)0733-9399(1993)119:9(1845).

87. J.A. Inaudi, Modulated homogeneous friction: A semi-active damping strategy, *Earthquake Engineering & Structural Dynamics*, 26(3): 361–376, 1998, https://doi.org/10.1002/(SICI)1096-9845(199703)26:3<361::AID-EQE648>3.0.CO;2-M.

88. S. Laflamme, D. Taylor, M. Abdellaoui Maane, J.J. Connor, Modified friction device for control of large-scale systems, *Structural Control and Health Monitoring*, 19(4): 548–564, 2012, https://doi.org/10.1002/stc.454.

89. D. Zhang, P. Pan, Y. Zeng, Y. Guo, A novel robust optimum control algorithm and its application to semi-active controlled base-isolated structures, *Bulletin of Earthquake Engineering*, 18(5): 2431–2460, 2020, https://doi.org/10.1007/s10518-019-00761-7.

90. D. Hrovat, P. Barak, M. Rabins, Semi-active versus passive or active tuned mass dampers for structural control, *Journal of Engineering Mechanics*, 109(3): 691–705, 1983, https://doi.org/10.1061/(ASCE)0733-9399(1983)109:3(691).

91. M. Setareh, Application of semi-active tuned mass dampers to base-excited systems, *Earthquake Engineering & Structural Dynamics*, 30(3): 449–462, 2001, https://doi.org/10.1002/eqe.19.

92. D. Demetriou, N. Nikitas, K.D. Tsavdaridis, Performance of fixed-parameter control algorithms on high-rise structures equipped with semi-active tuned mass dampers, *The Structural Design of Tall and Special Buildings*, 25(7): 340–354, 2016, https://doi.org/10.1002/tal.1261.

93. S.Y. Chu, S.W. Yeh, L.Y. Lu, C.H. Peng, A leverage-type stiffness controllable mass damper for vibration mitigation of structures, *Structural Control and Health Monitoring*, 24(4): e1896, 2017, https://doi.org/10.1002/stc.1896.

94. Y.F. Liu, T.K. Lin, K.C. Chang, Analytical and experimental studies on building mass damper system with semi-active control device, *Structural Control and Health Monitoring*, 25(6): e2154, 2018, https://doi.org/10.1002/stc.2154.

95. P. Brzeski, T. Kapitaniak, P. Perlikowski, Novel type of tuned mass damper with inerter which enables changes of inertance, *Journal of Sound and Vibration*, 349: 56–66, 2015, https://doi.org/10.1016/j.jsv.2015.03.035.

96. P. Brzeski, M. Lazarek, P. Perlikowski, Experimental study of the novel tuned mass damper with inerter which enables changes of inertance, *Journal of Sound and Vibration*, 404: 47–57, 2017, https://doi.org/10.1016/j.jsv.2017.05.034.

97. O. Altay, S. Klinkel, A semi-active tuned liquid column damper for lateral vibration control of high-rise structures: Theory and experimental verification, *Structural Control and Health Monitoring*, 25(12): e2270, 2018, https://doi.org/10.1002/stc.2270.

98. G.Y. Zhou, Shear properties of a magnetorheological elastomer, *Smart Materials & Structures*, 12(1): 139–146, 2003, https://doi.org/10.1088/0964-1726/12/1/316.

99. B. Dyniewicz, J.M. Bajkowski, C.I. Bajer, Semi-active control of a sandwich beam partially filled with magnetorheological elastomer, *Mechanical Systems and Signal Processing*, 60–61: 695–705, 2015, https://doi.org/10.1016/j.ymssp.2015.01.032.

100. D. Pisarski, T. Szmidt, C.I. Bajer, B. Dyniewicz, J.M. Bajkowski, Vibration control of double-beam system with multiple smart damping members, *Shock and Vibration*, 2016: 2438902, 2016, https://doi.org/10.1155/2016/2438902.

101. D. Pisarski, Decentralized stabilization of semi-active vibrating structures, *Mechanical Systems and Signal Processing*, 100: 694–705, 2018, https://doi.org/10.1016/j.ymssp.2017.08.003.

102. Y. Li, J. Li, W. Li, H. Du, A state-of-the-art review on magnetorheological elastomer devices, *Smart Materials and Structures,* 23(12): 123001, 2014, https://doi.org/10.1088/0964-1726/23/12/123001.

103. A.S. Bicos, Y.H. Pak, C.L. Trent, R.J. Uitto, Passive and active vibration suppression of large space structures, In: E. Udd, ed., *Fiber Optic Smart Structures and Skins II*, Vol. 1170, pp. 359–371, International Society for Optics and Photonics, SPIE, 1990, https://doi.org/10.1117/12.963111.

104. A.A. Ferri, B.S. Heck, Analytical investigation of damping enhancement using active and passive structural joints, *Journal of Guidance, Control, and Dynamics*, 15(5): 1258–1264, 1992, https://doi.org/10.2514/3.20977.

105. L. Gaul, R. Nitsche, Vibration control by interface dissipation in semi-active joints, *ZAMM – Journal of Applied Mathematics and Mechanics / Zeitschrift für Angewandte Mathematik und Mechanik*, 80: 45–48, 2000, https://doi.org/10.1002/zamm.20000801312.

106. L. Gaul, H. Albrecht, J. Wirnitzer, Semi-active friction damping of large space truss structures, *Shock and Vibration*, 11: 173–186, 2004, https://doi.org/10.1155/2004/565947.

107. L. Gaul, S. Hurlebaus, J. Wirnitzer, H. Albrecht, Enhanced damping of lightweight structures by semi-active joints, *Acta Mechanica*, 195: 249–261, 2008, https://doi.org/10.1007/s00707-007-0547-4.

108. J. Onoda, H.U. Oh, K. Minesugi, Semi-active vibration suppression of truss structures by electro-rheological fluid, *Acta Astronautica*, 40(11): 771–779, 1997, https://doi.org/10.1016/S0094-5765(97)00168-9.

109. D.J. Segalman, Modelling joint friction in structural dynamics, *Structural Control and Health Monitoring*, 13(1): 430–453, 2006, https://doi.org/10.1002/stc.119.

110. L. Gaul, R. Nitsche, The role of friction in mechanical joints, *Applied Mechanics Reviews*, 54(2): 93–106, 2001, https://doi.org/10.1115/1.3097294.

111. K. Minesugi, K. Kondo, Semi-active vibration suppression of large space structures with a variable axial stiffness member, In: *34th Structures, Structural Dynamics and Materials Conference*, La Jolla, CA, 1993, https://doi.org/10.2514/6.1993-1693.

112. J.M. Bajkowski, B. Dyniewicz, C.I. Bajer, Semi-active damping strategy for beams system with pneumatically controlled granular structure, *Mechanical Systems and Signal Processing*, 70–71: 387–396, 2016, https://doi.org/10.1016/j.ymssp.2015.09.026.

113. D.J. Inman, Active modal control for smart structures, *Philosophical Transactions of the Royal Society of London Series A: Mathematical, Physical and Engineering Sciences*, 359(1778): 205–219, 2001, https://doi.org/10.1098/rsta.2000.0721.

114. J.D. Simon, S.K. Mitter, A theory of modal control, *Information and Control*, 13(4): 316–353, 1968, https://doi.org/10.1016/S0019-9958(68)90834-6.

115. J.F. Magni, *Robust Modal Control with a Toolbox for Use with* MATLAB®, Springer, Boston, MA, 2002, https://doi.org/10.1007/978-1-4615-0637-9.

116. L. Gould, M. Murray-Lasso, On the modal control of distributed systems with distributed feedback, *IEEE Transactions on Automatic Control*, 11(4): 729–737, 1966, https://doi.org/10.1109/TAC.1966.1098463.

117. M.J. Balas, Active control of flexible systems, *Journal of Optimization Theory and Applications*, 25: 415–436, 1978, https://doi.org/10.1007/BF00932903.

118. H. Öz, L. Meirovitch, Optimal modal-space control of flexible gyroscopic systems, *Journal of Guidance and Control*, 3(3): 218–226, 1980, https://doi.org/10.2514/3.55975.

119. L. Meirovitch, H. Baruh, Control of self-adjoint distributed-parameter systems, In: *AIAA Guidance and Control Conference*, 1980, https://doi.org/10.2514/6.1980-1707.

120. L. Meirovitch, H. Baruh, Control of self-adjoint distributed-parameter systems, *Journal of Guidance, Control, and Dynamics*, 5: 60–66, 1982, https://doi.org/10.2514/3.56140.

121. L. Meirovitch, H. Baruh, Robustness of the independent modal-space control method, *Journal of Guidance, Control, and Dynamics*, 6(1): 20–25, 1983, https://doi.org/10.2514/3.19797.

122. L.Y. Lu, Seismic test of modal control with direct output feedback for building structures, *Structural Engineering and Mechanics*, 12(6): 633–656, 2001, https://doi.org/10.12989/sem.2001.12.6.633.

123. L.Y. Lu, Semi-active modal control for seismic structures with variable friction dampers, *Engineering Structures*, 26(4): 437–454, 2004, https://doi.org/10.1016/j.engstruct.2003.10.012.

124. B. Basu, S.R.K. Nielsen, A multi-modal control using a hybrid pole-placement–integral resonant controller (PPIR) with experimental investigations, *Structural Control and Health Monitoring*, 18(2): 191–206, 2011, https://doi.org/10.1002/stc.367.

125. A.K. Belyaev, A.V. Fedotov, H. Irschik, M. Nader, V.A. Polyanskiy, N.A. Smirnova, Experimental study of local and modal approaches to active vibration control of elastic systems, *Structural Control and Health Monitoring*, 25(2): e2105, 2018, https://doi.org/10.1002/stc.2105.

126. S. Etedali, A new modified independent modal space control approach toward control of seismic-excited structures, *Bulletin of Earthquake Engineering*, 15(10): 4215–4243, 2017, https://doi.org/10.1007/s10518-017-0134-6.

127. M. Ostrowski, A. Jedlińska, B. Popławski, B. Błachowski, G. Mikułowski, D. Pisarski, Ł. Jankowski, Sliding mode control for semi-active damping of vibrations using on/off viscous structural nodes, *Buildings*, 13(2): 348, 2023, https://doi.org/10.3390/buildings13020348.

128. S.P. Chepuri, G. Leus, Sensor selection for estimation, filtering, and detection, In: *2014 International Conference on Signal Processing and Communications (SPCOM)*, pp. 1–5, 2014, https://doi.org/10.1109/SPCOM.2014.6983912.

129. C. Papadimitriou, J.L. Beck, S.K. Au, Entropy-based optimal sensor location for structural model updating, *Journal of Vibration and Control*, 6(5): 781–800, 2000, https://doi.org/10.1177/107754630000600508.

130. C. Schedlinski, M. Link, An approach to optimal pick-up and exciter placement, In: *14th International Modal Analysis Conference*, pp. 376–382, IMAC, Dearborn, USA, 1996, https://doi.org/10.13140/2.1.3105.6327.

131. D.C. Kammer, Sensor placement for on-orbit modal identification and correlation of large space structures, *Journal of Guidance, Control, and Dynamics*, 14(2): 251–259, 1991, https://doi.org/10.2514/3.20635.

132. W.K. Gawronski, *Advanced Structural Dynamics and Active Control of Structures*, 1st ed., Springer, New York, NY, 2004, https://doi.org/10.1007/978-0-387-72133-0.

133. Y. Li, X. Wang, R. Huang, Z. Qiu, Actuator placement robust optimization for vibration control system with interval parameters, *Aerospace Science and Technology*, 45: 88–98, 2015, https://doi.org/10.1016/j.ast.2015.04.017.

134. G. Moloudian, M. Hosseinifard, S. Kumar, R.B.V.B. Simorangkir, J.L. Buckley, C. Song, G. Fantoni, B. O'Flynn, RF energy harvesting techniques for battery-less wireless sensing, Industry 4.0, and Internet of Things: A review, *IEEE Sensors Journal*, 24: 5732–5745, 2024, https://doi.org/10.1109/JSEN.2024.3352402.

135. J. Siang, M.H. Lim, M.S. Leong, Review of vibration-based energy harvesting technology: Mechanism and architectural approach, *International Journal of Energy Research*, 42(5): 1866–1893, 2018, https://doi.org/10.1002/ er.3986.

136. L. Zuo, X. Tang, Large-scale vibration energy harvesting, *Journal of Intelligent Material Systems and Structures*, 24: 1405–1430, 2013, https://doi.org/10.1177/1045389X13486707.

137. R. Sun, S. Zhou, L. Cheng, Ultra-low frequency vibration energy harvesting: Mechanisms, enhancement techniques, and scaling laws, *Energy Conversion and Management*, 276: 116585, 2023, https://doi.org/10.1016/j.enconman.2022.116585.

138. S. Kundu, H.B. Nemade, Piezoelectric vibration energy harvester with tapered substrate thickness for uniform stress, *Microsystem Technologies*, 27: 105–113, 2021, https://doi.org/10.1007/s00542-020-04922-6.

139. A. Anand, S. Kundu, Design of a spiral-shaped piezoelectric energy harvester for powering pacemakers, *Nanomaterials and Energy*, 8(2): 139–150, 2019, https://doi.org/10.1680/jnaen.19.00016.

140. I. Shahosseini, K. Najafi, *Mechanical Amplifier for Translational Kinetic Energy Harvesters*, Vol. 557, p. 012135, IOP Publishing, Awaji Island, Hyogo, 2014, https://doi.org/10.1088/1742-6596/557/1/012135.

141. C. Wang, Q. Zhang, W. Wang, Low-frequency wideband vibration energy harvesting by using frequency up-conversion and quin-stable nonlinearity, *Journal of Sound and Vibration*, 399: 169–181, 2017, https://doi.org/10.1016/j.jsv.2017.02.048.

142. P. Alevras, S. Theodossiades, Vibration energy harvester for variable speed rotor applications using passively self-tuned beams, *Journal of Sound and Vibration*, 444: 176–196, 2019, https://doi.org/10.1016/j.jsv.2018.11.007.

143. E.L. Wilson, *Three Dimensional Static and Dynamic Analysis of Structures: A Physical Approach with Emphasis on Earthquake Engineering*, 3rd ed., Computers and Structures, Berkeley, CA, 2000.

144. M. Ostrowski, B. Błachowski, B. Popławski, D. Pisarski, G. Mikułowski, Ł. Jankowski, Semi-active modal control of structures with lockable joints: General methodology and applications, *Structural Control and Health Monitoring*, 28(5): e2710, 2021, https://doi.org/10.1002/stc.2710.

145. W.L. Poston, R.H. Tolson, Maximizing the determinant of the information matrix with the effective independence method, *Journal of Guidance, Control, and Dynamics*, 15(6): 1513–1514, 1992, https://doi.org/10.2514/3.11419.

146. A. Isidori, *Nonlinear Control Systems*, 3rd ed. Springer, London, 1995, https://doi.org/10.1007/978-1-84628-615-5.

147. K. Kęcik, A. Mitura, S. Lenci, J. Warmiński, Energy harvesting from a magnetic levitation system, *International Journal of Non-Linear Mechanics*, 94: 200–206, 2017, https://doi.org/10.1016/j.ijnonlinmec.2017.03.021.

148. K. Kęcik, Energy recovery from a non-linear electromagnetic system, *Acta Mechanica et Automatica*, 12(1): 11–18, 2018, https://doi.org/10.2478/ama-2018-0002.

149. K. Kęcik, Assessment of energy harvesting and vibration mitigation of a pendulum dynamic absorber, In: *Mechanical Systems and Signal Processing*, Vol. 106, pp. 198–209, 2018, https://doi.org/10.1016/j.ymssp.2017.12.028.

150. D. De Klerk, D.J. Rixen, S.N. Voormeeren, General framework for dynamic substructuring: History, review and classification of techniques, *AIAA Journal*, 46(5): 1169–1181, 2008, https://doi.org/10.2514/1.33274.

151. M.S. Allen, D. Rixen, M. van der Seijs, P. Tiso, T. Abrahamsson, R.L. Mayes., Preliminaries: Primal and dual assembly of dynamic models, In: *Substructuring in Engineering Dynamics: Emerging Numerical and Experimental Techniques*, Vol. 594, pp. 5–24, Springer International Publishing, Cham, 2020, https://doi.org/10.1007/978-3-030-25532-9_2.

152. M. Ostrowski, G. Mikułowski, B. Błachowski, Ł. Jankowski, Experimental assessment of Bayesian and mode matching approaches for parametric identification of bolted connections, *Mechanical Systems and Signal Processing*, 201: 110652, 2023, https://doi.org/10.1016/j.ymssp.2023.110652.

153. M. Ostrowski, B. Błachowski, G. Mikułowski, Ł. Jankowski, Influence of noise in computer-vision-based measurements on parameter identification in structural dynamics, *Sensors*, 23(1): 291, 2023, https://doi.org/10.3390/s23010291.

154. B. Błachowski, A. Świercz, P. Gutkiewicz, J. Szelążek, W. Gutkowski, Structural damage detectability using modal and ultrasonic approaches, *Measurement*, 85: 210–221, 2016, https://doi.org/10.1016/j.measurement.2016.02.033.

155. M. Friswell, J.E. Mottershead, *Finite Element Model Updating in Structural Dynamics*, Springer, Dordrecht, 1995, https://doi.org/10.1007/978-94-015-8508-8.

156. J.E. Mottershead, M. Link, M.I. Friswell, The sensitivity method in finite element model updating: A tutorial, *Mechanical Systems and Signal Processing*, 25(7): 2275–2296, 2011, https://doi.org/10.1016/j.ymssp.2010.10.012.

157. K.V. Yuen, J.L. Beck, L.S. Katafygiotis, Efficient model updating and health monitoring methodology using incomplete modal data without mode matching, *Structural Control and Health Monitoring*, 13(1): 91–107, 2006, https://doi.org/10.1002/stc.144.

158. K.V. Yuen, *Bayesian Methods for Structural Dynamics and Civil Engineering*, John Wiley & Sons, 2010, https://doi.org/10.1002/9780470824566.

159. M.B. Hermansen, J.J. Thomsen, Vibration-based estimation of beam boundary parameters, *Journal of Sound and Vibration*, 429: 287–304, 2018, https://doi.org/10.1016/j.jsv.2018.05.016.

160. M. Brøns, J.J. Thomsen, Vibration-based estimation of boundary stiffness and axial tension in beams using added mass, *Journal of Sound and Vibration*, 487: 115617, 2020, https://doi.org/10.1016/j.jsv.2020.115617.

161. M. Ostrowski, B. Błachowski, B. Wójcik, M. Żarski, P. Tauzowski, Ł. Jankowski, A framework for computer vision-based health monitoring of a truss structure subjected to unknown excitations, *Earthquake Engineering and Engineering Vibration*, 22(1): 1–17, 2023, https://doi.org/10.1007/s11803-023-2154-3.

162. B. Błachowski, Modal sensitivity based sensor placement for damage identification under sparsity constraint, *Periodica Polytechnica Civil Engineering*, 63(2): 432–445, 2019, https://doi.org/10.3311/PPci.13888.

163. J.V. Beck, K.J. Arnold, *Parameter Estimation in Engineering and Science*, John Wiley & Sons, 1977, https://doi.org/10.1002/aic.690240233.

164. R.L. Fox, M.P. Kapoor, Rates of change of eigenvalues and eigenvectors, *AIAA Journal*, 6(12): 2426–2429, 1968, https://doi.org/10.2514/3.5008.

165. R.B. Nelson, Simplified calculation of eigenvector derivatives, *AIAA Journal*, 14(9): 1201–1205, 1976, https://doi.org/10.2514/3.7211.